THÈSE DE DOCTORAT

DE L'UNIVERSITÉ PIERRE ET MARIE CURIE

Spécialité : Physique

École doctorale : «Physique en Île-de-France»

réalisée

à SPEC CEA Saclay

présentée par

Kristinn JÚLÍUSSON

Pour obtenir le grade de :

DOCTEUR DE L'UNIVERSITÉ PIERRE ET MARIE CURIE

Sujet de la thèse :

Dynamique Zénon quantique en électrodynamique quantique avec circuit

Soutenue le 15/09/2016

devant le jury composé de:

Dr.	Peter Leek	Rapporteur
Dr.	Olivier Buisson	Rapporteur
Prof.	Jean-Michel Raimond	Examinateur
Dr.	Benjamin Huard	Invité
Dr.	Mazyar Mirrahimi	Invité
Dr.	Denis Vion	Directeur de thèse


UPMC
SORBONNE UNIVERSITÉS


DE LA RECHERCHE À L'INDUSTRIE
cea

Doctoral thesis at the University
Pierre and Marie Curie

Quantum Zeno dynamics in 3D circuit-QED

Presented by
Kristinn Júlíusson

On September 15th 2016 to jury members:
Dr. Peter Leek (reviewer)
Dr. Olivier Buisson (reviewer)
Prof. Jean-Michel Raimond
Dr. Benjamin Huard
Dr. Mazyar Mirrahimi
Dr. Denis Vion (thesis director)

Work conducted in the Quantronics group at the solid state physics department SPEC of CEA Saclay

Table of contents

Acknowledgments.
During this thesis period I have had the support of many people whom I would like to thank.

First of all I would like to thank my supervisor Denis Vion for his incredible effort to this work and guidance during the thesis, as well as interesting discussions about life in general and many a ride back to the train station. My co-supervisors Daniel Esteve and Patrice Bertet were also very helpful in solving particular problem as well as planning general course of the experiments. Many a thanks goes to Simon Bernon who worked as a post-doc on the project with me during the first 10 months. Our circuit-QED implementation of the quantum Zeno dynamics (QZD) is to a large extent his idea. Helene le Sueur was a great help when she joined the project during the tomography measurements of the QZD and contributed a lot to the implementation Maximum Likelihood. We benefited from a parametric amplifier made by Xin Zhou which made measurement a lot easier.

I had very good technical support from Pief Orfila especially with matters concerning the clean-rooms, and from Pascal Senat designing the cavities and other mechanical parts, and from our mechanical workshop I would like to thank Dominique Duet and Vincent Padilla. The support from Patrick Pari and Philippe Forget at the cryogenics lab at SPEC was extremely valuable when we had problems with our dilution refrigerator.

From outside the lab I would like to thank Pierre Rouchon for his help in developing the Maximum Likelihood algorithm we used to process our data and Mazyar Mirrahimi for fruitful discussions concerning measurement strategies and help in modeling the QZD numerically.

I very much like to thank my office mate Audrey Bienfait for good times and bad, countless lunches brought for me when I couldn't go to the canteen and rides back to Paris. My gratitude goes out to the rest of the Quantronics group for their help and company.

I would like to thank my roommates a during the period Coline Laugraud, Yann Bermond and David Gössmann for fantastic years, laughs and parties. And Finally I would like to thank my family and my parents Júlíus and Svanhvít for their love and support throughout it all.

Chapter 1

Introduction and summary

One of the fundamental postulates of quantum mechanics is the back action of a measurement on a quantum system. It is a non-unitary process which projects the system onto an eigenspace of the observable and the measurement outcome is the corresponding eigenvalue. Measurements are usually considered to be instantaneous and temporally separate events in between which the system evolves. In 1977 however, Misra and Sudarshan [32] put forth the theoretical framework for a continuously monitored quantum system and found that it suppresses the evolution of measurement outcomes. They named the phenomenon the quantum Zeno effect(QZE) in reference to a paradox by the Greek philosopher Zeno of Elea on blocked motion in classical dynamics.

Continuing from there but shifting the focus from measurement observables to the dynamics of the monitored system, initial theoretical work has been done by Facchi and Pascazio introducing the quantum Zeno dynamics(QZD). An experimental proposal put forth by Raimond *et al.* [40] for a cavity-QED system showed interesting dynamics in multidimensional subspaces created by the QZD. The work presented here addresses the experimental observation of QZD in a cavity-QED system based on superconducting circuits known as 3D circuit-QED.

This chapter first sets the framework for the experiments presented by tracing the history of quantum mechanics, the development of circuit-QED and its current state and outlook. The subsequent sections introduce the content of the thesis in an executive summary covering the experimental concept, technical building blocks, results, analysis and conclusions.

1.1 Quantum mechanics: From theory to experiments on single quantum systems

At the beginning of the 20th century experiments revealed that classical physics could not fully explain the behavior of atoms and their interaction with light. In response, quantum mechanics was created and by the 1930s a comprehensive theoretical framework had emerged for describing the behavior of atoms and sub-atomic particles. The most common interpretation of the formalism, known as the Copenhagen interpretation, contains some strange features that become even more surprising when considering individual quantum systems. Early on, observing these features was beyond experimental techniques and some physicists even believed that quantum theory was incomplete. One of the best known attempts at demonstrating that is the so called EPR paradox by Einstein, Podolsky, and Rosen [17]. In order to complete quantum theory, the skeptics proposed an incorporation of local hidden variables. In 1964 J.S. Bell published a theorem which proposes a way to test this local hidden variable hypothesis experimentally [9]. He introduced a correlation measure between two particles initially entangled, whose value has an upper bound which is lower in the hidden variable theory than in quantum theory. Improvements such as reformulations of Bell's theory and better experimental techniques on single quantum systems, led to an experiment by Aspect *et al.* in 1982 on photon pairs [3] where the value of the correlation measure exceeded that allowed in the hidden variable theory.

During the following decades, the measurement and control of individual quantum systems became a fruitful research field as acknowledged by the Nobel prize awarded to David Wineland and Serge Haroche in 2012. Wineland and his group managed to trap arrays of ions in an RF electric field trap, cool them down to their ground state and coherently manipulate them with lasers. The Haroche group on the other hand developed superconducting microwave cavities which could store photons for up to 130 ms. By letting highly excited Rydberg atoms pass through a cavity and interact with the photons they could perform a non-destructive measurement of a photon in the the cavity. This field is known as cavity quantum electro dynamics (cavity-QED).

The canonical example of a cavity-QED system is that of a two level system(TLS, also regarded as an effective spin 1/2) coupled to the electromagnetic field of the cavity (regarded as a single mode harmonic oscillator). When the interaction rate between the two systems

is stronger than their loss rates (so-called strong coupling regime) the cavity can probe the spin state in a non-destructive manner and vice versa.

Experiments in the single quantum system regime that started out with Rydberg atoms in cavities and trapped ions have since spread out to a variety of platforms for quantum mechanics such as semiconductor quantum dots, mechanical oscillators, cold atoms, or impurities in solids. One of the most successful implementation has been with superconducting circuits where the prospect of quantum information processing(QIP) has been a big incentive. These circuits are based on the LC-oscillator where the linear inductance is replaced by an element called a Josephson junction (JJ). The nonlinear inductance of the JJ breaks up the equidistant level spacing of a harmonic LC-oscillator, thus allowing two states to be isolated as a TLS which can represent a quantum bit (qubit). The TLS excitation frequency is usually in the few GHz range and operations such as transition between levels can be below 10 ns. The first superconducting qubit was demonstrated by Nakamura *et al.* [34] in 1999, and had a nanosecond. In 2002 Vion *et al.* [47] reported lifetimes of 500 ns with a circuit partly immune to decoherence and fitted with single shot qubit readout, thus truly opening measurements on individual quantum circuits. In 2004 a successful adaptation of cavity-QED to superconducting circuits was reported by Wallraff *et al.* [49] following a proposal by Blais *et al.* [6] of a superconducting qubit coupled to a transmission line microwave resonator, thereby creating the field of circuit-QED. In comparison with Rydberg atoms, these man made superconducting qubits have the benefit of parameter tailoring which allowed for stronger coupling than possible in cavity-QED. The ability to tailor the qubit design proved to be useful again when a new design called a transmon solved the debilitating problem of the qubit sensitivity to fluctuating charges in its surroundings (Koch *et al.* [28]).

The next significant improvement in the field of circuit-QED came in 2011 when Paik *et al.* redesigned the transmon qubit in order to couple it to the electric field inside a bulk 3D cavity resonator [37]. The reduced importance of lossy dielectrics in this 3D circuit-QED design yielded a sizable improvement coherence times, with both T_1 and T_2 around 100 μs [43] in single qubit circuits.

Recent experiments in 3D circuit-QED focus on the dynamics of coherent states in cavities, including superpositions thereof, both for fundamental physics experiments and Quantum information processing

[27][31]. As proposed by Raimond *et al.* [40] QZD provides a powerful tool to manipulate individual components of coherent states. In this thesis, the quantum Zeno dynamics is explored in a 3D circuit-QED system tailored for that purpose.

1.2 Thesis summary

The work presented in this thesis aims at exploring the quantum Zeno dynamics in a harmonic oscillator evolving under a coherent resonant drive.

We first discuss the general dynamics in an arbitrary Hilbert space before introducing a special case proposed for a cavity-QED experiment analog to Raimond *et al.* [40]. Thereafter the development of the experimental building blocks is described along followed by the sample characterization. Next a measurement technique called Wigner tomography is introduced followed by the experimental observation of the QZD. Numerical simulations of the experimental results are used to analyze the experimental imperfections before giving final conclusions.

1.3 General QZD

One of the fundamental postulates of quantum mechanics is the measurement postulate: The effect of a measurement on a quantum system is to project it onto the eigenstate corresponding to the measured eigenvalue. Let us consider an initial measurement giving the eigenvalue ϵ_i corresponding to the measurement projector P_i, and a Hamiltonian H acting on the system that does not commute with P_i (i.e. $[H, P_i] \neq 0$). Immediately after the measurement the probability of measuring ϵ_i is $\pi_i(0) = 1$ but after non-zero time t the unitary evolution $U(t) = \exp(-iHt)$ yields generically $\pi_i(t) < 1$. If the measurement however is repeatedly performed at intervals τ that are much shorter than the characteristic evolution time, the evolution of π_i away from unity is hindered and in the limit $\tau \to 0^+$ it is completely blocked. This is known as the quantum Zeno effect (QZE). Facchi *et al.* have in 3 papers [19][18][20] explored the QZE in the context of the evolution of the projected system as it divides Hilbert space into subspaces. The system

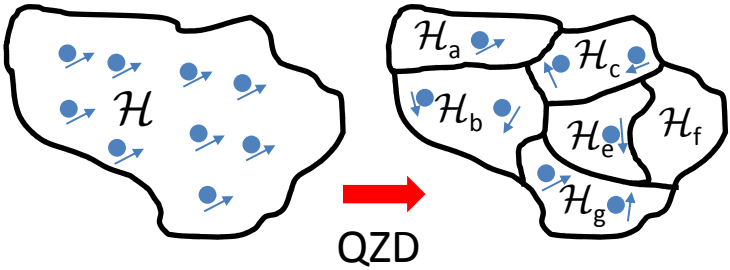

Figure 1.1. Schematic representation of the quantum Zeno dynamics. The QZD can be used to compartmentalize Hilbert space into subspaces, each one having different dynamics.

then evolves within each subspace, which gives rise to the quantum Zeno dynamics (QZD). Facchi *et al.* explain that in the $\tau \to 0^+$ limit, the measurements are a unitary process, and they extend the blocking effect to other types of unitaries coupling the initial system to external degrees of freedom.

In a proposal by Raimond *et al.*, the QZD of a coherently driven harmonic oscillator is explored in the context of cavity-QED [39][40]. The strong coupling of the electric field in the cavity to Rydberg atoms enables selective manipulation of any Fock states $|n\rangle$, the eigenstates of the operator measuring the number n of excitation or photons in the cavity. By either a projective measurement or a unitary evolution addressing only a specific Fock state $|n = n_0\rangle$ one can keep the population probability of this state at zero. This creates an exclusion circle (EC) of radius $\beta = \sqrt{n_0}$ in phase space and splits the Hilbert space $\mathcal{H} = \mathcal{H}_{n<n_0} \oplus \mathcal{H}_{n=n_0} \oplus \mathcal{H}_{n>n_0}$ into three parts. Although $\mathcal{H}_{n<n_0}$ and $\mathcal{H}_{n>n_0}$ both evolve under the same drive their different boundary conditions lead to different dynamics. Details are given in Chapter 2.

1.4 Designing a QZD setup for 3D circuit-QED

Implementing the experiment required both a conceptual and technical adaptation to circuit-QED, which required innovative solutions.

1.4.1 Theoretical design

We describe now how we met the challenge of combining Fock state selective manipulation while introducing minimal non-linearities in the harmonic oscillator, by using a transmon qubit.

A transmon is a multilevel superconducting circuit that we simplify here to a 3-level system (3LS) with levels $|g\rangle, |e\rangle$ and$|f\rangle$ and excitation frequencies ω_{ge} and $\omega_{ef} = \omega_{ge} + \alpha$. When coupled to a harmonic oscillator with resonance frequency ω_0 (see fig. 1.2), the system is described by a generalized Jaynes-Cummings Hamiltonian

$$H_{\mathrm{JC3}} = \hbar(\omega_0 a^\dagger a + \omega_{ge}|e\rangle\langle e| + (\omega_{ge} + \omega_{ef})|f\rangle\langle f| + g_0(a^\dagger a_q + a_q^\dagger a)\,),$$

where a and $a^\dagger$ are the annihilation and creation operators for the harmonic system, a_q and $a_q^\dagger$ the analogs for the transmon and g_0 (or vacuum Rabi splitting) between the two. In the dispersive case with detuning $\Delta_{ge} = \omega_0 - \omega_{\mathrm{ge}}$ much larger than g_0, a residual Kerr-nonlinearity $K = \alpha\Big(\frac{g_0^2}{\Delta_{ge}^2 + \alpha\Delta_{ge}}\Big)^2$ is inherited by the harmonic oscillator when the 3LS is in $|g\rangle$. This causes undesired dephasing between the Fock states as explained in chapter 2. For Fock state selective excitation of the Transmon while keeping K low, we devise a scheme where $\omega_{ef} = \omega_0$. This gives rise to new dressed states

$$|\pm, n\rangle = \frac{|e, n\rangle \pm |f, n-1\rangle}{\sqrt{2}} \quad \big(|q, n\rangle = |q\rangle \otimes |n\rangle\big),$$

with frequencies shifted to $\omega_{\pm,n}$, where $\omega_{\pm,n} = \omega_{ge} \pm \sqrt{2}\, g_0\sqrt{n}$. Consequently, Fock state dependent excitation of the Transmon is possible at frequency $\omega_{+,n}$, which can be used for manipulating Fock state $|n\rangle$ or mapping its occupation probability $p(n)$ onto the transmon excitation probability. This $\omega_0 = \omega_{ef}$ scheme yields a sufficient separation $\omega_{\pm,n+1} - \omega_{\pm,n} = \pm\sqrt{2}\, g_0(\sqrt{n+1} - \sqrt{n})$ between adjacent states even with a low g_0, which in return yields a small non linearity K when the 3LS is left in $|g\rangle$.

Figure 1.2 illustrates three protocols for implementing the QZD mentioned above, i.e blocking Fock state $|n = n_0\rangle$. The first two (see c and d) are described in [39], where a coherently driven cavity undergoes a unitary evolution $U(t) = \exp(-\mathrm{iHt}/\hbar)$ interrupted N times by either

projective measurements or unitary kicks considered to be instantaneous.

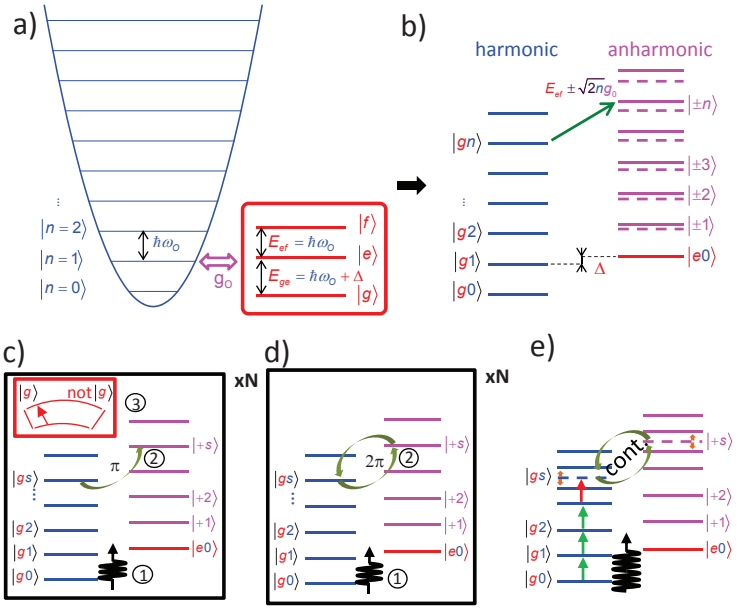

Figure 1.2. a) Harmonic oscillator is coupled to a 3 level atom, resonant with the $|e\rangle \rightarrow |f\rangle$ transition at $\omega_0/2\pi = \omega_{ef}/2\pi = 6.4$GHz. The $|g\rangle \rightarrow |e\rangle$ transition is off-resonant by $\Delta/2\pi = 260$ MHz. b) A coupling strength $g_0/2\pi = 8$ MHz is weak enough to preserve the harmonic oscillator when the atom is in its ground state but strong enough to induce an anharmonic oscillator when the atom is excited. This allows for photon number dependent manipulations of the atom. QZD can be induced by alternating a coherent drive pulse at ω_0 and blockade on Fock state $|n_0\rangle$ by either c) applying a π pulse at ω_{+,n_0} followed by a projective readout of the 3LS, d) applying a 2π pulse inducing a selective phase $(-1)^{\delta_{n,n_0}}|n\rangle$. e) The third method of inducing the QZD is by applying a continuous drive at ω_0 and another one at ω_{+,n_0} which splits up the $|n_0\rangle$ level rendering it off resonant from ω_s.

The third method is not presented in ref. [39] but has been used in our experiment and in [8][45]. It consists in applying a continuous tone at frequency ω_{+,n_0} and amplitude Ω_{block} to block $|n=n_0\rangle$ when its population probability is zero. Photons from this tone dress the states $|g,n_0\rangle$ by separating them by $2\Omega_{\text{block}}$. Once the blocking tone has been turned on, another continuous signal is applied at ω_s which drives the harmonic oscillator. Exciting the $|g,n_0\rangle$ state is however off-resonant and thus leaves the dynamics confined to $n < n_0$ and $n > n_0$. Details are given in chapter 2.

1.4.2 Physical implementation

We adapted the ideas described above to a 3D circuit-QED platform described in details in chapter 5. The 3LS is represented by the lowest three levels of a Transmon qubit with anharmonicity $\alpha / 2\pi = -260$ MHz, and the harmonic oscillator by a high Q mode (TE 120) of a superconducting parallelepiped cavity in aluminium made of two parts. This mode devoted to storing the quantum field is called storage mode. In order to maximize its internal quality factor Q_0 we use high purity aluminium (>99.99%) and avoid putting obstacles across the supercurrents lines. To achieve the resonance condition $\omega_{\text{ef}} = \omega_0$ the transmon junction has a SQUID geometry making it frequency-tunable with a magnetic field. Since magnetic field cannot penetrate the superconducting aluminium, the SQUID of the transmon is left outside the superconducting cavity. For this end, a part of the transmon chip sticks out of the cavity through a slit milled in a designated thin wall (1mm-thick), with the SQUID located inside a small copper cap (see fig. 1.3). The transmon geometry and location on the chip is designed such that it couples to the electric field inside the cavity. A Helmholtz coil is then used to control the magnetic flux threading the SQUID loop. For transmon readout, we use the third mode of the cavity (TE210) dispersively coupled to the transmon. As depicted in fig. 1.3, the resonance frequency ω_r of this readout mode depends on the transmon state $|g\rangle$, $|e\rangle$, or $|f\rangle$. For readout a microwave pulse at the resonance frequency corresponding to $|g\rangle$ is sent to the cavity. The transmitted amplitude then discriminates $|g\rangle$ from the other states (*not* $|g\rangle$). The storage mode requires as long a life time as possible. It also requires a relatively weak coupling of $g_0 / 2\pi = 8$ MHz to achieve a low Kerr non-linearity $K / 2\pi = 500\,\text{Hz}$ nevertheless strong enough to resolve at least 15 photon number states. On the contrary, the readout mode is strongly coupled to the transmon with $g_r / 2\pi = 150$ MHz for good readout contrast, and has a low Purcell limited quality factor $Q_r = 1.2 - 1.8 \cdot 10^4$ for fast enough readout. These parameters are achieved by placing the cavity slit (and thereby the transmon) close to a node of the storage mode, and to an antinode of the readout mode, given the field distribution of these modes inside the cavity, analogous to ref [29]. Following the same principle, we couple very weakly the storage mode to the ports, leaving its quality factor limited by internal losses, while coupling strongly the readout mode. Moreover the coupling is asymmetrical such that the Q-factor of the readout mode is mostly

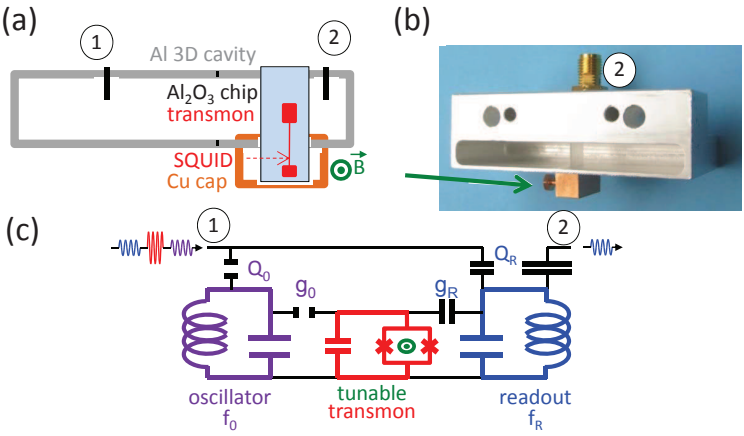

Figure 1.3. a) Illustration of the 3D circuit QED implementation. An Al cavity with two ports (1), (2). A transmon qubit on a sapphire substrate is inserted into the cavity through a slit in the wall such that it is partially outside the cavity. It is covered with a Cu cap allowing a magnetic field to penetrate the SQUID. b) A photograph of one half of the cavity with the transmon and Cu cap mounted. c) A lumped element representation of the system. Microwave signals arrive at (1) and leave via (2). Ports a are weakly coupled to the oscillator (internal loss limited) and strongly coupled to the Readout mode (external loss limited) in a asymmetric manner, favoring photons leaving via (2). The frequency-tunable transmon is strongly coupled to the readout mode ($g_r/2\pi = 150$MHz) but weakly coupled to the oscillator $g_0/2\pi = 8$ MHz. d) Transmission through the readout mode when the transmon has been prepared in $|g\rangle$(red), $|e\rangle$(green) and $|f\rangle$(black).

limited by its coupling to the output port. For quantitative determination of the design parameters we use a 3D finite-element microwave simulation software called CST [53] (see chapter 6.2). The simulated design is shown in fig. 1.4. We start with an empty cavity consisting of a 3D volume and bounded by a perfect conductor. Ports are then defined as the external boundaries of the coupling pins. To characterize an empty CST simulates the S-parameter matrix in a chosen frequency range or retrieves directly the eigenmode frequencies and Q-factors.

The sapphire chip is added can be added to the structure as well as the transmon in the form of 2D metallic sheets and a port at the location of the SQUID [35]. The admittance of the fixed part of the coupled system $Y(\omega) = Z^{-1}(\omega)$ is then simulated as a 1 port device. Exporting

the simulated admittance and adding in parallel the tunable Josephson inductance of the SQUID yields the total admittance $Y_{\text{total}}(\omega)$, and the resonance frequencies ω_{res} of the coupled system are determined by $\text{Im}[Y_{\text{total}}(\omega_{\text{res}})] = 0$ as depicted in fig. 1.4e. Varying the added inductance simulates a magnetic field variation applied to the SQUID and yields the anticrossing of the transmon with the various modes, determining g_0 and g_r at the smallest resonance separation as shown in fig. 1.4f. The behavior of the total admittance at low frequencies $\omega \ll \omega_{\text{res}}$ is $\text{Im}[Z_{\text{total}}(\omega)] \simeq \frac{-1}{\omega C}$ which gives and estimate on C and consequently E_C. In this manner we tune the shape and location of the transmon to reach the desired parameters. We found that our simulations underestimate C, g_0 and g_r by about 20%.

1.5 Sample fabrication and sample characterization

Getting the setup together requires development of a few individual elements. First we made and analyzed a 3D-transmon with state of the art lifetimes. That transmon design was then modified to fit a cavity in a sample optimized for the QZD.

1.5.1 Fabrication and characterization of a 3D transmon

At the beginning of the PhD period the field of 3D circuit-QED was quite new and no 3D qubit had been measured in the group. The first task was therefore to make a 3D transmon, as reported in details in chapter 5. We were particularly interested in the energy relaxation time T_1 and coherence time T_2 because of the improvements reported by early experiments in 3D circuit-QED. Frequency tunability being an advantage for characterizing the transmon decoherence sources, we designed this transmon with a SQUID and put it in a copper cavity transparent to magnetic field. This transmon has similar dimensions to the ones already reported by Paik *et al.* [37] and is fabricated on a high resistivity Si substrate (>4000 Ωcm). Its anharmonicity is $\alpha/2\pi = -358\,\text{MHz}$ and its coupling to the first cavity mode is $g_r/2\pi = 90\,\text{MHz}$.

In our experiment the low quality factor Q∼7000 of the Cu cavity at $\omega_0/2\pi$=7 GHz happens to be the main relaxation channel for the transmon. In the dispersive regime, this relaxation via the cavity mode ,

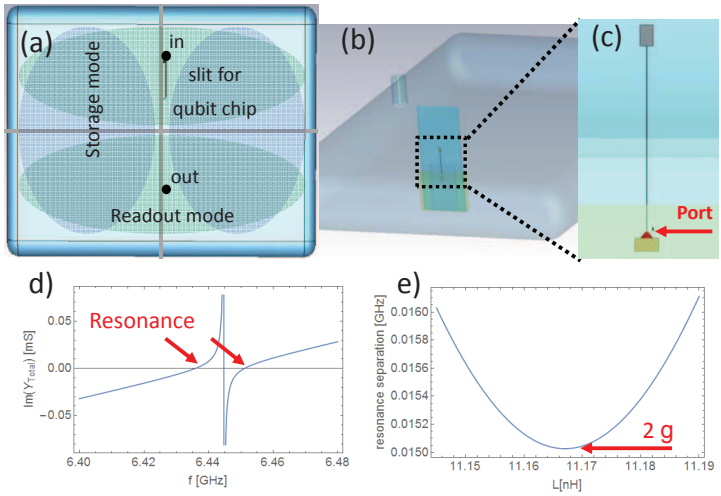

Figure 1.4. Design and simulation of the system. a) Schematic of the geometric distribution of the storage and readout mode within the cavity. Slit, the input port and are shown at the node/antinode of the storage/readout mode. b) A screen shot of the of the finite-element simulation cavity. c) A zoom-in on the simulated transmon with a port at the location of the SQUID. d) The simulated admittance $\mathrm{Im}[Y(\omega)]$ after adding the SQUID inductance. The roots $\mathrm{Im}[Y(\omega_{\mathrm{res}})]=0$ represent resonance frequencies. e) The anticrossing is simulated varying the SQUID inductance. The minimum separation is the coupling strength g_0.

known as Purcell relaxation, is given by the Purcell decay rate $\Gamma_{\mathrm{Purcell}} = \kappa(g_0/\Delta_{ge})^2$, with $\kappa = \omega/Q$ the cavity decay rate. As depicted in fig. 1.5, T_1 increases at low ω_{ge} where an increased detuning Δ_{ge} lowers $\Gamma_{\mathrm{Purcell}}$. Relaxation times $T_1 > 40\mu s$[1.1] are reached before limited readout contrast and lower T_2 prevent further T_1 measurements at low frequencies. The inset of fig. 1.5b shows T_2 at various frequencies. Three terms contribute to the decoherence rate :

$$\Gamma_2 = \frac{\Gamma_1}{2} + \Gamma_{\varphi,\mathrm{Th}} + \Gamma_{\varphi,\phi}.$$

The first term is the contribution of relaxation that sets the upper limit $T_2 \leqslant 2T_1$, and the two other ones are dephasing rates, $\Gamma_{\varphi,\mathrm{Th}}$ due to the residual thermal population of photons in the storage mode and $\Gamma_{\varphi,\phi}$

1.1. Throughout the thesis lifetimes will be defined as $\pi_x(T_x) = 1/e$ where $\pi_x(0) = 1$, and decay rates will be defined as $\Gamma_x = T_x^{-1}$.

due to the flux noise in the SQUID loop. Both effects induce noise on transmon frequency, the degree of which varies with the transmon frequency in different ways. The photon noise affects the cavity frequency pull $\chi = g_0^2(1/\Delta_{ge} - 1/\Delta_{ef})$ per photon in the cavity and has a greater noise contribution at small detunings Δ_{ge}. In addition to the thermal population, the photon number noise also determined by the mode decay rate(i.e. $\Gamma_{\varphi,\mathrm{th}}(\chi, n_{\mathrm{th}}, \kappa)$). A thermal photon population of 0.22% was measured in the cavity. The amount of flux noise in the SQUID loop translates into frequency noise and scales as $|\partial\omega_{ge}/\partial\phi|$, hence having no noise contribution at the maximal frequency. The flux noise is characterized by its spectral density and was found to be predominantly 1/f noise with $8\,\mu\phi_0/\sqrt{\mathrm{Hz}}$ at 1 Hz.

Another Transmon was made on a sapphire substrate, which is more compatible with high-Q cavities as it has a lower loss tangent than silicon. The parameters were very similar to the ones discussed and well suited for the QZD experiment, as discussed in chapter 5.

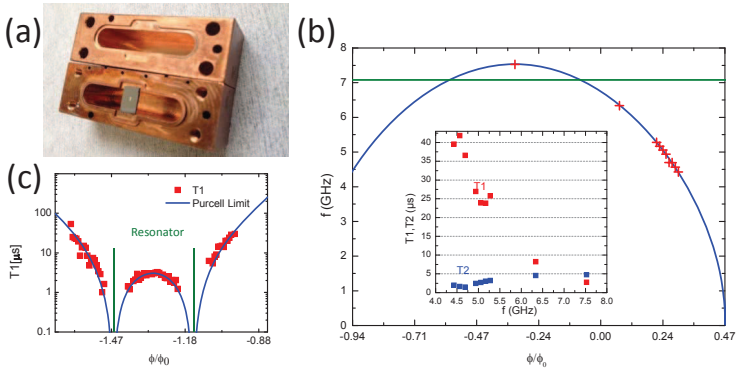

Figure 1.5. a) A Transmon fabricated on a Si substrate in a Cu cavity. b) The expected behavior of the excitation frequency transmon with a SQUID(blue line) under a flux bias ϕ is fitted to the measured excitation frequencies(red crosses). The green line indicates the resonance frequency of the cavity. Inset) T_1 and T_2 at different frequencies. The Purcell decay subside as detuning from the cavity increases at the same time as the sensitivity to flux noise increases and lowers T_2. c) The measured T_1 (red dot) compared with the Purcell limit (blue line). The frequency is maximized at $\phi/\phi_0 = -0.31$ and is lowered, crossing the resonator (green lines), when varying the bias in either direction. b) and c) contain data from two different cooldowns of the same sample.

1.5.2 Building blocks and parameters of the setup

An aluminium cavity designed after a CST simulations was machined by a workshop using a digital mill. The two measured cavities had a storage mode with Q-factor up to $Q_0 = 2 \cdot 10^6$ and $Q_0 = 1 \cdot 10^7$, the latter having a slit parallel to the supercurrents of the storage mode. Further description is found in chapter 6. The transmon consists of two Al pads with dimensions of hundreds of microns separated by a few micron wide wire. The first design, as measured in the Cu cavity, had a pad separation of 50 μm. In order to have a SQUID outside the cavity, the separation was drastically increased to ∼3mm when the new cavity was redesigned (see fig. 1.6c).

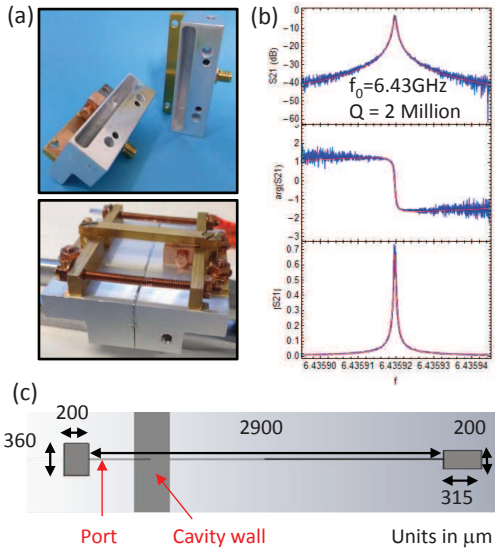

Figure 1.6. Building blocks of the setup. a) Aluminium cavity with a Cu cap and a transmon on a sapphire chip inside. The two halves are closed with an In seal. b) A Lorentzian with a resonance frequency $\omega_0 / 2\pi = 6.43$ GHz and a quality factor $Q_0 = 2 \cdot 10^6$ is fitted to the transmission of the storage mode. c) Schematic of the transmon used in the QZD experiments.

1.5.3 Sample characterization

The sample was cooled down to 30 mK in a setup described in chapter 3. Pulses are generated with a microwave signal IQ-mixed and shaped with an arbitrary waveform generator to both manipulate and readout

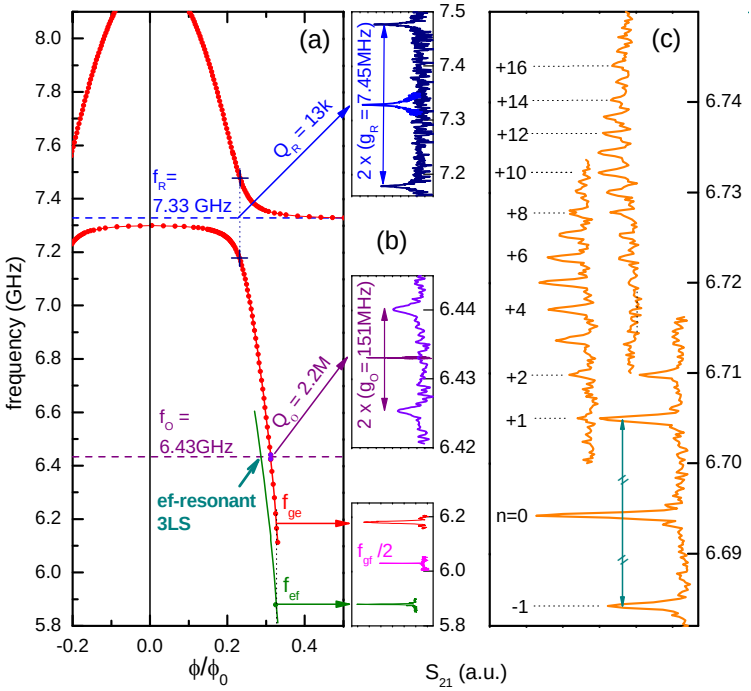

Figure 1.7. Spectroscopic characterization of the QZD sample. a) Transmon $\omega_{ge}/2\pi$(red) and $\omega_{ef}/2\pi$(green) frequencies with varying flux bias. The bare readout mode(blue dashed) and storage mode(purple dashed) frequencies are indicated. b) Measurements of the anticrossings with the readout and storage mode as well as the anharmonicity of the Transmon. c) The + ladder photon number spectrum of the storage mode up to 16 photons are observed when $\omega_s = \omega_{\mathrm{ef}}$.

the sample. A Helmholtz coil generates a magnetic field to tune the transmon frequency.

Figure 1.7 shows a summary of spectroscopic characterization of the sample: The couplings of the transmon to the storage and readout modes are $g_0/2\pi = 8\,\mathrm{MHz}$ and $g_r/2\pi = 150\,\mathrm{MHz}$, respectively, and the anharmonicity is $\alpha/2\pi$ =-260 MHz. The resonance condition $\omega_{ef} = \omega_0$ can be reached and it is possible to resolve the photon number splitting up to more than 15 photons. This experiment gives shorter T_1 than for the test transmon in the Cu cavity: $5\,\mu s$ intrinsic T_1 reduced to 1.5-2.5 μs by the Purcell effect at the operating point. This is however long enough to go forth with the quantum Zeno experiment. With the long-

lived storage mode, it enabled us to implement the Zeno blockade and observe the quantum Zeno dynamics (QZD) by Wigner tomography.

1.6 Wigner tomography, experimental results and analysis

To present the experimental results we first introduce the Wigner function, which is a common representation of the quantum field in a harmonic oscillator. Next we explain the protocol for creating and measuring the QZD, and describe the data obtained for three types of evolutions. Lastly, we discuss the experimental imperfections and decoherence of the Zeno dynamics.

1.6.1 QZD analysis with the Wigner tomography

The Wigner function $W(\beta)$ is a quasi-probability distribution bijective to the density matrix ρ, and can be represented as $W(\beta) = \mathrm{Tr}[\hat{D}(\beta)\hat{P}\hat{D}(-\beta)\rho]$, where $\hat{D}(\alpha) = \exp(\beta\hat{a}^\dagger - \beta^*\hat{a})$ is the coherent displacement operator, $\hat{P}$ is the photon number parity operator, and α is the complex-valued amplitude of the field. The Wigner function is convenient to represent coherent states $|\beta\rangle = \hat{D}(\beta)|0\rangle$, which are the eigenstates of the coherent drive Hamiltonian, as well as their quantum superpositions. Furthermore, using the property that $W > 0$ for all classical states can be used to identify non-classical states.

There are several ways of experimentally reconstructing the Wigner function in a tomographic manner with the use of a Transmon and the ones relevant are discussed in more detail in chapter 6.

If one can perform the parity measurement $\langle\hat{\mathrm{P}}\rangle$ then the Wigner function can be mapped following the mathematical formulation given above.

In our setup, we cannot perform a global parity measurement but we can Fock state-selectively excite the transmon up to a truncation $|n_{\max}\rangle$, which are used to implement truncated parity measures $\hat{P}'$ and $\hat{P}''$ depicted in fig. 1.8d, 1.8e and 1.8f. Figure 1.8a shows a reconstructed Wigner function using the truncated parity measure $\hat{P}''$. It consists in applying $\backsim n_{\max}/2$ simultaneous π pulses exciting the transmon for any odd state up to $n_{\max}$ (in our case $n_{\max}$=10) and thus maps the truncated parity $\hat{P}'' = \Sigma_{n=\mathrm{odd}}|+,n\rangle\langle g,n|$ onto the transmon.

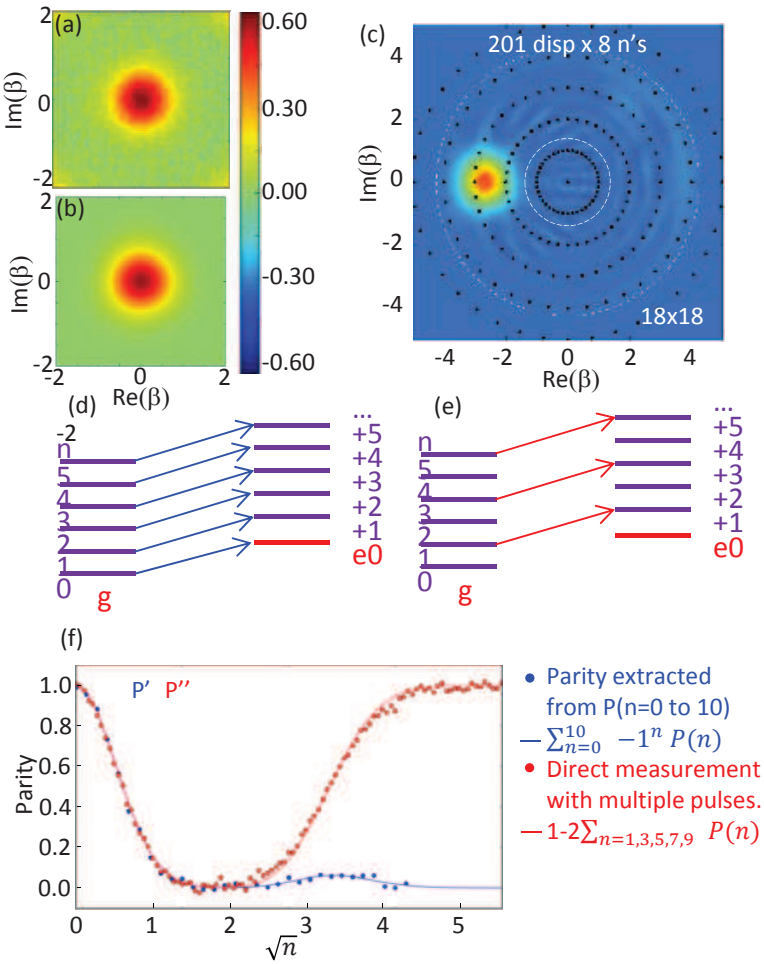

Figure 1.8. Reconstruction of the Wigner function. a) Wigner function of the vacuum state measured pixel by pixel using the truncated parity operator P'' shown in f). b) Wigner function of the vacuum state calculated from a density matrix reconstructed with the maximum likelihood method. c) Reconstructed Wigner function using maxlike of a coherent state $|\beta = -7\rangle$ in a Hilbert space truncated to 18 photons. The black dots represent the displacements $\{\beta_i\}$ in the tomography sequence. d) The parity can be reconstructed from the photon number distribution but requires a separate measurement for every Fock state. e) All the odd photon number state can be simultaneously excited with a multiplexed pulse consequently mapping the parity onto the Transmon state and hence require only one measurement. f) The measured parity of the vacuum state using the methods in f) and e). Diminished Fock state resolution leads us to truncate your parity operators to 10 photons which causes errors in our parity estimate already at 4 photons.

This is however an inefficient method limited to a small part of Hilbert space. We therefore switched to a numerical method called maximum likelihood (maxlike) where, instead of measuring $W(\beta)$ directly, ρ is first reconstructed and then used to calculate $W(\beta)$. The method takes as an input a set of measurement observables and their experimentally measured values, and outputs the density matrix that is most likely to give those same values. The Wigner function can then easily be calculated once ρ is known. The freedom of choosing a set of observables alleviates the truncation restriction and we measure the photon number distribution in combination with displacement pulses as depicted in fig. 1.8b and 1.8c. Reconstructing ρ with maxlike requires much fewer measurement than mapping the Wigner function pixel by pixel and thus is much more efficient. In comparison, the pixel-by-pixel reconstruction in fig. 1.8a took 100 times longer to measure than using maxlike as done in fig. 1.8b.

1.6.2 QZD: Confined, accelerated and elongated

Protocol

The quantum Zeno dynamics with continuous tone blockade at n_0 is performed with the pulse sequence described in fig. 1.9. Starting in the vacuum state, a first optional step is to prepare a different coherent state $|\beta \neq 0\rangle$. Then, two tones are applied simultaneously to induce the Zeno dynamics: (i) a blockade tone with frequency ω_{+n_0} and amplitude Ω_{block}, and (ii) a drive tone with frequency ω_s, amplitude ε, and zero phase ϕ. To record the evolution, we let it unfold for increasing durations t_Z, and measure the observables for the maxlike reconstruction of ρ with a displacement pulse, Fock state selective excitation pulse and readout.

We have applied this protocol to observe three variations of the QZD. Snapshots of the evolutions can be seen in fig. 1.10.

Confined Zeno dynamics inside the exclusion circle

The quantum Zeno dynamics of a system confined to the Hilbert space $\mathcal{H}_{n<n_0}$ is observed for n_0=3 as seen in fig. 1.10a and n_0=4 as described in chapter 7. Starting in the vacuum state the system is driven along the positive real axis, undergoes a phase flip as it hits the blockade, creating a cat-like state before returning to the vacuum state. In an evolution over 2 such periods lasting a total of $26\,\mu s$ the height of the peak has lowered by half and its shape become distorted.

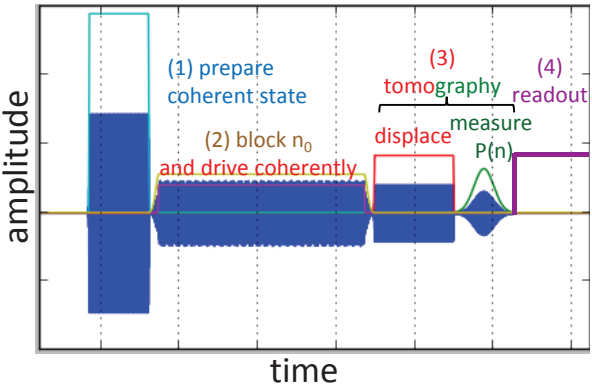

Figure 1.9. Protocol used for all QZD experiments. 1) A displacement pulse $D(\beta)$ is optionally applied to initialize the field in a coherent state $|\beta \neq 0\rangle$. 2) Evolution under QZD. The continuous Zeno blockade tone is switched on as well as the coherent cavity drive. 3 and 4) After evolution over a time t_Z tomography is performed: the field is displaced by $D(\alpha)$ for several values of α. After each displacement the photon number distribution is measured from $n=0$ to $n_{\max}$.

The frames taken at 6.5 and 19.5 μs show that the cat-like states take greater extremes at negative values of $\mathrm{Im}[\alpha]$ and demonstrate non-classical dynamics with negative values of W. The Kerr factor has no visible effect on the evolution and the long lifetime of the cavity and the amount of photon number splitting allows us to comply with the inequality $\kappa_0 \ll \varepsilon \ll \Omega_{\mathrm{block}} \ll |\omega_n - \omega_{n+1}|$, where $\kappa_0 = \omega_0 / Q_0$.

Accelerated Zeno dynamics: going through an exclusion disk

The favorable sample parameters allowed us to explore the QZD further in the subspace $\mathcal{H}_{n>n_0}$, as proposed in [40]. This requires a coherent state preparation outside the exclusion circle, now set at $n_0 = 2$, and subsequently applying the blockade and drive. In fig. 1.10b the initial state $\left|\beta = -\sqrt{7}\right\rangle$ is crashed into the middle of the exclusion circle where it undergoes a π phase shift and continues its motion along the real axis from the opposite side of the exclusion circle. This has the appearance of an acceleration in phase space and creates a cat-like state midway through the acceleration with fringes inside the EC. As the state as reemerged and continues its motion a part of it is left inside the EC.

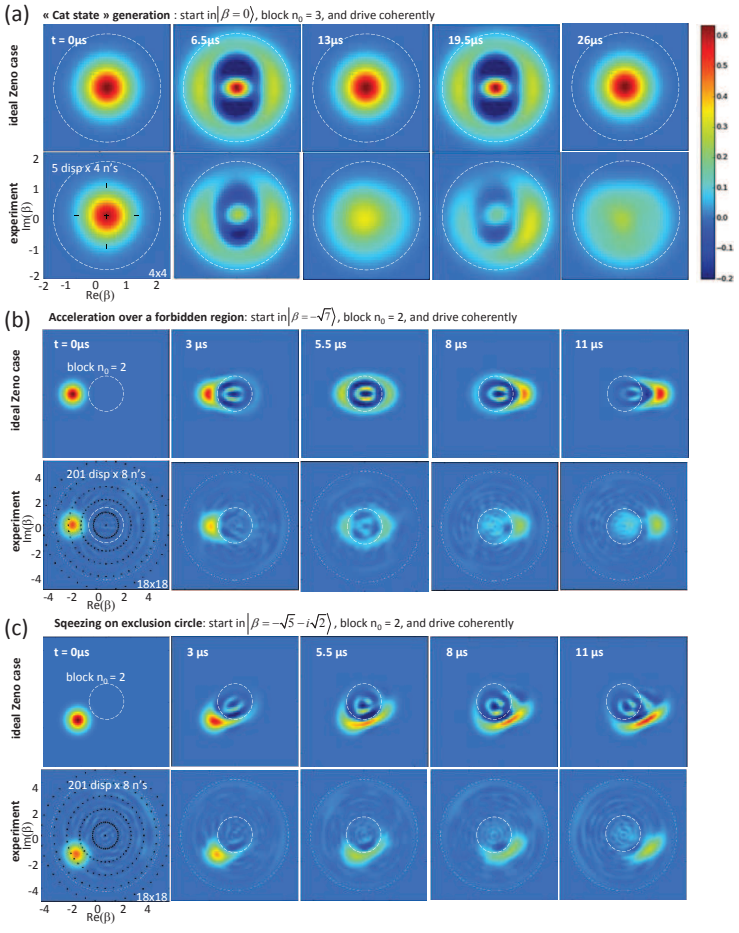

Figure 1.10. Three examples of quantum Zeno dynamics: confinement, tunneling and squeezing. For each set we compare the data in the bottom row to the ideal case in the top row (see section 1.2.9). a) QZD blocked at $n_0 = 3$. showing the reflection on the exclusion circle with negativity clearly visible at half a period and still present at 1.5 periods. b) Acceleration through the exclusion circle. As it is driven to the right the state smears out at the border and reappears on the opposite side. Midway through it resembles a Schrödinger cat state. c) By starting off center from the origin and driving tangentially into the exclusion circle, a squeezed-like state is produced. Black dots represent the displacements used for the tomography.

Squeezing from Zeno dynamics

In fig. 1.10 c the initial state $|\beta = -\sqrt{5} - i\sqrt{2}\rangle$ is prepared to align $\mathrm{Im}[\beta] = \sqrt{n_0}$ with the bottom part of the exclusion circle causing it to crash tangentially into it, yielding an elongated state with large and small extensions along the circle tangent and radius, respectively.

1.6.3 Decoherence analysis in QZD

In order to understand our experimental results and why they deviate from the ideal simulations seen in fig. 1.10 we seek to reproduce the experimental data with numerical simulations, taking into account dephasing and relaxation of the system as well as the non-ideal implementation of the blockade. For that end we use a quantum optics toolbox in Python called QuTiP [25]. An in-depth discussion is found in chapter 7.

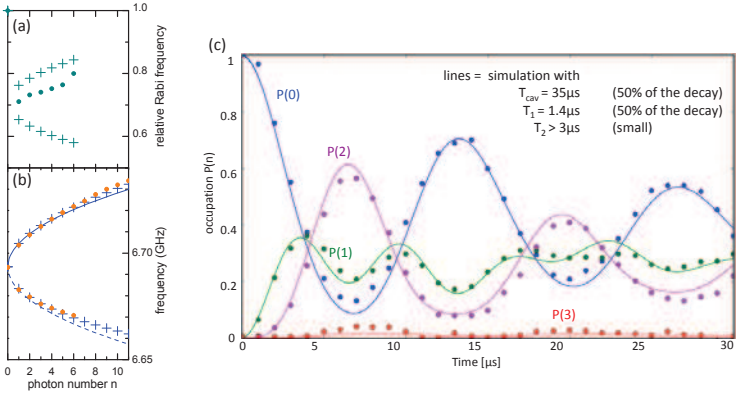

Figure 1.11. Comparison between simulation of the system and data. a) We diagonalize the full Hamiltonian and retrieve the photon number splitting. The simulated values match the measurements and deviate slightly from the well know $\sqrt{n}$ due to the presence of the 3rd level of the Transmon. b) The extracted Rabi frequencies are only semi-quantitative. c) Probabilities p(n) obtained by simulating the quantum Zeno dynamics confined in an exclusion circle at $n_0 = 3$ (lines) and extracted from the experiment shown in fig. 1.10.a

To simulate the ideal Zeno dynamics of a harmonic oscillator in fig. 1.10 we follow the path laid out by Raimond [39] with N stroboscopic alternations between a coherent drive $U(t/N)$ and unitary kicks U_K:

$$\rho(t) = U_Z^{\dagger}(t)\,\rho_0\,U_Z(t)$$

with $U_Z(t,N) = [U_K U(t/N)]^N$.

In simulating our experiments, the storage mode is modeled as a harmonic oscillator truncated at 20 - 40 levels, coupled to a 3-level system representing the transmon and considered as quasi-harmonic (same creation operator as for a harmonic oscillator despite the anharmonicity). The input parameters $\omega_{ef} = \omega_0$, ω_{ge} and g_0 as well as the decay rates κ_0, Γ_1, and Γ_2 are those measured in the experiment. The coupled undriven Hamiltonian is diagonalized to obtain the eigenvalues and eigenstates. Then the photon number resolved qubit frequencies $\omega_{\pm n}$ are calculated, both for the symmetric and antisymmetric superpositions $|\pm, n\rangle$, as well as the Rabi frequencies of each transition as seen in fig. 1.11a. The $\omega_{\pm n}$ match perfectly the data whereas Rabi frequency are only semi-quantitative due to the crudeness of the harmonic approximation for the transmon.

The confined Zeno dynamics is then simulated during a bit more than two periods: the coherent cavity drive and the Zeno blockade drive at frequencies ω_0 and $\omega_{n=n_0}$, respectively, are added to the total Hamiltonian. The photon number probabilities $p(n)$ are finally plotted in fig. 1.11c. The simulated decay parameters T_1, T_2 and κ_s match those measured in the experiment but the simulated drives are up to 30% stronger. We furthermore use the model to estimate the influence of the different experimental imperfections such as leakage of the Zeno barrier, the effect of T_1 and κ and more. As explained in chapter 8, we find that the Zeno blockade tone dephases the Fock states adjacent to the one being blocked. The simulations also show that the Transmon is non-negligibly excited in state $|+n_0\rangle$, thereby making the system sensitive to the relatively short T_1 of the transmon. The rates κ_s and Γ_1 are found to be the main sources of decoherence, both contributing a similar amount. The leakage through the blockade was found to be about 7% per period.

1.7 Conclusions and outlook

During this PhD period we have built a 3D circuit-QED setup with parameters optimized for observing the quantum Zeno dynamics (QZD) of the electromagnetic field in a superconducting microwave cavity. We succeeded in making cavities with quality factors of up to 10 million at $\omega_0 \,/\, 2\pi \sim 6.5$GHz. Selective Fock state manipula-

tion was achieved by partially inserting a tunable transmon qubit in the cavity and leaving its SQUID loop outside, in order to tune its frequency magnetically and match the resonance condition $\omega_0 = \omega_{ef}$. The transmon was placed close to the electric field node of the storage mode, therefore yielding a relatively weak cavity-transmon coupling $g_0/2\pi =$ 8 MHz and a low Kerr nonlinearity below 500 Hz. Despite this small g_s, the resonance condition yields however a large separation of 11 MHz $\times$ $(\sqrt{n+1} - \sqrt{n})$ between the line used to address Fock states $|n\rangle$ and the adjacent line. The occupation probability p(n) of any $|n\rangle$ is measured by exciting the transmon at ω_{+n} conditionally to the occupation of $|n\rangle$, and measuring the microwave transmission of another cavity mode with a low $Q \sim 15k$ coupled to the transmon with $g_r/2\pi = 150$MHz.

With this setup we managed to observe several versions of the QZD under a coherent drive using a continuous blocking tone: We confined the evolution to the Hilbert space $\mathcal{H}_{n<n_0}$ by blocking n_0=3 or 4. By preparing a coherent state outside the exclusion circle in $\mathcal{H}_{n>2}$ and subsequently driving the field toward it we could observe the acceleration of the movement through the circle. Finally we produced a squeezed-like state by crashing a coherent state into the side of the exclusion circle.

Our experimental setup is a good candidate to continue toward implementing QZD in a stroboscopic manner and demonstrating the phase space tweezers proposed in [40]. A few improvements could be made: First, the Fock state selectivity could be improved with a larger g_0 giving larger photon number splitting without suffering from significant non-linearities. Second, relaxation during operations could be reduced with Optimal control pulses allowing fast manipulations while minimizing the off-resonant drive of the adjacent transitions. A longer T_1 would help by making possible to use longer, more selective pulses with smaller decay during manipulations as well as readout.

Chapter 2
Theoretical background

In this chapter the theoretical background behind the experiments is presented. First the quantum Zeno effect (QZE) and quantum Zeno dynamics (QZD)[2.1] are introduced on a conceptual level for an arbitrary system with a discrete energy spectrum.

In this thesis we induce and observe the QZD of the electromagnetic field inside a cavity. This is done by using a superconducting transmon qubit inserted into the cavity. This particular circuit QED system is presented in second section.

The last section describes the implementation of QZD in such a cavity QED system. It illustrates how the QZD can be used to tailor the field in a cavity using 'phase space tweezers'.

2.1 The quantum Zeno Dynamics

We discuss the theory of the quantum Zeno effect and its generalization, the quantum Zeno dynamics, following refs [18][19][20] .

Let us first recall some of the fundamental behavior of quantum system in (discrete) Hilbert space $\mathcal{H}$ represented by a density matrix ρ. This matrix ρ has eigenvalues λ_i with corresponding eigenvectors $|\lambda_i\rangle$ forming an orthonormal basis in $\mathcal{H}$ and can be written as

$$\rho = \sum_i \lambda_i |\lambda_i\rangle\langle\lambda_i|, \tag{2.1}$$

with the normalization condition $\Sigma_i \lambda_i = 1$. When only one λ_i is non-zero the system is in a pure state $|\lambda_i\rangle$. Under the action of a Hamiltonian H the system evolves according to the Schrödinger equation

$$i\hbar \frac{d\rho}{dt} = [H, \rho] \tag{2.2}$$

2.1. The effect is named after the ancient philosopher Zeno of Elea and refers to his paradox described in ref. [20]

leading to a unitary evolution operator $U(t)$:

$$\rho(t) = U(t)\rho(0)U^{\dagger}(t). \tag{2.3}$$

Any measurement on the system is described by an observable operator

$$\hat{O} = \Sigma_j \epsilon_j \hat{P}_j, \tag{2.4}$$

where $\{\epsilon_j\}$ are the possible measurement outcomes, and $\{\hat{P}_j\}$ are the projectors onto the corresponding eigenspaces, satisfying $P_j = P_j^{\dagger}$, $P_j P_j^{\dagger} = P_j^2 = P_j$ and $\Sigma_j P_j = \mathbb{1}$. The outcome ϵ_j of a measurement at time t is obtained with probability

$$\pi_j(t) = \mathrm{Tr}\big(\rho(t)\hat{P}_j\big). \tag{2.5}$$

After receiving a measurement outcome ϵ_j the system updated density matrix is:

$$\rho = \rho_j = \frac{\hat{P}_j \rho \hat{P}_j}{\pi_j}. \tag{2.6}$$

2.1.1 QZD with projective measurements

The quantum Zeno effect (QZE) arises when frequent enough projective measurements suppress the evolution of the measured eigenvalues, as shown by Misra and Sudarshan [32].

Let us assume that a time independent Hamiltonian H induces a unitary evolution $U(t) = \exp(-i\,H t)$, that an observable $\hat{O}$ with $[\hat{H}, \hat{O}] \neq 0$ is repeatedly measured. The first measurement after a time τ gives ϵ_i with the probability

$$\pi_i(\tau) = \mathrm{Tr}[P_i U(\tau) P_i\, \rho(0)\, P_i U^{\dagger}(\tau) P_i], \tag{2.7}$$

which in general is less than unity and leaves the system in ρ_i as given by eq. 2.6. We now interrupt the unitary evolution with a succession of N measurements during the period t. We consider the particular case when all measurements give ϵ_i, which leads to the following state

$$\rho_i^{(N)}(t) = \frac{V_N(t)\rho(0)V_N^{\dagger}(t)}{\pi_i^{(N)}(t)} \qquad V_N(t) \equiv [P_i U(t/N) P_i]^N. \tag{2.8}$$

The denominator

$$\pi_i^{(N)}(t) = \mathrm{Tr}[V_N(t)\rho(0)V_N^{\dagger}(t)], \tag{2.9}$$

which ensures the normalization of the density matrix, represents the probability of measuring ϵ_i in every instance.

By expanding $U(t)$ and taking the limit $N \to \infty$ we get

$$\begin{aligned} V_N(t) &= [P_i(1 - iHt/N + O(1/N^2)P_i)]^N \\ &= P_i[1 - iHt/N + O(1/N^2)]^N \\ &\overset{N\to\infty}{\to} P_i \exp(-iP_iHP_it) \equiv U_Z(t), \end{aligned} \tag{2.10}$$

where

$$H_Z \equiv P_iHP_i, \tag{2.11}$$

defines a *Zeno Hamiltonian*.

When the system is continuously observed, the probability of finding the same eigenvalue ϵ_i throughout a time period t is

$$\Pi_i(t) = \lim_{N\to\infty} \pi_i^{(N)}(t) = \mathrm{Tr}[U_Z(t)\rho_i U_Z^\dagger(t)] = \mathrm{Tr}[\rho_i P_i] = 1. \tag{2.12}$$

In words, the QZE freezes the evolution of the observable O, such that it always yields the initial outcome ϵ_i.

Facchi and Pascazio [19] pointed out that, although the QZE freezes ϵ_i, it does not prohibit the evolution of $\rho_i(t)$ within the subspace $\mathcal{H}_i$ corresponding to ϵ_i. Indeed an (uninterrupted) unitary evolution $\hat{U}(t)$ due to $\hat{H}$ can lead to $\rho(t)$ spreading out of $\mathcal{H}_i$ (if $\left[\hat{H}, \hat{P}_i\right] \neq 0$). However, the repeated measurements result in the unitary evolution $U_Z(t)$ due to H_Z, and confine ρ to $\mathcal{H}_i$ with no leak of probability into $\mathcal{H}_{i\perp}$ ($\mathcal{H} = \mathcal{H}_i \oplus \mathcal{H}_{i\perp}$).

The result in eqs. 2.8, 2.9 and 2.10 is generalized in [20] to multiple Zeno subspaces $\mathcal{H}_i$ that span the entire Hilbert space $\mathcal{H} = \bigoplus_i \mathcal{H}_i$.

2.1.2 QZD with unitary kicks

Facchi and Pascazio [20][18] show that the same dynamics as obtained in the last section can be induced by replacing the non-unitary measurements with instantaneous unitary processes (unitary kicks) :

When interrupting the evolution under $\hat{U}(t)$ N times with an instantaneous unitary kick U_K, the expression of the total unitary becomes

$$U_K^{(N)}(t) = [U_K U(t/N)]^N. \tag{2.13}$$

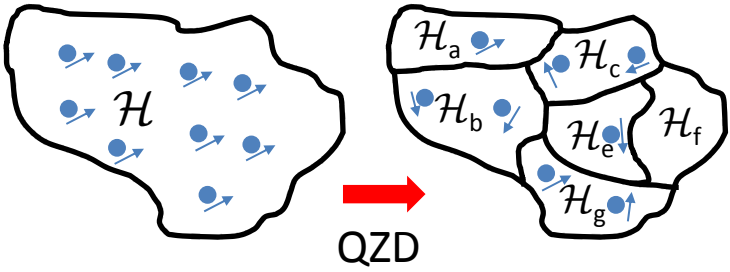

Figure 2.1. Schematic representation of the quantum Zeno dynamics. The QZD can be used to compartmentalize Hilbert space into subspaces, each one having different dynamics.

To derive the evolution of eq. 2.10 let us consider an auxiliary unitary

$$W_N(t) \equiv U_K^{\dagger N} U_K^{(N)}(t) \underset{N\to\infty}{\longrightarrow} \mathcal{U}(t) = \exp(-iH_Z t), \tag{2.14}$$

which $N \to \infty$ limit (derived in ref. [18]) gives rise to a Zeno Hamiltonian

$$H_Z = \sum_j P_j H P_j, \tag{2.15}$$

with P_j the eigenprojectors of U_K ($U_K P_j = e^{i\lambda_j} P_j$). From eq. 2.13 and 2.14 the stroboscopic evolution can be expressed as

$$U_K^{(N)}(t) = [U_K U(t/N)]^N \sim U_K^N e^{-iH_Z t} \tag{2.16}$$

for $N \to \infty$. The Hamiltonian in eq. 2.15 is the generalization of eq. 2.11 and illustrates that the evolution under $U_K^{(N)}$ takes place in each subspace $\mathcal{H}_j = \hat{P}_j \mathcal{H}$ independently.

2.1.3 QZD with continuous coupling

In addition to projective measurements and the unitary kicks the QZD can also be induced by coupling the system to an auxiliary one. The coupling Hamiltonian KH_C where K is the coupling strength yields the system Hamiltonian (omitting the Hamiltonian of the auxiliary system)

$$H_K = H + KH_C. \tag{2.17}$$

The resulting unitary operator $\hat{U}_K(t) = \exp(-iH_K t)$.

Similarly to eq. 2.14, an auxiliary unitary gives the Zeno dynamics

$$\exp(iKH_C t)U_K(t) \underset{K\to\infty}{\longrightarrow} \mathcal{U}(t) = \exp(-iH_Z t), \tag{2.18}$$

where

$$H_Z = \sum_j P_j H P_j \tag{2.19}$$

is the Zeno Hamiltonian and P_n are the eigenprojectors of H_C, with the corresponding eigenvalues η_n and eigensubspaces $\mathcal{H}_n$:

$$H_C = \sum_j \eta_j P_j, \tag{2.20}$$

From this one can conclude that the unitary evolution due to H_K is

$$\begin{aligned} U_K &\sim \exp(-iKH_C t)\mathcal{U}(t) \\ &= \exp\big(-i\Sigma_j\big(K\eta_j\hat{P}_j + \hat{P}_j H\hat{P}_j\big)t\big) \end{aligned} \tag{2.21}$$

which yields the Zeno subspaces.

The seemingly different operations presented in the last thee sections indeed give the same dynamics given by eqs. 2.10, 2.16 and 2.21: The separation of Hilbert space into Zeno subspaces with independent unitary dynamics. This separation is essentially a consequence of the destruction of phase coherence between the subspaces.

Deviations from the ideal case occurs when N and K in eq. 2.10, 2.16 and 2.21 are finite, or when the projections or unitary kicks are not instantaneous. This leads to probability leakage between Zeno subspaces, established by the underlying unitary drive $\hat{U}$, that is not fully blocked by the one of the three methods mentioned above. The characteristics of the leakage depend on the blockade method and will be discussed in the context of cavity QED in section 2.3.

2.2 Cavity QED

The experiments in this thesis use cavity QED, implemented in superconducting circuits, to observe the QZD. A transmon qubit is placed inside a 3D cavity resonator, where the electric dipole moment of the transmon couples to the electric field of the cavity.

In this section the basics of cavity QED will be introduced in three parts: First the physics of a cavity resonator is explored, and an equivalent circuit model is presented and quantized. Then, based on the quantized circuit, superconducting qubits are derived by introducing the Josephson junction. Starting from the Cooper pair box, the basics of the transmon are described followed by a section on the general TLS. The last part covers the coupling of the harmonic cavity with a TLS in the Jaynes-Cummings model, and an extension to a three level system. This leads to a model well suited for our QZD experiments.

2.2.1 Harmonic oscillator

Here we outline the physics of a cavity resonator by first describing the electric fields and deriving an equivalent circuit model for each mode. The coupling to two ports is then added to the model and the key features of the impedance, admittance and scattering matrices are presented. Lastly the circuit is quantized followed by an introduction on Fock states and coherent states

2.2.1.1 Cavity resonator

The resonators used in these experiments are approximately rectangular cuboids carved into a metal block. The electric fields are derived from Maxwell's equations for a box with boundary conditions of a perfect conductor [38][13].

Let us consider an empty box with the dimensions (d_x,d_y,d_z) along the (x,y,z) directions as shown in fig. 2.2. The electric field inside the cavity is $\vec{E} = (E_x, E_y, E_z)$ with

$$E_n = E_{n0}\left[\cos(k_n n) \prod_{m \neq n} \sin(k_m m)\right] e^{i\omega t}. \tag{2.22}$$

Here E_{n0} are the electric field amplitudes and the wave vector projections $k_n = \pi l_n / d_n$ define the mode indices $l_n \in \mathbb{N}_0$ ($\Sigma_n l_n \geqslant 2$). The field oscillates at a frequency

$$\omega_{(l_x,l_y,l_z)} = k_{(l_x,l_y,l_z)}\, c \quad \text{with} \quad k_{(l_x,l_y,l_z)} = \sqrt{k_x^2 + k_y^2 + k_z^2}, \tag{2.23}$$

and c the speed of light. Each mode is thus a standing wave with the mode index l_n indicating the number of anti-nodes along coordinate n.

The electric and magnetic fields of each mode can be written as

$$\vec{E} = k^2 q \vec{\boldsymbol{\varepsilon}} \quad \text{and} \quad \vec{B} = k\dot{q}\vec{\boldsymbol{h}}$$

with q the generalized mode amplitude having the generalization of a charge, and $\vec{\boldsymbol{\varepsilon}}$ and $\vec{\boldsymbol{h}}$ are the vectors of the electric and magnetic fields respectively. Integrating the energy density of the fields over the volume gives

$$E_{\mathrm{el}} = \frac{\varepsilon_0}{2}\int E^2 d\mathcal{V} = \frac{q^2}{2C} \quad \text{and} \quad E_{\mathrm{ma}} = \frac{1}{2\mu_0}\int H^2 d\mathcal{V} = \frac{L\dot{q}^2}{2}, \tag{2.24}$$

which defines an effective inductance L and capacitance C [54]:

$$L_{(l_x,l_y,l_z)} = \mu k^2_{(l_x,l_y,l_z)}\mathcal{V} \quad \text{and} \quad C_{(l_x,l_y,l_z)} = \frac{\varepsilon}{k^4_{(l_x,l_y,l_z)}\mathcal{V}}, \tag{2.25}$$

with the volume $\mathcal{V} = abd$. From this one can write expressions

$$\omega_{(l_x,l_y,l_z)} = \frac{1}{\sqrt{LC}} \quad \text{and} \quad Z_{r(l_x,l_y,l_z)} = \sqrt{\frac{L}{C}}, \tag{2.26}$$

with Z_r is the impedance of the mode. Furthermore, losses in the cavity walls can be represented by an effective resistance R. Therefore an equivalent LCR-oscillator representation exists as show in fig. 2.2 b, with a quality factor

$$Q_{\mathrm{int}} = R/Z_r. \tag{2.27}$$

In our experiment one dimension of the cavity is much shorter than the other two, such that the lowest frequencies have the corresponding mode index zero. Taking $d \ll a, b$ means $l_z = 0$ for the lowest modes, which have only one electric field component E_z.

Coupling to two ports

To couple energy in and out of the cavity, two antenna protrude into the cavity through a hole in the wall as shown in fig. 2.2a. The coupling strength κ depends on the electric field strength at location of the hole and the length of the antenna.

In the circuit model in fig. 2.2b, the ports are represented by two capacitors C_1 and C_2 coupled to two resistors representing the transmission lines to which they are attached.

2.2.1.2 LCR-circuit representation and S-parameters

We now use the circuit model to characterize a mode of the cavity, including its coupling to the to two ports, and see how these characteristics can be measured in practice.

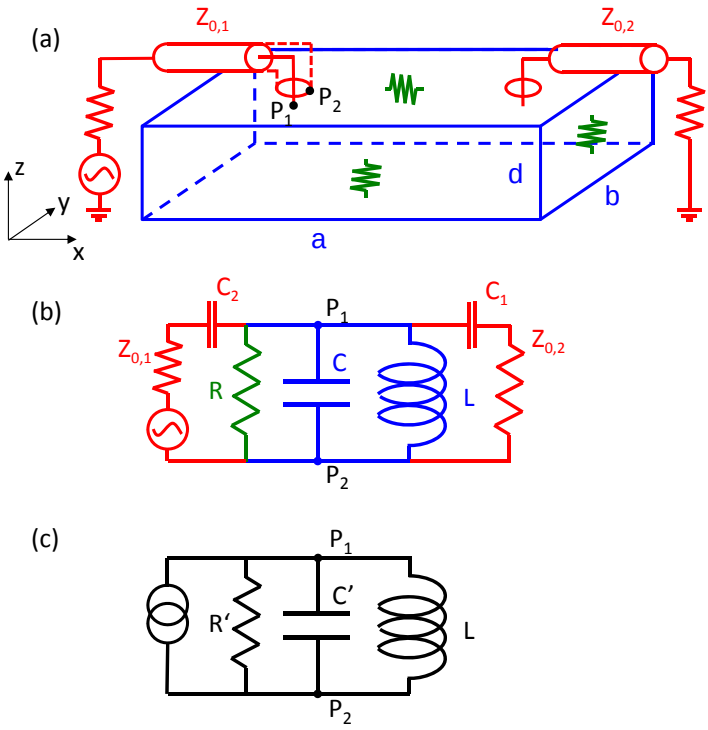

Figure 2.2. 3D cavity resonator. a) Schematic of a cavity coupled to s source and a load with coaxial cables. The loss in the walls is represented by resistances. b) Circuit model representation of a mode of the cavity c) LCR-circuit equivalent to b)

The circuit in fig. 2.2 b can be transformed into the LCR- model shown in fig. 2.2 c using the Norton-Thevenin theorem and approximating the series combination of C_i and $Z_{0,i}$ $(i=1,2)$ to a parallel one when $\omega \sim \omega_0$.

This results in modified resistance R' and C'. R' is interpreted as the real part of the admittance of the total circuit $\mathrm{Re}(Y) = \mathrm{Re}(Z^{-1})$:

$$\frac{1}{R'} \simeq \frac{1}{R} + \frac{1}{R_1} + \frac{1}{R_2}, \tag{2.28}$$

where for each port i

$$\frac{R_i}{Z_{0,i}} = \frac{1}{(Z_{0,i}\omega_0 C_i)^2} + 1; \tag{2.29}$$

and C' is given by

$$C' = C + \sum_{i=1,2} \frac{C_i}{(Z_{0,1}\omega_0 C_i)^2 + 1}. \tag{2.30}$$

This gives rise to a modified resonance frequency $\omega_0' = 1/\sqrt{LC'}$ and quality factor $Q_{\mathrm{tot}} = R'/Z_r$ which can be decomposed into

$$Q_{\mathrm{tot}}^{-1} = Q_{\mathrm{int}}^{-1} + Q_1^{-1} + Q_2^{-1}. \tag{2.31}$$

For each component of Q_{tot} a coupling rate is defined as $\kappa = \omega_0'/Q$. These rates add up: $\kappa_{\mathrm{tot}} = \kappa_{\mathrm{int}} + \kappa_1 + \kappa_2$. Both κ_1 and κ_2 represent the energy transfer rate through the ports while κ_{int} is the energy loss rate inside the resonator.

Scattering parameters

The lines coupling to the two cavity ports are coaxial cables with waves traveling through them. At the port the voltage and currents are

$$V_i = V_i^+ + V_i^- \tag{2.32}$$
$$I_i = I_i^+ - I_i^-, \tag{2.33}$$

with $V_i^+(I_i^+)$ and $V_i^-(I_i^-)$ represent the voltage(current) of the incident and reflected waves off port i respectively. These parameters are used to define three 2x2 matrices: The impedance matrix [Z];

$$Z_{\mathrm{ij}} = \left.\frac{V_i}{I_j}\right|_{I_{i\neq j}=0} (\text{port } i \text{ open})$$

the admittance matrix [Y];

$$Y_{\mathrm{ij}} = \left.\frac{I_i}{V_j}\right|_{V_{i\neq j}=0} (\text{port } i \text{ shorted})$$

and the scattering matrix [S];

$$S_{\mathrm{ij}} = \left.\frac{V_i^-}{V_j^+}\right|_{V_{i\neq j}^+=0} (\text{all ports terminated with } a \text{ load}).$$

The matrices [Z] and [Y] characterize the internal microwave network represented by the blue and green elements in fig. 2.2 b, while [S] characterizes the full circuit in the figure.

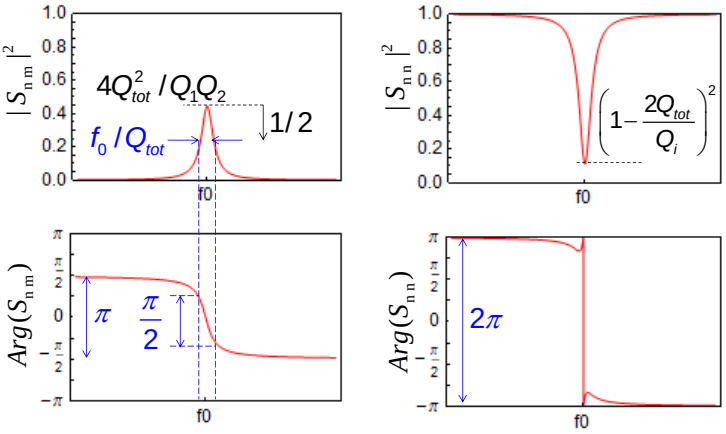

Figure 2.3. Scattering parameters of transmission and reflection around a resonance frequency f_0. The width of the Lorentzian transmission peak gives Q_{tot}. Components Q_i corresponding to individual ports can be determined by the depth of the reflection, leaving the internal Q_{int} to be determined by subtraction from Q_{tot}.

The parameters of [S] are the reflection ($i = j$) and transmission ($i \neq j$) coefficients of the device, and their value around a resonance frequency ω_0' of a mode are

$$S_{\mathrm{nn}} = -\frac{\left(1 - 2\frac{Q_{\mathrm{tot}}}{Q_n}\right) + i2Q_{\mathrm{tot}}\left(\frac{\omega}{\omega_0'} - 1\right)}{1 + \mathrm{i}Q_{\mathrm{tot}}\left(\frac{\omega}{\omega_0'} - 1\right)}, \tag{2.34}$$

$$S_{\mathrm{nm},n\neq m} = \frac{2\frac{Q_{\mathrm{tot}}}{\sqrt{Q_nQ_m}}}{1 + i2Q_{\mathrm{tot}}\left(\frac{\omega}{\omega_0'} - 1\right)}, \tag{2.35}$$

$$\arg(S_{\mathrm{nm},n\neq m}) = -\mathrm{atan}\left(2\,Q_{\mathrm{tot}}\left(\frac{\omega}{\omega_0'} - 1\right)\right), \tag{2.36}$$

and are plotted in fig. 2.3. The energy transmission $|S_{\mathrm{ij}}|^2$ takes a Lorentzian shape in frequency and the full width at half maximum (FWHM) of the peak is the decay rate $\kappa_{\mathrm{tot}}{=}\omega_0/Q_{\mathrm{tot}}$. The individual Q_i (and κ_i) components can then be obtained from eqs. 2.25, 2.26, 2.27.

The cavity used in the experiment is not exactly a rectangular cuboid. The circuit model can however still be used with lumped element parameters extracted from numerical simulations, using the following method:

We choose two points P_1 and P_2 on one of the ports as shown in fig. 2.2 a, one on the inner conductor and the other on the wall of the port (ground). Figure 2.2 b,c show the location of these point in the circuit model. The simulator calculates the admittance

$$Y_{P_2P_1}(\omega) = Z^{-1}_{P_1P_1}(\omega) = \frac{1}{R'} + i\omega C' - \frac{i}{\omega L} \tag{2.37}$$

as seen from these two points. The individual elements and ω_0' can be obtained using the following identities

$$\mathrm{Im}[Y(\omega_0')] = 0, \quad C' = \frac{\mathrm{Im}[Y'(\omega_0')]}{2}, \quad R' = \frac{1}{\mathrm{Re}[Y(\omega_0')]}. \tag{2.38}$$

2.2.1.3 Quantizing the LC-circuit

To describe a resonator quantum mechanically we consider the RCL circuit presented in the last section, but disregard its resistance and coupling to the two ports. Analogous to the energy of a classical circuit given in eq. 2.19 the quantum Hamiltonian is

$$\hat{H} = \frac{\hat{Q}^2}{2C} + \frac{\hat{\Phi}^2}{2L} \tag{2.39}$$

where the charge and flux operators $\hat{Q}$ and $\hat{\Phi}$ are canonical conjugate variables $[\hat{Q}, \hat{\Phi}] = i\hbar$. By defining the bosonic creation and annihilation operators

$$\hat{a^\dagger} = \sqrt{\frac{1}{2\hbar Z_r}}(\hat{\Phi} + \mathrm{i}Z_r\hat{Q}) \tag{2.40}$$

and

$$\hat{a} = \sqrt{\frac{1}{2\hbar Z_r}}(\hat{\Phi} - \mathrm{i}Z_r\hat{Q}), \tag{2.41}$$

the Hamiltonian can be written in second quantization as

$$\hat{H} = \hbar\omega_0\left(\hat{a}^\dagger\hat{a} + \frac{1}{2}\right). \tag{2.42}$$

Here $\hbar\omega_0$ is the energy[2.2] per photon, $\hat{n} = \hat{a}^\dagger\hat{a}$ is the photon number operator, and the $1/2$ represent the vacuum fluctuation which will from here on be omitted.

2.2.1.4 Coherent states and Fock states

This section covers two types of quantum states that are central to the physics in this thesis: The eigenstates of the photon number operator $\hat{n}$, called photon number states or Fock states, and the states generated by a classical sinusoidal source called coherent states, which are also the eigenstates of the annihilation operator $\hat{a}$

Fock states

The eigenvalue spectrum of $\hat{n}$ is non-degenerate and made of non-negative integers n. The associated Fock states are represented by $[n\rangle$ such that $\hat{n}|n\rangle{=}n|n\rangle$ and they form an infinite orthonormal basis in Hilbert space. In light of eq. 2.31, the Fock states are also the eigenstates of the harmonic oscillator Hamiltonian where the eigenvalues are

$$E_n = \langle n|\hat{H}|n\rangle = n\hbar\omega_0 \tag{2.43}$$

and consist of n energy quanta of $\hbar\omega_0$ called photons, hence the term photon number operator for $\hat{n}$.

The photon number spectrum is often represented by a ladder as shown in fig. 2.4. As these operators add or remove ($\hat{a}^\dagger$ or $\hat{a}$) one elementary excitation, i.e.

$$\hat{a}^\dagger|n\rangle = \sqrt{n+1}|n+1\rangle \quad \text{and} \quad \hat{a}|n\rangle = \sqrt{n}|n-1\rangle, \tag{2.44}$$

their application can be seen as going a step up or down the ladder, respectively. This intuitively describes the creation of a Fock state $|n\rangle$ from the vacuum as climbing up the ladder in n steps, which is formally expressed using eq 2.30

$$|n\rangle = \frac{\hat{a}^{\dagger n}}{\sqrt{n!}}|0\rangle. \tag{2.45}$$

Coherent states

Coherent states arise from the applying a coherent drive, described in a frame rotating at the drive frequency, by the Hamiltonian [23]

$$\hat{H}_{\text{drive}} = \zeta^*\,\hat{a} + \zeta\,\hat{a}^\dagger \tag{2.46}$$

2.2. We speak equally of energies and frequencies as they are related simply by $\hbar$.

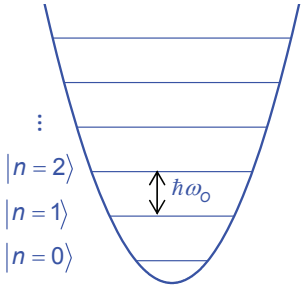

Figure 2.4. A quantized harmonic oscillator. The equidistant energy levels are depicted as a Fock state ladder.

with ζ the drive amplitude. The resulting unitary evolution is

$$\hat{U}_{\text{drive}}(t) = \exp\left(-i\,\hat{H}_{\text{drive}}\,t\right). \tag{2.47}$$

When the drive is applied for a time t_{drive}, $\hat{U}_{\text{drive}}(t_{\text{drive}})$ becomes the displacement operator

$$\hat{D}(\beta) = e^{\beta^*\hat{a} - \beta\,\hat{a}^\dagger} \tag{2.48}$$

with $\beta = \zeta t_{\text{drive}}$ the complex displacement. $\hat{D}(\beta)$ satisfies

$$\begin{aligned} \hat{D}(\beta)^{-1} &= \hat{D}(\beta)^\dagger = \hat{D}(-\beta) \\ \hat{D}(\beta_1)\hat{D}(\beta_2) &= \hat{D}(\beta_1+\beta_2)e^{(\beta_1\beta_2^* - \beta_1^*\beta_2)/2} \\ \hat{D}(0) &= \mathbb{1}. \end{aligned} \tag{2.49}$$

If the system is initially in $|0\rangle$ the state created by $\hat{D}$ is a coherent state with amplitude β:

$$\hat{D}(\beta)|0\rangle = |\beta\rangle. \tag{2.50}$$

Coherent states are similar to classical states of light, as they are defined by a complex number, and thus have an amplitude $|\beta|$ and a phase $\arg(\beta)$ in the phase space of the electric field as shown in fig. 2.5a. Unlike classical states though, coherent states are not a point in phase space but a Gaussian distribution since $\Delta\text{Re}(\beta), \Delta\text{Im}(\beta) \geqslant 1/2$.

The effect of the operators $\hat{a}$ on $|\beta\rangle$ is

$$\hat{a}|\beta\rangle = \beta|\beta\rangle, \tag{2.51}$$

which gives the expectation value of the photon number operator

$$\langle\hat{n}\rangle = \langle\beta|\hat{n}|\beta\rangle = |\beta|^2. \tag{2.52}$$

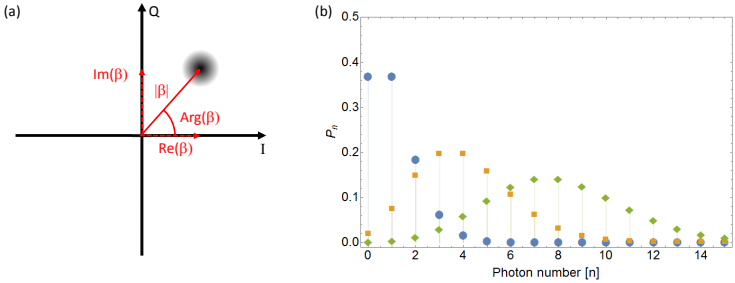

Figure 2.5. Coherent state. a) The representation of a coherent state in the IQ phase space of the electric field in the cavity. The state can be seen as analogous to a classical field, characterized with an amplitude and a phase. b) Three examples of Fock state distributions for coherent states with amplitudes $\beta = 1, 2$ and $\sqrt{8}$.

The representation of a coherent state in the Fock state basis is

$$|\beta\rangle = \sum_n c_n |n\rangle = e^{-|\beta|^2/2} \sum_n \frac{\beta^n}{\sqrt{n!}} |n\rangle \tag{2.53}$$

which reveals a Poissonian photon number probability distribution

$$P_\beta(n) = |c_n|^2 = e^{-|\beta|^2} \frac{|\beta|^{2n}}{n!}, \tag{2.54}$$

depicted in fig. 2.5b.

2.2.2 Superconducting qubit

Superconducting qubits are lumped element circuits composed of inductors, capacitors and elements called Josephson junctions (JJ) which can be regarded as non-linear inductors. The non-linear character of the JJ leads to non equidistant energy level of the circuit such that two levels can be used as a qubit.

The different types of superconducting qubits vary in the number and configuration of JJs as well as the relative energies in the different components of the circuit. The various qubit types (phase qubit, flux qubit, fluxonium, Cooper pair box etc) are discussed in ref [15]. The qubit used in this thesis is the transmon which is a derived from the Cooper pair box (CPB).

2.2.2.1 The Josephson junction

A Josephson junction consists of two superconductors separated by an insulating barrier. The charge carriers in the superconductors on either side are described by a macroscopic wave functions with well defined phases φ_1 and φ_2 as shown in fig. 2.6a. Josephson predicted that the phase $\phi = \varphi_1 - \varphi_2$ would result in Cooper pairs tunneling through the barrier, giving rise to a supercurrent and a voltage [26]

$$I = I_c \sin(\phi) \tag{2.55}$$

$$V = \phi_0 \frac{\partial \phi}{\partial t}. \tag{2.56}$$

Here the critical current I_c is the maximal current the junction can support and $\phi_0 = \hbar/2e$ is the flux quantum.

From eq 2.41 and 2.42 one can derive an inductance

$$L_J(\phi) = \frac{\phi_0}{I_c \cos(\phi)} \approx L_{J0}\left[1 + \frac{\phi^2}{2} + \mathcal{O}(\phi^4)\right] \tag{2.57}$$

with the Josephson inductance L_{J0} and a series exposing a non-linear behavior, which is a key attribute of the JJ circuits.

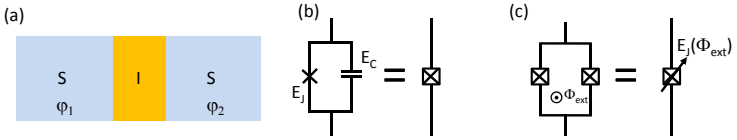

Figure 2.6. Josephson junction. a) Two superconductors separated by an insulator, with a phases φ_1 and φ_2. b) The circuit representation of a junction is a cross. The box is drawn around it represents the capacitance. c) Two JJ in parallel form a SQUID loop which can be seen as a single junction tunable with an external magnetic flux through the loop.

The energy of the junction is

$$E = E_J(1 - \cos(\phi)) \tag{2.58}$$

where $E_J = I_c\ \phi_0$ is the Josephson energy. Taking into account the energy from the capacitance between the two superconductors C_J, the quantized Hamiltonian of the junction is

$$\hat{H}_{JJ} = E_C + E_J(1 - \cos(\hat{\phi})) \tag{2.59}$$

where the $E_C = \hat{Q}^2/(2C_J)$ is the same as in eq(2.28) and the second is the Josephson Hamiltonian with quantum phase $\hat{\phi}$.

DC-SQUID

A JJ with a tunable E_J can be obtained by placing two JJ in parallel, which forms a loop known as a superconducting quantum interference device (SQUID)[14], and is shown in fig. 2.6c. Assuming perfect symmetry between the junction $I_c = I_{c1} = I_{c2}$, the phase difference across each junction are ϕ_1 and ϕ_2, and are equal in the absence of external flux. However, if a magnetic flux Φ_{ext} penetrates the SQUID it induces a difference between the two phases

$$\phi_2 - \phi_1 = \Phi_{\text{ext}}/\varphi_0 \,[\text{mod}\, 2\pi] \tag{2.60}$$

with $\Phi_0 = 2\pi\varphi_0 = h/2e$ the quantum of magnetic flux. The critical current of the SQUID now depends on Φ_{ext}:

$$I_{c,\text{SQ}}(\Phi_{\text{ext}}) = 2I_c\left|\cos\left(\pi\frac{\Phi_{\text{ext}}}{\Phi_0}\right)\right|.$$

As a result, both the Josephson inductance L_{J0} and Josephson energy E_J become tunable with Φ_{ext}:

$$L_{\text{SQ0}}(\Phi_{\text{ext}}) = \frac{\phi_0}{I_c(\Phi_{\text{ext}})} \tag{2.61}$$

$$E_{\text{SQ}}(\Phi_{\text{ext}}) = 2\phi_0 I_c\left|\cos\left(\pi\frac{\Phi_{\text{ext}}}{\Phi_0}\right)\right|. \tag{2.62}$$

2.2.2.2 Cooper pair box

A Cooper pair box (CPB) is an electrical circuit as shown in fig. 2.7, where a small superconducting island is connected to a superconducting electrode by a JJ, and to a gate voltage through a capacitor. The charging energy of one electron in the CPB is

$$E_C = \frac{e^2}{2C_\Sigma} \tag{2.63}$$

with $C_\Sigma = C_g + C_J$ the total capacitance of the island.

Electrons tunnel through JJ in Cooper pairs so the energy needed to add/remove one pair to/from the island is $4E_C$. In the so called charge regime $E_C \gtrsim E_J$, the eigenstates are almost pure charge states $|n_{\text{CP}}\rangle$, corresponding to an exact number n_{CP} of excess Cooper pairs (hence the name charge qubit).

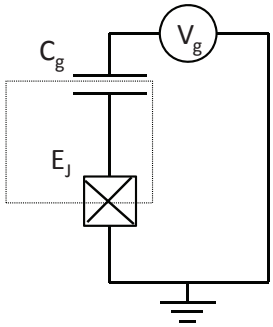

Figure 2.7. Cooper pair box. Superconducting island (dotted line) is connected to the ground via a JJ and to a voltage gate.

By tuning the gate voltage V_g one can control the number of Cooper pairs in the island. V_g can be expressed as a reduced charge number

$$n_g = \frac{V_g C_g}{e^2}. \tag{2.64}$$

The conjugate operator to $\hat{n}_{\mathrm{CP}}$ is the phase operator of the JJ $\hat{\phi}$ and the Hamiltonian of the CPB is

$$\hat{H}_{\mathrm{CPB}} = 4E_C(\hat{n}_{\mathrm{CP}} - n_g)^2 - E_J\cos(\hat{\phi}). \tag{2.65}$$

$\hat{H}_{\mathrm{CPB}}$ can be written in the phase basis as

$$\hat{H}_{\mathrm{CPB}} = 4E_C\left(\frac{1}{i}\frac{\partial}{\partial\phi} - n_g\right)^2 - E_J\cos(\hat{\phi}). \tag{2.66}$$

This Hamiltonian can be solved exactly and its eigenenergies are [12]

$$E_{k\geqslant 0} = E_C\mathcal{M}_A\left[n + 1 - (k+1)[\mathrm{mod}\,2] + 2n_g(-1)^k, -\frac{E_J}{2E_C}\right], \tag{2.67}$$

where $\mathcal{M}_A$ is the characteristic value of the even Mathieu function. The lowest energy levels of the CPB as a function of n_g are shown in fig. 2.8 for different ratios E_J/E_C. They form parabolas that anticross and yield energy bands bands E_k. Note that at the degeneracy point $E_k(n_g = 1/2)$ the CPB is less sensitive to noise on n_g as $\partial(E_1 - E_0)/\partial n_g = 0$. Operating there was a key to the long coherence time of the Quantronium CPB [47].

The dispersion of band k is

$$\nu_k = |E_k(n_g = 0) - E_k(n_g = 1/2)|. \tag{2.68}$$

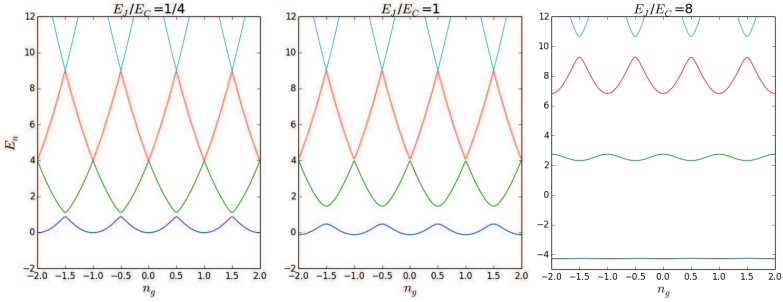

Figure 2.8. Energy levels of a charge qubit. For the CPB $E_J \gtrsim E_C$ the energy levels are sensitive to variations in n_g. As E_J/E_C increases the levels become more flat although the n_g sensitivity is greater in higher levels.

and decreases with E_J/E_C. By increasing the value of E_J/E_C above 50 the CPB enters the phase regime and is called a transmon. The lowest energy levels become almost completely flat and insensitive to n_g while some sensitivity remains in the higher levels. In return the separation between the levels becomes increasingly similar.

Transmon

To reach the transmon regime a shunt capacitor C_S is placed in parallel with the JJ as shown in fig. 2.9 a, which is equivalent to fig. 2.8a with C_g being replaced by $C_g + C_S$. Usually the electrodes on either side of the JJ in a transmon are of a similar size and not grounded, giving resemblance to a dipole in an external field E, as shown in fig. 2.9 b.

In the transmon regime approximate values of the energies are [28]

$$E_k \simeq -E_J + \sqrt{8E_C E_J}\left(k + \frac{1}{2}\right) - \frac{E_C}{12}(6k^2 + 6k + 3). \tag{2.69}$$

The transition energies, defined as $E_{\mathrm{nm}} = E_m - E_n$, give

$$E_{ge} = \sqrt{8E_C E_J} - E_C. \tag{2.70}$$

The price to pay for decreasing the noise sensitivity with a shunt capacitor is a lower anharmoniciy $\alpha \equiv E_{12} - E_{01} \simeq -E_C$: The lowest levels of the transmon can therefore be seen approximately as a weakly anharmonic ladder, with the steps decreasing by α at each step.

The charge dispersion defined in eq. 2.57 scales as

$$\nu_n \propto \exp\left(-\sqrt{2E_J/E_C}\right) \tag{2.71}$$

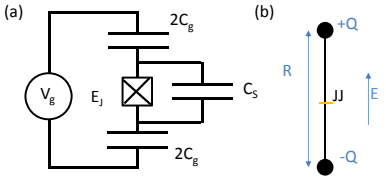

Figure 2.9. Transmon qubit. a) Circuit diagram of a transmon as a SQUID with a shunt capacitor in parallel. b)Antenna representation of a transmon

which allows for a significant increase of E_J/E_C compare to the CPB before suffering from crowding of the transition frequencies $E_{\mathrm{nm}}/\hbar$.

2.2.2.3 Transmon as a two level system

As any multi level system, the Hamiltonian of the transmon can be written as

$$\hat{H}_{\mathrm{Tr}} = \sum_l \hbar\omega_l |l\rangle\langle l| \tag{2.72}$$

where the levels, starting from the ground state, are denoted as $|g\rangle, |e\rangle$, $|f\rangle, |h\rangle$...

A transmon is often regarded as a TLS (qubit) by excluding all but the $|g\rangle$ and $|e\rangle$ levels. Moreover, for a multilevel system the two level formalism can be applied to the transition between any two levels. It is therefore useful to introduce some of the notation developed for qubits.

Bloch sphere representation

The Hilbert space of a qubit is two dimensional and its eigenstates can be represented as vectors

$$|g\rangle = \begin{pmatrix} 0 \\ 1 \end{pmatrix} \text{ and } |e\rangle = \begin{pmatrix} 1 \\ 0 \end{pmatrix}, \tag{2.73}$$

and the Hamiltonian as

$$\hat{H}_{\mathrm{qb}} = \frac{\hbar\omega_{ge}}{2}\hat{\sigma}_z, \tag{2.74}$$

where ω_{ge} is the excitation frequency.

The general representation of

a qubit state is a 2x2 density matrix expressed as

$$\rho = \frac{1}{2}(\mathbb{1} + \vec{a}\cdot\vec{\sigma}), \tag{2.75}$$

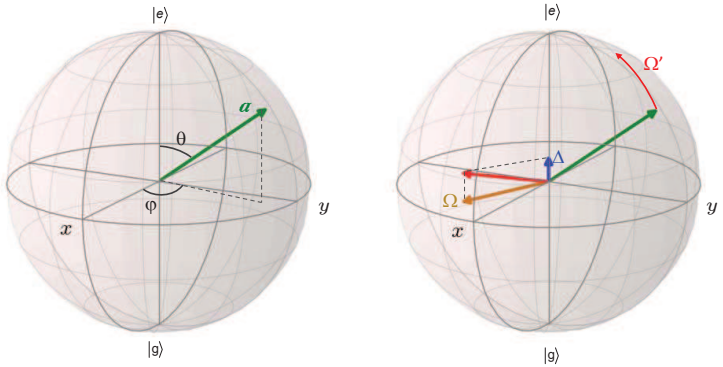

Figure 2.10. Bloch sphere is a sphere with radius 1. a)State of a qubit can be represented as a vector $\vec{a}$ on the Bloch sphere. $|\vec{a}| = 1$ for a pure state. b)Applying a coherent drive causes the Bloch vector to rotate around an axis $\vec{d}$.

with $\vec{\sigma} = (\hat{\sigma}_x, \hat{\sigma}_y, \hat{\sigma}_z)$ a vector of the Pauli matrices

$$\hat{\sigma}_x = \begin{pmatrix} 0 & 1 \\ 1 & 0 \end{pmatrix} \quad \hat{\sigma}_y = \begin{pmatrix} 0 & -i \\ i & 0 \end{pmatrix} \quad \hat{\sigma}_z = \begin{pmatrix} 1 & 0 \\ 0 & -1 \end{pmatrix}. \tag{2.76}$$

The Bloch vector $\vec{a}$ allows for a visual representation of the qubit state on the Bloch sphere shown in fig 2.10 a. A pure state

$$|q\rangle = \cos\left(\frac{\theta}{2}\right)|g\rangle + e^{i\varphi}\sin\left(\frac{\theta}{2}\right)|e\rangle \tag{2.77}$$

satisfies $|\vec{a}|=1$ and can be represented as a point on the surface of the Bloch sphere, defined by its polar and azimuthal angles θ and φ.

A mixed state is a point inside the Bloch sphere ($|\vec{a}|<1$ in eq, 2.75) and is reduced to the origin $|\vec{a}|=0$ for a maximally mixed state.

Coherent driving

The Bloch vector rotates under a coherent drive at a frequency ω_{dr}

$$\hat{H}_{\mathrm{dr}} = \frac{\hbar A_{\mathrm{dr}}}{2}\cos(\omega_{\mathrm{dr}} t + \varphi_{\mathrm{dr}})\hat{\sigma}_x \tag{2.78}$$

with A_{dr} the amplitude and φ_{dr} the phase of the drive. The joint qubit-drive Hamiltonian in the rotating wave approximation (RWA):

$$\hat{H}^{\mathrm{RWA}}_{\mathrm{qb+dr}} = \frac{\hbar}{2}[\Delta\,\hat{\sigma}_z + \Omega(\cos(\varphi_{\mathrm{dr}})\hat{\sigma}_x + \sin(\varphi_{\mathrm{dr}})\hat{\sigma}_y)], \tag{2.79}$$

with the detuning $\Delta = \omega_{ge} - \omega_{\mathrm{dr}}$ and $\Omega \propto A_{\mathrm{dr}}$ the Rabi frequency. As depicted in fig 2.10b, the Bloch vector is driven around an axis $\vec{d}$ defined by the phase of the drive φ_{dr} and the ratio of the detuning Δ and the Rabi frequency Ω. In the resonant case $\Delta = 0$ the rotation axis $\vec{d}$ is in the equatorial plane leading to a rotation along a meridian at the Rabi frequency Ω. In the off-resonant case $\Delta \neq 0$ the Bloch vector rotates at a modified Rabi frequency $\Omega' = \sqrt{\Delta^2 + \Omega^2}$ and furthermore, the phase φ between $|g\rangle$ and $|e\rangle$ oscillates at a frequency Δ.

Relaxation and dephasing

Under free evolution the qubit interaction with its environment gives a relaxation rate Γ_1 and free induction decay rate Γ_2. These two effects are calculated by separating the Hamiltonian into its longditudinal and transverse parts $\hat{H}_{\mathrm{qb}} = \vec{h}_{\mathrm{qb}} \cdot \vec{\sigma} = (h_{\mathrm{qb},x}\ \sigma_x + h_{\mathrm{qb},y}\ \sigma_y + h_{\mathrm{qb},z}\ \sigma_z)$. The sensitivity of the Hamiltonian to a noise source in an environment variable λ is then treated as a perturbation $\delta\hat{H}^{(\lambda)}_{\mathrm{qb}} = -\hbar\,/\,2\ \vec{\hat{D}}_\lambda\ \delta\lambda$, where $\vec{\hat{D}}_\lambda \equiv 1\,/\,\hbar\ \left(\partial\vec{h}_{\mathrm{qb}}\,/\,\partial\lambda\right)$. Detailed discussions on relaxation and decay can be found in ref. [24].

The transversal part $\hat{D}_{\lambda,\perp}$ ($\perp$=x, y) represents noise involving exchange of energy with the environment. Since $\hbar\omega_{ge} \gg k_B T$ this is dominantly an emission of energy from the qubit at a rate Γ_{rel}, but a small thermal excitation rate Γ_{ex} can still be present summing up to Γ_1=Γ_{rel}+Γ_{ex}. The individual rates follow from Fermi's golden rule:

$$\Gamma_{\mathrm{rel}} \ = \ \frac{\pi}{2}\,\hat{D}^2_{\lambda,\perp} S_\lambda(\omega_{ge}), \tag{2.80}$$

$$\Gamma_{\mathrm{ex}} \ = \ \frac{\pi}{2}\,\hat{D}^2_{\lambda,\perp} S_\lambda(-\omega_{ge}), \tag{2.81}$$

with $S_\lambda(\omega_{ge})$ the noise spectral density of λ around ω_{ge}. Assuming a weak coupling to a short-correlated and cold ($\Gamma_{\mathrm{rel}} \gg \Gamma_{\mathrm{ex}}$) environment, the qubit excitation probability p_e decays as

$$p_e(t) = p_e(0) e^{-\Gamma_1 t}. \tag{2.82}$$

The free induction decay rate is composed of two parts; a contribution from relaxation and one from dephasing:

$$\Gamma_2 = \frac{\Gamma_1}{2} + \Gamma_{\varphi}. \tag{2.83}$$

The dephasing rate Γ_φ is due to the low frequency fluctuations of the transition frequency $\omega_{ge}(\lambda)$, which depend on the noise spectral density S_λ of λ and on the sensitivity coefficient $\hat{D}_{\lambda,z}$.

In the case of a flat noise spectrum

$$\Gamma_{\varphi,W} = \pi S_{\omega_{ge}}(\omega = 0) = \pi \hat{D}^2_{\lambda,z} S_\lambda(\omega = 0). \tag{2.84}$$

This leads to an exponential decay $\exp(-\Gamma_{\varphi,W}\, t)$ of the off diagonal elements of the density matrix.

In the case of 1/f noise with spectral density $S_\lambda(\omega) = A_{1/f}/|\omega|$, the decay takes a Gaussian form $\exp(-\Gamma^2_{\varphi,1/f} t^2)$ with

$$\Gamma^2_{\varphi,1/f} = A_{1/f} \hat{D}^2_{\lambda,z} \ln\left(\frac{1}{\omega_{\mathrm{ir}}\, t} + \mathcal{O}(1)\right) \tag{2.85}$$

depending weakly on t and ω_{ir} a protocol dependent cut-off frequency.

2.2.3 Cavity and circuit QED

Historically cavity QED is the physics of cavities made of two highly reflective mirrors with an atom trapped between them as depicted in fig. 2.11 a. This in a nutshell is the physics of a harmonic oscillator coupled to a spin. The same situation can be created with superconducting circuits, and thus circuit-QED can be seen as a subbranch of cavity-QED.

In this section the canonical example of cavity-QED, a harmonic oscillator coupled to a spin-1/2, will be discussed first in the form of the Jaynes-Cummings Hamiltonian. We specifically look at the two cases; a spin resonant with the cavity, and a spin far off-resonant from it. Thereafter the effects of additional levels, as present in the transmon, modify the system. The particular case of where the $|e\rangle \to |f\rangle$ transition is resonant with the harmonic oscillator $\omega_{\mathrm{ef}} = \omega_0$ is explicitly considered.

The first section follows an outline presented in detail in ref. [23] and the second one is based on ref. [28].

2.2.3.1 Jaynes-Cummings model

The Jaynes-Cummings Hamiltonian is composed of three terms representing the harmonic oscillator $\hat{H}_{\mathrm{HO}}$, the spin-1/2 (qubit) $\hat{H}_{\mathrm{qb}}$ and their interaction $\hat{H}_I$. $\hat{H}_{\mathrm{HO}}$ and $\hat{H}_{\mathrm{qb}}$ are expressed in eq. 2.42 and eq. 2.65 while H_I will be introduced here.

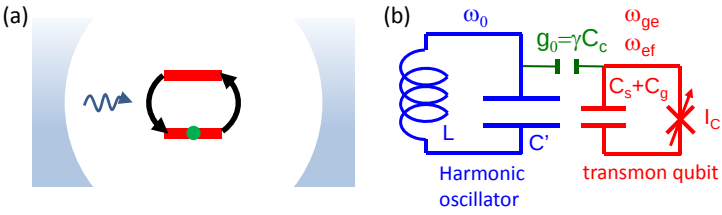

Figure 2.11. a) Schematic of a cavity QED system with a cavity coupled to a TLS. On resonance, the energy oscillates between the two systems. b) Equivalent circuit representation of a cavity mode coupled to a transmon with a coupling strength g_0.

The interaction arises from the spin dipole $\vec{\hat{d}}$ coupling to the electric field $\vec{\hat{E}}_{\mathrm{HO}}$ of the cavity, and writes in the frame rotating at the frequency of the field

$$H_I = -\vec{\hat{d}} \cdot \vec{\hat{E}}_{\mathrm{HO}} = -[d^* \hat{\sigma}_- + d\,\hat{\sigma}_+] \cdot i[\zeta^* \hat{a} + \zeta\,\hat{a}^\dagger]. \tag{2.86}$$

Expanding the product gives four terms, two of which are proportional to $\hat{\sigma}_- \hat{a}$ and $\hat{\sigma}_+ \hat{a}^\dagger$, and play a minor role in the dynamics when the harmonic oscillator frequency ω_0 and the spin frequency ω_{qb} are close. In the RWA these terms are neglected, yielding

$$H_I = -i\hbar g_0[\hat{a}\,\hat{\sigma}_+ + \hat{a}^\dagger \hat{\sigma}_-], \tag{2.87}$$

where $2g_0 = d\zeta\,/\,\hbar$ is the vacuum Rabi frequency, the frequency at which the two systems exchange a photon when resonant. In terms of the circuit in fig 2.11 b, the coupling $g_0 = 2\beta \mathrm{eV}^0_{\mathrm{rms}} \langle g|\hat{n}_{\mathrm{CP}}|e\rangle$ with $\beta = C_C\,/\,(C_C + C_s + C_g)$ and $V^0_{\mathrm{rms}} = \sqrt{\hbar\omega_0/2C'}$ being the zero-point voltage fluctuations of the mode [28] (see also sections 2.2.1 and 2.2.2).

Considering for a moment the uncoupled system the eigenenergies are $\hbar(n\omega_0 \pm \omega_{\mathrm{ge}}/2)$ and the eigenstates are noted $|g,n\rangle$ and $|e,n\rangle$. In the case of a small detuning $\Delta_{ge} = \omega_{ge} - \omega_0$ the states form doublets of $|e,n\rangle$ and $|g,n+1\rangle$, each one having $n+1$ elementary excitations. By including the coupling H_I again the Hamiltonian restricted to the doublet n is

$$\hat{H}_n = \hbar\omega_0\, n\mathbb{1} + \frac{\hbar}{2}[\Delta_{ge}\,\hat{\sigma}_z + \mathrm{sg}_n \hat{\sigma}_y], \tag{2.88}$$

with $g_n = g_0\sqrt{1+n}$. By diagonalizing $\hat{H}_n$ one gets the eigenenergies

$$E_n = \hbar\omega_0 n \pm \frac{\hbar}{2}\sqrt{\Delta_{ge}^2 + 4g_n^2} \tag{2.89}$$

and the corresponding eingenstates

$$\begin{aligned} |+,n\rangle &= \cos(\theta_n/2)|e,n\rangle + i\sin(\theta_n/2)|g,n+1\rangle \\ |-,n\rangle &= \sin(\theta_n/2)|e,n\rangle - i\sin(\theta_n/2)|g,n+1\rangle \end{aligned} \tag{2.90}$$

with the mixing angle $\theta_n = \arctan(2\,g_n\,/\,\Delta_{ge})$. These 'dressed' eigenstates can thus according to eq. 2.61 be represented on a Bloch sphere with $\varphi = \pi/2$.

Two regimes will now be discussed: the resonant regime with $\Delta_{ge} = 0$ and the dispersive one with $|\Delta_{ge}| \gg g_0$.

Resonant regime

In the uncoupled resonant regime the eigenstates are given by eq. 2.90 with $\theta_n = \pi/2$, and the eigenenergies are degenerate. The coupling lifts that degeneracy according to eq. 2.72, separating the levels by $2\hbar g_n$.

In the undressed basis the evolution of the quantum state is as follows: Starting from $|\psi(0)\rangle = |e,n\rangle$ and switching on the coupling, the evolution under the Hamiltonian 2.71 is

$$|\psi(t)\rangle = \cos(g_n t)|e,n\rangle + \sin(g_n t)|g,n+1\rangle \tag{2.91}$$

and corresponds to an oscillation between $|g,\ n+1\rangle$ and $|e,\ n\rangle$ at frequency $2g_n$.

Dispersive regime

In the dispersive regime $|\Delta_{ge}| \gg g_0$ the energies are only slightly shifted from those of an uncoupled system and we keep the same names for the eigenstates. Mathematically, a unitary transformation that eliminated the qubit-cavity interaction to lowest order followed by an expansion in $\chi_0 = g_0\,/\,\Delta_{\mathrm{ge}}$ yields the effective dispersive Hamiltonian [6] [2.3]

$$\hat{H}_{\mathrm{eff}} = \hbar\Big[\omega_0\,\hat{a}^\dagger\hat{a} + \Big(\frac{\omega_{ge}}{2} + \chi_0\hat{a}^\dagger\hat{a}\Big)\hat{\sigma}_z\Big] \tag{2.92}$$

$$= \hbar\Big[(\omega_0 + \chi_0\hat{\sigma}_z)\hat{a}^\dagger\hat{a} + \frac{\omega_{ge}}{2}\hat{\sigma}_z\Big]. \tag{2.93}$$

2.3. Note that the omitted vacuum energy $\hbar\omega_0/2$ gives rise to a (Lamb) shift of ω_{ge}.

Grouping terms by $\hat{\sigma}_z$ or $\hat{a}^\dagger\hat{a}$ in eqs. 2.92 and 2.93 emphasizes that one subsystem can probe the other: The second term in eq. 2.92 shows that for each photon in the cavity the qubit frequency is shifted by $2\chi_0$, thus allowing one to probe spectroscopically the probability distribution of the Fock states $p(n)$ by mapping it onto the qubit excitation. The first term in eq. 2.93 shows that the resonance frequency of the harmonic oscillator is shifted by $+(-)\chi_0$ when the qubit is in $|e\rangle$ ($|g\rangle$). A probe signal at $\omega_0 \pm \chi_0$ reveals thus the state of the qubit.

An important point is that the coupling of the qubit to the harmonic oscillator with a finite Q_{tot} provides a new relaxation channel for the qubit at a rate [28]

$$\kappa_{\text{Purcell}} = \kappa_{\text{tot}} \frac{g_0^2}{\Delta_{ge}^2}. \tag{2.94}$$

This is know as the Purcell effect.

2.2.3.2 Circuit QED for a transmon

Most of the results derived in the last section for a TLS are also valid when higher levels are included. This section cover the essential differences (see [28] for details).

The Hamiltonian is now a generalization of the Jaynes-Cummings Hamiltonian:

$$\hat{H}_{\text{Tr}} = \sum_k \hbar\omega_k |k\rangle\langle k| + \hbar\omega_0\, \hat{a}^\dagger\hat{a} + \hbar \sum_{l,m} g_{lm} |l\rangle\langle m| (\hat{a} + \hat{a}^\dagger). \tag{2.95}$$

The coupling energies g_{lm} are negligible except for adjacent levels ($l = m \pm 1$). In that case

$$g_{k+1\,k} \propto \langle k+1|\hat{n}_{\text{CP}}|k\rangle \approx \sqrt{\frac{k+1}{2}} \left(\frac{E_J}{8E_C}\right)^{1/4}, \tag{2.96}$$

and transmon couplings thus scales as

$$g_{k+1\,k} \approx \sqrt{k+1}\, g_0. \tag{2.97}$$

In the dispersive regime $g_0 \ll |\Delta_{ge}|, |\Delta_{ef}|$ the effective Hamiltonian in eq. 2.93 is still valid but with

$$\chi_0 = \chi_{ge} - \chi_{ef}/2, \tag{2.98}$$

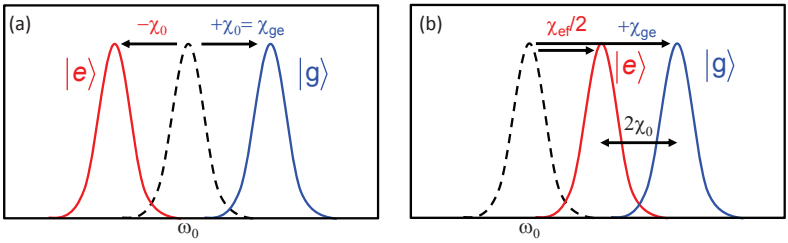

Figure 2.12. Dispersive shift of a harmonic oscillator. a) Coupling to a TLS leads to symmetric shift around the bare resonance frequency ω_0. b) Adding a third level destroys the symmetry and the shift depends on the anharmonicity α(see text).

where

$$\chi_{ge} = \frac{g_0^2}{\Delta_{ge}} \quad \text{and} \quad \chi_{ef} = \frac{\left(\sqrt{2}g_0\right)^2}{\Delta_{ef}} \tag{2.99}$$

represent the shift of the uncoupled eigenenergies due to the $|g\rangle \rightarrow |e\rangle$ and $|e\rangle \rightarrow |f\rangle$ transitions. This means that the shifts are no longer symmetric with respect to the uncoupled levels as shown in fig. 2.12.

A non-linearity (named Kerr non-linearity) of the harmonic oscillator emerges when the generalized Jaynes-Cummings Hamiltonian is expanded in the dispersive limit to higher order than done in eq. 2.93. This introduces an additional term

$$\hat{H}_{\text{Kerr}} = \frac{K}{2}\hat{a}^\dagger\hat{a}^\dagger\hat{a}\hat{a} \tag{2.100}$$

to the oscillator Hamiltonian eq. 2.42, with (ref [35] and eq. 2.98)

$$K = \frac{1}{\alpha}\left(\frac{\chi_0}{2}\right)^2 = \frac{\alpha}{4}\left(\frac{g_0^2}{\Delta_{ge}^2 + \alpha\Delta_{ge}}\right)^2 \underset{\Delta_{ge}\gg\alpha}{\longrightarrow} \frac{\alpha}{4}\left(\frac{g_0}{\Delta_{ge}}\right)^4. \tag{2.101}$$

Using the addressability of individual Fock states has been a key element in experiments on manipulating the field of a 3D cavity dispersively coupled to a transmon[27][48]. This requires a large coupling g_0 and a moderate detuning Δ_{ge} for adequate separation $2\chi_0$ between adjacent Fock state dependent excitation frequencies. This large separability comes however with a price of an increased Kerr-nonlinearity eq. 2.101. This causes dephasing between the Fock states $|n\rangle$ and thus limits the lifetime of coherent states.

2.2.3.3 e-f/cavity resonance condition

In order to reduce the Kerr non-linearity while still having the Fock state addressability we device a new scheme depicted in fig 2.13. The general idea is to have ω_{ef} resonant with ω_0 to maximize the separation between Fock state dependent transmon frequencies for a fixed g_0. Conversely a g_0 smaller than in the dispersive case can be used reach the same order of magnitude for the separation. This reduced g_0 together with the resonant condition yields a much smaller non-linearity K as shown below.

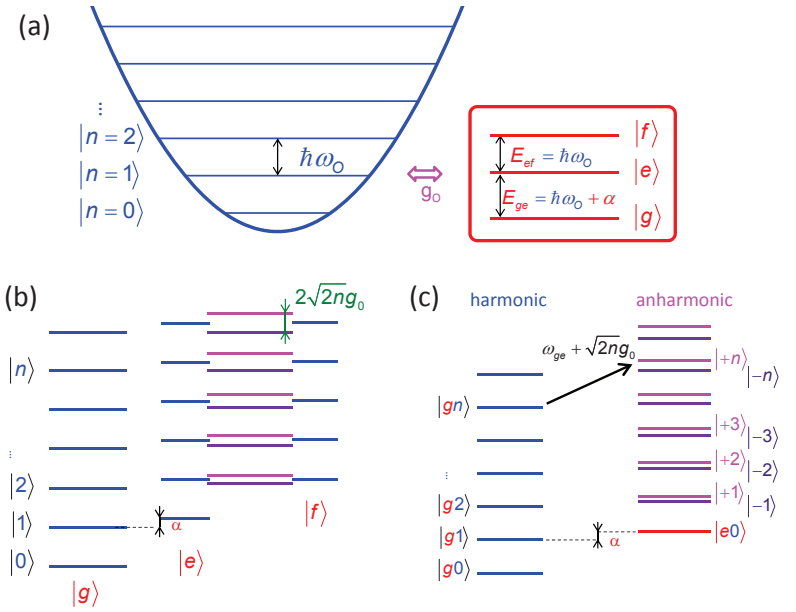

Figure 2.13. An 'ef-resonant' cavity-transmon system. a) The harmonic oscillator is coupled to a frequency tunable transmon. b) The levels of the uncoupled system laid out as three harmonic oscillators corresponding to $|g\rangle$, $|e\rangle$ and $|f\rangle$, showing that the levels $|e, n+1\rangle$ and $|f, n\rangle$ degenerate. When the coupling is included the the degeneracy is lifted by $\sqrt{2n}\,g_0$. The levels $|g, n\rangle$ are off-resonant by α and thus almost unaffected. c) The eigenstates $|g, n\rangle$ form a quasi harmonic ladder which can be excited to $|\pm, n\rangle$ at Fock state dependent frequencies $\omega_{n,\pm}$.

An exact calculation of the energy levels is found in appendix A but an intuitive picture of the system can be obtained by considering $|e\rangle$ and $|f\rangle$ as a TLS resonantly coupled to the cavity mode with a coupling strength $\sqrt{2}g_0$. As discussed above, this forms dressed states

$$|\pm, n\rangle = \frac{|e, n+1\rangle \pm |f, n\rangle}{\sqrt{2}}, \tag{2.102}$$

with eigenenergies $(n+1)\omega_0 \pm \sqrt{2n}g_0$. As a result the excitation frequency

$$\omega_{\pm,n} = \omega_{ge} \pm \sqrt{2n}g_0 \tag{2.103}$$

of the transition $+n \equiv |g, n\rangle \rightarrow |\pm, n\rangle$ becomes Fock-state dependent with a separation

$$\delta_{\pm,n} = \omega_{\pm,n+1} - \omega_{\pm,n} \approx \pm\sqrt{2}g_0(\sqrt{n+1} - \sqrt{n}) \tag{2.104}$$

that decreases with n. We thus refer to the two non-linear ladders $|+, n\rangle$ and $|-, n\rangle$ shown in fig. 2.13.

The inherited Kerr non-linearity expressed in eq 2.100 is not valid here as it assumes $g_0 \ll \Delta_{ef}$, but direct diagonalization gives

$$K_{ef} = 2\alpha\left(\frac{g_0}{\alpha}\right)^4. \tag{2.105}$$

It is interesting to compare the separation of the photon number peaks given by eq. 2.103 and the Kerr factor in eq. 2.105 to the separation $2\chi_0 \approx 2\alpha(g_0/\Delta_{ge})^2$ and Kerr factor eq. 2.101 in far dispersive regime $\Delta_{ge} \gg \alpha$. The separation of the Fock state dependent transmon excitation frequencies can be made of the same order in both cases, i.e. $2\chi_0 \approx \delta_{\pm,n}$ for small n, by choosing a coupling g_0' much smaller than g_0. The non-linearity is strongly reduced in the ef-resonant case by a factor $K/K_{ef} = (\Delta_{ge}/g_0)^4/32$ with $\Delta_{ge} \gg g_0$. As shown in chapter 6 we reach a value of $K_{ef} = -350$Hz in our experiment.

The system resulting from the $\omega_0 = \omega_{ef}$ resonance is thus a quasi-harmonic oscillator with individual Fock state addressability. The next section illustrates how the QZD can be implemented in such a system.

2.3 QZD in cavity QED

In ref. [39] and [40] J.M Raimond *et.al* discuss theoretically the QZD of a coherently driven harmonic oscillator in the context of cavity QED. They choose projectors $\{P_i\}_i = \{P_s, P_{s\perp}\}$, where $P_s = |s\rangle\langle s|$ is the projector onto the Fock state $|n=s\rangle$ and $P_{s,\perp} = \mathbb{1} - |s\rangle\langle s|$, to create the Zeno subspaces $\mathcal{H}_{n=s}$ and $\mathcal{H}_{n\neq s}$ ($\mathcal{H} = \mathcal{H}_{n=s} \oplus \mathcal{H}_{n\neq s}$). The Zeno subspace $\mathcal{H}_{n\neq s}$ is a harmonic oscillator with the level $|n=s\rangle$ removed such that a transition between $\mathcal{H}_{<s}$ and $\mathcal{H}_{>s}$ is suppressed. This separation of $\mathcal{H}_{<s}$ and $\mathcal{H}_{>s}$ can be depicted as an exclusion circle (EC) in phase space as shown in fig. 2.15. Note that though $\mathcal{H}_{n\neq s} = \mathcal{H}_{<s} \oplus \mathcal{H}_{>s}$ is a single Zeno subspace, individually $\mathcal{H}_{<s}$ and $\mathcal{H}_{>s}$ are not.

In section 2.1 three ways of inducing the QZD were discussed: Projective measurement, unitary kicks and continuous coupling to an external degree of freedom.

To implement the first two in cavity QED, as proposed by Raimond *et.al*, a small displacement pulse $D(\beta)$ alternates with proper Rabi rotations on the $|g, s\rangle \rightarrow |+, s\rangle$ transition as shown in fig 2.14. A π rotation followed by a readout of the transmon implements the projective measurement, where as a 2π Rabi rotation implements a unitary kick reversing the phase of $|s\rangle$. For an arbitrary Rabi angle ϕ the kick becomes non-unitary. Raimond *et.al* show however that for a non-zero β and a large ϕ the evolution is close to being QZD. This protocol can be regarded of a stroboscopic version of continuous coupling to an external degree of freedom presented in section 2.1.3.

Experimental demonstrations of QZD so far (including this thesis) implement it by coupling continuously to an external degree of freedom [45][8]. In our scheme this means driving the $|g, s\rangle \rightarrow |+, s\rangle$ transition continuously at a rate Ω implementing the coupling strength K from eq. 2.17. From a different perspective, this way of blocking can also be described by the Autler-Townes effect.

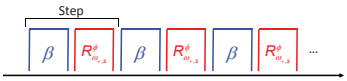

Figure 2.14. Protocol for implementing the QZD with unitary kicks decomposed into N steps. Each steps consists of a displacement by β and a Rabi rotation ϕ on the $|g, s\rangle \rightarrow |+, s\rangle$ transition at $\omega_{+,s}$.

This section covers three instances of QZD implemented with unitary kicks and a section on the evolution when using non-unitary pulses as simulated in ref. [40] which illustrates the robustness of the process. A particularly interesting example of using the QZD to manipulate superposed coherent states, the phases space 'tweezers' [39], is then summarized. Finally we illustrate how the Autler Towns effect leads to QZD.

2.3.1 QZD in cavity QED using unitary kicks

As discussed in section 2.1.2, the QZD can be induced by interrupting underlying unitary evolution $\hat{U}(t)$ N times with a unitary kick $\hat{U}_K$ (eq. 2.11). We consider $\hat{U}(t)$ to be a coherent drive at frequency ω_0, as defined in eq. 2.45 and when interrupted N times, $\hat{U}(t/N)$ becomes the displacement operator $\hat{D}(\beta)$ where $\beta = -i\zeta t/(N\hbar)$.

The unitary kick $\hat{U}_K$ is implemented as a 2π Rabi rotation on the $|g,s\rangle \rightarrow |+,s\rangle$ transition such that

$$\hat{U}_K = \mathbb{1} - 2|s\rangle\langle s|. \tag{2.106}$$

The steps of the unitary evolution operator are thus $\hat{U}_K\hat{D}(\beta)$.

Three examples of evolutions in $\mathcal{H}_{n\neq s}$ were simulated in ref. [40] for s=6 (EC of radius $\sqrt{6}$), and N=49 and $\beta = 0.1$ (int$(2\sqrt{6}/\beta)$=N. Figure 2.15 shows snapshots of the evolutions using Wigner's representation (see chapter 4).

The top row, fig 2.15 a, shows the confinement inside the EC: Starting in $|0\rangle$ the amplitude increases along the positive real axis until it reaches $\sim$2 when it "collides" with the EC at $N = 15$. This causes a rapid π phase shift, giving an amplitude ~ -2 at $N = 35$. Midway through the shift, at $N = 25$, a coherent superposition state of the two phases is created. At $N = 45$ the state has almost returned to the vacuum.

In fig 2.15 b and c the initial states are $|\alpha = -5\rangle$ and $|\alpha = -4 + i\sqrt{6}\rangle$, respectively, following otherwise the same evolution. In the fig 2.15 b the field collides with the EC at $N = 20$ and undergoes a π phase shift, creating a superposition state at $N = 25$, and emerging as a coherent state on the right side of the EC. This has the appearance of the state accelerating its movement in phase space over the EC.

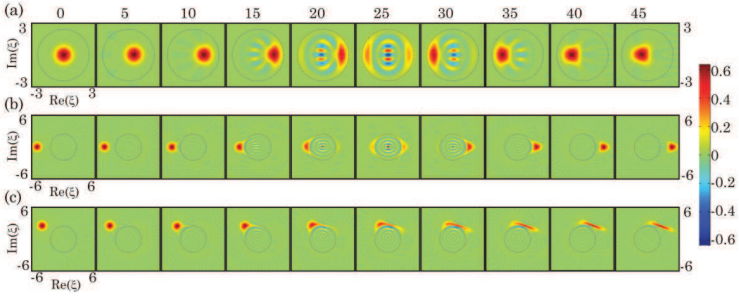

Figure 2.15. Snapshots of numerical simulations of the cavity state undergoing the QZD with $\beta = 0.1$ and $s = 6$, at every fifth step. a) Starting in the vacuum state, the dynamics is periodic inside $\mathcal{H}_{<6}$, with a period of 50 steps. b) The initial state $|\alpha = -5\rangle$ is in $\mathcal{H}_{>6}$. It collides with the EC from the outside and creates a superposition state at $N = 25$ steps. c) Starting in $\left|\alpha = -4 + i\sqrt{6}\right\rangle$ the state collides tangentially with the EC resulting in an squeezed state. Figure reproduced from ref. [40]©.

Figure 2.15 c shows a tangential collision with the EC resulting in an squeezed state with fluctuations perpendicular to the tangent smaller than the vacuum fluctuations.

2.3.2 QZD in cavity QED using non-unitary kicks

In section 2.1 the QZD is discussed in the limit $N \to \infty$ and $K \to \infty$. This is unattainable in practice leading to imperfect QZD. These imperfections are studied in ref. [40] for the case of the confinement by an EC at $s = 6$ described in the previous section, but with an arbitrary Rabi angle $0 \leqslant \phi \leqslant 2\pi$ and variable displacement β per step, keeping $N\beta = 2\sqrt{6}$:

When $\phi \neq 2\pi$ the rotation is no longer a unitary in $\mathcal{H}$. However, by considering the total cavity-transmon Hilbert space $\mathcal{H}_{\text{tot}} = \mathcal{H} \oplus \mathcal{H}_{\text{tr}}$, the kick

$$\hat{U}_K = e^{-i\phi/2}\hat{P}_+ + e^{i\phi/2}\hat{P}_- + \hat{P}_\perp \tag{2.107}$$

is unitary with

$$\hat{P}_\pm = |u_\pm\rangle\langle u_\pm|, \quad |u_\pm\rangle = \frac{|g, s\rangle \pm |+, s\rangle}{\sqrt{2}}, \tag{2.108}$$

and $\hat{P}_\perp = \mathbb{1} - \hat{P}_+ - \hat{P}_-$.

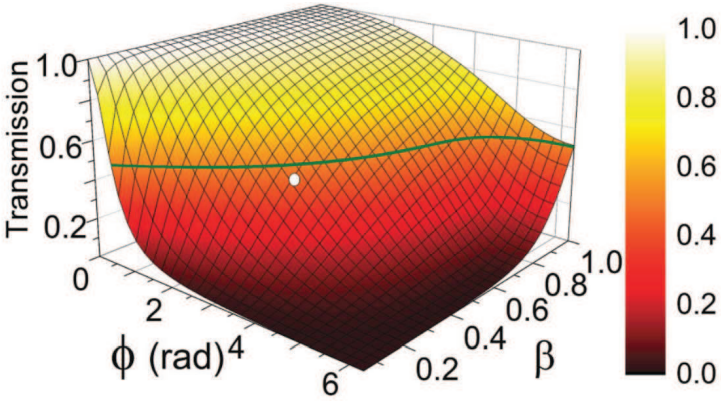

Figure 2.16. Two measures of the robustness of the QZD. The quantum state is evaluated after a total displacement of $2\sqrt{6}$ for varying Rabi angles ϕ and numbers of interruptions $N = \mathrm{int}(2\sqrt{6}\,/\,\beta)$. The transmission of the EC is obtained by comparing the weight of the wave function on either side of the EC. The green line indicates 50% transmission. Figure from ref [40]©

In order to study the imperfections of the QZD when the displacement per step β are not infinitely small and the kicks are limited in size Raimond *et.al.* simulate the evolution for $0.05 \leqslant \beta \leqslant 1$ and $0 \leqslant \phi \leqslant 2\pi$. The 'transmission' $\mathcal{T}$ through the EC is defined as [40]:

$$\mathcal{T} = \frac{w_{>s}^2}{w_{<s}^2 + w_{>s}^2}, \tag{2.109}$$

where $w_{>s}^2$ and $w_{<s}^2$ represent the weight of the wave function outside and inside the EC. $\mathcal{T}$ is shown in fig. 2.17. The graph illustrates that $\mathcal{T}$ is low for a moderate values of β and ϕ, and that the QZD is a robust process.

2.3.3 Phase space tweezers

In ref. [39] and [40] J.M Raimond *et.al* also propose a clever and versatile way to use the QZD for manipulating coherent states in phase space, named the phase space 'tweezers', which is worth summarizing here: This enables the displacement of individual components of superposed coherent states

$$|\psi\rangle = c_1|\beta_1\rangle + c_2|\beta_2\rangle \tag{2.110}$$

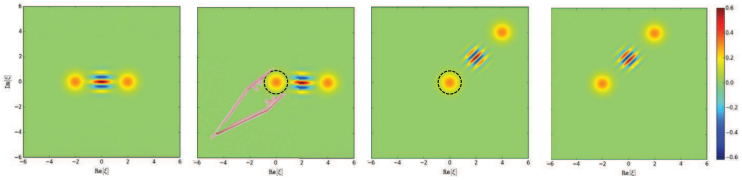

Figure 2.17. Method to manipulate a superposition of coherent states with the phase space 'tweezers'.

provided that the overlap is small ($|\beta_1 - \beta_2| \gg 1$). As shown in fig. 2.17, in order to displace $|\beta_2\rangle$ but not $|\beta_1\rangle$ one first applies $\hat{D}(-\beta_1)$ creating

$$\hat{D}(-\beta_1)|\psi\rangle = c_1|0\rangle + c_2|\beta_2 - \beta_1\rangle. \tag{2.111}$$

Placing the EC now on $s=1$, e.g. with a unitary kick, and applying a coherent drive displaces the 'free' component $|\beta_1 - \beta_2\rangle$ while $|0\rangle$ is kept in place. Removing the EC and applying a displacement $\hat{D}(\beta_1)$ restores $|0\rangle$ to $|\beta_1\rangle$.

Repeating this sequence allows for almost arbitrary tailoring of coherent states in phase space.

2.3.4 QZD in cavity QED via continuous coupling

In our cavity QED experiment the QZD is implemented with continuous coupling as presented in section 2.1.3. This done by driving continuously the $|g,s\rangle \to |+,s\rangle$ transition at a Rabi frequency Ω. With the notations of section 2.1.3 the driving Hamiltonian

$$KH'_C = \frac{\Omega}{2}|s\rangle\langle s| \otimes \left(|+\rangle\langle g| + |g\rangle\langle +|\right) \tag{2.112}$$

in $\mathcal{H} \otimes \mathcal{H}_{\mathrm{tr}}$ reduces to

$$KH_C = \frac{\Omega}{2}|s\rangle\langle s| \tag{2.113}$$

in $\mathcal{H}$, which leads to the projectors P_s and $P_{s\perp}$, and Hilbert spaces $\mathcal{H}_{n=s}$ and $\mathcal{H}_{n\neq s}$ already mentioned.

To shed a different light on the physics we also describe below the effect of the continuous drive in terms of dressed states and the Autler-Townes effect.

Applying a continuous drive at frequency $\omega_d \simeq \omega_{+,s}$ drives the transition $|g,\, s\rangle \rightarrow |+,\, s\rangle$. By considering these two levels as a TLS the Hamiltonian of the driven system in the rotation frame is given by eq. 2.79. It can be rewritten as

$$\hat{H} = \hbar\left(\Delta|+,s\rangle\langle+,s| + \frac{\Omega}{2}(|+,s\rangle\langle g,s| + |g,s\rangle\langle+,s|) \right), \tag{2.114}$$

by taking the phase of the drive $\varphi_{\mathrm{dr}} = 0$ and rescaling the energy by $\hbar\Delta/2$, with $\Delta = \omega_{+,s} - \omega_d$. Going back to the lab frame, each of the eigenenergies corresponding to $|g,s\rangle$ and $|+,s\rangle$ are split by

$$E_{\pm} = \Delta \pm \frac{\sqrt{\Omega^2 + \Delta^2}}{2}, \tag{2.115}$$

creating an anticrossing as shown in fig. 2.18a [2.4]. This is known as the Autler-Townes doublet [11].

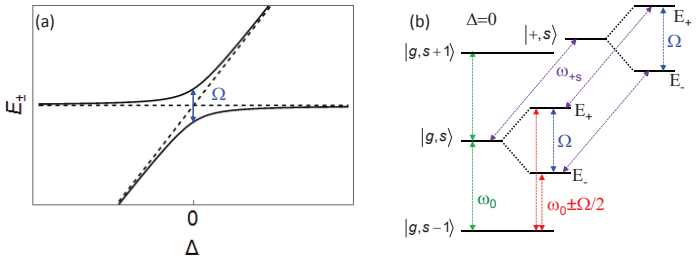

Figure 2.18. Energy levels shift due to strong coherent driving. a) Single energy level of a TLS (horizontal dotted line) anticrosses with the energy of a drive field (increasing dotted line) at $\Delta \sim 0$, forming dressed states E_+ and E_-. b) Schematic of part of the transmon-cavity level structure when driving at $\omega_{+,s}$ (i.e. $\Delta = 0$). The excitation spectrum from $|g,\, s\rangle$ has split into a doublet and is no longer resonant with ω_0, thus implementing an EC at $|n = s\rangle$.

2.4. The rate Ω is only approximately the same for the two levels as explained in ref

Going back to the ef-resonant system and considering the case of a resonant drive $\omega_d = \omega_{+,s}$, the levels around $|g, s\rangle$ are depicted in fig. 2.18 b; The energy levels of both $|g, s\rangle$ and $|+, s\rangle$ are split by Ω such that the transition between them independent of Ω, and thus still $\omega_{+,s}$. However, the levels split from $|g, s\rangle$ are not resonant with the harmonic ladder. This effectively removes the $|s\rangle$ Fock state from the ladder creating an EC at $n = s$.

Ideally the drive is perfectly selective; influencing only the $|g,\ s\rangle$ state while leaving the $|g,\ n \neq s\rangle$ states unaffected. The finite separation between $\omega_{+,n=s}$ and $\omega_{+,n\neq s}$ however results in a non-zero off-resonant shift of the $\omega_{+,n\neq s}$ transition, the influence being greatest with the neighboring transitions at $\omega_{+,s+1}$ and $\omega_{+,s-1}$. This spoils the harmonicity of the ladder and the selectivity of the EC. These parasitic effects limit the practical values Ω as discussed in chapter 7.

Chapter 3

Measurement setup, instruments and techniques

This chapter describes the various technical aspects of the experiment. We start of by explaining the transmon fabrication process and give the specific recipes, then we introduce the working principle of a dilution refrigerator used to cool the sample and lastly discuss the microwave signal generation and detection techniques used for the measurements.

3.1 Qubit fabrication

The transmons are fabricated with a technique known as double angle evaporation and is well suited for making Josephson junctions. It is based on suspending a mask, made by electron-beam lithography (EBL), over a substrate as depicted in fig. 3.1. Evaporating Al at two different angles sequentially with an oxidation step in between creates a partial overlap of the two Al depositions separated by an insulating Al_2O_3 layer creating a Josephson junction. The mask is made with two layers of different resists, the bottom one being more sensitive to the electron beam leading to a void beneath the top layer, called an undercut. Here we describe the general principles of the different fabrication steps while the recipes can be found in section 3.5.

3.1.1 Substrate choice and resist deposition

The transmons are fabricated on a low loss substrates, either high resistivity Si (ρ_{Si}>4000 Ωcm) or sapphire (Al_2O_3). Both come in the form of commercial monocrystalline 2 inch diameter wafers, 330 μm thick with a c-axis crystal orientation in the case of Sapphire and 300 μm thick with a 50 nm SiO_2 layer and a [100] orientation for Si. The SiO_2

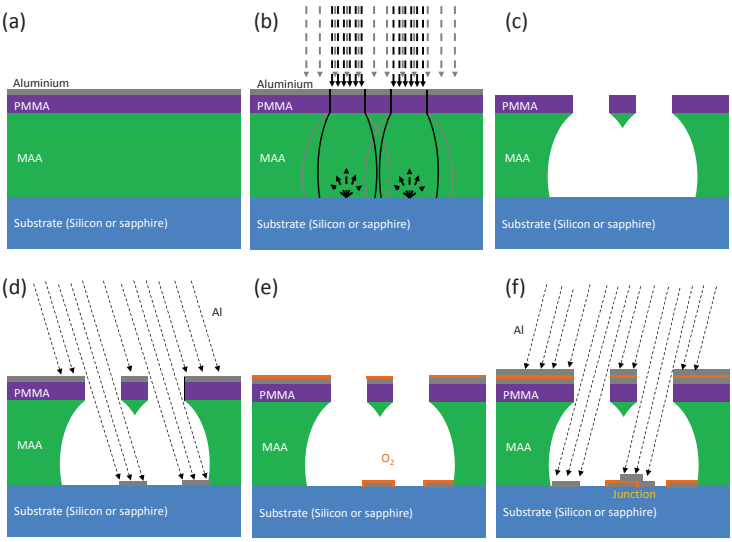

Figure 3.1. Transmon fabrication process. a) The two resist layers and an (optional) Al layer prepared on a substrate. b) Electron beams shot at a high dose (black) break up the resist molecules. A low dose bombardment at the surrounding mainly affects the lower layer. c) The Al layer is removed with KOH and subsequently the exposed resist is dissolved in MIBK. d) The first layer of Al is deposited at an angle. d) Exposure to O_2 creates an insulating Al_2O_3 layer. f) A second layer of Al is deposited at an opposite angle where the overlap with the first Al layer forms a Josephson junction.

is removed with hydrofluoric acid (HF). A Si substrate was used for the first sample because a fabrication recipe was at hand. Later, a recipe for sapphire fabrication was developed because it has a lower loss tangent than Si.

Various steps can be taken to ensure a clean wafer. Their application to the different samples are found in the recipe.

- Acetone to remove grease.
- O_2 plasma either in an asher or a reactive ion etcher (RIE) is used to burn off organic residues.
- Commercial resist remover (remover 1165 from Shipley).
- Machine rinsing the wafer with high pressure water jets.
- HF bath removes various materials e.g. SiO_2 of Si.

After a water or an acetone rinse, the wafer is rinsed in isopropanol (IPA) which is the easy to dry by blowing N_2. Lastly, just before depositing the bilayer, the accumulated water vapor can be evaporated from the wafer by placing it on a hotplate and letting it cool after.

The mask is made out of two polymer layers (i.e. bilayer) mixed with a solvent, which is evaporated during baking. First is a layer of copolymer MMA-MAA (methyl methacrylate - methacrylic acid) and then on top of that a layer of PMMA (polymethyl methacrylate). PMMA has the role of a mask and should be as thin as possible, representing a 2D mask, down to the limit of breaking. The copolymer suspends the PMMA off the substrate without blocking the Al deposition and its thickness depends on the Al evaporation angles and shift of the mask pattern needed.

For deposition each resist layer the wafer is placed onto a spinner and a few drops of the resist placed at its center, such that it covers most of the wafer. During the spinning the resist spreads out to a layer whose thickness depends on spinning speed and the viscosity of the resist. Spinning at a higher speed for a few seconds at the end can remove the thick resist bump that tends to accumulate at the edge of the wafer. After spinning, the resist is baked on a hot plate and becomes hard as solvents evaporate from it. The thickness of the layer is measured by optical interferometry using Filmetrics F20 Thin Film Measurement System.

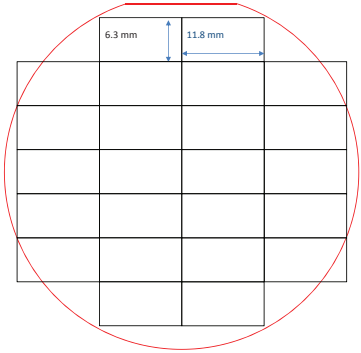

Figure 3.2. A 2 inch wafer is diced into chips of relevant dimensions, either 6.3x11.8 mm^2 or 6.0x9.0 mm^2.

During EBL the accumulation of charge must be avoided. I the case of an insulating substrate like sapphire a thin layer of Al is Evaporated on top of the bilayer.

Having prepared the wafer, it is diced into chips of the appropriate dimensions for each experiment. With silicon this can be done by using a diamond scriber along the crystal orientations of the wafer and cleaving afterwards. Scraping and breaking is more challenging with sapphire due to its non-orthogonal crystal symmetry and are therefore diced with a dicing saw. After dicing the chips are ready for EBL.

3.1.2 Electron beam lithography

The effect of an electron beam on the resist is to break the polymer molecules into smaller pieces, making them soluble in a developer. The higher sensitivity of the lower layer to this effect, as well as the scattering of the incoming electrons off the substrate, produces a volume called an undercut, where the copolymer is removed from underneath the PMMA. The undercut can be enhanced by an "undercut box", where an area around the structure is exposed with a weak dose such that the PMMA is minimally affected as depicted in fig. 3.1. Where two undercuts overlap a bridge is formed in the PMMA and is a key feature in producing Josephson junctions, as will be discussed in the forthcoming.

The equipment used for electron-beam lithography is a Raith e-line masker with a few nanometer precision interferometric stage. The chip is mounted on a stage where clamps hold it in place. The electrons striking the sample discharge through the substrate and the stage or via the charging layer and the clamps. The corners of the chip are gently scratched to facilitate focusing. The stage is subsequently loaded into the SEM via loadlock and reaches an operating pressure of $< 6 \cdot 10^{-6}$ mbar.

The sample is exposed with a 25 keV beam at a current varying with the beam aperture and is measured with a Faraday cup. For the transmon pads we use about 4.5 nA and around 18 pA. Before starting the exposure however, the tilt of the chip is calibrated for with focusing on 3 corners of the sample for subsequent planar interpolation of the focus, and the geometric aberrations of the beam deflections are calibrated for using the interferometric stage enabling automatic correction. After synchronizing the software coordinate system to the location of the chip, a macro automatically runs the exposure process. The exposure file (GDSII) of the two different transmon geometries is shown in fig. 3.3. The structures away from the junctions are dosed

strongly to ensure all the resist will be removed. Around the junction the dose has been tuned down to ensure the fine structure of the mask remain intact. A rectangular area around the SQUID, exposed at a very low dose, is the undercut box. Details are given in the recipe.

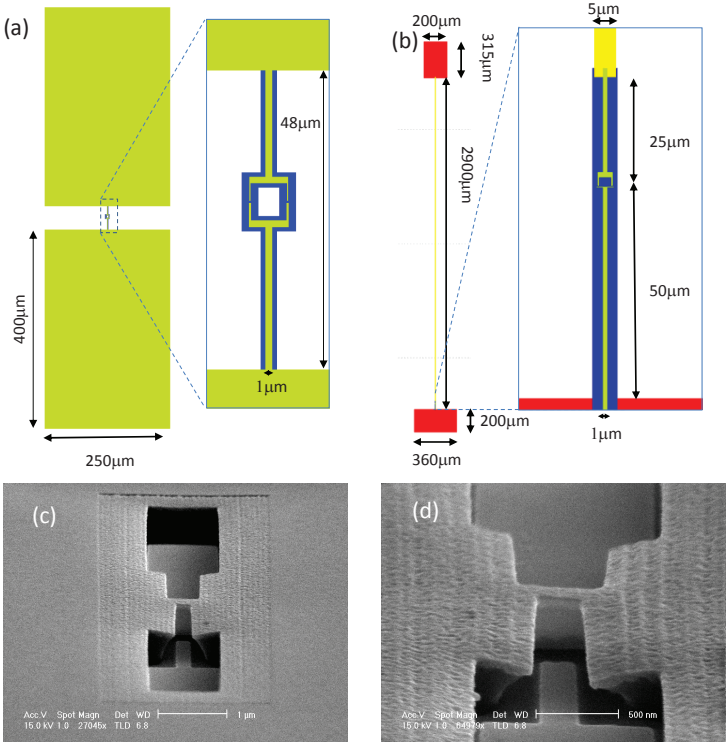

Figure 3.3. Electron beam lithography pattern of the transmons. a) and b) are snap shots of the GDSII exposure files controlling the shapes traced out by the electron beam. The color represents the dose in reference to a 250 $\mu C/cm^2$ nominal dose with ∼10%(blue), ∼100%(green) and ∼190%(red). a) The first transmon design used in a Cu cavity while the one in b) is used in the QZD experiment. c) Bilayer mask after exposure and development. We see the frame of the undercut box around the main pattern. d) Bridge in the PMMA: The bending of the structure is due to the stress induced by the imaging electron beam. c) and d) are test structure for tuning the doses of the undercut boxes and the main pattern.

After e-beam exposure the sample is developed by immersing the chip in various liquids and shaking it gently. If a charging layer is in place it is first removed in a 20 g/mol solution of KOH, rinsed in deionized water and dried with N_2. It is important to dry the sample well and prevent water droplets from evaporating on the surface of the as it leaves dirt behind. When the bilayer is uncovered the exposed parts are dissolved in MIBK(methyl isobuty ketone) solution, 25% MIBK 75% IPA, rinsed in IPA and thoroughly dried with N_2.

After developing some resist residues may still remain on the substrate below the mask. They are removed with O_2 -plasma ashing or RIE at a high O_2 pressure and low acceleration voltage.

3.1.3 Metal evaporation

With the mask prepared the transmon is made by double angle evaporation using either a Plassys MEB 550S e-gun or Plassys MEB 450 e-gun. In both cases the sample is clamped onto a stage that can rotate around an axis perpendicular to the evaporation direction. We also cover the chip with a metallic mask which prevents deposition on the edges of the chip. After mounting, the chamber is pumped down to $\sim 10^{-6}$ mbar or below.

Before the Al deposition, the substrate is cleaned in-situ by ion milling with a neutralized beam of Ar^+ ions at 500 eV at both deposition angles. Thereafter the first layer of Al of ∼25nm is deposited, followed by an oxidation step where a few mbars of the Ar/O_2 mixture fills the camber for around 5 to 10 min. Lastly the second Al layer of 35 to 60 nm is deposited. Care must thus be taken with electrostatic discharge when handling the sample from this point forward. Finally the remaining resist is removed in a liftoff procedure described in the recipe. The oxidation of the junction continues for some time after the sample has been exposed to air. Therefore we saturate the oxidation by heating the sample on a hot plate.

3.1.4 Liftoff, characterization and mounting

The Josephson energy E_J of the SQUID can be calculated from its normal state resistance R_n, using Ambegaokar Baratoff reflection [2]

$$E_J = \frac{h\,\Delta(T=0)}{8\,R_n\,e^2},$$

where h is Plancks constant, $\Delta(T=0)$ is the superconducting gap of Al at T=0, and e is the electric charge.

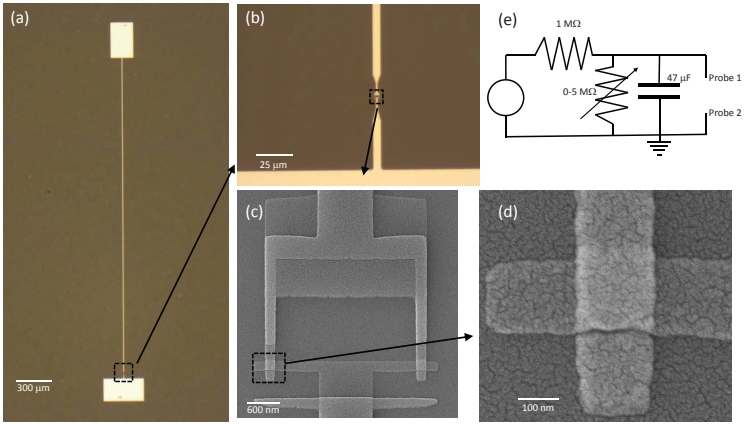

Figure 3.4. Images of the fabricated transmon. a) and b) optical images. c) SEM image of the squid. d) SEM image of a Josephson junction. e) The circuit used to protect and measure the SQUID resistance R_n.

The room temperature resistance between the two pads is therefore measured with a probe station, a multimeter and a circuit designed to protect the sample from electrical discharge when placing the probes. Essentially, a tunable resistance is lowered to shunt the sample while the probes are being lowered or raised. Then, to measure it, the tunable resistance is increased, passing all the current through the sample. The junction resistance is then calculated from the two resistance tunings, taking into account the resistance of the Al wires of the transmon. The room temperature resistance is known to increase by 20% at 4K. Scaling by that amount allows us to calculate E_J.

If the calculated E_J is close to the targeted value the transmon is mounted in the cavity. For the first experiments, the chip was placed in a designated groove in in the Cu cavity with small pieces of compressed indium as seen in fig. 3.5a. A thin indium wire is placed around the outside of a rim which is then compressed when the cavity is closed with its other half. For the other experiments the transmon is first mounted in a Cu cap and blocked with a manually tightened screw to avoid breaking the chip. The part of the chip now protruding from the Cu cap is then inserted into the slit of the cavity (which has already been closed with an indium seal). Finally a Cu bar is placed on top of the cap and fastened to keep it in place.

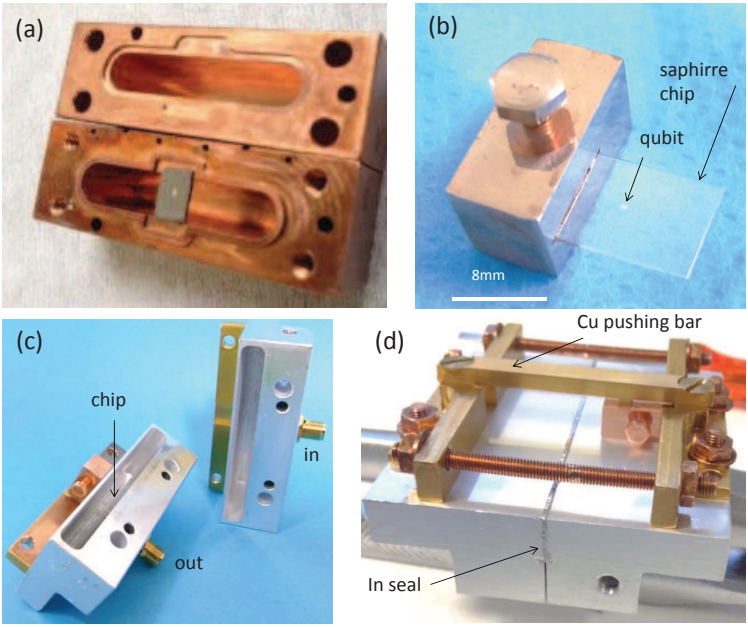

Figure 3.5. a) A transmon of the first type mounted in a groove of a Cu cavity. b) The QZD transmon mounted in a Cu cap. c) The cavity closed with an indium seal and the Cu cap secured with a pusher bar. d) The Transmon mounted in the open cavity.

3.1.5 Fabrication recipe

The following table contains the recipes for the three qubits used in this thesis. Sample 1 and 2 were fabricated on Si and sapphire, respectively, and are both transmons of the first type as shown in fig. 3.3a. Sample 3 was used in the QZD and is a transmon of the type shown in fig. 3.3b.

Table 3.1.

Sample	**KJ6ch27**	**KJ15ch11**	**KJ19ch1**
Wafer	**SiO_2 50 nm/ Si 300 μm**	**Al_2O_3 330μm**	**Al_2O_3 330μm**
Wafer preparation	**Dip in HF to remove SiO_2** **Rinse in water** **Rinse in IPA** **Dry**	**Remover 1165@60°C 10min + 1min in ultrasound. Twice in separate baths.** **Water jet machine 180s, dry 140s, heater 9, rinse in IPA.** **O_2 plasma ashing at 0.2 mbar (17cc) and 100W for 1 min.** **Acetone @45°C for 2 min in ultrasound.** **IPA @45°C for 2 min in ultrasound** **Dry**	**O_2 plasma reactive ion etching @ 0.3mbar(50cc) 50W for 1 min** **Buffer HF 2 min** **Rinse in water** **Rinse in IPA** **Dry** **Dry vapor @110°C for 2 min, and cool afterwards.**

Spinning	**MMA/MAA 8.5 EL 10: drops put in the center of the wafer.** **Spin at 2000 rpm for 60 s + 6000 rpm for 2 s** **Bake @170°C for 120 s** **Measure thickness of 545 nm** **PMMA 950k A3 (AFM/STM) drops put in the center of the wafer.** **Spin at 4000 rpm for 60 s + 8000 rpm for 2 s** **Bake @170°C for 15 min** **Measure thickness of 113 nm**	**MMA/MAA 8.5 EL 10: drops put in the center of the wafer.** **Spin at 2000 rpm for 60 s + 6000 rpm for 2 s** **Bake @180°C for 5 min** **Measure thickness of 593 nm** **PMMA 950k A3 (AFM/STM) drops put in the center of the wafer.** **Spin at 4000 rpm for 60 s + 6000 rpm for 2 s** **Bake @180°C for 15 min** **Measure thickness of 120 nm**	**MMA/MAA 8.5 EL 10: drops put in the center of the wafer.** **Spin at 1250 rpm for 60 s + 8000 rpm for 4 s** **Bake @180°C for 5 min** **Measure thickness of 709 nm** **PMMA 950k A3 (AFM/STM) drops put in the center of the wafer.** **Spin at 3250 rpm for 60 s + 8000 rpm for 4 s** **Bake @180°C for 15 min** **Measure thickness of 139 nm**
Discharging layer	**None**	**Evaporate 10 nm of Al**	**Evaporate 10 nm of Al**
Dicing	**Scribe pack side with a diamond scriber.** **Break into chips**	**Spin UV3 resist 2000rpm, bake @120°C for 2 min** **Dice 150 μm deep on the back side with a dicing saw.** **Remove UV3 resist in IPA bath for 1 min** **Break into chips**	**Spin UV3 resist 2000rpm, bake @130°C for 1 min** **Spin UV3 resist 2000rpm, bake @75°C for 15 s** **Measure thickness of 1000 nm** **Dice from the back with a dicing saw, 75 μm per pass.** **Remove UV3 resist in IPA bath for 1 min**

Electron beam exposure	**Dose:** **Big structures** **275 $\mu C/cm^2$** **Small structures** **325 $\mu C/cm^2$** **Undercut boxes** **50 $\mu C/cm^2$** **Beam current:** **Big structures** **4.6 nA** **Small structures** **113 pA** **Undercut boxes** **113 pA**	**Dose:** **Big structures** **325 $\mu C/cm^2$** **Small structures** **300 $\mu C/cm^2$** **Undercut boxes** **30 $\mu C/cm^2$** **Beam current:** **Big structures** **4.7 nA** **Small structures** **24.4 pA** **Undercut boxes** **24.4 pA**	**Dose:** **Big structures** **475 $\mu C/cm^2$** **Small structures** **450 $\mu C/cm^2$** **Undercut boxes** **15 $\mu C/cm^2$** **Beam current:** **Big structures** **5.24 nA** **Small structures** **23 pA** **Undercut boxes** **23 pA**
Development	**Remove exposed resist MIBK in IPA (1:3) for 50s** **Rinse in IPA** **Dry well**	**Remove charging layer 20g/mol in KOH for 27 s** **Rinse in water** **Dry well** **Remove exposed resist MIBK in IPA (1:3) for 60s** **Rinse in IPA** **Dry well**	**Remove charging layer 20g/mol in KOH for 35 s** **Rinse in water** **Dry well** **Remove exposed resist MIBK in IPA (1:3) for 60s** **Rinse in IPA** **Dry well**
Mask precleaning	**None**	**None**	**O_2 plasma reactive ion etching @ 0.3mbar(50cc), 66V for 12s**
Evaporation	**Pump vacuum $6.7 \cdot 10^{-8}$ mbar** **Ar ion milling 5mA for 2s at two angles 27° and -27°** **Evaporate 25 nm of Al at 1 nm/s at an angle of 27°** **Oxidize for 3:10 min 30 s @6.7 mbar** **Evaporate 35 nm of Al at 1 nm/s at an angle of 27°**	**Pump vacuum $1.7 \cdot 10^{-7}$ mbar** **Ar ion milling 5mA for 2s at two angles 28° and -30°** **Evaporate 25 nm of Al at 1 nm/s at an angle of 28°** **Oxidize for 3:10 min 30 s @6.7 mbar** **Evaporate 60 nm of Al at 1 nm/s at an angle of -30°**	**Pump vacuum $2.5 \cdot 10^{-6}$ mbar** **Ar ion milling 5mA for 2s at two angles -27° and 23°** **Evaporate 25 nm of Al at 1 nm/s at an angle of -27°** **Oxidize for 10 min 30 s @13.7 mbar** **Evaporate 60 nm of Al at 1 nm/s at an angle of 23°**

Lift off	**Acetone @60°C for 3 min + squirting jets with pipette** **Rinse in IPA** **Bake sample on a hot plate @100°C for 1 min to saturate oxidation**	**Same**	**Same**
Junction resistance measurement	**Make sure probes, sample stage, tweezers and sample box are all grounded** **Place the sample on the stage and turn of the lights to reduce conduction through the substrate.** **Increase the shunt resistance to pass the current through the sample. Measure 1.0063 MΩ** **Resistance of the wire negligible** **Junction resistance 9-6.3-2.0 = 4.3 kΩ**	**Same** **Increase the shunt resistance to pass the current through the sample. Measure 1.0084 MΩ** **Resistance of the wire negligible** **Junction resistance 9-8.4-3.6 = 4.8 kΩ**	**Same** **Increase the shunt resistance to pass the current through the sample. Measure 1.0090 MΩ** **Resistance of the wire 0.4 kΩ** **Junction resistance 9-4.7-0.4 = 3.9 kΩ**

3.2 Cryogenic setup

In our experiments we cool the samples down to low temperature $T_{\text{fr}} \sim$ 30mK such that the system is in its ground state and thermal excitation is negligible compared to the Transmon excitation energy: $k_B T_{\text{fr}} \ll \hbar\omega_{\text{ge}}$, where k_B is Boltzmanns constant. Aluminium used in the sample and the NbTi used in the low temperature cabling have critical temperatures $T_C \gg T_{\text{fr}}$. In order to reach these low temperatures the sample and

a large part of the electrical setup is placed inside a dilution refrigerator.

3.2.1 Dilution refrigeration

Dilution refrigerators are machines with several stages at different temperatures down to $T_{\mathrm{fr}} \sim 10$ to 50mK. There are two cooling steps, first cooling from room temperature to a few K where a second process takes over and cools down to T_{fr}. The first step divides the refrigerator into either "wet fridges", which use a liquid He^4 reservoir to cool down to 4 K, or "dry fridges" that use a pulse tube, a machine that pumps He^4 through a membrane in a closed cycle loop to cool down to 3-5 K.

The second cooling step is called dilution shown in fig. 3.6a is based on closed loop circulation of a He^3/He^4 mixture. The mixture, already being in thermal contact with the 3-5 K reservoir, is compressed into a mixing chamber through a high impedance line where it condenses and is pumped out through a low impedance line with a still, before being re-injected, forming a closed loop. Pumping at the still evaporates mainly He^3 as it has a much higher partial pressure than He^4, cools the still to 0.7-1 K. Thermally coupling the still to the injection line cools the re-injected helium and once the mixture goes below the triple point at 870mK it splits up into two phases, a He^3 concentrated and a He^3 dilute phase. The pumping of He^3 through the still is from the dilute phase which requires that the concentration equilibrium be regained with He^3 from the concentrated phase. This process costs energy, which is supplied by the environment and thus cools it.

3.2.2 Mounting the sample

We used an in-house made wet refrigerator for the first experiments with the first type of transmon in a Cu cavity, and an also home-made dry refrigerator prototype for the QZD experiment. The setups being similar, only that for the dry fridge is presented in detail below unless noted otherwise.

As shown in fig. 3.6b, the cavity is mounted to a Cu plate and sits inside a Helmholtz coil. Semi-flex SMA cable connect to the coupling ports and a Cu braid tightened onto the cavity is used for improved

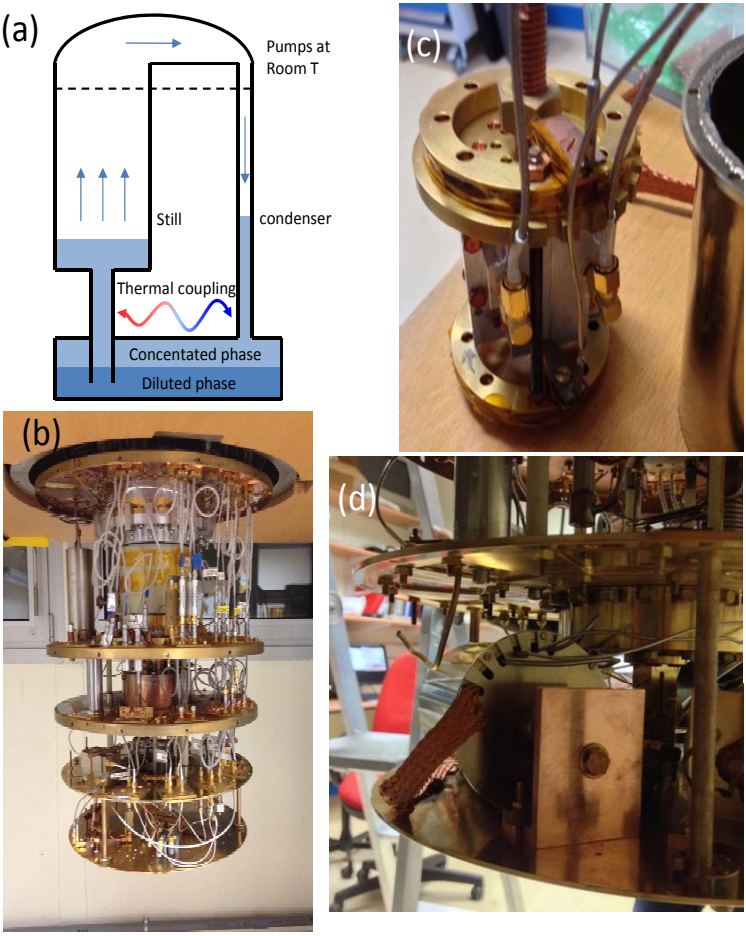

Figure 3.6. Our experiments are performed in dilution refrigerators. a) Dilution refrigeration principle. The He^3 / He^4 mixture separates into He^3 concentrated and dilute phases. Pumping on the diluted phase perturbs the phase equilibrium and the system uses the energy from its environment to restore it. b) The inside of a dilution fridge of the dry type. c) The sample inside a μmetal can, mounted onto the coldest stage of the fridge. d) The sample mounted between two coils and connected to semi-flex SMA cables.

thermalization. The setup is placed in a μ-metal can to shield the sample from stray magnetic fields. The closed μ-metal can is then mounted onto the mixing chamber plate of the dilution refrigerator.

3.2.3 Fridge circuitry

A diagram of the electrical circuitry is shown in fig. 3.7. It includes a bifilar dc line A1 for biasing the Helmholtz coils, and five coaxial lines: the main circuit is made of the input microwave line C3 connecting the microwave sources to the input port of the cavity, and the main output microwave line D2 connecting the cavity output port to the measurement setup at room temperature. This output line includes a parametric amplifier, which also uses three secondary input lines for microwave pumping (C4), dc biasing (B1), and optionally testing the amplifier (C2) without passing the signal through the cavity.

All lines go from room temperature to 30 mK through three other stages at 70K, 4K, and 1K. The coaxial ones are 2.2 mm in diameter and have SMA connectors between the different stages. The material is chosen with the perspective of having thermal conductivity sufficiently low to limit the thermal flow between successive stages, while keeping the electrical conductivity high enough to limit the microwave losses: CuNi rigid cables with an attenuation of 4 dB at 7 GHz are used from room temperature to 4K. Then superconducting NbTiN rigid cables with an attenuation lower than 1 dB are used from 4K to the mixing chamber plate. At the mixing chamber semi-flexible Cu cables connect the different components.

The electromagnetic noise along the lines is thermalized using a combination of attenuators, filters, and isolators: Attenuators are placed only along input microwave lines C2, C3 and C4 because input signals can always be increased whereas the small output signal on D2 should be preserved. Then two pairs of dissipative low pass filter (IR) and non- dissipative 4-8 GHz bandpass filters are used on C3 and D2 to protect the cavity-transmon sample from radiation outside the 4-8GHz window. Finally a double isolator is added on output line D2 to protect the sample from the noise propagating backward from the amplification chain.

The output signal on D2 first passes through the filters and the double isolator mentioned above, through the direct path of a directional coupler (see explanation below), and is then routed with a double circulator to a quantum limited 17dB gain parametric amplifier (JPA) operated in reflexion (see 3.3.4 for details). The returned amplified signal is routed by the same circulator to a 32 dB gain HEMT (high electron mobility transistors) amplifier placed at 4K.

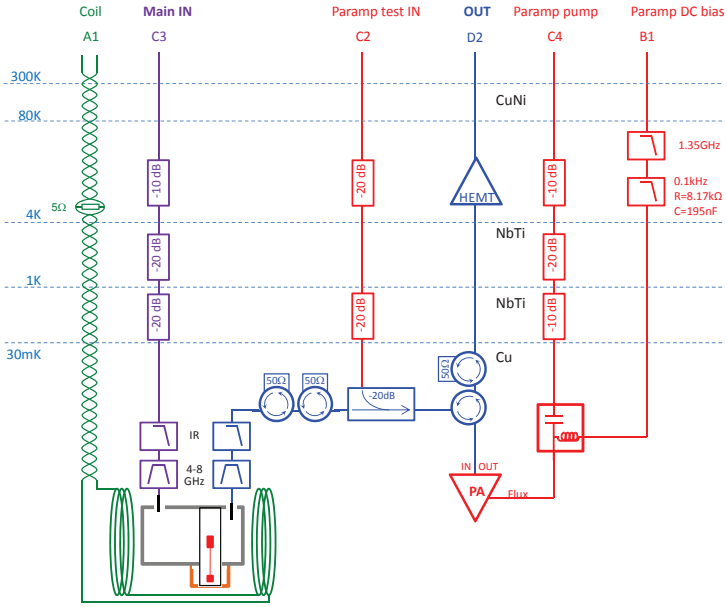

Figure 3.7. Schematics of the electrical circuitry inside the refrigerator. We have three RF signal input lines: C3 to send signals to the experiment, C2 to probe the paramp and C4 to pump the paramp. D2 is the signal detection line. Lines A1 and B1 are for the DC bias of the sample and paramp respectively

On the JPA side, the dc bias line B1, whose function is to align the frequency of the JPA with the cavity readout mode, is RC-low pass filtered at 4K. This dc line and the pumping line C4 are both connected to the paramp flux port with a bias tee (see 3.3.4). The C2 line devoted to testing the paramp, is coupled to it with a 20 dB directional coupler. That has the advantage of attenuating the input noise by 20 dB without attenuating the output signal.

3.3 Microwave measurements

In this section the different measurement setups and equipment are described.

3.3.1 Vectorial Network Analyzer measurements

A vectorial network analyzer (VNA) measures the 2x2 complex scattering matrix $\{S_{\mathrm{ij}=1,2}\}$ of a two-port 'device under test' as a function of frequency. For our experiments, two microwave VNAs (Anritsu 37397C and Keysight N5232A) have been used to characterize individual components or the whole electrical setup inside the refrigerator or at room temperature, tune the coupling of each cavity port pin from S_{11} and S_{22}, determine quality factors of the readout and storage cavity modes by S_{21} measurements, and map their resonance frequency as a function of the magnetic flux applied to the transmon (anticrossings).

3.3.2 Signal generation

For spectroscopic measurement involving more than one microwave tone or microwave pulses rather than continuous waves, the home-made microwave setup shown in fig. 3.8 is used. This setup on one hand generates control signals made up of pulses and continuous signals at different frequencies, and on the other detects signals coming from the sample in a process known as homodyne detection; where a probe signal is sent to the sample and the returning signal is mixed with a local oscillator at the same frequency, yielding a DC signal that is easy to measure with an analog-to-digital converter (ADC).

Signal generation

The input signals are generated with microwave sources mixed with signals from an arbitrary waveform generator (AWG). For microwave sources we used Agilent E8257D and Anritsu MG3692A, Tektronix 5014C for AWG, Yokogawa for DC voltage generators and HMC-C041 and HMC-C009 IQ-mixers from Hittite. All RF equipment are phase locked to a 10 MHz clock generated by the AWG. In addition, a 1 GHz reference phase locking is used between the two generators for the readout tone and the paramp pump (see 3.3.4 and 4.1.1 for further information). After IQ-mixing the amplitude of the signal is fine tuned with a voltage variable attenuator (VVA) and subsequently combined with similarly generated signal, high-pass filtered and split up. One part goes to the fridge and one to an oscilloscope or a spectrum analyzer for and monitoring.

As mentioned above, the signal is created by IQ-mixing which will now be explained. The microwave source sends a signal $\mathrm{LO}(t) = I_0 \cos(\omega_{\mathrm{LO}}\, t)$ to the LO port of the mixer and the AWG send sig-

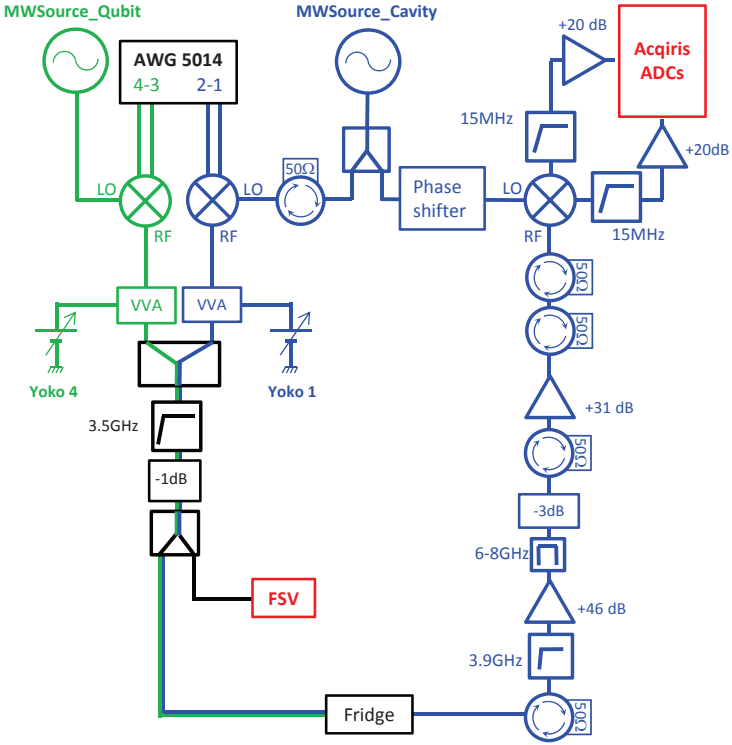

Figure 3.8. Room temperature microwave setup. Signals are generated by IQ-mixing a continuous microwave tone with pulse shaped IF signals from an AWG. The VVA sets the power range of the signals that are then combined, filtered and finally enter the fridge. We split up the readout tone into a probe signal and a local oscillator signal (LO) signal for homodyne detection. The signal returning from the fridge is amplified and demodulated before entering the ADC data acquisition card.

nals $I(t)$, $Q(t)$ to the in-phase and quadrature-phase port I and Q. The resulting signal at the RF output is then

$$\mathrm{RF}(t) = I(t)\cos(\omega_{\mathrm{LO}}\, t) + Q(t)\sin(\omega_{\mathrm{LO}}\, t).$$

For the control signal we do heterodyne modulation where quadrature signals are at a frequency ω_{IF} in a pulse envelope s(t), $I(t) = s(t)\cos(\omega_{\mathrm{IF}} t - \phi)$ and $Q(t) = s(t)\sin(\omega_{\mathrm{IF}} t - \phi)$. The resulting signal is

then at $\omega_{\mathrm{LO}} - \omega_{\mathrm{IF}}$,

$$\mathrm{RF}(t) = s(t)\cos[(\omega_{\mathrm{LO}} - \omega_{\mathrm{IF}})\,t + \phi].$$

This allows for flexible pulse generation with the AWG as s(t) is the shape function of the pulse, ω_{IF} sets the frequency within ∼400MHz range from ω_{LO} and ϕ can be set arbitrarily for different pulses and even vary with time.

Signal detection

The returning signal from the fridge passes through an amplifier chain as depicted in fig. 3.8. Filters, attenuators and circulators are used to reduce reflections between the components and filter out noise at frequencies different from the detection signal as it can saturate the amplifiers. This amplifier chain was located 2-3 meters away from the signal generation setup to minimize amplification of stray radiation.

The GHz frequency signal is too fast for our data acquisition card so we demodulate it. The process is the reverse from the modulation described above with $\omega_{\mathrm{IF}} = 0$. The probe signal is split up, one part goes to the LO of the mixer while the other part is sent to the fridge, comes back through the amplifier chain and to the RF of the mixer. This creates signals at the I and Q ports, one at $\sim 2\omega_{\mathrm{LO}}$ and on DC, which after low-pass filtering become $I(t) = s(t)\cos(\phi)$ and $Q(t) = s(t)\sin(\phi)$. Finally each quadrature is amplified before going to two ports of an analog-to-digital data acquisition card Acqiris xc200.

Mixer calibration

In reality the mixers are imperfect and do not follow exactly the behavior just described above. When no signal is applied to the I and Q ports a signal at ω_{LO} leaks through to the RF output. This leakage can be minimized by tuning small dc voltages on the I and Q ports. The effect of the remaining leak is small if no transition in the experiment is at ω_{LO}. In addition, the I and Q ports are not exactly $\pi/2$ out of phase and have a small amplitude imbalance. This causes small signals to appear at the opposite sideband frequency $\omega_{\mathrm{LO}} + \omega_{\mathrm{IF}}$ (and other harmonic frequencies of the modulation). By iteratively tuning the amplitude and phase of the I and Q RF signals to compensate for the mixer imperfections, the opposite sideband and harmonics are minimized.

3.3.3 Parametric amplification

As described in section 3.3.2 a Josephson parametric amplifier (JPA) first amplifies the output signal at 30mK. This JPA described in detail in [52] adds the minimum noise allowed by quantum mechanics to the signal. Here we give a brief description of its principle and how it is operated.

In a parametric amplifier a signal at ω_S is amplified by a transfer of energy from a pump tone at ω_P. In our superconducting circuits the transfer medium is a lumped element LC-resonator with a resonance frequency ω_R. Having the inductance L (partially or entirely) made up of a SQUID or, as in our case, a SQUID array makes it tunable in magnetic flux, which allows for the parametric pumping. We pump at twice the signal frequency $\omega_P \simeq 2\omega_S \simeq 2\omega_R$, on a dedicated line distinct form the signal line. This pumping induces three wave mixing $\omega_P = \omega_S + \omega_I$, where ω_I is the frequency of a complimentary idler signal. In the non-degenerate mode $\omega_p \neq 2\omega s$ resulting in $\omega_S \neq \omega_I$, the gain of the reflected signal is

$$|G_S|^2 = 1 + |G_I|^2 = 1 + \frac{4\epsilon_r^2}{[1 - \epsilon_r^2 + \delta_r^2 - \Delta_r^2]^2 + 4\Delta_r^2},$$

where $\delta_r = (\omega_P / 2 - \omega_R) / \Gamma_a$ is the pump-resonance detuning, $\Delta_r = (\omega_S - \omega_p / 2) / \Gamma_a$ is the signal-pump detuning, $\epsilon_r = \omega_R a_P / \Gamma_a$ is the pumping strength, Γ_a is the amplitude decay rate and a_P is the relative pump strength. When $\omega_S = \omega_I$ the signal and the idler are degenerate and the gain becomes sensitive to the phase χ between the signal and the pump:

$$|G_{S,\mathrm{deg}}|^2(\chi) = 1 + 4\epsilon_r \frac{2[\epsilon_r - \delta_r \cos(2\chi)] + (1 + \epsilon_r^2 + \delta_r^2)\sin(2\chi)}{(1 - \epsilon_r^2 + \delta_r^2)^2}.$$

For our experiments, the JPA is operated in this degenerate mode. First the JPA resonator frequency is tuned with a dc flux bias to the frequency of the signal to be amplified $\omega_S \simeq \omega_R$. Then a pump tone is applied at $\omega_P = 2\omega_S$; the power is increased until either amplification or deamplification of the signal is clearly seen. At this stage the phase χ of the pump tone is tuned to maximize the amplification. Finally the pump power is adjusted to reach a gain of ∼18dB.

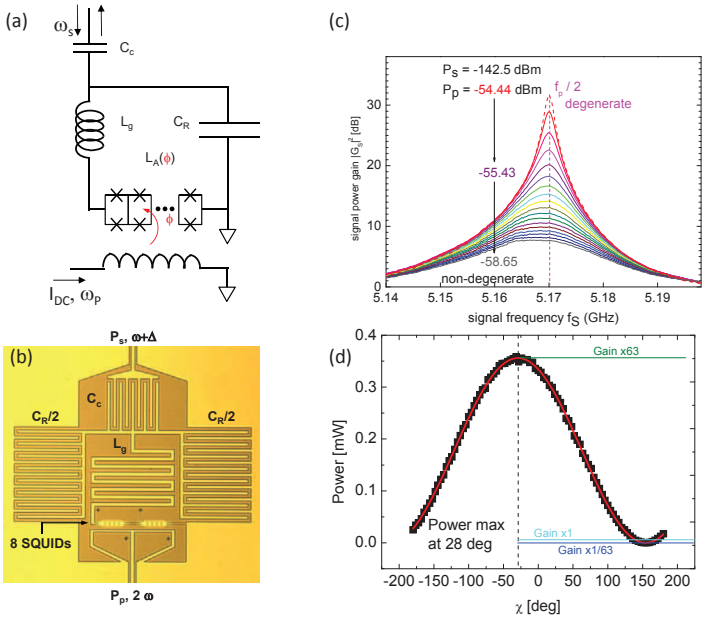

Figure 3.9. a) Lumped element circuit model of a paramp. A one port LC-resonator has a tunable inductance by using a squid array. The input signal ω_S is amplified and reflected when a pump tone $\omega_P \simeq 2\omega_S$ inductively pumps the squid array via the separate pump line. b) Optical image of the paramp. c) Gain curves for varying pump power from a paramp of the same design. d) When operated in the degenerate mode $\omega_P = 2\omega_S$, the gain $|G_{S,\mathrm{deg}}|$ depends on the phase χ between ω_P and ω_S.

Chapter 4
Measurement techniques

This chapter covers some of the measurement procedures used to characterize the cavities and the transmons used in this thesis. The first section addresses the characterization of a transmon qubit, and the second one how we characterize the quantum state of a cavity mode.

4.1 Transmon

The coupling strength g_0 of the transmon to a cavity mode at frequency ω_0 is determined by sweeping the ω_{ge} frequency of the transmon around ω_0 with an external magnetic flux. Measuring with a VNA the transmission spectrum of the cavity around ω_0 results in an anticrossing separated by $2\,g_0$ when $\omega_0 = \omega_{ge}$.

The transmon is characterized in the dispersive regime where $|\omega_0 - \omega_{ge}| \gg g_0$.

4.1.1 Resonator spectroscopy

An example of an anticrossing obtained by VNA measurement of the transmission of one of our cavity modes with the transmon in $|g\rangle$ is shown if fig. 4.1a. When the transmon frequency ω_{ge} is swept across ω_0 using a flux bias, it yields two resonance peaks with the minimal peak separation giving the coupling strength g_0. This behavior is observed at low power i.e. the single photon regime. In fig. 4.1b taken at $\phi\,/\,\phi_0 \simeq 0.4$ for instance, the resonance at low power is indeed at the dispersively shifted frequency $\omega_0 - \chi_{ge}$. At high power the resonance frequency shifts back to that of the bare cavity ω_0. This effect is attributed to the saturation of the transmon by the probe field [42]. Knowing χ_{ge}, g_0 and ω_0 one can in principle calculate the frequency ω_{ge} of the transmon.

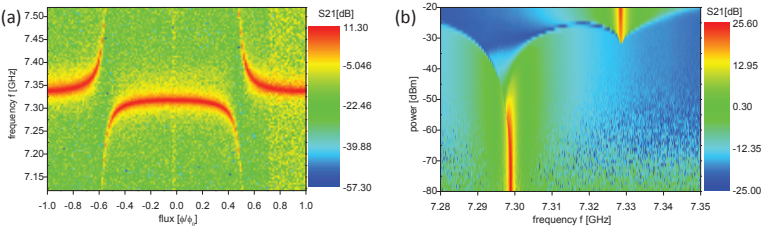

Figure 4.1. Transmission measurement of a cavity resonator coupled to a tunable transmon. a) Anticrossing when sweeping ω_{ge} across ω_0 using a flux bias. The two resonance peaks, separated by $2g_0$ when $\omega_{ge}=\omega_0$, give the coupling strength. b) Transmission around ω_0 in the dispersive limit as a function of input power. At low power the resonance frequency is shifted due to the coupling to the transmon. When the power is increased the resonance frequency eventually switches back to ω_0.

4.1.2 Readout signal

The transmon state is measured in the low power regime (typically 10-100 photons). Figure 4.2.a shows a schematic illustration of typical cavity mode resonances for the transmon prepared in $|g\rangle$, $|e\rangle$ and $|f\rangle$. When sending a probe signal at the frequency $\omega_0^{(g)}$, the transmitted amplitude $A^{(g)} \neq A^{(e)} \neq A^{(f)}$ provides a measurement of the state in a single shot and projects it. In practice however the overlap between the peaks is so small that $A^{(e)} \approx A^{(f)} \approx 0$ and only a clear discrimination can be made between $|g\rangle$ and $|\bar{g}\rangle$=not $|g\rangle$. Figure 4.2b shows 3 measured spectra, averaged over thousands of repetitions, after preparing separately the states $|g\rangle$, $|e\rangle$ and $|f\rangle$. The non-zero transmission A_0 at $\omega_0^{(g)}$ for $|e\rangle$ and $|f\rangle$ is because of partial relaxation during readout. The probability of the transmon state ending in $|g\rangle$ is thus

$$P_g = \frac{A}{A^{(g)}}. \tag{4.1}$$

The initial probability of being in $|g\rangle$, correcting for relaxation, can be deduced following a calibration presented in section 4.2.1.

To construct the amplitude signal A we use the homodyne detection setup described in chapter 3. A microwave pulse at frequency ω is sent to the cavity and the I and Q quadratures of the field are measured with the ADC. The sampling rate Γ_{samp} varies from 0.5 to 0.025 GS/s and the samples $I(t_i)$ and $Q(t_i)$ $(i=0,...,n_{\text{samp}})$ form time traces consisting of $n_{\text{sanp}}=50$ to 1000 points spanning a time $t_{\text{samp}}=$

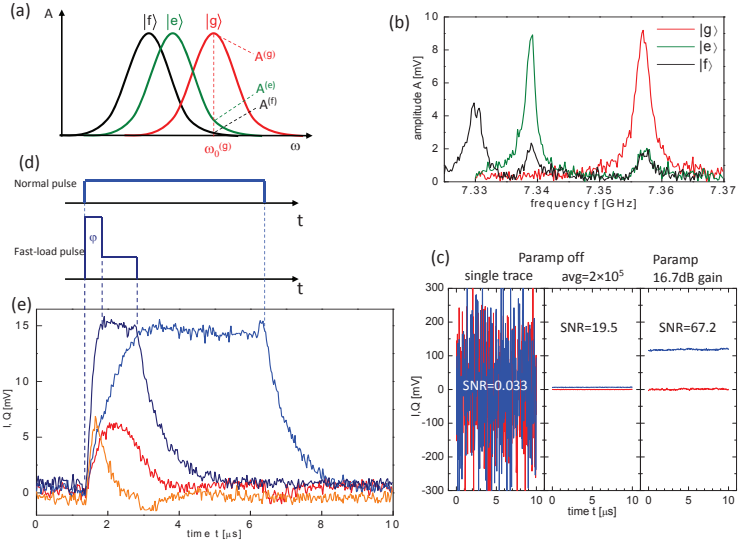

Figure 4.2. Dispersive readout. a) Schematic illustration of the resonator peaks corresponding to the transmon states $|g\rangle$, $|e\rangle$ and $|f\rangle$. The transmon is read out by applying a probing pulse at $\omega_0^{(g)}$. b) Measured transmission spectrum when the transmon is prepared in $|g\rangle$, $|e\rangle$ or $|f\rangle$. c) Continuous I and Q signals (see fig. 3.7 and 3.8 for setup) at $\omega_0^{(g)}$ when all the signal is put on one quadrature. Signal-to-noise rations (SNR) are indicated for a single trace, averaging $2 \cdot 10^5$ traces, and adding a paramp. d) and e) Comparison of normal and 'fast-load' pulses. The fast-load pulse reaches the final amplitude three times faster than the normal one, thus recording the transmon state sooner after its preparation.

$n_{\text{samp}}/\Gamma_{\text{samp}}$ between 100 ns and 40 μs long. Each time trace (see fig. 4.2c)has a Gaussian noise larger than the signal, even at maximum transmission $\omega = \omega_0^{(g)}$. By averaging $N = 10^2$ to 10^5 traces the noise is reduced such that the pulse can be detected in $\bar{I}(t_i) = (\Sigma_n I_n(t_i))/N$ and $\bar{Q}(t_i)(\Sigma_n Q_n(t_i))/N$, as shown in fig. 4.2d,e. Finally a time average is taken over $\bar{I}(t_i)$ and $\bar{Q}(t_i)$ giving two scalars, $I = (\Sigma_{i=j}^{i=k}\bar{I}(t_i))/(k-j)$ and $Q = (\Sigma_{i=j}^{i=k}\bar{Q}(t_i))/(k-j)$, which are translated to an amplitude and a phase

$$A = \sqrt{I^2 + Q^2} \quad \text{and} \quad \varphi = \text{atan}\left(\frac{Q}{I}\right). \tag{4.2}$$

Removing I and Q offsets

Offsets I_{off} and Q_{off} on the measured quadratures I and Q are minimized but are in practice never zero. As a result the measured quadratures are $I(\omega) = A\cos(\omega x/c) + I_{\text{offset}}$ and $Q(\omega) = A\sin(\omega x/c) + Q_{\text{offset}}$, where x is the total length of the microwave circuit, c the speed of light in the cables, and ω the frequency of the measured homodyne signal. Consequently, when sweeping ω in spectroscopy of a cavity mode the amplitude is

$$A' = \sqrt{A^2 + I_{\text{offset}}^2 + Q_{\text{offset}}^2 + 2A(I_{\text{offset}}\cos(\omega x/c) + Q_{\text{offset}}\sin(\omega x/c))}$$

A' has both a constant offset and oscillating terms causing ripples in the background of the spectrum. By measuring the quadratures with and without the probe signal we can subtract these effects and obtain A.

Optimal readout pulse length and integration time

In most experiments the transmon is manipulated with a sequence of pulses, and then readout. Immediately after the manipulation the transmon starts to relax, diminishing the signal $A = A^{(g)} - A^{(e)}$ in time. This suggests it is therefore better to measure the transmon state immediately after the manipulation and integrate over a short time period. However integrating over longer times t_{int} increases the signal-to-noise ratio (SNR) as $1/\sqrt{t_{\text{int}}}$. The two effects combined yield

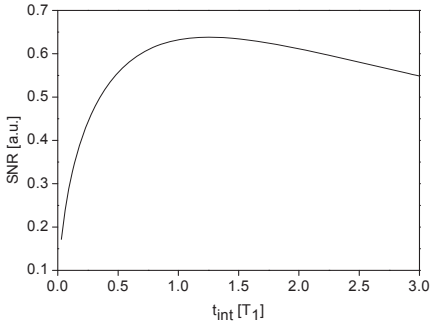

Figure 4.3. The signal-to-noise ratio (SNR) of the readout signal as a function of integration time. The maximum SNR is at $\sim 1.2T_1$.

$$\text{SNR} \propto \frac{1 - e^{-t_{\text{int}}/T_1}}{\sqrt{t_{\text{int}}}}, \tag{4.3}$$

which has a maximum at $t_{\text{int}} = 1.2T_1$ and was typically used in the QZD experiments presented later in this thesis.

Fast loading of the readout probe signal

To minimize the loss of the readout signal due to transmon relaxation during the rise time of the field, it is important to load the mode as quickly as possible.

At a constant amplitude ξ at the input port the cavity amplitude ζ increases as $\xi(1 - e^{-t\kappa_{\text{in}}})$ as shown in fig. 4.2 d. A two-amplitude-step readout pulse as depicted in fig. 4.2 e can be used to 'load' the cavity faster. The short kick at the beginning of the pulse is typically 3 times higher in amplitude than the rest and lasts until the amplitude has reached the steady state value of the lower step. Normally the two steps have the same phase but in cases when the cavity mode is slightly non- linear a compensation phase is applied φ. This sort of fast loading is explored further in ref [30].

4.1.3 Qubit spectroscopy

The transmon frequencies are obtained with two-tone spectroscopy, either pulsed or continuous. The corresponding protocols are shown in fig. 4.4:

Pulsed spectroscopy consists in applying a pulse whose frequency ω is swept and whose length well exceeds T_1 and T_2. Thereafter a readout pulse is applied at $\omega_0^{(g)}$. When $\omega = \omega_{ge}$ the transmon is driven to the maximal mixture of $|g\rangle$ and $|e\rangle$, causing a dip in the transmitted amplitude. When $\omega = \omega_{gf}/2$ the $|g\rangle \rightarrow |f\rangle$ transition is driven in a two photon process from which the anharmonicity $\alpha = 2\omega_{ge} - \omega_{gf}$ can be determined. Because this is a second order process it typically requires about 10 dB more drive power than the $|g\rangle \rightarrow |e\rangle$ transition. Spectroscopy on the $|e\rangle \rightarrow |f\rangle$ transition is done by preparing the transmon in state $|e\rangle$ (explained below) before the spectroscopy pulse is applied, and by mapping the population of $|e\rangle$ to the ground state $|g\rangle$ afterwards for a clear readout signal.

Sweeping a continuous tone has the benefit of the transmon state not decaying during readout. Another consequence is that photons of the readout pulse are present in the cavity while the qubit is being manipulated. This is a way to probe the photon number splitting (see section 2.2.3.1) but is less suitable than pulsed spectroscopy for precise determination of transmon levels.

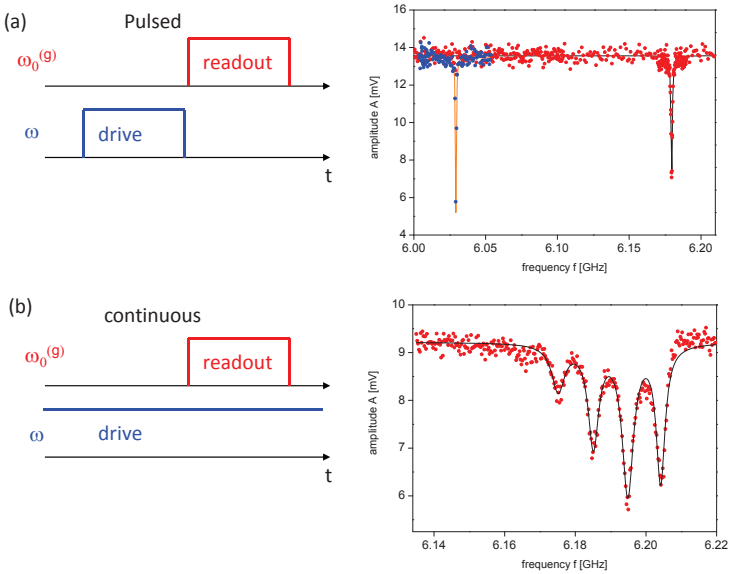

Figure 4.4. Transmon spectroscopy: protocols and example measurements a) Pulsed spectroscopy shows a dip in the transmission amplitude at ω_{ge} (red). The blue curve shows the two-photon $|g\rangle \rightarrow |f\rangle$ transition at $\omega_{gf}/2$. b) In continuous spectroscopy the signal is stable throughout the readout pulse. This scheme also reveals the photon number peaks.

4.1.4 Rabi oscillations of the transmon

Once a transition frequency between two transmon levels has been determined, the Rabi rotations on this transition can be calibrated: a resonant pulse with an amplitude $\zeta(t)$ induces a rotation of an angle $\phi \propto \int \zeta(t)dt$ proportional to the area of the pulse. In practice square or Gaussian pulse shapes are used, whose amplitude or the duration is varied. The protocol and measurements of the latter case is depicted in fig. 4.5, showing a Rabi oscillation

$$A = a + b\cos(\Omega t)\exp(-\Gamma_R t) \tag{4.4}$$

at the Rabi frequency Ω decaying over time with a rate Γ_R due to relaxation and dephasing of the transmon. Here a and b are the offset and amplitude of the oscillations depending on the whole setup. Fitting the data to eq. 4.4 one extracts Ω, which allows for precise Rabi

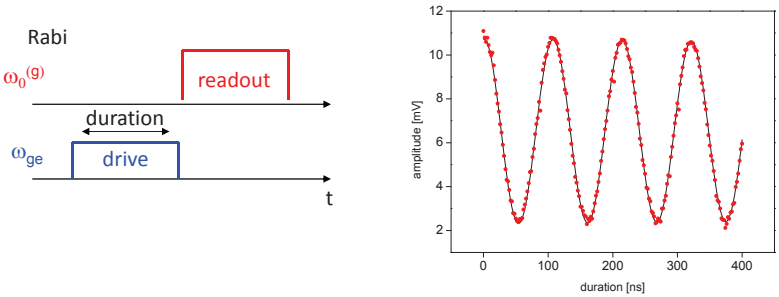

Figure 4.5. Rabi oscillations: protocol and example measurement. When varying the duration of a square pulse the excitation probability of the transmon oscillates at Rabi frequency $\Omega/2\pi = 9.26$ MHz.

rotations. Note that in the case of frequency crowding, unwanted off-resonant driving of other transitions may occur. This can be reduced by optimal pulse shaping.

4.1.5 Energy relaxation of the transmon

To measure the energy relaxation time T_1 we use the calibrated Rabi rotations to prepare the transmon in $|e\rangle$ with a Rabi angle $\phi = \pi$. By varying the delay time τ before readout one can map the exponential decay shown in fig. 4.6. The measured data points are fitted with a function $f(\tau) = a + be^{-\tau/T_1}$. Note that in the case of a frequency tunable transmon, T_1 varies with the transmon-cavity detuning due to the Purcell effect discussed in chapter 2.

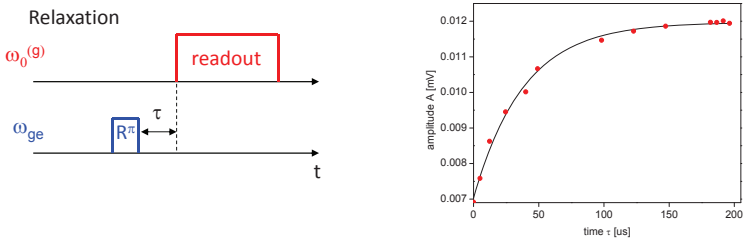

Figure 4.6. Relaxation time: protocol and example measurement. By exciting the transmon and varying the time before its state is read out, one can map the exponential decay. Here $T_1 = 39\,\mu s$.

4.1.6 Free induction decay of the transmon

The free induction decay time is measured by a procedure called Ramsey interferometry. The protocol is depicted in fig. 4.7. It consists of a $\pi/2$ rotation driven at a small detuning $\delta = \omega_d - \omega_{ge}$. The detuning frequency $\delta/2\pi$ is typically in the 0.5 - 2 MHz range. This prepares a state $1/\sqrt{2}(|g\rangle + |e\rangle)$ on the equator of the Bloch sphere, which precesses around the Z-axis at a frequency δ. After a time τ a phase $\varphi = \delta\tau$ has accumulated yielding $1/\sqrt{2}(|g\rangle + e^{i\varphi}|e\rangle)$. When a second $\pi/2$ pulse is applied the probability to measure measure $|g\rangle$ becomes $\pi_g = \cos^2(\varphi/2)$. This induces oscillations, called Ramsey fringes, at frequency $\delta/2\pi$ when the precessing time τ is varied as shown in fig. 4.7. This gives the transition frequency $\omega_{ge}/2\pi$ with a precision of $\sim$ 0.1MHz which is typically better than the precision from spectroscopy.

As discussed in section 2.2.2 a free induction decay rate Γ_2 is comprised of the relaxation rate Γ_1 and the pure dephasing rate Γ_φ, as show in eq. 2.83. This results in a decaying amplitude of the Ramsey fringes. The decay is exponential when the Γ_2 is dominated by Γ_1 or if the noise spectral density S_φ is white. This is usually the case and the measured data shown in fig. 4.7 can thus be fitted with $f(t) = a + b\cos(\delta\tau/2\pi)e^{-\tau/T_2}$. In case 1/f noise the decay becomes Gaussian and requires different protocol dependent analysis as discussed in chapter 5.

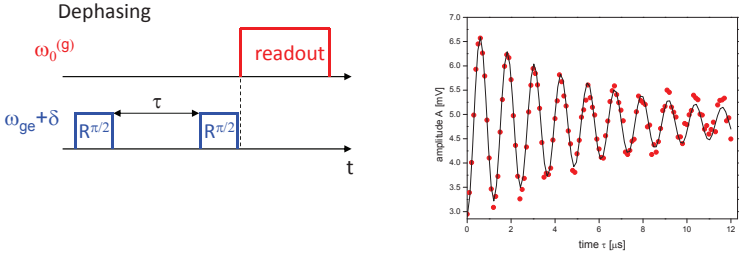

Figure 4.7. Ramsey fringes: protocol and example measurement. Two $\pi/2$ pulses at a frequency $\omega_{ge} + \delta$, separated by a varying time τ, induce oscillations in the transmon excitation probability at frequency $\delta/2\pi$=0.83 MHz The oscillations decay with a free induction decay rate Γ_2, giving $T_2 = 6.5\,\mu s$.

Hahn echo refocusing

A 'refocusing' protocol, called Hahn echo, can be applied to dynamically reduce the dephasing rate Γ_φ. It consists in adding a π pulse midway between the two $\pi/2$ pulses in the Ramsey protocol with $\delta = 0$ depicted in fig. 4.8. By considering the low frequency part of S_φ as quasi-static over τ, the total phase $\varphi = \varphi_s + \varphi_f$ accumulated can be decomposed into a static part φ_s and a high frequency noise contribution φ_f. The evolution over the sequence is:

$$\begin{aligned} \frac{|g\rangle + |e\rangle}{\sqrt{2}} \quad & \text{wait } \tau/2 \quad \frac{|g\rangle + e^{i\varphi_1/2}|e\rangle}{\sqrt{2}} \\ & \pi \text{ pulse} \quad \frac{|e\rangle + e^{i\varphi_1/2}|g\rangle}{\sqrt{2}} \\ & \text{wait } \tau/2 \quad \frac{e^{i\varphi_2/2}|e\rangle + e^{i\varphi_1/2}|g\rangle}{\sqrt{2}}. \end{aligned}$$

The static part of φ_1 and φ_2 is the same and cancel, leading to a random phase involving only the high frequency part $(\varphi_{f,1}+\varphi_{f,2})/2$.

This leads to an exponentially decaying echo signal $f(t) = a + be^{-\tau/T_2^E}$, as shown in fig. 4.8 , with a decay rate $\Gamma_2^E < \Gamma_2$.

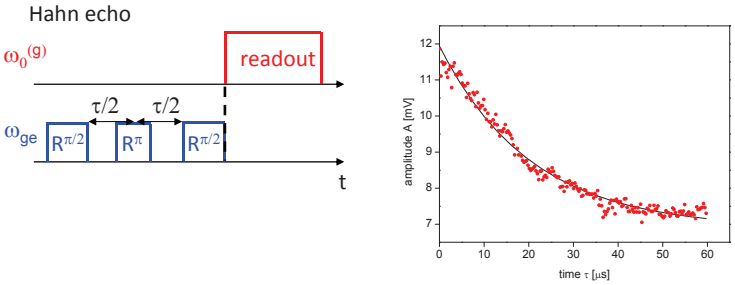

Figure 4.8. Hahn echo:: protocol and example measurement. The Hahn echo protocol dynamically decreases the dephasing rate. With $\delta = 0$, a π pulse after $\tau/2$ leads to partial refocusing of the phase information at τ. Here $T_2^E = 20.5\,\mu s$.

4.2 Cavity field characterization

In our QZD experiment manipulation and characterization of the quantum state of a cavity mode is needed. This is done with microwave pulses resonant with the cavity mode and mapping the state of the mode onto the transmon in a tomographic manner. The transmon is read out with a different cavity mode as discussed in chapter 6.

Here a calibration method of the displacement pulses and photon number distribution is presented. Then we discuss the Wigner function and two tomographic methods to measure it. The principal method uses a Maximum Likelihood algorithm which is presented at the end of the chapter.

4.2.1 Mapping Fock state occupation to transmon excitation

The photon number distribution of a cavity mode is measured by mapping the probability $p(n)$ for each n individually onto the transmon excitation probability by applying a π pulse at $f_{+,n}$ (see fig. 2.13b) and subsequently reading out the transmon state. In our experiment this procedure needs to be calibrated due to partial relaxation during the π pulse an the readout.

4.2.2 Calibrating Fock state probability measurements and displacements

The displacement of the field amplitude ζ in the cavity mode at frequency ω_0 is calibrated with respect to the length and amplitude ξ of a coherent pulse at ω_0. The scaling between the two is approximately linear for drive times $t \ll T_{\text{cav}}$. The calibration is done by varying the amplitude of the applied pulse and analyzing the variation of the photon number distribution:

In the ef-resonant system, the Rabi frequencies Ω_n and decay times vary for the different $|g, n\rangle \rightarrow |+, n\rangle$ transitions. The frequencies Ω_n can be measured (see chapter 6) but the amplitude A_n of each of the photon number peak must be scaled with a calibration factor c_n compensating for transmon relaxation during readout, to give the photon number probability $p(n) = A_n / c_n$. To determine c_n we assume that the distribution $p(n)$ from a displacement pulse is Poissonian $P_{\bar{n}}(n)$ with an expectation value $\bar{n} \propto \beta^2$ varying linearly with the area of the pulse, as

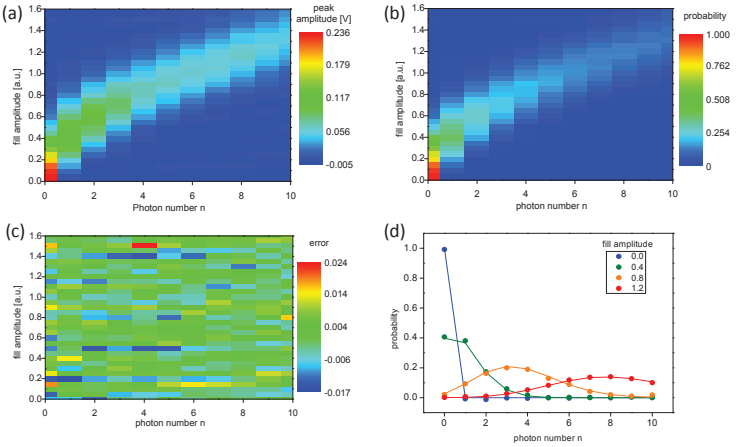

Figure 4.9. Calibration of the photon number probability measurements and the cavity filling rate. a) Raw signal amplitude of the first 11 photon number peaks. b) After a calibration procedure the amplitudes are translated into probabilities and the filling pulse amplitude into cavity field amplitude. c) Difference between the experimental calibrated probabilities and theoretical Poissonian distributions. d) Theoretical Poissonian distributions and calibrated photon number probabilities for a few fillings.

expected for a coherent drive. The drive field increment $\partial\beta$ and scaling factors c_n are extracted from a collective fit to measurements of the photon number peaks for various displacements. Figure 4.9a,b,c show the raw data, the calibrated probabilities, as well as the residual error between model and the calibrated data. This error is below 2.5% and is homogeneously distributed, which confirms the validity of the model and the quality of the calibration.

As a self consistency check the rescaled data $p(n) = A_n / c_n$ as a function of ξ is compared with the Poissonian distribution value $P_{\bar{n}}(n)$ obtained from $\partial\beta$.

4.2.3 Wigner function and Wigner tomography

In this thesis the quantum state of a cavity mode defined by it density matrix ρ is graphically represented in phase space, i.e. the plane of the complex field amplitude ζ, by the so-called Wigner function

$$W(\zeta) = \frac{1}{\pi\hbar}\int \langle \mathrm{Re}(\zeta - y)|\rho|\mathrm{Re}(\zeta + y)\rangle e^{i2y\,\mathrm{Im}(\zeta)/\hbar} dy. \qquad (4.5)$$

This function which is a bijective mapping of ρ [23][39], has many features well suited for visualizing characteristics of quantum field:

-It is a real-valued quasi-probability distribution in the range $-2/\pi \leqslant W(\zeta) \leqslant 2/\pi$ which remain non-negative for any classical field state, meaning that negative values clearly indicate a quantum character of the field.

-A coherent state $|\beta\rangle$ appears as a 2D Gaussian centered at $\zeta = \beta$ with a width $1/\sqrt{2}$ representing the quantum fluctuations on both quadratures.

-The Wigner function also clearly discriminates between a statistical mixture and a coherent superposition of two coherent states $|\beta_1\rangle$ and $|\beta_2\rangle$: In both cases two Gaussians are centered at β_1 and β_2 while the coherent superposition has additional fringes between them.

The Wigner function can also be expressed as [23]

$$W(\zeta) = \frac{2}{\pi}\mathrm{Tr}[\hat{D}(\zeta)\hat{P}\hat{D}(-\zeta)\rho] \tag{4.6}$$

where $\hat{P}$ is the photon number parity operator with the expectation value

$$\langle\hat{P}\rangle = \sum_{n\,\mathrm{even}} p(n) - \sum_{n\,\mathrm{odd}} p(n). \tag{4.7}$$

The value of $W(\zeta)$ at a specific point in phase space is measured by applying a displacement pulse $\hat{D}(-\zeta)$ and measuring $\langle\hat{P}\rangle$. Measuring $W(\zeta)$ using displacements and parity measurements for a multiple values of ζ spanning a window in phase space is called Wigner tomography.

In cavity and circuit QED several methods can be used to map directly the parity of the field onto the excitation of a real or an artificial atom. In the dispersive limit where the photon number splitting is equidistant for all n, this can be achieved with Ramsey interferometry as explained in [23][45][48]. Due to the non-equidistant separation of the photon number peaks in our ef-resonant scheme, two alternative methods of mapping the parity onto the transmon state are used: first, the photon number probabilities in eq. 4.7 can be measured individually as explained in section 4.2.1. Second, the parity can be mapped directly onto the transmon state with a composite pulse made of the superposition of π pulses at all $f_{+,n_{\mathrm{odd}}}$ (up to a truncation), as will be demonstrated in chapter 6. However, the decreasing separation $\delta_{+,n}$

between adjacent $f_{+,n}$ forces a truncation at low n, which limits the mappable window in phase space. We thus switch to a more standard tomographic method involving measurements of $p(n)$ for only the lowest few n.

4.2.4 Standard quantum field tomography

In this method we reconstruct the density matrix ρ in the Hilbert space $\mathcal{H}_{\rm tr}$ truncated to $n_{\rm tr}$ Fock states, with a procedure called maximum likelihood [22][21], and subsequently calculate the Wigner function.

The truncation $n_{\rm tr}$ is chosen sufficiently large such that the anticipated ρ has a trace $T(\rho) \simeq 1$ in $\mathcal{H}_{\rm tr}$, but not at larger values as it is futile and time consuming. Now an $n_{\rm tr} \times n_{\rm tr}$ complex valued hermitian matrix with unit trace is characterized by $n_{\rm tr}^2 - 1$ real numbers, which requires in principle sampling at least $n_{\rm tr}^2 - 1$ different measurement observables.

In our case of a cavity field, the measured observables $\{p_{n,\alpha}\}$ correspond to $m_{\rm dis}$ different displacement pulses $\hat{D}(\alpha)$, each followed by measurements of $p(n)$ for the lowest $m_{\rm Fock}$ Fock states. The displacements cover either the full Hilbert space or a smaller area in phase space containing the full weight of the anticipated W. As an example see fig. 4.10a (black dots). The number $m_{\rm Fock} < n_{\rm tr}$ of measured Fock states (4 to 7 typically) is in practice limited by the decreasing $\delta_{+,n}$ for high n as discussed in section 2.2.3.3. These $m_{\rm dis} \times m_{\rm Fock}$ measurements make up a data set $\{p_{n,a}\}$ that is used to reconstruct ρ as will be explained in section 4.2.4.1.

As discussed in section 4.2.2 the data $\{p_{n,a}\}$ have a Gaussian noise with a standard deviation $\sigma < 1\%$. By oversampling $m_{\rm dis} \times m_{\rm Fock} = k \times n_{\rm tr}^2$ $(k > 1)$ precision of the reconstruction of ρ can be improved.

4.2.4.1 Maximum Likelihood treatment

The density matrix ρ is reconstructed from the data set $\{p_{n,\alpha}\}$ with a maximum likelihood method. To explain the essence of the method we consider a complete set of M projectors $\{\hat{P}_i\}$ corresponding to measurements on N identically prepared states ρ giving the data set $\{n_i\}$, where n_i counts the number of outcomes ϵ_i. From the data set a frequency $f_i = n_i / N$ is defined to estimate the probability $\pi_i = {\rm Tr}[\rho \hat{P}_i]$. We consider now the likelihood functional

$$\mathcal{L}(\rho) = C \prod_i {\rm Tr}(\rho \hat{P}_i)^{n_i}, \tag{4.8}$$

defined as the probability of getting $\{n_i\}$ for a given ρ. Here C is a combinatory factor irrelevant for what follows. The density matrix ρ_{ML} maximizing $\mathcal{L}$ is by definition the state that gives $\{n_i\}$ most likely.

Global maximization of $\mathcal{L}(\rho)$ is in general not efficient for traditional numerical methods. An alternative algorithm is based on a fixed point method iteratively applying the operator

$$R(\rho) = \sum_i \frac{f_i \hat{P}_i}{\mathrm{Tr}[\rho \hat{P}_i]}, \tag{4.9}$$

i.e. $\rho_{i+i} = R(\rho_i)\rho_i R(\rho_i)$, starting from an initial guess matrix ρ_0.

We see that as $\rho \to \rho_{\mathrm{ML}}$, $f_i \to \mathrm{Tr}[\rho \hat{P}_i]$ and $R \to \mathbb{1}$, such that $R(\rho_{\mathrm{ML}})\rho_{\mathrm{ML}} = \rho_{\mathrm{ML}}$. More details on Maximum Likelihood can be found in refs [22][21], including incomplete sets of projectors and cases where the errors due to the imperfect measurements are incorporated.

As mentioned above our data set has a Gaussian noise, a case not covered in refs [22][21], so that the formalism was adapted in collaboration with Pierre Rouchon at Mines-ParisTech. The essence of the method is presented here below and a more complete description and the optimization algorithm are given in appendices B and C.

The projectors $\{P_i\}$ we use, denoted now $\{\boldsymbol{E}_{n,\alpha}\}$, are a combination of displacement pulses and Fock state projectors $\boldsymbol{E}_{n,\alpha} = \hat{D}(-\alpha)|n\rangle\langle n|\hat{D}(\alpha)$, while the data set $Y \equiv \{p_{n,\alpha}\}$ verifies $p_{n,\alpha} = \mathrm{Tr}[\rho \boldsymbol{E}_{n,\alpha}] + \eta_{n,\alpha}$, with $\eta_{n,\alpha}$ being a Gaussian noise with a standard deviations $\sigma_{n,\alpha}$.

For Y the probability of having all $p_{n,\alpha} \in [s_{n,\alpha},\ s_{n,\alpha} + ds_{n,\alpha}]$ knowing ρ reads

$$\mathbb{P}\left(Y \in \prod_{n,\alpha} [s_{n,\alpha}, s_{n,\alpha} + ds_{n,\alpha}] \middle| \rho \right) =$$
$$\exp\left(-\sum_{n,\alpha} \frac{(s_{n,\alpha} - \mathrm{Tr}[\rho \boldsymbol{E}_{n,\alpha}])^2}{2\sigma_{n,\alpha}^2} \right) \prod_{n,\alpha} \frac{ds_{n,\alpha}}{\sigma_{n,\alpha}\sqrt{2\pi}}. \tag{4.10}$$

Using this expression, the Bayesian Mean estimate of the density matrix is given by

$$\rho_{\mathrm{BM}} = \frac{\int_{\mathcal{D}} \rho \exp(f(\rho))\mathbb{P}_0(\rho) d\rho}{\int_{\mathcal{D}} \exp(f(\rho))\mathbb{P}_0(\rho) d\rho},$$

where $\mathcal{D}$ is the convex set of density operators, $\mathbb{P}_0(\rho)$ is some prior probability law of ρ, and

$$f(\rho) = -\sum_{n,\alpha} \frac{(\mathrm{Tr}[\rho \boldsymbol{E}_{n,\alpha}] - p_{n,\alpha})^2}{2\sigma_{n,\alpha}^2} \tag{4.11}$$

is the logarithm of the likelihood function to be maximized.

When $\rho \approx \rho_{\mathrm{ML}}$, it is known that ρ_{ML} is a good approximation of ρ_{BM}.

We not that the targeted ρ_{ML} obeys [46] the following necessary and sufficient conditions that there exists a scalar λ_{ML} such that:

$$[\rho_{\mathrm{ML}}, \nabla f(\rho_{\mathrm{ML}})] = 0 \quad \text{and} \quad \lambda_{\mathrm{ML}} P_{\mathrm{ML}} \leqslant \nabla f_{\mathrm{ML}} \leqslant \lambda_{\mathrm{ML}} \mathbb{1}, \tag{4.12}$$

where

$$\nabla f(\rho) = -\sum_{n,\alpha} \frac{\mathrm{Tr}[\rho \boldsymbol{E}_{n,\alpha}] - p_{n,\alpha}}{\sigma_{n,a}^2} \boldsymbol{E}_{n,\alpha}. \tag{4.13}$$

is the gradient of f at ρ and P_{ML} is the orthogonal projector on the range of ρ_{ML}.

The maximization of f can then be achieved by a gradient algorithm with orthogonal projection on $\mathcal{D}$. A single iteration is expressed as

$$\rho_{k+1} = \Pi[\rho_k + g \nabla f(\rho_k)] \tag{4.14}$$

where $g > 0$ is a normalization parameter limiting the Hessian $\|\nabla^2 f\|$ such that $1 \lesssim g\|\nabla^2 f\| \lesssim 10$, and Π is the orthogonal projection onto the set of physical density matrices, i.e. Hermitian non-negative matrices with unit trace.

Figure 4.10 shows the reconstructed Wigner function from artificially generated data. In absence of noise the reconstructed density matrix is identical to the original one independent of the initial guess ρ_0. In fig. 4.10 b a Gaussian noise with $\sigma = 1\%$ has been added to the data. This results in ripples in the Wigner function of the reconstructed matrix.

More details can be found in appendix B as well as a method to estimate the effect of $\sigma_{n,\alpha}$ on the Wigner function.

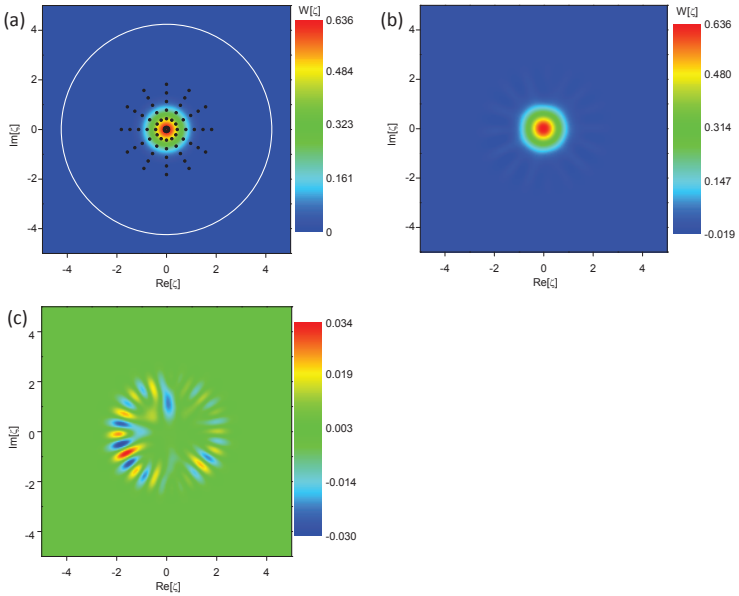

Figure 4.10. Reconstruction of the Wigner function of $|\beta = 0\rangle$ using our Maximum likelihood on artificially generated data $\{p_{n,\alpha}\}$ with n=0-8 and 72 displacement pulses α . a) The method reconstructs the vacuum state perfectly. The white circle shows the truncation of the Hilbert for the numerical processing and the black dots show the displacements α used in the tomography. b) Ripples appear in the reconstructed Wigner function when a Gaussian noise with $\sigma = 1\%$ is added to the data. c) The difference between the initial Wigner functions in a) and b) shows the ripples more clearly.

Chapter 5

Reaching long lifetimes in 3D circuit-QED

The first experiments performed during this thesis were aimed at achieving long lifetimes (several tens of μs) of a transmon as reported in [37][43]. In contrast to these works we used a magnetically tunable transmon inside a Cu cavity, through which an external magnetic field can be applied. The lower cavity lifetime compared to a superconducting cavity results in a shorter Purcell limit of the transmon relaxation time (see section 2.2.3.1), but enables a decoherence analysis at different frequencies.

5.1 Design

5.1.1 Copper cavity

In the experiment the lowest mode of the Cu cavity is coupled to the transmon. The design is based on the design in ref. [37]: the cavity is roughly a cuboid of dimensions $27\times33\times6$ mm^3 with rounded edges to facilitate fabrication. Two small holes are pierced in one of the walls, through which electric field is coupled to the cavity using proper SMA connectors playing the roles of two antennas. This design, shown in fig. 5.1a, is simulated in a finite element simulation software, as will be discussed in chapter 6, and gives a frequency $f_0 = 7.15$ GHz of the fundamental mode. A Cu cavity based on the simulated design was fabricated by the in-house workshop and is shown in fig. 5.1b. It

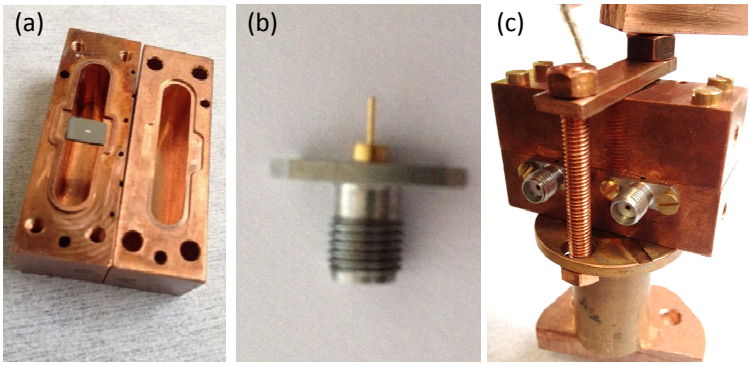

Figure 5.1. Sample and assembly parts. a) Transmon on a Si chip placed in a Cu cavity before it is closed. b) SMA coupling pin. c) Cu cavity closed and mounted on a coil, the axis of which is aligned with the transmon SQUID.

consists of two blocks which are screwed together with Cu screws to form the cavity. One part has a rim around the edge of the cavity with a groove for the transmon chip. The other part has a groove around the edge of the cavity, into which the rim of the other part fits. An In seal is placed around the rim before closing and is then compressed as the two halves are pressed together. This ensures good connection and eliminated radiation through the cut between the two halves. The pins used to couple to the cavity are made from Cu but are gold coated. They are filed down the length to give the right coupling. Measuring the transmission spectrum of an empty cavity at 77 K gives a resonance frequency $f_0 = 7.358$ GHz, but with a Si chip at 30 mK the bare resonance is shifted to 7.078 GHz as the relative permittivity of Si is $\varepsilon_r^{\mathrm{Si}} = 11.68$.

5.1.2 Transmon qubit

The transmon design has been described in chapter 3. It is based on the design of the transmon that I used in my master thesis and in ref [1], where two $500\times250\ \mu m^2$ pads are separated by 130 μm and give a coupling $g_0 = 180$ MHz. Here, we reduce the pad size to $400\times200\ \mu m^2$ and the separation to $50\,\mu m$ to get roughly half the coupling.

The transmon is mounted in the cavity with a small piece of In pressed on the corner of the chip to hold it in place. An external coil is then aligned with the transmon SQUID and attached to the cavity. The setup is then mounted and well thermalized with Cu at the lowest stage of a wet dilution refrigerator, and finally cooled down to 30 mK.

A note on the setup

A key element in achieving long lifetimes is to make sure that all stray fields and radiations are eliminated. As a part of that, the absorptive infra-red and microwave band-pass filters from section 3.2.3 are added to the setup. In addition the innermost copper shield of the dilution stage is doubled with a $\mu-$ metal shield painted inside with absorptive paint ; a Cu mesh grid covered in a $\sim$5 mm thick layer of absorptive Eccosorb rubber is also attached to the bottom of the shield.

5.2 Characterization

Two samples with long T_1 were measured: KJ6ch10 fabricated on Si and KJ15ch11 fabricated on sapphire.

5.2.1 Transmon on Si substrate

5.2.1.1 Spectroscopic characterization and T_1 measurements

Once the sample has been cooled the transmon is characterized using the standard methods described in section 4.1.

With the VNA the bare resonator is characterized by measuring the transmission spectrum in the high-power regime shown in fig. 5.2a, yielding a frequency $f_0 = 7.079$ GHz and a quality factor $Q_0 = 7000$ limited mostly by internal losses ($Q_{\text{ext}} = 47000$, $Q_{\text{int}} = 8200$). Switching to lower spectroscopy powers, the magnetic flux penetrating the SQUID is swept yielding the anti crossing shown in fig. 5.2b. At resonance $f_0 = f_{ge}$ the peak separation gives $g_0 = 90$ MHz as shown in fig. 5.3c. The spectrum is measured with a few tens of photons such that the bare resonance is also visible in the middle.

We switch to pulsed two-tone spectroscopy to determine the transmon spectrum. Figure 5.3a shows the measured transmon frequency f_{ge} (red dots) and the dispersively shifted resonator frequency

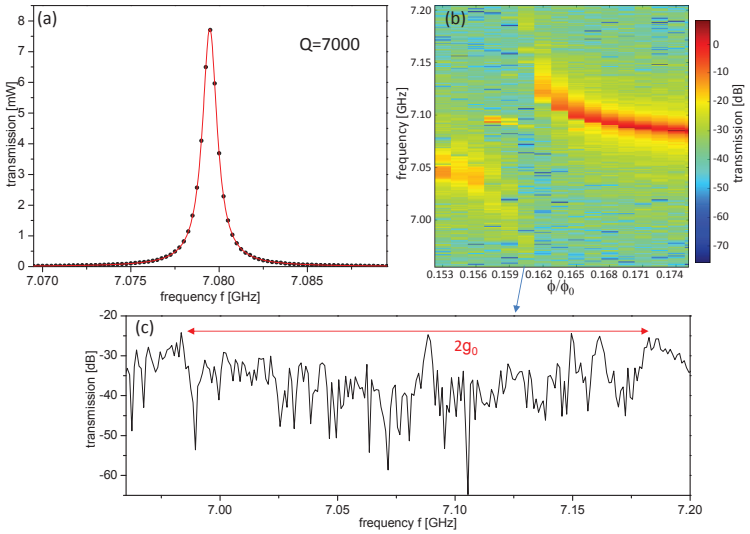

Figure 5.2. Resonator spectra. a) Spectrum in the high power regime yields the intrinsic resonance frequency f_0 and quality factor of the resonator. b) VNA transmission spectra showing the anticrossing of the transmon and the resonator as the flux ϕ penetrating the SQUID is swept. c) Spectrum around f_0 at $\phi/\phi_0 = 0.160$ when $f_0 = f_{ge}$. The separation of the hybridized transmon-resonator peaks indicated yields the coupling strength g_0. The presence of a few tens of photons results in the intrinsic resonance frequency being also visible in the middle, as well as multi-photon peaks [5].

$\tilde{f}_0$ (green dots) as a function of the flux penetrating the SQUID. The back line $f_{ge}^{\max}\sqrt{\cos(\pi\phi/\phi_0)}$ with $f_{ge}^{\max} = 7.565$ GHz the maximum transmon frequency corresponds to the expected behavior of a tunable transmon according to eqs. 2.62 and 2.70. The transmon spectrum in fig. 5.3b is taken at $\phi/\phi_0 = -0.26$ and shows both $f_{ge} = 6.252$ GHz and $f_{gf/2} = 6.093$ GHz, yielding the anharmonicity $\alpha = 2(f_{gf/2} - f_{ge}) = -318$ MHz. Taking $E_C = -\alpha$ and using eq 2.70 yields the Josephson energy $E_J^{\max} = 23.131$ GHz at zero flux.

We measure the transmon relaxation rate $\Gamma_1 = 1/T_1$ at different frequencies as shown in fig. 5.3c (black dots). It follows the Purcell limit (red line) from eq. 2.94 when the detuning $\Delta = f_{ge} - f_0$ is small but deviates from it as the detuning increases. The blue line is a calculated rate $\Gamma_1 = \Gamma_{1,\text{int}} + \Gamma_{\text{Purcell}}$ with an intrinsic relaxation rate

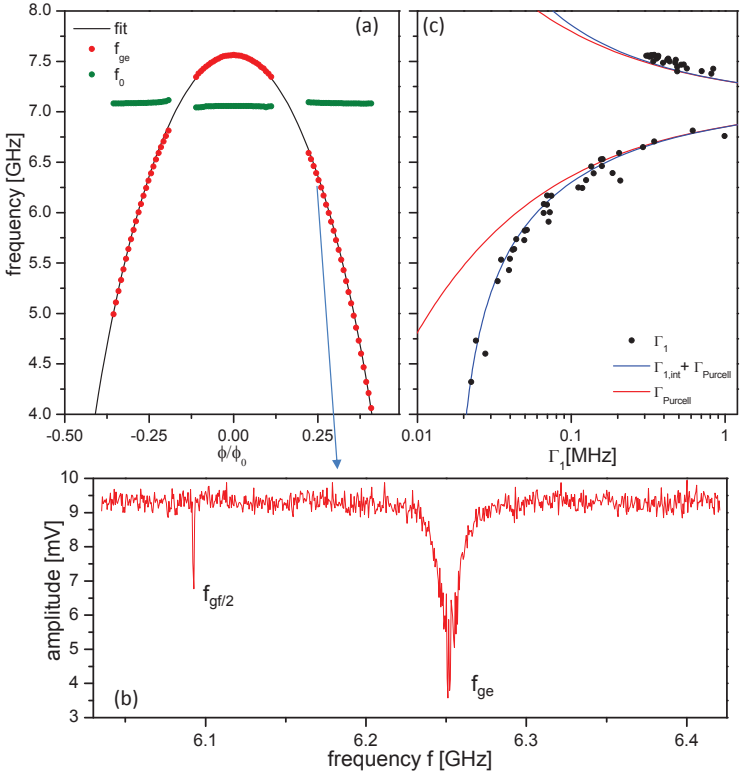

Figure 5.3. Spectroscopic and relaxation time characterization. a) Transmon frequency f_{ge} (red dots) and resonator frequency f_0 (green dots) as a function of the flux ϕ penetrating the SQUID. The black line is the calculated transmon frequency $f_{ge}^{\max}\sqrt{\cos(\pi\phi/\phi_0)}$. b) Transmon spectrum at $\phi/\phi_0 = 0.258$ showing both f_{ge} and $f_{gf/2}$. c) Relaxation rate Γ_1 measurements (black dots) as a function of f_{ge}. The Purcell limit (red line) is plotted for comparison as well as the calculated $\Gamma_1 = \Gamma_{1,\mathrm{int}} + \Gamma_{\mathrm{Purcell}}$ (blue line) with $\Gamma_{1,\mathrm{int}} = 0.0154\,\mathrm{MHz}$, yielding a good fit with the data.

$\Gamma_{1,\mathrm{int}} = 0.0154\,\mathrm{MHz}$ corresponding to $T_{1,\mathrm{int}} = 65\,\mu s$, and fits well to the measured data.

5.2.1.2 Thermal excitations

The energy fluctuations of the electromagnetic environment (either thermal or out-of-equilibrium) can cause non-zero photon population in the resonator and excitations of the transmon.

To estimate this photon population in the resonator we measure the relative amplitude of the photon number peaks corresponding to $|n=0\rangle$ and $|n=1\rangle$ as shown in fig. 5.4, using a $T_p = 12\,\mu s$ long spectroscopic pulse with amplitude corresponding to a Rabi frequency $\Omega_R/2\pi$=1.11 MHz. The transmon excitation probability $p_{e,0} = 0.50$ at $f_{ge,n=0} = 6.329$ GHz (corresponding to Fock state $|n=0\rangle$) is estimated using the Bloch equations to be . A fit of the whole spectrum by two Lorentzians with the same width yields the excitation probability $p_{e,1} = 0.013$ at $f_{ge,n=1} = 6.322$ GHz, from the relative comparison of the two peak amplitudes.

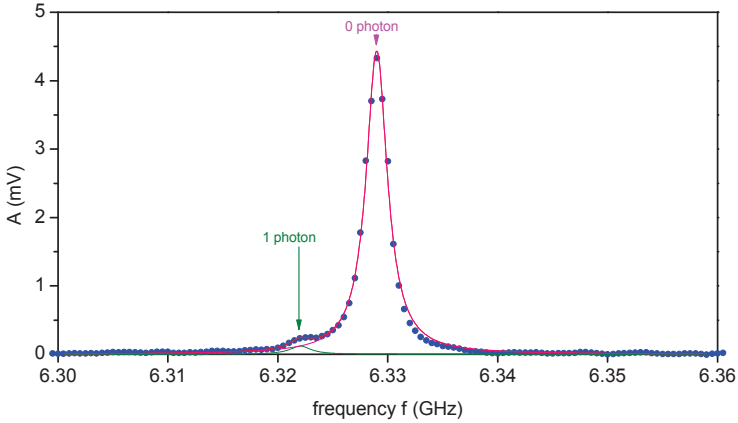

Figure 5.4. Transmon spectroscopy. The transmon excitation frequency f_{ge} shifts by $-\chi/\pi = -7$ MHz per photon. A big peak is observed at $f_{ge,n=0} = 6.329$ GHz, corresponding to no photons in the resonator, and a small peak is observed at $f_{ge,n=1} = 6.322$ GHz corresponding to a single photon in the resonator. The peaks, fitted with two Lorentzians with a width of 2.35 MHz, have amplitudes 0.12 and 4.43 mV.

To calculate the thermal population $\bar{n}_{\rm th}$ yielding this value of $p_{e,1}$ we consider that the photon number inside the cavity fluctuates with rising and lowering rates γ_+ and γ_- (where γ_- is the cavity decay rate κ). From the low value of $p_{e,1}$ compared to $p_{e,0}$ we anticipate a very small number $\bar{n}_{\rm th}$ and thus a low $\gamma_+ \simeq \bar{n}_{\rm th}\gamma_-$. We therefore only consider the case of only one photon entering (and possibly exiting) the cavity during the pulse.

The measured excitation $p_{e,1}$ is simply the product of the excited population $\sin^2(\pi f_R \tau)$ acquired during the overlap of the Rabi pulse and the presence of one photon, by the probability $\sim 1-\bar{n}_{\rm th}$ to have zero photon at $t=0$, the probability $\gamma_+ e^{-\gamma_- t_1} dt_1$ to have one photon entering the cavity between t_1 and t_1+dt_1 , the probability $\gamma_- e^{-\gamma_- \tau}\, d\,\tau$ to have the photon leaving after τ, the probability $e^{-\gamma_+(T_p-t_1-\tau)}$ that a second photon does not enter, and the probability $e^{-\Gamma_1(T_p-t_1-\tau)}$ that the transmon has not relaxed at the end of the Rabi pulse, integrated over $t_1 < T_p$ and $\tau < T_p - t_1$.

From the more detailed discussion of appendix C we get

$$p_{e,1} \simeq \frac{k^2}{2(1+k^2)(u+u^2)}\left(\frac{1+k^2}{k^2+(1+u)^2} - e^{-\Gamma_1 T_p}(1+u)\right) e^{-\gamma_- \bar{n}_{\rm th} T_p}\, \bar{n}_{\rm th} \qquad (5.1)$$

with $k = \Omega_R / \gamma_-$ and $u = \Gamma_1 / \gamma_-$. Solving this equation numerically yields a thermal population $\bar{n}_{\rm th} = 0.22\%$. This corresponds to a photon temperature $T_{\rm ph} = 56\,{\rm mK}$ calculated from the Bose-Einstein distribution.

Symmetrically, we try to estimate the thermal population of the transmon from the amplitudes A_e and A_g of the resonator peaks at frequencies $f_0^{(e)}$ and $f_0^{(g)}$, corresponding to the transmon states $|e\rangle$ and $|g\rangle$ respectively, with $A_e / A_g = p_e / p_g$. First the resonator frequencies $f_0^{(g)}$ and $f_0^{(e)}$ are located by pulsed spectroscopy as shown in fig. 5.5a, where the red spectrum is measured right after preparing the transmon in state $|e\rangle$. The magenta spectrum averaged using a VNA with the transmon at thermal equilibrium, shows a main Lorentzian peak at $f_0^{(g)}$, which is fitted and subtracted from the measurement. This yields the background shown in green fig. 5.5b. No second peak is detected at $f_0^{(e)}$ beyond the noise level yielding an upper bound on the thermal transmon excitation $p_{e,\rm th}$ of 0.5%.

5.2.1.3 Dephasing

We measure the free induction decay rate Γ_2 from Ramsey oscillations at a few transmon frequencies f_{ge}, as shown in fig. 5.6b (green dots), as well as the the decay rate Γ_2^E (magenta dots) from Hahn echo sequences (see section 4.2.6), which cancels the dephasing due to low frequency noise. These values are not necessarily true rates, since the Ramsey and echo signals decay non exponentially at certain magnetic fluxes;

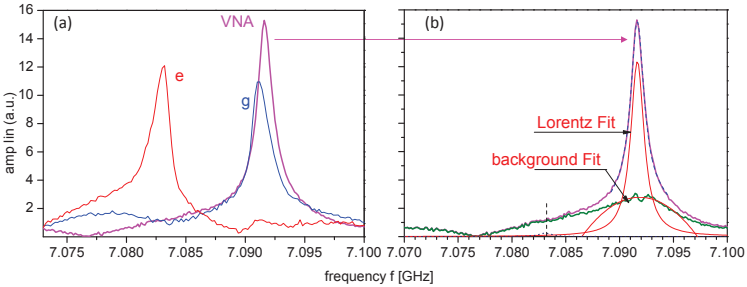

Figure 5.5. Resonator spectra for determining the thermal excitation of the transmon. a) Resonance spectra measured with the transmon in $|g\rangle$ (blue) and $|e\rangle$ (red) using the pulsed measurement setup. For improved SNR and to be in the single photon regime, the spectrum corresponding to $|g\rangle$ is averaged over night using a VNA (magenta). b) An interval of two linewidths is used to fit the VNA curve by a Lorentzian on top of a polynomial background (red lines). Subtracting the fitted Lorentzian from the measured curve gives the background (green), possibly containing a Lorentzian contribution at $f_0^{(e)}$ (dashed vertical line).

consequently, they have to be understood as the inverse of the time at which the signal has decayed by 1/e.

At $\phi/\phi_0 = 0$, where $f_{ge} = f_{ge}^{\max}$, we measure the same value $\Gamma_2 = \Gamma_2^E = 0.154\,\mathrm{MHz}$. At lower frequencies we observe an increase in Γ_2 but a decrease in Γ_2^E. To explain this behavior we consider three contributions to Γ_2 and Γ_2^E: the contribution $\Gamma_1/2$ from transmon relaxation, the dephasing rate Γ_{th} due to thermal photons in the resonator, and the dephasing rate Γ_{sq} due to flux noise in the SQUID:

The contribution $\Gamma_1/2$ on Γ_2 and Γ_2^E (see eq. 2.83) is shown as a blue line in fig. 5.6b, taking the fitted Γ_1 from fig. 5.3b.

The transmon dephasing is attributed to thermal photon noise in the resonator and to flux noise in the transmon squid:

The dephasing rate [43]

$$\Gamma_{\mathrm{th}} = \frac{\kappa}{2}\mathrm{Re}\left[\sqrt{\left(1+\frac{4i\chi}{\kappa}\right)^2+\left(\frac{16i\,\bar{n}_{\mathrm{th}}}{\kappa}\right)}-1\right] \tag{5.2}$$

is due to thermal photons randomly entering and exiting the cavity, and hence stark shifting f_{ge}. The expression eq 5.2 is plotted in fig. 5.6b (purple line) but note that its value is only valid in the dispersive regime.

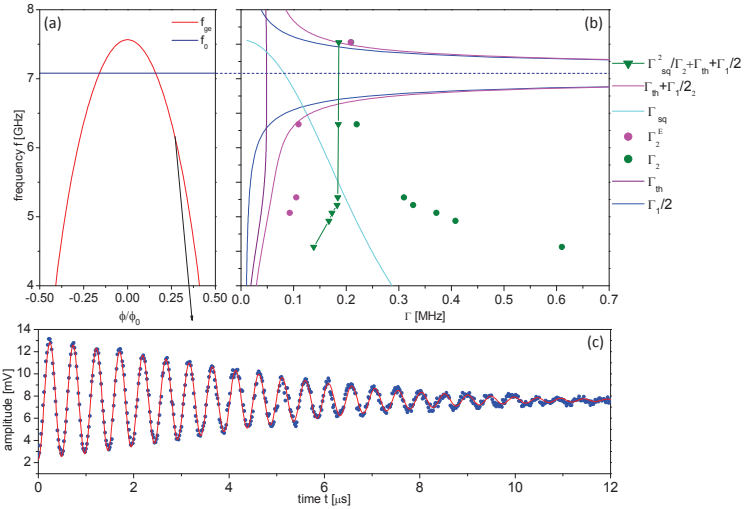

Figure 5.6. Dephasing rates at different frequencies f_{ge}. a) Fitted transmon frequency f_{ge} (red line) and indication of the resonator frequency f_0 (dark blue line). b) Measured free induction rate Γ_2 (green full circles) and echo rates Γ_2^E (magenta full circles). The different calculated contributions $\Gamma_1/2$ (blue line), Γ_{th} (purple line) from thermal resonator photons, and Γ_{sq} (cyan line) from 1/f flux noise are shown. The summed up values $\Gamma_1/2+\Gamma_{\mathrm{th}}$ (magenta line) and $\Gamma_1/2+\Gamma_{\mathrm{th}}+\Gamma_{\mathrm{sq}}^2/\Gamma_2$ (green triangle+line) are plotted for a comparison with Γ_2^E and Γ_2 respectively. b) Ramsey fringes measured (blue dots) at $\phi/\phi_0=0.268$, and fitted to oscillations in a combined exponential and Gaussian decay envelope $f(t)=a+b\cos(\delta t)e^{-\Gamma' t-(\Gamma_{\mathrm{sq},1/f}t)^2}$, yielding $\Gamma'=0.078\,\mathrm{MHz}$ and $\Gamma_{\mathrm{sq},1/f}=0.146\,\mathrm{MHz}$.

The last contribution, due to the flux noise spectral density S_ϕ, is in the case of a white noise (see section 2.2.2)

$$\Gamma_{\mathrm{sq,w}}=4\pi^3\left|\frac{\partial f_{ge}}{\partial\phi}\right|^2 S_\phi(f=0), \tag{5.3}$$

and in the case of a $1/f$ noise with $S_\phi=A_{1/f}/f$ and $A_{1/f}$ the spectral density at 1 Hz

$$\Gamma_{\mathrm{sq},1/f}^2=\left|\frac{\partial f_{ge}}{\partial\phi}\right|^2 A_{1/f}\ln\left(\frac{1}{\omega_{\mathrm{ir}}\tau}\right), \tag{5.4}$$

where the Ramsey and echo decay $e^{-(\Gamma_{\mathrm{sq},1/f}t)^2}$ is Gaussian. To estimate $S_\phi(f=0)$ and $A_{1/f}$ in the above equations, we measure Ramsey fringes at $f_{ge} = 6.157$ GHz, where the flux noise starts to be the dominant contribution, and fit it with $f(t) = a + b\cos(\delta t)e^{-\Gamma' t-(\Gamma_{\mathrm{sq},1/f}t)^2}$ as shown in fig. 5.6c. We find $\Gamma' = 78$ kHz $\backsimeq \Gamma_1/2 + \Gamma_{\mathrm{th}} = 88$ kHz (see magenta line in fig. 5.6b), which means the white flux noise is a minor contribution that we neglect. The fit gives also $\Gamma^2_{\mathrm{sq},1/f}$ yielding $A_{1/f} = 8.3\,\mu\phi_0/\sqrt{\mathrm{Hz}}$, by taking $\tau = 12\,\mu s$ (the longest measurement sequence) and $\omega_{\mathrm{ir}}/2\pi = 1$kHz (the repetition rate of the experiment). This value is comparable to the flux noise observed in SQUIDS all over the world for the past 30 years[50], and yields the cyan line plotted in fig. 5.6b. Because this last contribution is Gaussian , we'll 'sum-up' all the contributions at the experimental time $T_2 = 1/\Gamma_2$ as $\Gamma_1/2+\Gamma_{\mathrm{th}}+\Gamma^2_{\mathrm{sq},1/f}/\Gamma_2$, for a valid comparison with the measured Γ_2 (same 1/e decay). Let's now discuss the results:

At $\phi/\phi_0 = 0$ the sensitivity to flux noise is zero, the contribution from flux noise is thus zero, and the calculated value $\Gamma_1/2 + \Gamma_{\mathrm{th}}$ (magenta line) fits the measured value of Γ_2. Moreover the contributing noise is white, such that the echo cannot cancel a significant fraction of it, and $\Gamma_2 \simeq \Gamma_2^E$. When the frequency is decreased, the sensitivity to flux noise increases, the corresponding contribution increases quickly, and makes the total Γ_2 increase by a factor 3. As this noise is essentially at low frequency, the echo cancels a large fraction of it, so that $\Gamma_2 \simeq \Gamma_1/2+\Gamma_{\mathrm{th}}$ within a factor 1.7 . At low frequency, where the flux noise contribution becomes dominant, the $\Gamma_{\mathrm{sq},1/f}$ deduced from the fit at intermediate frequency (cyan line) seems to underestimate the effect (it is far from the bottom green circles): hence the discrepancy of up to a factor 3 between the measured Γ_2 (green circles) and the total calculated Γ_2 (green triangles). The reason for this underestimation remains not understood.

5.2.2 Transmon on Sapphire substrate

The transmon KJ15ch11 discussed here had the same dimensions as the transmon in section 5.2.1 but was fabricated on a sapphire substrate with a low loss tangent, which is important for future experiments in high-Q cavities.

The purpose of this sample was on one hand to verify that we could reproduce a long Γ_1 with the new recipe developed for sapphire substrate. On the other hand we wanted to improve Γ_2 at the optimal cavity-transmon detuning for readout by having the maximum transmon frequency well below the resonator frequency: indeed at high frequencies f_{ge}, the sensitivity to flux noise $|\partial f_{ge}/\partial_\phi|$ is low, and Γ_2^E and Γ_2 are only bounded by $\Gamma_1/2$, which is fixed by the detuning. We thus reduce $E_J^{\max}$ to achieve this goal. Since all other parameters are kept the same, we will only discuss these new goals.

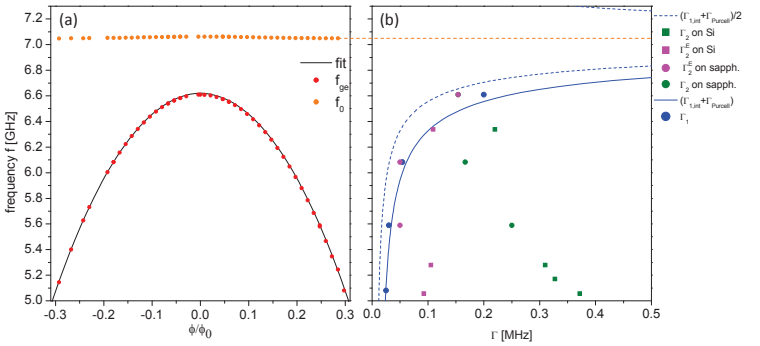

Figure 5.7. Spectroscopic and decoherence characterization. a) Transmon frequency f_{ge} (red dots) and resonator frequency f_0 (orange dots) as a function of the flux ϕ penetrating the SQUID. The black line is the calculated transmon frequency $f_{ge}^{\max}\sqrt{\cos(\pi\phi/\phi_0)}$. b) Relaxation rate Γ_1 (blue dots) fits the calculated rate $\Gamma_{1,\text{int}}+\Gamma_{\text{Purcell}}$ with $\Gamma_{1,\text{int}}=0.013$ MHz. The free induction decay rate Γ_2 (green dots) and Hahn echo rate Γ_2^E (magenta dots), as a function of f_{ge}, are compared to the corresponding values of the previous sample on Si (green and magenta squares). The lower limit $(\Gamma_{1,\text{int}}+\Gamma_{\text{Purcell}})/2$ of Γ_2 and Γ_2^E is shown as a blue dashed line. Neither thermal photon number $\bar{n}_{\text{th}}$ nor the flux spectral density S_ϕ were measured in this experiment.

The transmon and resonator frequencies f_{ge} and f_0 are mapped in fig. 5.7a. The maximum transmon frequency $f_{ge}^{\max}=6.62$ GHz gives $E_J^{\max}=18.9$ GHz, E_C being the same as for the previous sample.

The transmon relaxation and free induction decay are measured at three to four different frequencies as shown in fig. 5.7b. The measured Γ_1 (blue dots) are very similar to those in the previous sample and a calculated $\Gamma_1=\Gamma_{1,\text{int}}+\Gamma_{\text{Purcell}}$ (blue line) with an intrinsic $\Gamma_{1,\text{int}}=0.013$ MHz fits the data.

This sample yields values of Γ_2 (green dots) and Γ_2^E (magenta dots) a factor 1.5 to 2 lower than the previous sample (green and magenta squares), as expected. The rate Γ_2 increases with lower f_{ge} while Γ_2^E is close to $\Gamma_1/2$ (blue dashed line), illustrating once more the effect of the echo sequence on low frequency noise.

5.3 Conclusion

We successfully fabricated and characterized a flux tunable transmon qubits, fabricated both on Si or sapphire substrates, coupled to the fundamental mode of a 3D Cu cavity resonator. We measured an upper bound of 0.5% on the thermal excitation of the transmon and a thermal population of in the cavity $\bar{n}_{\text{th}} = 0.22\%$, which is lower than achieved in similar experiments [8][43].

The relaxation time T_1 reaches $\sim 40\,\mu s$ at high transmon-resonator detuning but is still limited by the Purcell effect. The intrinsic lifetimes, estimated by removing the Purcell contribution, are $65\,\mu s$ and $77\,\mu s$ for the Si and sapphire substrates respectively, which is of the same order as the longest lifetimes observed today [43][37][16]. Measurements of T_2^E indicate that T_2 could be close to $2T_1$ when the $1/f$ flux noise is negligible (even at high values $T_1 \sim 40\,\mu s$). This can be achieved for a small frequency range f_{ge} near $\phi\,/\,\phi_0 = 0$ by choosing $E_J^{\max}$ appropriately.

As a conclusion the parameters as well as an appropriate $E_J^{\max}$ are well suited for QZD experiments. However, our implementation required a re-design of the transmon geometry for reasons explained in chapter 6. We observed a lower T_1, probably for the following reason: In the new design the pads are further apart (3 mm) and connected by a few μm wide wire, causing a high concentration of the electric field. Such narrow structures have been shown to have shorter relaxation times than broader ones[16].

Chapter 6
Design and characterization of an sample suited for QZD

This chapter discusses the design and characterization of the sample used for the QZD experiments presented in chapter 7.

6.1 Design and fabrication

We designed a 3D circuit-QED system that realizes the ef-resonant scheme presented in chapter 2, where a high-Q mode of a cavity resonator is coupled to a transmon with a weak coupling constant. Another cavity mode, with a low-Q and a strong coupling constant, is dispersively coupled to the transmon and used to readout its state. We refer to the high-Q mode as the 'storage mode' or 'oscillator', and the low-Q mode as the 'readout mode'. A circuit diagram of the system is depicted in fig. 6.1.

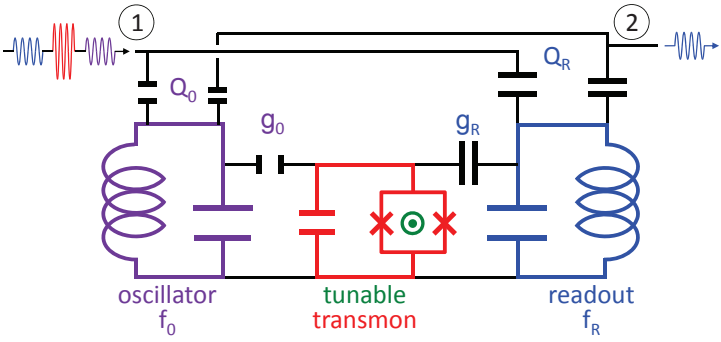

Figure 6.1. A circuit diagram of two modes of a cavity coupled to a transmon. The transmon and the so-called storage mode at frequency f_0 represent the harmonic oscillator and 3LS in the ef-resonant scheme discussed in chapter 2. The additional mode at f_R is used to readout the transmon state.

To estimate the target parameters well-suited for QZD experiments we consider a cavity approximated by a cuboid with dimensions [x=44, y=56, z=6] mm. The storage mode is the TE 120 mode at frequency $\omega_0 / 2\pi \sim 6.4$ GHz and the readout mode, TE 210, is at frequency $\omega_R / 2\pi \sim 7.3$ GHz, as shown in fig. 6.2. We try to obtain the highest Q_{int} possible for the storage mode, expecting at least ∼1 million as seen in [37]. The readout mode is strongly overcoupled at $Q_{\text{tot}} \sim 10$k for fast readout and should have a much larger Q_{int}. In order to overcouple the readout mode and undercouple the storage mode simultaneously, we place the coupling pins close to an electric field node of storage mode and an antinode of the readout mode.

To induce a photon number splitting $\delta_{\pm,n} \sim g_0\left(\sqrt{2(n+1)} - \sqrt{2n}\right) > 2$ MHz (see section 2.2.3.3) up to $n = 10$ we target $g_0 \sim 10$ MHz. We target $\alpha \simeq E_C = 450$ MHz that yields a small Kerr effect $K_{ef} = 220$ Hz, which corresponds to a shift of $1/3$ of the storage mode linewidth at 10 photons (assuming $Q = 1M$). Minimum transmon lifetimes T_1 and T_2 of $1\mu s$ are needed, and a coupling $g_R > 100$ MHz to the readout mode is targeted. For the Josephson energy in the absence of a flux bias we target $E_{J,\text{Max}} \sim 20$ GHz, yielding $f_{ge} = 8$ GHz, which is high enough to measure the anticrossing with the readout mode. The different couplings to the two modes is achieved by careful placement

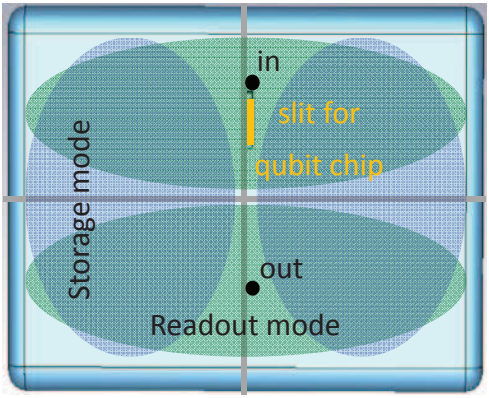

Figure 6.2. Schematic representation of the field distribution of the TE120 storage mode (blue) and TE210 readout mode (green), having orthogonal node planes. A slit for inserting the transmon (yellow) and the two ports (black dots) are placed close to a storage mode node and to a readout mode antinode.

of the transmon with respect to the fields nodes and antinodes of both modes using the same logic as for the coupling pins.

Transmon fabrication is not precise enough to make a non-tunable transmon that fulfills the ef-resonant condition. Consequently the transmon has to include a SQUID to be tunable with magnetic flux. This poses a challenge since achieving a high-Q of the cavity requires it to be superconducting and thereby screening all magnetic field. We solve the problem by inserting the transmon only partially into the cavity such than one pad is inside and couples to the field modes, whereas the other pad as well as the SQUID are outside the cavity, where a magnetic field can be applied. The transmon is inserted through a slit made in one of the cavity walls that has been made particularly thin (∼1mm).

6.1.1 Cavity

Finite element microwave simulations were used to precisely determine the cavity geometry. Two cavities were then machined and assembled, before being tested to verify that they were suited for QZD experiments.

6.1.1.1 3D simulations

The actual cavity design is essentially a cuboid, with the same dimensions as in the last section, where some of the edges have been rounded for the purpose of practical machining. It is simulated in a 3D simulation software named CST microwave studio [53]. The two cavity ports are located 0.5 mm away from the storage mode node plane as shown in fig. 6.3 a. They are made of 3 mm long and 2 mm diameter holes, added to the geometry as vacuum cylinders, and 0.6 mm diameter coaxial Cu pins (cylinders) whose length can be varied.

The slit, the sapphire chip and the Cu block are added to the model as shown in fig. 6.3b-d. The slit is place on the wall opposite to the pins and centered 0.45 mm away from the storage node plane. The shape of the slit is the same in the cavity wall as in the Cu block shown in fig. 6.3d. The slit edges are 0.5 mm wide to guide the 0.33 mm thick chip while the center is wider (0.7 mm) to avoid scratching the transmon and lessen the coupling to potentially lossy metals. The sapphire chip is extends from the bottom wall of fig. 6.3b, throughout the slit, and into the Cu block. In CST the coupling pins and Cu block are modeled as normal metal with the room temperature resistivity of Cu, the sapphire

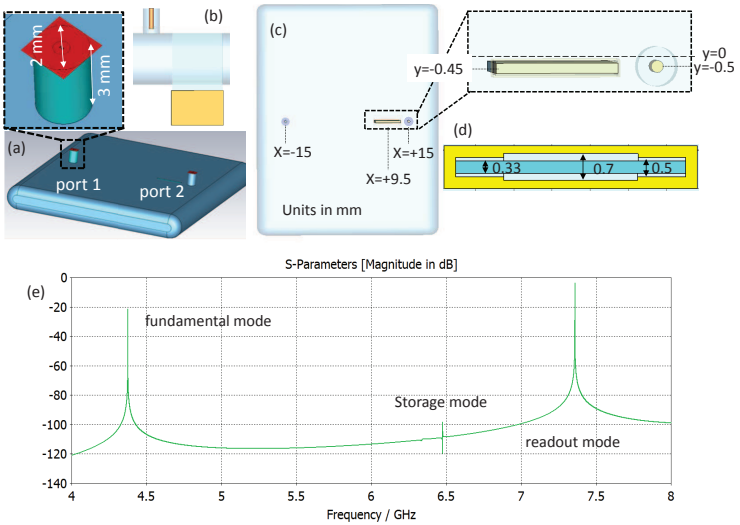

Figure 6.3. Cavity-chip design and corresponding simulations. a) Two coaxial cylindrical ports are placed on the top wall cavity. b) Cross section view of the port (top), cavity (center), Cu block (bottom) with a sapphire chip. c) Port and chip locations d) Slit geometry. e) Simulated transmission spectrum between the two ports showing the frequencies of the first 3 resonances of the cavity.

chip a lossless block with relative permittivity $\varepsilon_r = 9.3$, the rest of as vacuum with lossless walls

The simulated transmission spectrum between the two ports is shown in fig. 6.3 e. It shows resonances of the first three modes of the cavity at 4,4 GHz (fundamental mode TE 110), 6.4 GHz (storage mode TE 120) and 7.3 GHz (readout mode TE 210). Note that the frequency sampling of the simulator is not sufficient to resolve the resonance line shapes.

Figure 6.4 shows the electric field and surface current distributions of the modes. The presence of the sapphire chip induces a notable asymmetry between the two antinodes of the readout mode.

The cavity is carved out of two blocks of metal which are then put together as shown in the next section. With that in mind we attempt to obtain the highest-Q possible for the storage mode by cutting the cavity along the node of the readout mode such that the supercurrents of the storage mode are parallel to the cut and thus not perturbed.

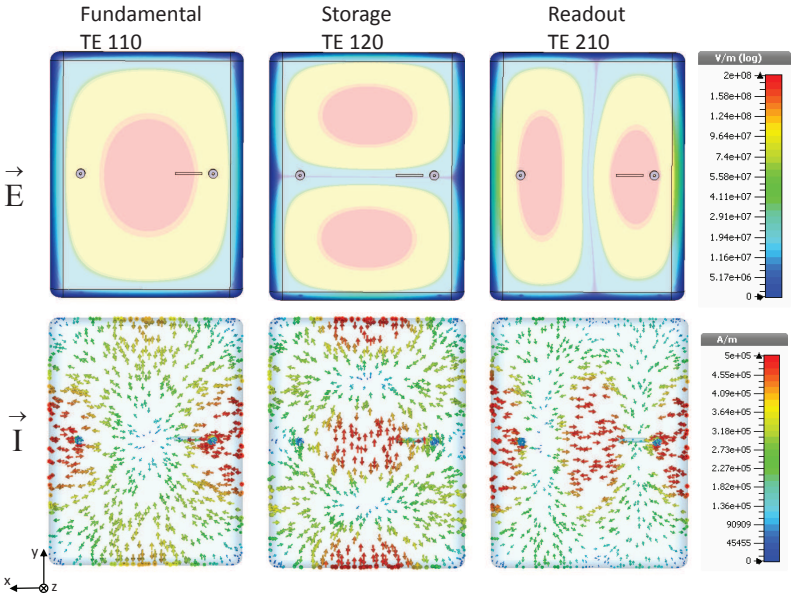

Figure 6.4. Electric field and current distributions of the modes. The absolute value of the electric field, which is almost completely along the z axis (in and out of the plane). The presence of the sapphire chip with $\varepsilon_r = 9.3$ distorts the distribution of the field.

6.1.1.2 Realization and testing

First, two identical cavities are made by an external workshop according to the design described above, but without the slit and the Cu block, which are added later by the in-house workshop. The bulk of the cavity is made of a high purity aluminium (N4) and additional assembling parts are made of copper, with some being goldened to prevent oxidation. The coupling pins are SMA feedthroughs with a Cu wire soldered into the hole on one end. The SMA throughs are then screwed into the cavity wall, until the Cu pin enters into the cavity through a small hole, and is then fastened with a nut. This way the penetration of the pin into the cavity can be easily adjusted. By measuring the S-matrix at room temperature the coupling of each pin can be tuned in-situ as explained in chapter 2. The coupling pins and the two final designs of the cavity, varying by the orientation of the slit, are shown in fig. 6.5.

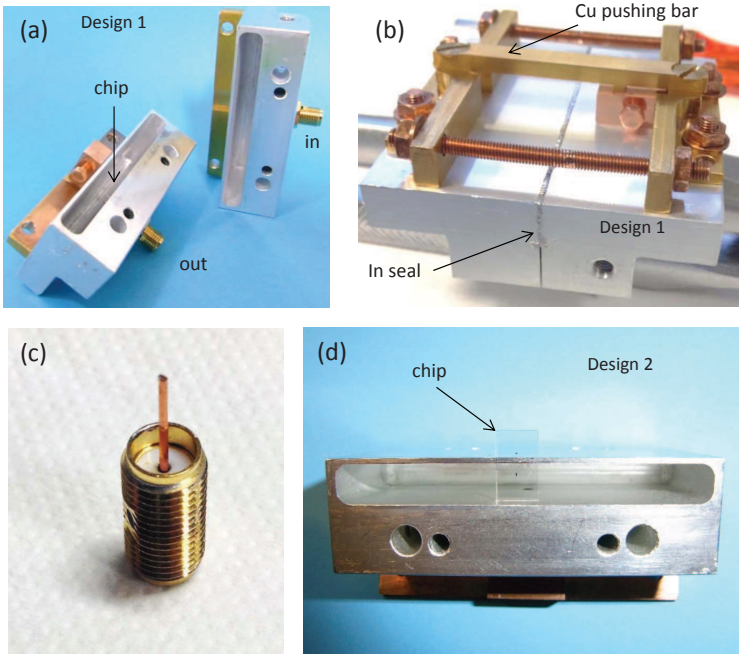

Figure 6.5. The Al cavities and assembling parts. a) The two parts of the cavity. One wall of the cavity is only 1 mm thick and has a slit through which the transmon is inserted. A part of the transmon, including the SQUID, remains outside the thin cavity wall. The opposite wall has two holes for coupling pins. b) The two parts of the cavity are closed with an indium seal to ensure good conductivity between the two halves. A Cu block covering the part of the transmon protruding out of the cavity is pushed down by a gold-coated Cu bar. c) Cavity pins are made by soldering a Cu wire into one end of an SMA trough. d) A second generation of the cavity design where the slit has been rotated gave $Q_0 = 10$ million.

The internal quality factors Q_{int} of the different modes, at different steps towards the final design, are estimated from measurements of the external quality factors $Q_{1,2}$ at room temperature (see section 2.2.1.2) and from the total quality factor Q_{tot} measured at 30 mK. Anticipating Q_{int} of order 1 million, we choose $Q_{1,2} \sim 100$k on the readout mode in order to overcouple the readout mode without undercoupling excessively the storage mode: Like this the sensitivity to estimate $Q_{\text{int},R}$ is enough while the transmitted signal at the storage mode frequency is sufficiently strong.

The first preparation step after machining the cavities was to clean them in an ultrasonic bath of acetone and to chemically polish them for 15 hours in a bath of $\{4H_3PO_4,4CH_3COOH,1HNO_3,1H_2O\}$, removing roughly 20 μm of material. Measurements at 34 mK gave $Q_{0,\mathrm{int}} \sim 5M$ and $Q_{R,\mathrm{int}} \sim 20k$ for both cavities. Thereafter one of the cavities was developed towards its final state. The Q_{int}'s at each step are listed in table 6.1: The slit lowers $Q_{0,\mathrm{int}}$ to $0.6\,M$. Three steps followed after that; the slit was covered with a Cu block, a sapphire chip was inserted in it and an indium seal between the two cavity parts was added, with no clear effect on $Q_{0,\mathrm{int}}$. On the contrary, $Q_{R,\mathrm{int}}$ remained low compared to the other modes until the In seal was added, indicating that the poor connectivity between the two cavity halves was dominating losses.

The transmission measurements of the three modes after the last development step is shown in fig. 6.6. With these Q-factors we proceed with towards the QZD experiment, overcoupling the readout mode ($Q_{R,\mathrm{tot}} \sim$ 10-20k). The storage mode remains strongly undercoupled with $Q_{0,\mathrm{int}} \simeq Q_{0,\mathrm{tot}}$ in the range from 0.7 -2.2M at 30 mK, depending on the quality of the In seal.

The cavity design was slightly modified for the other cavity where the slit was aligned parallel to the supercurrents of the storage mode. After removing another $20\,\mu m$ of material with chemical polishing it was measured to have $Q_{0,\mathrm{tot}} = 10M$. This cavity design was however implemented late in the thesis period and we never managed to couple it successfully to a transmon.

6.1.2 Transmon qubit

The transmon design for the QZD experiment is significantly modified from the design presented in chapter 5. The mode couplings and anharmonicity is estimated from CST simulations while the lifetimes T_1 and T_2 are tested experimentally.

6.1.2.1 3D simulations

Inspired by refs. [43][35] the transmon-cavity system is simulated to estimate the couplings g_0, g_R and the anhamonicity α. This is done by adding to the previous simulation the two transmon electrodes modeled as 2D sheets of perfect conductors on the sapphire block (see fig. 6.7a). The pin ports are removed and the SQUID is replaced by an internal port.

Table 6.1. Table of internal quality factors measured at cryogenic temperatures for different preparations of the cavity.

Preparation	Fundamental	Storage	Readout
Cleaned and chemically etched, no In seal	$>1.5M$	$5.5M$	$20k$
Slit made	$4.0M$	$0.6M$	$3.6k$
Slit covered with Cu block	$2.3M$	$1.0M$	$17k$
Slit with sapphire chip and Cu block	$1.6M$	$1.2M$	$10k$
Slit with sapphire chip and Cu block; cavity closed with In seal	$2.1M$	$0.8M$	$750k$

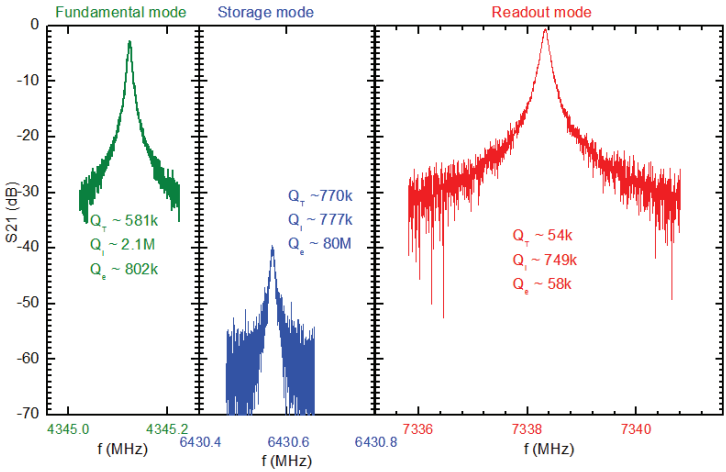

Figure 6.6. Resonances of the cavity after the last preparation step with the estimated total, internal and external quality factors Q_T, Q_i and Q_e. All internal Q-factors are over 0.7 million.

The total admittance $Y_{\text{total}}(\omega)$ of the transmon-cavity system is the sum of the admittance $Y_S(\omega)$ seen from the port in the simulation and of the SQUID admittance $Y_J(\omega) \simeq 1/iL_J\omega$.

The resonance frequencies given by $\text{Im}[Y_{\text{total}}] = 0$ (see section 2.2.1.2) now includes the transmon mode. By varying L_J this mode can be brought close to a cavity mode. These two modes (cavity and

transmon) repel each other, as shown in fig. 6.7 b, which reproduces the anticrossing with the minimal separation $2g$, as shown in fig. 6.7 c. The anharmonicity α is estimated from the charging energy E_C, with $\alpha \simeq E_C = e^2 / 2C_\Sigma$ (eq 2.63). C_Σ is here the simulated total capacitance $C_S = 1 / i\omega Y_S(\omega)$ seen from the port, at frequencies ω much lower than all cavity resonances. We thus simulate $Y_S(\omega)$ at $\omega/2\pi = 1\,\text{GHz}$ and get $E_C \simeq \alpha$.

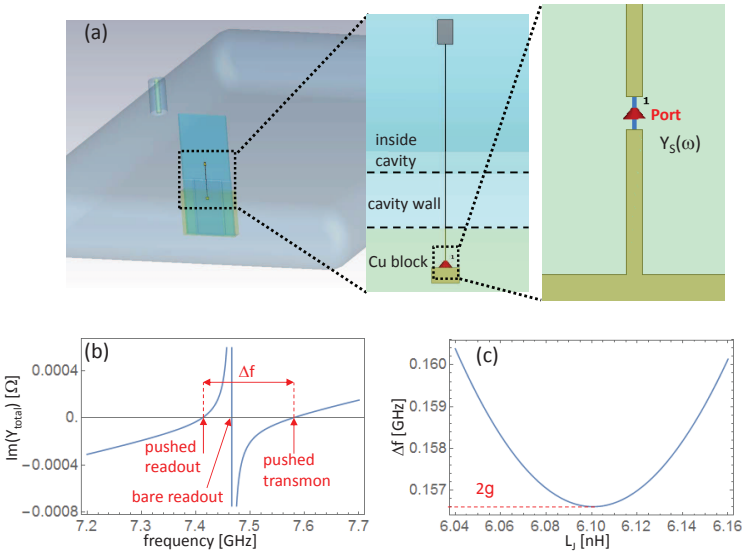

Figure 6.7. Simulating the transmon coupling to cavity mode (readout mode taken as an example). a)The transmon geometry is added to the cavity with the SQUID replaced by an internal port. b) Total admittance of the transmon-cavity system at a particular SQUID inductance L_J, showing the bare readout frequency and the two hybridized transmon-readout modes on either side c) Separation between two hybridized modes as a function of L_J. The minimum yields the coupling constant g.

In the simulations the bottom pad is placed 0.5 mm below the top of the Cu block, with the port 50 μm above the pad (see fig. 2.3b). A $1\,\mu m$ wide wire extends from the bottom pad to the top pad located inside the cavity. The couplings g_0, g_R are varied by changing the

pad separation and the dimensions of the top pad as shown in fig. 6.8a,b. The value of g_0 is governed by its distance to the storage mode node. After the values of g_0 and g_R have been determined, the width of the bottom pad can be varied to get the targeted E_C with only a small effect on the couplings.

A geometry with pad dimension 200x200 μm^2 (top) and 200x400 μm^2 (top), separated by 2.9 mm and located 0.78 mm away from the node of the storage mode, we get $g_R = 120$ MHz, $g_0 = 7.5$ MHz and $E_C = 493$ MHz, with which we proceed to experimental testing.

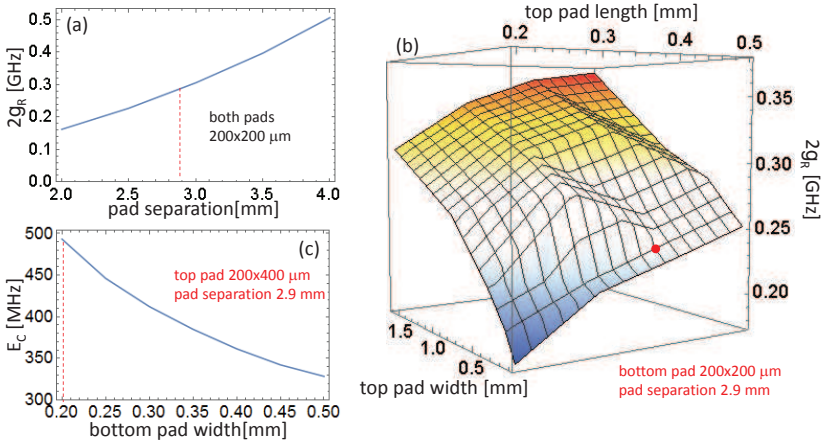

Figure 6.8. Determining transmon geometry from CST simulation to reach targeted couplings and charging energy. a) Influence of pad separation on the coupling g_R to the readout mode. b) influence of the dimensions of the top pad (the one inside the cavity) on g_R. c) Charging energy E_C as a function of the bottom pad width. The red marks indicate the final set of parameters.

6.1.2.2 Realization and testing of preliminary samples

We fabricated and tested four preliminary transmons with the dimensions described above (see fig. 6.9) using a similar recipe as for sample KJ19ch1 (see section 3.1.5).

The first three transmons had problems such as a very short $T_1 =$ 500 ns, being shorted, and having unexplained instable behavior. The fourth sample gave the first impression of being suitable for the QZD experiments: From a room temperature measurement of the SQUID

resistance $R_{J,\mathrm{RT}} = 4.1\,k\Omega$, we estimate a maximum Josephson energy $E_{J,\mathrm{Max}} = 28$ GHz at zero flux (see section 2.1.4). From anticrossings measured at 34 mK we get couplings $g_0 = 8$ MHz and $g_R = 150$ MHz. The measured resonance frequencies of $f_{ge} = \omega_{ge}/2\pi$, $f_{ge}/2$ and $\widetilde{f_R}$ as a function of the flux bias ϕ are shown in fig. 6.10 a. The anhamonicity

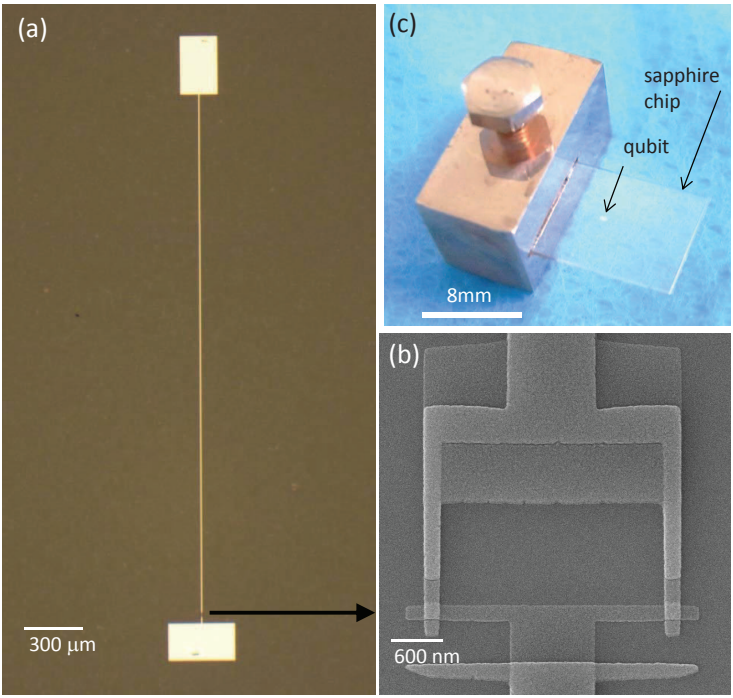

Figure 6.9. Transmon KJ19ch1 used in the QZD experiments. a) Two pads are separated by a ∼3 mm long wire with a SQUID located ∼50 μm above the bottom pad. b) The SQUID is made up of two 200x200 nm^2 junctions in a loop with an area of 1.1x2.6 μm^2. c) Transmon fabricated on a sapphire chip and mounted in the Cu block.

α, estimated as twice the separation between f_{ge} and $f_{gf}/2$, varies from 230 MHz at $\phi/\phi_0 = 0$ to 500 MHz at $\phi/\phi_0 = 0.4$. We attribute this variation partly to the strong coupling to the readout mode that shifts the $|e\rangle$ and $|f\rangle$ levels to a different extent, and partly to the possible change of the transmon capacitance C_Σ between 8 and 5 GHz.

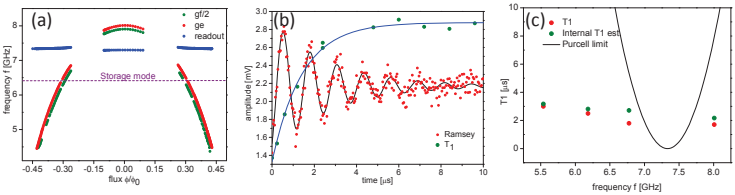

Figure 6.10. Characterization of the fourth preliminary transmon qubit. a) Mapping of f_{ge}, $f_{gf}/2$ and $\tilde{f}_R$ as a function of flux ϕ. b) Relaxation and Ramsey fringe measurements at $\phi = 0$, yielding $T_1 = 1.5\,\mu s$ and $T_2 = 2.8\,\mu s$. c) Measured T_1 (red dots) for different values of f_{ge}. Black line shows the Purcell limit of T_1 whereas the green dots show the intrinsic T_1 after removing the Purcell contribution.

Figure 6.10 b shows relaxation-and dephasing time measurements at $\phi / \phi_0 = 0$, where f_{ge}=8.01 GHz, giving $T_1 = 1.5\,\mu s$ and $T_2 = 2.8\,\mu s$ (see protocol in section 4.1). T_1 was measured for different f_{ge} and compared with the estimated Purcell limit due the its coupling to the readout mode. Figure 6.10 c shows an intrinsic $T_1 = 3\,\mu s$ but at the ef-resonant condition $\omega_{ge} = \omega_0 + \alpha = 2\pi \times 6.76\,\text{GHz}$, it is reduced to $1.8\,\mu s$ because of the Purcell effect.

At this ef-resonant working point, where $\alpha = -320\text{MHz}$, we discovered a problem making this seemingly usable sample ill-suited for the QZD experiments. The energy of the level $|f\rangle$ happens to be unstable. This is observed by tuning the transmon frequency to 50 MHz below the ef-resonance, i.e. $f_{ge} = 6.71\,\text{GHz}$, exciting the transmon to $|e\rangle$ and performing spectroscopy of the $|e\rangle \rightarrow |f\rangle$ transition. Figure 6.11 a shows the monitoring of the resonance peak over 17 hours and fig. 6.11 b shows a few selected traces. The resonance varies from being a single peak at 6.378 GHz to two peaks separated by up to ∼7MHz.

This behavior studied in ref [44] is due to fluctuating charges: As described in chapter 2 (see fig. 2.8), the energy levels of the transmon are modulated as a function of the reduce charge n_g, with a period of one Cooper pair 2e, and with an amplitude that increases with E_C. Two types of n_g fluctuations are here in play: Electrons in dielectrics in the vicinity of the transmon electrodes move around, yielding a drift in n_g. In addition the number of out-of-equilibrium quasi-particles, with charge e, fluctuates rapidly which induces jumps $\Delta n_g = 0.5$ [44], and therefore two branches of each energy band.

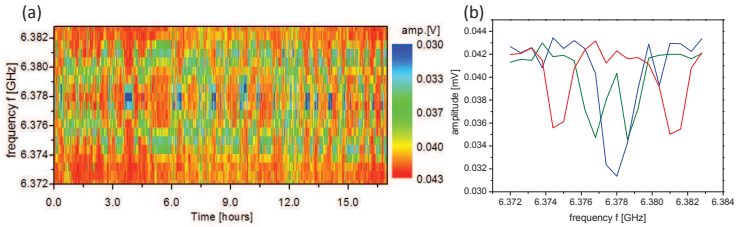

Figure 6.11. Spectroscopy of the $|e\rangle \rightarrow |f\rangle$ transition. a) Repeated spectroscopy over a 17-hour period showing two resonances with a frequency separation varying from 0 to 7 MHz. b) Three cross section from a.

The two peaks shown in fig. 6.11 correspond to the two branches of the $|f\rangle$ level, whose separation varies with n_g. For $n_g = \pm 0.25$ [2e] the energies are degenerate for the two parities, resulting in a single peak, while at $n_g = 0$ the separation is maximal and equal to the dispersion of the energy band ν_f(eq. 2.68). The dispersion $\nu_f = 7$ MHz observed here corresponds to $E_C = 427 \pm 2$ MHz, according to calculations of the exact Hamiltonian of the transmon coupled to the readout modem using the measured couplings and transition frequencies.

This results shows that a new transmon geometry with smaller E_C is needed, keeping similar coupling parameters g_0 and g_R.

6.2 Characterizing the sample used in the QZD experiment.

The fifth fabricated transmon sample (KJ19ch1) was well suited for the QZD experiment.

Its pad dimensions are modified to achieve the same couplings to the modes but a ∼25% lower E_C. This results in a $5\,\mu m$ wide wire and pad sizes to 360x200 μm^2 and 200x315 μm^2, as shown in chapter 3. Simulations give $E_C = 385$ MHz, $g_0 = 7.5$ MHz and $g_R = 117$ MHz, and fabrication as described in chapter 3 yields $E_{J,\mathrm{Max}} = 30$ GHz, estimated from room temperature resistance of the SQUID.

The coupling pins to the cavity were asymmetrically tuned for better detection efficiency, with Q_{in}=116k and $Q_{\mathrm{out}} = 20$k on the input and output ports. This amounts to $Q_{\mathrm{ext}} = 17$ k.

6.2.1 Spectroscopic characterization

Once the sample is at 34 mK the transmission spectrum is measured with a vector network analyzer (VNA) as a function of the applied flux ϕ. The hybridized frequencies $\tilde{f}_R$ and f_{ge} extracted from the spectra are shown in fig. 6.12a (red dots). At $\phi\,/\,\phi_0 = 0.23$ and 0.31 the frequency f_{ge} anticrosses with the readout and storage modes giving

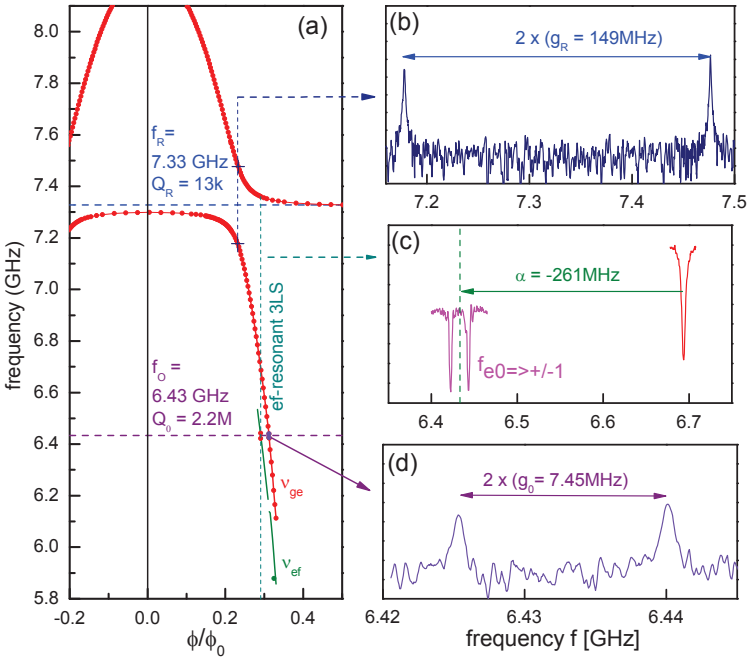

Figure 6.12. Spectroscopic characterization of the system. a) Measured transition frequencies as a function of the magnetic flux ϕ applied though the transmon SQUID. Blue and purple horizontal dashed lines correspond to the readout and storage mode frequencies f_R and f_0, red dots to the hybridization of f_{ge} and f_R and the green line to f_{ef}. The 'ef-resonant' condition is obtained at $f_0 = f_R$. b) Transmission spectrum at $f_R = f_{ge}$ determining the transmon coupling g_R to the readout mode. c) Transmon $|e\rangle \rightarrow |f\rangle$ (magenta) spectroscopy at $f_0 = f_{ef}$. The double peak corresponding to the transitions $|e0\rangle \rightarrow |\pm 1\rangle$ shows the ef-resonant working point. Spectroscopy on $|g\rangle \rightarrow |e\rangle$ (red) showing f_{ge} yields the anharmonicity α. d) Transmission spectrum at $f_0 = f_{ge}$ determining the transmon coupling g_0 to the storage mode.

$g_R = 149$ MHz and $g_0 = 7.45$ MHz, respectively (fig. 6.12b,d). The second excitation frequency f_{ef} is obtained by pulsed $|e\rangle \rightarrow |f\rangle$ spectroscopy as for fig. 6.11 described in the previous section. This time it is stable and is displayed as the green line in fig. 6.12a. Figure 6.12c shows the transmon spectrum at $\phi/\phi_0 \simeq 0.291$, where the ef-resonance $\tilde{f}_0 = f_{ef}$ occurs ($\tilde{f}_0 = 6.4328$ GHz is the dispersively shifted frequency - see appendix A). The red resonance line shows $f_{ge} = 6.694$ GHz, and the magenta line the $|e\rangle \rightarrow |f\rangle$ spectroscopy. It reveals two peaks at $\tilde{f}_0 \pm 10.4$ MHz, representing the transitions $|e0\rangle \rightarrow |-1\rangle$ and $|e0\rangle \rightarrow |+1\rangle$. The green vertical dashed line midway between the two magenta peaks indicates $\tilde{f}_0 = f_{ef}$, yielding an anharmonicity $\alpha = -261$ MHz, which corresponds to $E_C = 238$ MHz.

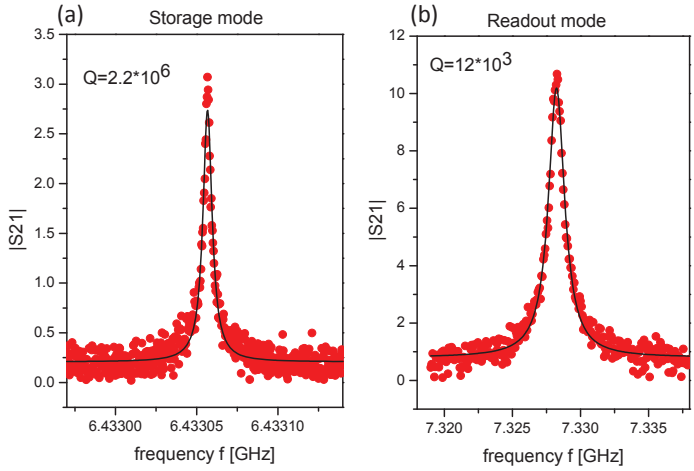

Figure 6.13. Bare resonance peaks of a) the storage mode with $f_0 = 6.43306$ GHz and $Q_0 = 2.2$ million, and b) the readout mode with $f_R = 7.328$ GHz and $Q_R = 12$ thousand.

At $\phi/\phi_0 = 0.5$, f_{ge} is almost zero and transmons effect on the cavity modes is negligible. Figures 6.13a,b show the resonance peaks of the storage and readout modes respectively at that point, revealing $Q_0 = 2.2$ million and $Q_R = 12$ thousand. This entails that the lifetime of the storage mode is $T_0 = 54\,\mu s$. The sample was warmed up to room

temperature due to technical reasons a three times during the measurement period, but the sample was never disturbed. A degradation in Q_0 was observed each time: $2.2 \rightarrow 1.9 \rightarrow 1.6 \rightarrow 1.2$ million. We speculate that the repeated cycle of thermal contraction and expansion degraded the quality of the In seal.

The relaxation time of the transmon was measured when f_{ge}= 6.18 GHz, giving $T_1 = 4.1\,\mu s$ and is shown in fig. 6.15 a. Subtracting the Purcell effect gives an intrinsic lifetime $T_1 = 6.2\,\mu s$.

6.2.2 Characterization at ef-resonance

The sample is now characterized further at the flux bias $\phi/\phi_0 = 0.291$, where the sample is at the ef-resonance.

6.2.2.1 Fine tuning the ef-resonance

The ef-resonant point is reached by fine tuning the flux bias using the following method: The storage mode is populated with a coherent field with $\bar{n} \simeq 1$ using a weak 150 ns pulse. Spectroscopy around f_{ge} is then performed. With $\bar{n} \simeq 1$ the $|n = 0\rangle$ and $|n = 1\rangle$ Fock state population probabilities are $p(0) \simeq p(1) \simeq 0.36$ such that the three transitions $|g0\rangle \rightarrow |e0\rangle$, $|g1\rangle \rightarrow |-1\rangle$ and $|g1\rangle \rightarrow |+1\rangle$ are observed. The flux bias is then tuned such that the frequency separation of the peaks is equal, i.e. $\delta_{-,0} = \delta_{+,0}$, as shown in fig. 6.14, where $\delta_{-,0}$=10,4 MHz and $\delta_{+,0} = 10$, 4 MHz with an error of $\pm$0.1MHz. This is in accordance with the predicted value of $\sqrt{2}\,g_0 = 10.5$ MHz.

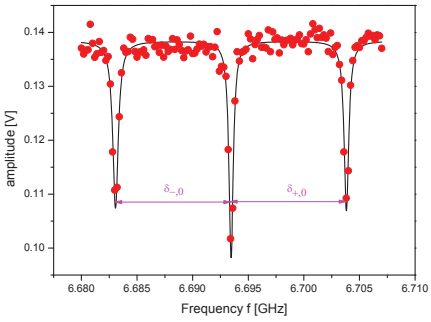

Figure 6.14. The equal separation $\delta_{-,0} = \delta_{+,0}$ of $f_{\pm,1}$ from f_{ge} indicates the ef-resonance at $\phi/\phi_0 = 0.291$.

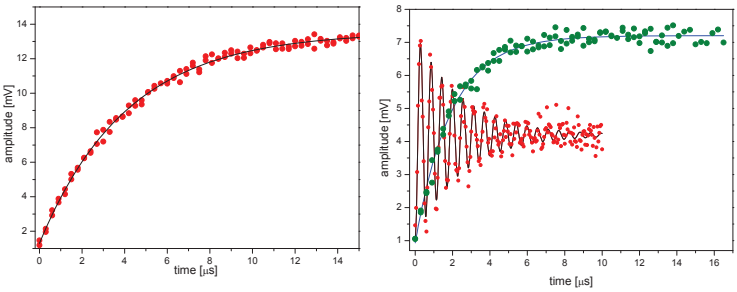

Figure 6.15. Transmon lifetimes. a) Relaxation time measurement when $f_{ge} = 6.18$ GHz giving $T_1 = 4.1\,\mu s$. b) Relaxation time measurement and Ramsey fringes at the ef-resonance giving $T_1 = 1.9\,\mu s$ and $T_2 = 2.4\mu s$

6.2.2.2 Characterizing the transmon lifetimes

Figure 6.15 b shows the relaxation time and Ramsey fringe measurements giving $T_1 = 1.9\,\mu s$ and $T_2 = 2.4\,\mu s$, which is sufficient for manipulating and measuring the individual Fock states at low photon numbers.

6.2.2.3 Spectroscopy of the photon number splitting

The Fock state dependent transitions $f_{\pm,n}$ are found by repeating the same type of spectroscopy, varying the filling $\bar{n}$ to populate the different Fock states. Figure 6.16a shows the peaks at frequencies f_n for $n = -1$, 0, 1, ..., 16, resulting from three values of $\bar{n}$, and reproduce approximately the Poissonian distribution as will be discussed in the next section. In fig. 6.16b the experimentally measured frequencies (orange dots) are compared to the analytical calculations (including 3 transmon levels) from appendix A and to the numerical diagonalization of an effective oscillator-transmon Hamiltonian including also the fourth level of the transmon $|h\rangle$.

Note that the difference between the analytical calculations and numerical diagonalization of the Hamiltonian with three levels is indistinguishable. A fair agreement is observed between the experiment and

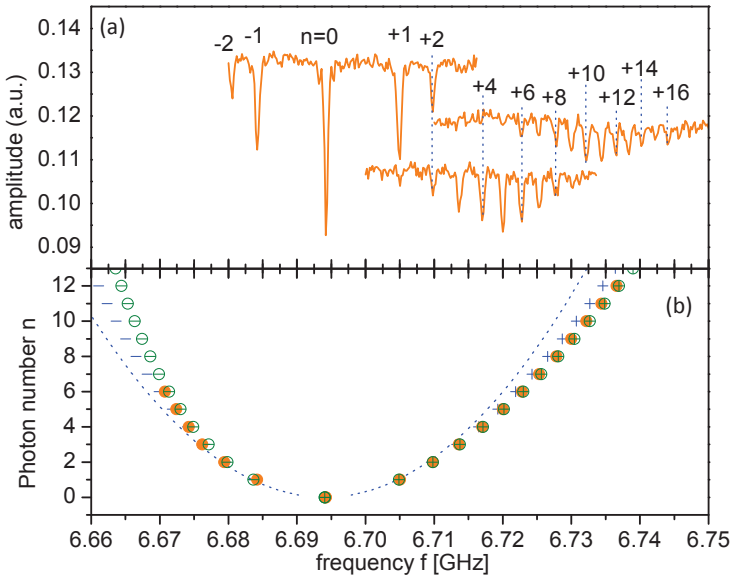

Figure 6.16. Photon number splitting at ef-resonance. a) Transmon excitation spectra around f_{ge} for three different fillings of the storage mode (horizontally shifted for clarity), showing the transitions for f_n with $n \in \{-2, -1, 0, +1, ..., +17\}$. b) Transition frequencies f_n (orange dots) are compared with calculations from appendix A (blue + and - signs) and numerical calculations which include the transmon level $|h\rangle$ (green, circled + and - signs). The dotted line shows $f_{ge} \pm \sqrt{2n}\, g_0$.

the effective four level transmon model where the values of f_0, g_0, g_R, as well as f_{ge}, α are extracted from measurements, and the energy $3f_{ge} - 848\,\mathrm{MHz}$ of level $|h\rangle$ is calculated from g_R and $\tilde{f}_R$.

This shows that the photon number splitting is greater for the + ladder than for the - ladder, which is a consequence of the non-resonant transmon levels $|g\rangle$ and $|h\rangle$.

6.2.3 Measuring the Fock state probabilities

This section contains three calibrations needed to measure accurately the occupation probabilities $p(n)$ of the different Fock states. The height of the photon number peaks when a π pulse is applied need to

be mapped to $p(n)$. In addition to calibrating π pulses with Rabi oscillation, we apply two calibrations. One that scales the readout signal, which varies with the storage mode filling, to $S_n \in [0, 1]$ and another that maps the signals S_n to $p(n)$, taking into account the relaxation of the transmon during the π pulse or the readout.

6.2.3.1 Calibrating π pulses on the $+, n$ transitions

The Rabi rotation on the $+n$ transitions are calibrated at frequencies $f_{+,n}$ for $n = 0, ..., 10$ and a filling $\bar{n} \simeq n$ for each $f_{+,n}$. The Rabi oscillations shown in fig. 6.17a are induced with Gaussian-shaped pulses with a standard deviation $\sigma = 140\,\text{ns}$ and a total length of 6σ, and are varied in amplitude ξ. The amplitudes of the oscillations decrease with n as expected from the Poissonian distribution of the coherent state $|\sqrt{\bar{n}}\rangle$. The Rabi frequencies $\Omega_{\pm,n}$ are show in fig. 6.17b(dots). The Rabi frequencies for $n > 0$ are $\sim\sqrt{2}$ slower than for $n = 0$ because of the hybridized character of the former. For $n = +1, ..., +10$ the Rabi frequency increases slightly. The numerical calculations (circles) capture the change in Rabi frequency between $n = 0$ and $n > 0$. It however predicts decreasing Rabi frequency with n for the + ladder and an increasing Rabi frequency for the - ladder. We have not managed to explain this discrepancy.

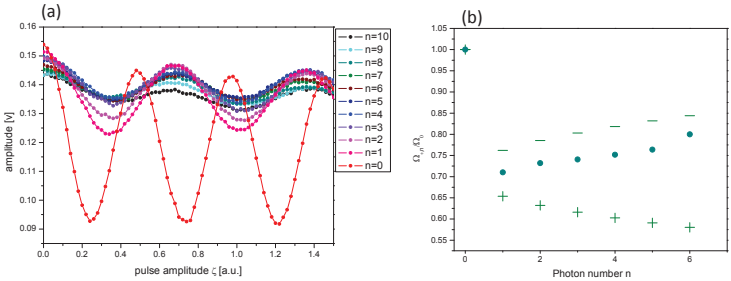

Figure 6.17. Calibration of the Fock state Rabi angles of the $+n$ transitions for $n \in [0, 10]$. a) Rabi oscillations using a Gaussian shaped pulse with varying amplitude ζ. b) The Rabi frequencies $\Omega_{+,n}$ normalized to Ω_0 from measurements (dots), and numerical simulations of $\Omega_{+,n}/\Omega_0$ (+) and $\Omega_{-,n}/\Omega_0$ (-).

6.2.3.2 Calibrating the transmon readout

We refer to the transmitted amplitude $A^{(g)}$ at the top of the readout mode when the transmon is in $|g\rangle$ as the 'base line' (see section 4.1.2). When the population of the storage mode is increased a decrease of the base line is observed, as shown in fig. 6.18. This decrease is due to a cross-Kerr effect making the resonance frequency of the readout mode depend on the state of the storage mode. In any experiment involving both filling of the storage mode and driving of the transmon, this effect is taken into account by measuring first the base line $A^{(g)}$ leaving the transmon in $|g\rangle$, before measuring A in the complete sequence. The signal $S = 1 - A / A^{(g)}$ corresponds thus to the probability of the transmon being excited.

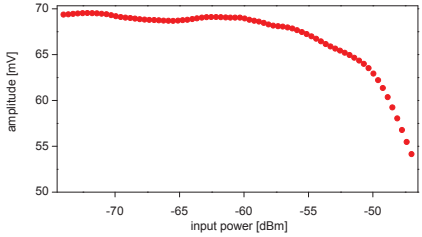

Figure 6.18. Readout base line $A^{(g)}$ as a function of the input power of a continuous drive at the storage frequency $\tilde{f}_0$. Input power of -72.8 dBm corresponds to $\bar{n}$=1.

6.2.3.3 Calibrating the photon number probabilities

The signals $S_{+,n}$ following π pulses on the $+n$ transition are mapped to Fock state occupation probabilities $p(n)$ using the calibration method discussed in section 4.2.1. A 300 ns square pulse is used to create a coherent state $|\beta\rangle$, where $\bar{n} = \beta^2$ is varied over 26 values by changing the pulse amplitude ζ , followed by a π pulse on the frequencies $f_{+,n}$ for $n = 0, ..., 10$. A waiting time $\sim 6T_0$ is taken between each repetition of the measurements to let the field in the storage mode decay. Each point (n, ζ) is averaged over 40000 sequences.

From the calibration we get the filling speed $k = \beta / \zeta = 2.29 V^{-1}$ and the calibration coefficients $c_n = S_{+,n} / p(n)$=$\{0.764, 0.835, 0.847, 0.846, 0.833, 0.854, 0.846, 0.834, 0.847, 0.832, 0.841\}$, for n=0,...,10. The calibrated probabilities $p(n)$ are shown in fig. 6.19 as a function of A. The bottom panel shows the Poissonian distributions $P_{\bar{n}}(n)$ with $\bar{n} = (kA)^2$and probabilities $p(n)$ for a few values of A. The discrepancy between the two is within the 2σ error bars with the standard deviation $\sigma 0.6\%$.

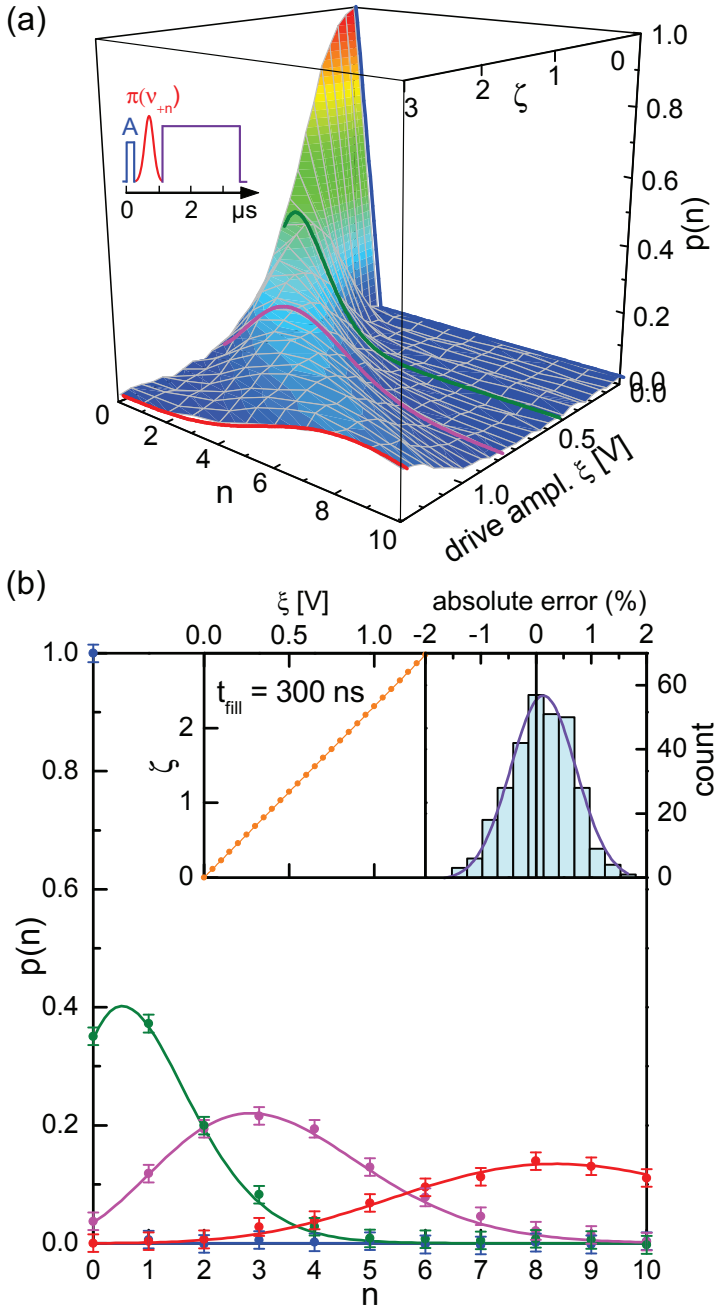
(a)
π(ν+n)
A
0
2
μs
3
2
ζ
1
0
1.0
0.8
0.6
0.4
0.2
0.0
p(n)
0
2
4
6
8
10
n
0.0
0.5
1.0
drive ampl. ξ [V]
(b)
ξ [V]
0.0
0.5
1.0
absolute error (%)
-2
-1
0
1
2
t_fill = 300 ns
ζ
2
1
0
60
40
20
0
count
1.0
0.8
0.6
0.4
0.2
0.0
p(n)
0
1
2
3
4
5
6
7
8
9
10
n

Figure 6.19. Generation and measurement of coherent states $|\beta\rangle$ in the storage mode: a state is obtained from a $0.3\mu s$ long square pules and amplitude ζ at frequency $\tilde{f}_0$; a π pulse on one of the $+n$ transitions then excites conditionally the transmon and the amplitude of the peak $A_{+,n}$ is measured. a) Occupation probability $p(n)$ of Fock state $|n\rangle$ for $n \in [0, 10]$ and for increasing ζ. $p(n)$ is obtained by dividing $A_{+,n}$ by a calibration factor c_n resulting from a fit of the coherent model $\beta(\zeta) = k\zeta$ to the whole dataset. b) $p(n)$ cuts (indicated in a) at $\zeta = 0$ (blue), 0.45 (green), 0.8 (magenta) and 1.3 (red) showing both the measured probabilities $p(n) = A_{+,n} / c_n$ (dots with $\pm 2\sigma$ error bars) and Poissonian distributions with expectation values β^2. The left inset confirms the linear increase of β with ζ and yields the top scale of panel a. Residual error between data and fir are homogeneously distributed over the whole dataset (similar to the example shown in chapter 4) in a Gaussian manner with a standard deviation $\sigma = 0.6\%$ and a shift of 0.1% (right inset). Lower inset is the reconstruction of the Wigner function of a targeted state $\left|\beta = -\sqrt{5} + i\sqrt{2}\right\rangle$ using the tomography and maximum likelihood method.

With the c_n coefficients giving access to $p(n)$, a full characterization of the mode can be performed using one of the quantum state tomography methods of section 4.2.2.

6.2.4 Non-linearities of the storage mode

We now demonstrate experimentally the low Kerr factor at the ef-resonance. With $g_0 = 7.45$ MHz and $\alpha = -261$ MHz eq. 2.105 gives a Kerr factor $K_{ef} = -346$Hz per photon. However, when diagonalizing numerically the Hamiltonian of the system including $|h\rangle$, the Kerr effect is found to be even smaller, depend on n, and to chancel and revers sign at about 20 photons. Because this ultra-small Kerr effect is much slower than the relaxation time $T_0 = 54\,\mu s$ it is very difficult to measure dynamically, by either recording the trajectory of a field in phase space as in [51][27], or the power dependence of the resonance line shape at short times as in the supplementary material of [27]. Consequently, we simply measure the steady-state power transmission spectrum $P_2(f)$ around $\tilde{f}_0$ for several input powers P_1, using the VNA with measuring bandwidth of $1\text{kHz} \ll 1/T_0$. The corresponding curves are shown in fig. 6.20 a (dots) in arbitrary units of the transmitted power P_2 (left scale).

Analyzing quantitatively the dataset requires a precise knowledge of the average photon number $\bar{n}$ in the storage mode as a function of

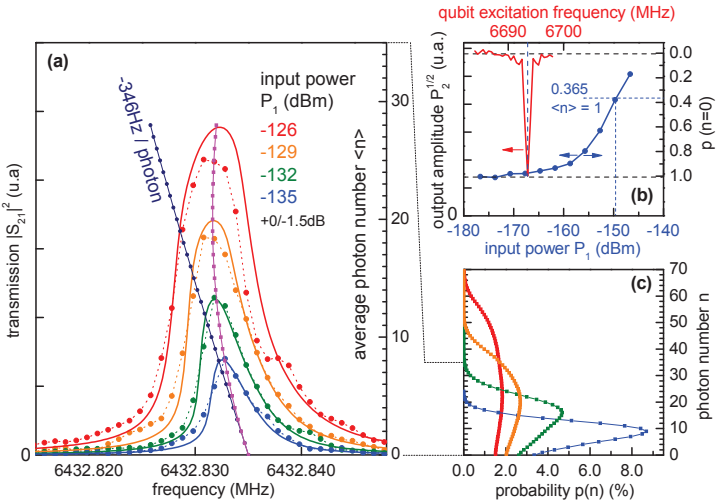

Figure 6.20. Steady-state non-linearities of the storage mode in the ef- resonant condition. a) Transmitted power (in linear units) measured with the VNA (dots joined be dotted lines) for input powers P_1 varying from -135 dBm to -126 dBm by steps of 3 dB. Solid lines are the steady-state average photon number $\bar{n}$ in the storage mode simulated numerically for the same P_1 values according to calibration,{ and for(where?) $P_1 = -149.6$ dBm ($\bar{n} = 1$) at resonance}. The non-linearity in frequency calculated with 4 transmon levels (magenta line) is smaller that the -346 Hz/photon Ker constant (dark blue line). A large non-linearity in power is however observed (see text). b) Calibration of P_1 versus $\bar{n}$. Red: Spectroscopy of the $|g0\rangle \rightarrow |e0\rangle$ transition with a calibrate π pulse and no filling in the storage mode. Blue: measurement of the transmission signal at f_{ge} (vertical blue dashed line), indicating the occupation probability $p(0)$, as the storage mode is filled with a continuous drive at increasing power P_1. The average photon number $\bar{n}$ reaches 1 when $P_1 = -149.6$dBm (thin blue dashed line). c) Simulated photon number distributions $p_\infty(n)$ at the top of each simulated resonance of panel a. Note the 0.25 scaling factor for $\bar{n} = 1$

f and P_1. This precise knowledge is difficult to obtain, first because of the very weak coupling between the input and output ports, and second due to the large systematic errors of 1.5 dB and 3 dB on the transmission of the input and output lines respectively. Therefore further in-situ calibration and data analysis is performed: using the modulation-demodulation setup (see chapter 3), a continuous tone is applied at $\tilde{f}_0$ at varying powers P_1 and the occupation probability $p(0)$ of the vacuum

measured, as shown in fig. 6.20b. Assuming a Poissonian distribution, $\bar{n} = 1$ when $p(0) = 0.365$ which corresponds to a nominal value $P_{1,1} = -149.6$ dBm.

Then quantum simulations of the storage mode coupled to the effective 4 level transmon are performed using the QuTiP python toolbox[25], the already mentioned parameters and the experimentally calibrated P_1. The solid lines on fig. 6.20a show the simulated transmission spectra for values of $\bar{n}$ corresponding to P_1, using the steady-state solver of QuTiP. By scaling vertically the experimental curves such that the simulation and experiment match for $P_1 = -135$ dBm, we obtain a fair agreement for all curves, leading to the following results: First, the resonance lines display indeed a very small Kerr effect, with a shift towards lower frequency with increasing P_1 that is significantly smaller than K_{ef} (oblique dark blue line), and changing sign between $\bar{n} = 15$ and 25, in good agreement with the calculated shift (magenta line). A second and unanticipated result is that although the non-linearity in frequency is small, a large non-linear in input power is observed, with P_2 and $\bar{n}$ increasing by only a factor 3 when P_1 is increased by a factor 8.

Simulating the time evolution of the system initialized in its ground state and then driven coherently at $\tilde{f}_0$ reveals the cause of this non-linearity: due to the small hybridization of the storage mode with the transmon (see appendix A), and the finite lifetimes (T_1, T_2) of the latter, the field starts perfectly coherent at the beginning of the dynamics and slowly becomes incoherent when approaching the steady state. The decoherence speed increases with $\bar{n}$ as illustrated in fig. 6.20 c where the photon number distribution $p_{P_{1,\infty}}(n)$ obtained from the steady state solver at the top of each resonance curve of fig. 6.20 a: although $p_{P_{1,\infty}}(n)$ corresponds almost exactly to the Poissonian distribution at times scales relevant for the calibration discussed in the last section, the distribution becomes increasingly non-Poissonian for larger $\bar{n}$. This means that large coherent states can only be obtained at times shorter than a few tens of T_2, which was the case in the previous section where the total operation sequence (create state+tomography) was $t \simeq 3T_2/5$.

6.3 Measuring the Wigner function

As mentioned in section 4.2.2 the Wigner function at point β in phase space can be directly measured by a displacement $D(-\beta)$ and a parity

measurement of the field (eq. 4.4) using two different methods. These method are here implemented with a truncation at 10 photons i.e. with truncated parity operators

$$P' = \sum_{n=\text{even}}^{n=10} p(n) - \sum_{n=\text{odd}}^{n=10} p(n) \tag{6.1}$$

and

$$P'' = 1 - 2 \sum_{n=\text{odd}}^{n=10} p(n). \tag{6.2}$$

In the first case the $p(n)$ are measured separately using the method described above in section 6.2.3. In the second case the odd photon number states are excited simultaneously up to n=9 with superimposed Gaussian pulses. The selectivity of these pulses is limited by their Gaussian frequency distribution and off-resonant driving. We test this selectivity by driving Rabi oscillations on $|g0\rangle \rightarrow |e0\rangle$ with the storage mode in $|n = 0\rangle$, while at the same time applying the off-resonant superimposed pulses at frequencies $f_{+,n}$ for $n \in \{1, 3, 5, 7, 9\}$. Figure 6.21 shows the Rabi oscillations with and without the off-resonant tones. The additional tones disturb the Rabi oscillations significantly after 1.5 periods. However, by having alternate phases, i.e. a π phase for $n \in \{3, 7\}$, the disturbance after a π pulse is small.

Since the parity should not reveal the photon number and the photon number signals $S_{+,n}$ are different, we use different Rabi angles ϕ_n on each transition $+n$ to ensure the indistinguishability. More precisely the ϕ_n are adjusted to give equal signals $S_{+,n}(\phi_n) = \min_n(S_{+,n})$.

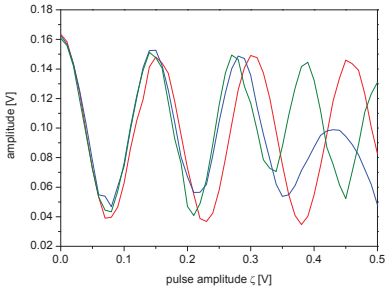

Figure 6.21. Influence of off-resonant driving. Rabi oscillations with a single tone at f_{ge} drives the $|g0\rangle \rightarrow |e0\rangle$ transition (red). Adding frequency tones at $f_{+,n}$ for $n \in \{1, 3, 5, 7, 9\}$ disturbs the Rabi oscillations (blue). The off resonant effect is reduced by having an opposite phase π for $n \in \{3, 7\}$ (green.)

The two truncated-parity measures are tested on the vacuum state as shown in fig. 6.21a, where dots are the measured values and the lines are calculated values from eqs 6.1 and 6.2. The truncated parity measures follow the expected Gaussian decrease in $\sqrt{n}$ with a half-width at half-maximum of $1/\sqrt{2}$, but only up to $\sqrt{n} \simeq 2.5$ where errors occur.

We use the parity measure P'' to map the Wigner function of the vacuum state, pixel by pixel, as shown in fig. 6.21b. This measurement consisted in 2500 measurements in phase space which is significant over sampling for state defined by 63 real numbers in an 8 dimensional Hilbert space. The yellow color at the corners of the graph shows the effect of the truncation. As a comparison the Wigner function in fig. 6.21c is reconstructed using the maximum likelihood method discussed in section 4.2.4, with 5 displacements β and $n \in [0, 4]$. The density matrix ρ, in a Hilbert space truncated to 10 photons using the maximum likelihood algorithm.

These two method will also be used in chapter 7 to observe the quantum Zeno dynamics of the field

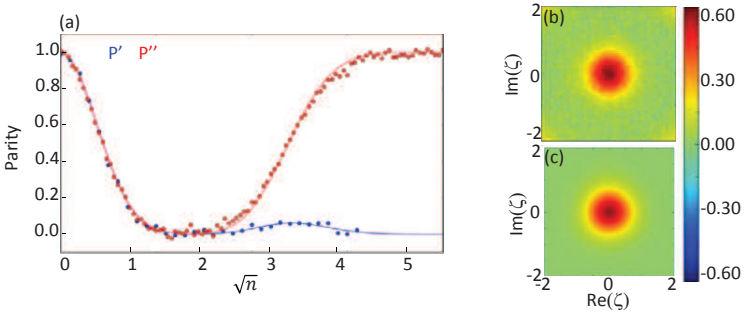

Figure 6.22. Truncated parity measures and measured Wigner functions. a) The two parity measure P'(blue) and P''(red) applied to the vacuum state. The measurements (dots) behave as calculations predict (lines) and give correct measures of the parity up to $\sqrt{n} \sim 2.5$, where the truncation starts to have an effect. b) Measurement of the Wigner function using P''. c) Reconstruction of the Wigner function from measurements using the maximum likelihood method.

Chapter 7

Experimental observation of quantum Zeno dynamics

With all the tools described in the previous chapters in place, we show in this last chapter the QZD in our ef-resonant system, where a continuous blocking tone at $f_{+,n}$ for $n \in \{2, 3, 4\}$ compartmentalizes Hilbert space into $\mathcal{H}_{<n}$ and $\mathcal{H}_{>n}$. This separation is represented by an an exclusion circle (EC) in phase space. We investigate the dynamics under a continuous drive of the storage mode at frequency f_0. The first section shows how the drive strengths at f_0 and $f_{+,n}$ are chosen. The second section shows QZD confined inside the exclusion circle (EC) corresponding to $n=3$ or $n=4$, and compares the experimental results with numerical simulations taking into account the different decoherence channels. The last section shows two cases of a state being prepared outside the EC at $n=2$, and colliding with it either head on or tangentially. Lastly, we summarize some of the experimental work on QZD done by other groups during the thesis period.

7.1 Probing the Zeno blockade strength

Our QZD protocol consists in applying simultaneously a Zeno blocking tone at a particular frequency $f_{+,n}$, and a coherent drive to the storage mode at $\tilde{f}_0$, as shown in fig. 7.1. Square pulses with Gaussian rise and fall are used to limit their frequency spread. The Gaussian

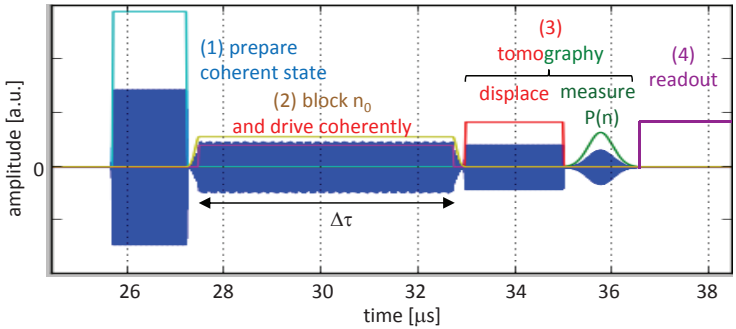

Figure 7.1. Pulse sequence for inducing the QZD and subsequent tomography of the field in the storage mode. The different steps are indicated on the graph. The empty pulses in colors represent the pulse envelopes. The dense blue filling represents the product of the envelopes with the IF frequency used to generate the actual microwave pulses using heterodyne modulation.

ends are truncated at 3σ, with $\sigma = 80\,\text{ns}$ and $10\,\text{ns}$ for the blocking and filling pulses, respectively. The pulses are aligned such that the plateaus are reached simultaneously, which ensures the storage mode is never driven in the absence of a blocking tone.

In order to probe the blocking strength, we start with the storage mode in the vacuum state, (no step 1) and displace the dimensionless field ζ in the IQ-plane (see section 4.2.3) at a constant rate $\dot{\zeta} = 0.27\,\mu s^{-1}$ for up to $30\,\mu s$, while applying a blocking tone at $n = 3$ with a Rabi frequency $\Omega_{+,3}/2\pi$ varying from 0 to $2\dot{\zeta} = 0.54$ MHz. The Fock state occupation probabilities $p(n)$ for $n \in \{0, ..., 4\}$ are then measured, see fig. 7.2. At low Rabi frequency the monitored photon number states are gradually populated with maximas at times $\sim$0, 4, 6, 7.5, 8.5 μs and remain empty after that. This evolution of the Fock state populations is expected in the absence of Zeno blockade. At Rabi frequency $\Omega_{+,3}/2\pi \simeq \dot{\zeta} = 0.27\,\mu s^{-1}$, an oscillation in the population of the Fock states $|0\rangle$, $|1\rangle$ and $|2\rangle$ with a period of about $15.5\,\mu s$ gradually appears, meanwhile the population of $|3\rangle$ and $|4\rangle$ is suppressed. The oscillation and suppression become gradually clearer as the Rabi frequency reaches $\Omega_{+,3}/2\pi = 2\dot{\zeta}$. The period of the oscillations decreases towards the asymptotic Zeno period $T_z = 2\pi/\sqrt{3}\,\dot{\zeta} \simeq 14\,\mu s$ expected from a coherent drive in a Hilbert space truncated to three levels.

The 'transmission' $\mathcal{T} = 1 - \Sigma_{n=0}^{2} p(n)$ across the EC after one period

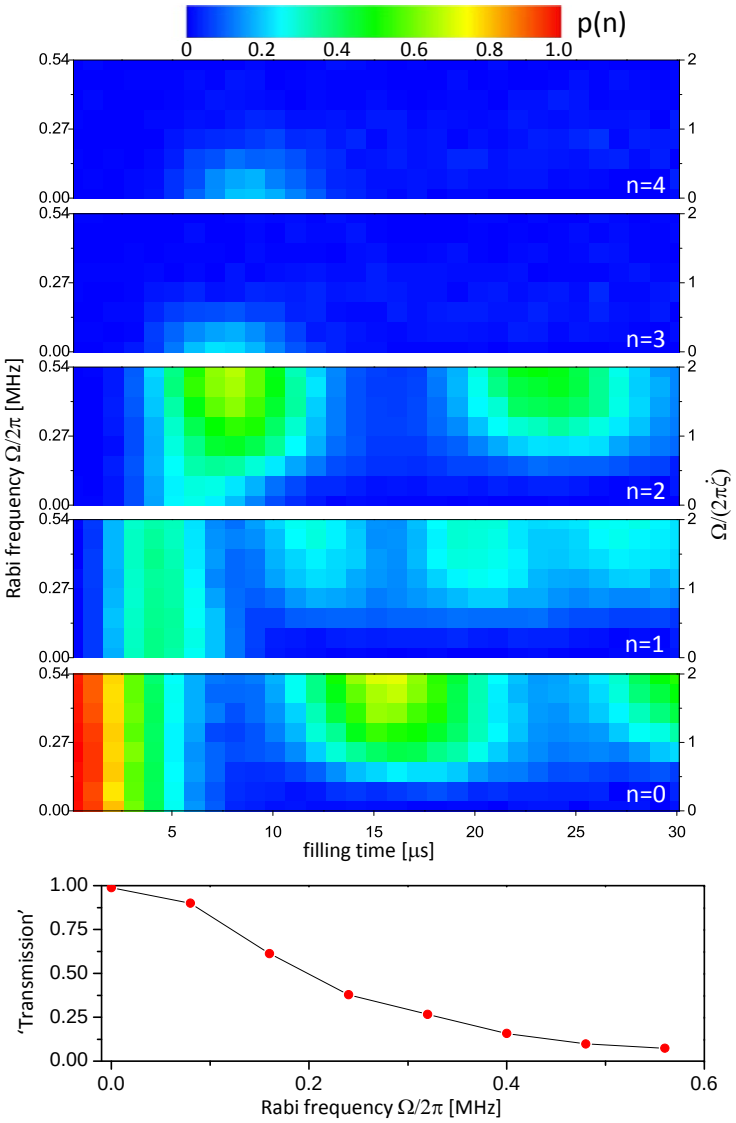

Figure 7.2. Probing the Zeno blocking strength on Fock state $|n = 3\rangle$. a) Occupation probabilities $p\,(n)$ for $n = 0, ..., 4$ as a function of the filling time at a fixed filling rate $\dot{\zeta} = 0.27\,\mu s^{-1}$, and of the blocking strength $\Omega_{+,3}$ at frequency $f_{+,3}$. b) Loss of population inside the EC $\Sigma_{n=0}^{2} p(n)$ after one period ('transmission'), as a function of blocking strength $\Omega_{+,3}$.

is reduced down to 7% when blocking at the maximum strength $\Omega_{+,3}/2\pi = 0.54\,\text{MHz}$, as shown in fig. 7.2b. This transmission decreases down to 7%, a value close to the 5% obtained from simulations described later in this chapter. Using a higher Rabi frequency would further reduce the transmission and improve the blockade of Fock state $|3\rangle$, but at the expense of also blocking $|2\rangle$ partially, as we discuss now.

The $f_{+,2}$ and $f_{+,4}$ transition frequencies are $\delta_{+,2} = 3.9$ MHz and $\delta_{+,3} = 3.3\,\text{MHz}$ away from the blocking frequency $f_{+,3}$ (see fig. 6.16). These transitions are thus off-resonantly driven around a vector of the $\{|gn\rangle, |+n\rangle\}$ Bloch sphere at an angle $\theta_n = \arctan(\Omega_{+,3}/\delta_{+,n})$ with the z-axis (see section 2.2.2.3). These angles are 8° and 9° for $n = 2$ and 4, and would correspond to a population transfer from $|g2\rangle$ to $|+2\rangle$ up to 14% in absence of cavity drive ($\dot{\zeta} = 0$). In presence of drive during the QZD, the population of $|+2\rangle$ is however much lower (a few percent) as simulations will show.

To emphasize this off-resonant drive effect, we perform another experiment exaggerating the effect. Instead of varying the amplitude of the blocking tone, we keep it fixed at the same maximum value as before and sweep its frequency f between $f_{+,2}$ and $f_{+,4}$ (see fig. 7.3). The white dashed lines indicate the Zeno blockades at the exact frequencies $f_{+,n_{\text{block}}}$ with $n_{\text{block}} \in \{2,3,4\}$, with increasing Zeno periods. In between, when blocking at intermediate frequency $(f_{+,2} + f_{+,3})/2$ or $(f_{+,3} + f_{+,4})/2$, the blockade is suppressed substantially but not completely: oscillations in $p(n)$ remain up to ∼30% due to off-resonant driving (and partial blocking) of the adjacent transitions. The off-resonant driving effect at these intermediate frequencies, although exacerbated, confirms that it is detrimental to increase the blocking strength further.

The filling rate $\dot{\zeta} = 0.27\,\mu s^{-1}$ used here yields about two Zeno period in $30\,\mu s$, a time of the order T_{cav}. Since slowing down the filling would lead to fewer Zeno periods during the cavity lifetime, we choose to keep this filling rate for the next experiment. We also keep the maximum Zeno blocking strength $\Omega_R/2\pi = 0.54$ MHz, since it balances the few percent off-resonant population of $|+2\rangle$ against the 5-7% leak through the EC.

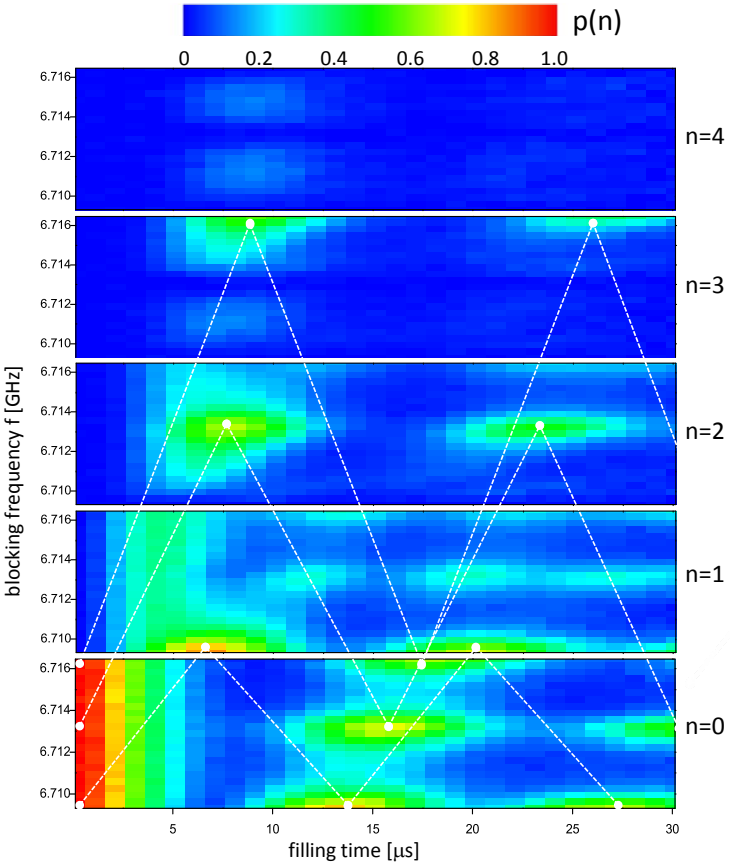

Figure 7.3. Occupation probabilities $p\,(n)$ for $n=0,...,4$ as a function of the filling time at a fixed filling rate $\dot{\zeta}=0.27\mu s^{-1}$, and blocking frequency f at a fixed amplitude (yielding $\Omega_{+,3}/2\pi=2\dot{\zeta}$). The white dashed lines indicate the oscillations in $p(n)$ when blocking at the proper frequencies $f_{+,2}$, $f_{+,3}$ or $f_{+,4}$. Midway between these frequencies the blockade does not go to zero and the population of the vacuum state returns once to $\sim$30%.

7.2 QZD inside an exclusion circle

The full description of the cavity field evolution will be presented here in the form of the Wigner function. Then we will analyse the evolution of $p(n)$ by simulating the evolution numerically.

7.2.1 Wigner function snapshots of confined QZD

Having chosen the blocking and filling strengths, we induce the quantum Zeno dynamics of the storage mode field confined inside the EC with a radius $|\zeta| = \sqrt{3}$. The Wigner function of the field is obtained at different times through out a $30\,\mu s$ period (two Zeno periods), using Wigner tomography with the truncated parity measure P'' discussed in section 6.3. Figure 7.4a shows snapshots of the evolution every quarter-period The amplitude increases along the positive real axis until it reaches the EC and a sharp phase inversion occurs. Thereafter the state returns back to the origin, completing one period. At half-integer periods a 'cat-like' state is observed with two components located at at $\zeta \simeq \pm 1.1$, with fringes in the center indicating a coherent superposition of the two components. Cross sections of the Wigner function along the white dashed lines in fig. 7.4a are plotted in fig. 7.4b. These curves show the negative parts of the Wigner function, reaching -0.23 and -0.19 after half a period, and -0.09 and -0.03 after 1.5 period. After two periods the amplitude maximum is again centered at the origin but with a smaller value, and a bigger spread of the state. We attribute this deformation to limited coherence times $T_{\text{cav}} = 47\,\mu s$ ($Q_0 = 1.9$ M), $T_1 = 1.9\,\mu s$, and $T_\varphi = 9\,\mu s$ in this second experimental run.

Artifacts due to the truncated parity measure P'' appear as artificially high values of W in the corners of the frames in fig. 7.4a. We thus turn to the maximum likelihood method (maxlike) presented in section 4.2.4. By the time this was implemented, the experiment was in its third run with $T_{\text{cav}} = 39\,\mu s$ ($Q_0 = 1.6$ M), $T_1 = 1.6\,\mu s$, and $T_\varphi = 9\,\mu s$.

Figure 7.5 shows a repetition of the same experiment, with the new sample parameters and using the maxlike method. The shorter lifetimes result in a faster decay of the Zeno dynamics, shown by the diminished negative values of the Wigner function: Compared to the ideal Zeno dynamics shown in section 2.3.1, we also observe an asymmetry of the Wigner function, with a higher amplitude at $Q > 0$ visible

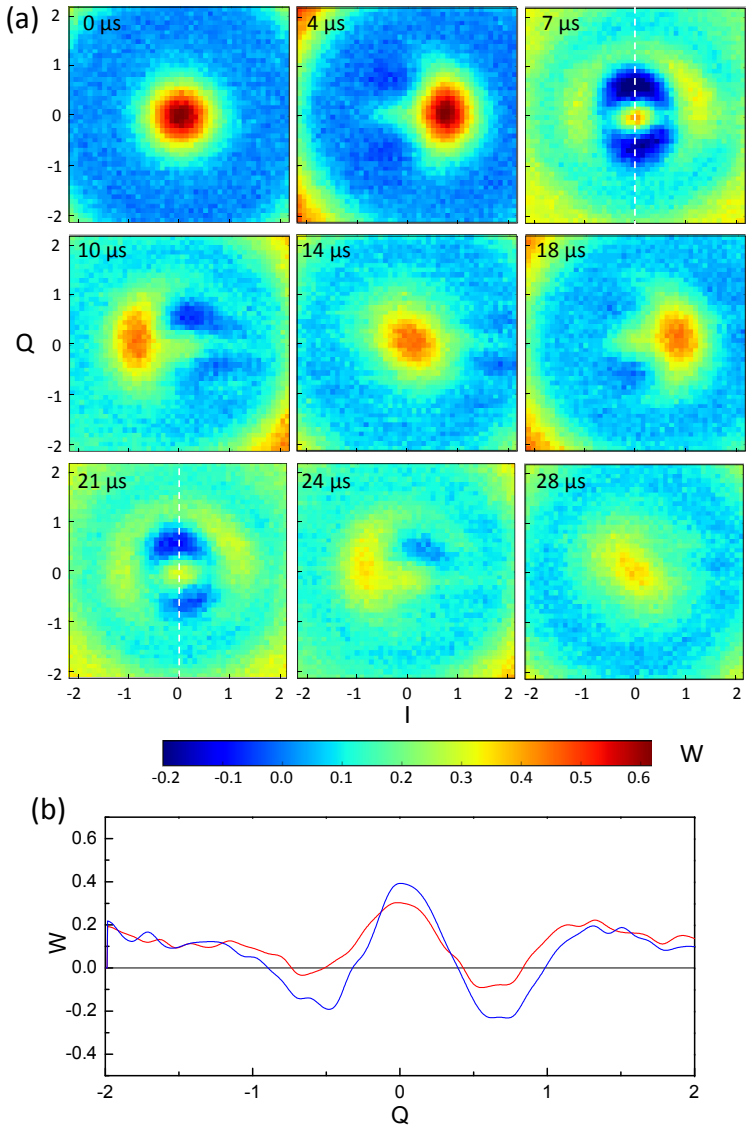

Figure 7.4. Measured QZD of the field initially in the vacuum state, confined inside the exclusion circle of radius $\sqrt{3}$ (blockade on n=3), and recorded using the parity measure P''. a) Snap shots of the Wigner function taken every quarter-period, at times indicated in each frame. b) Cross section of the Wigner function along the white dashed lines at $7\,\mu s$ (blue, 0.5 period) and $21\,\mu s$(red, 1.5 period).

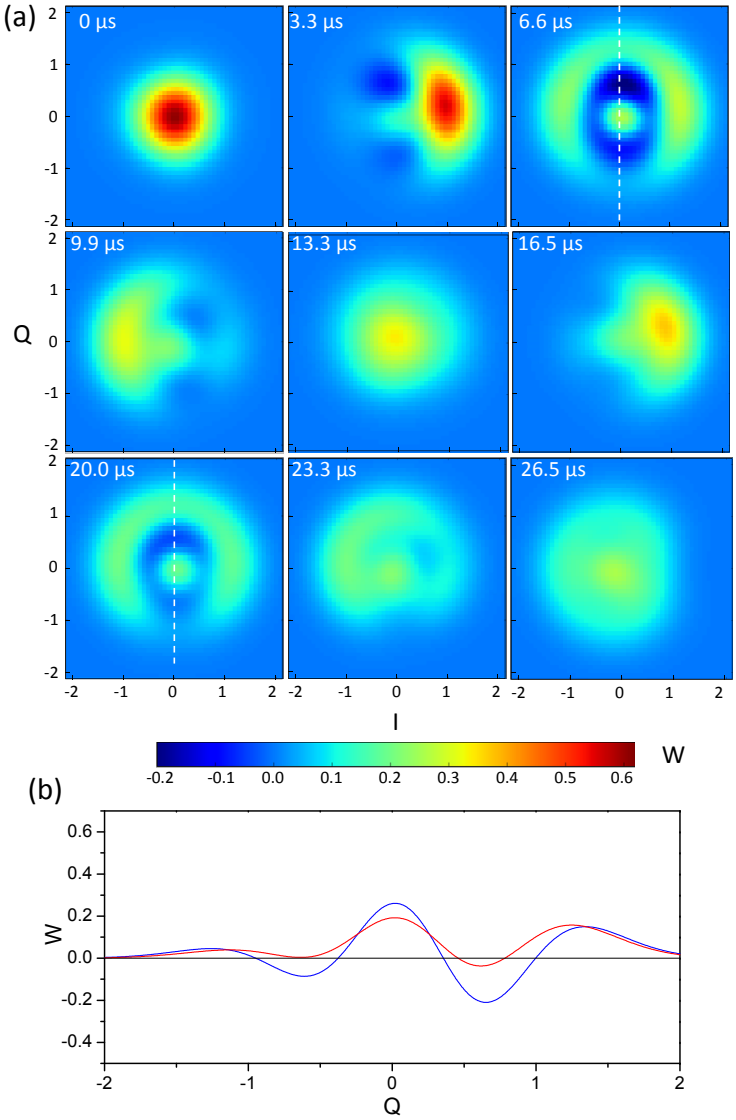

Figure 7.5. Measured QZD of the field initially in the vacuum state, confined in the exclusion circle of radius $\sqrt{3}$ (blockade on n=3), and reconstructed with the maxlike method from section 4.2.4. Here $p_{n,\beta}$ is measured for $n \in \{0, 1, 2, 3\}$ and $\beta \in \{0, 1, -1, i, -i\}$, and the reconstructed density matrix is 4×4. a) Snap shots of the Wigner function taken every quarter-period, at times indicated in each frame. b) Cross section of the Wigner function after 0.5 (blue) and 1.5 (red) periods.

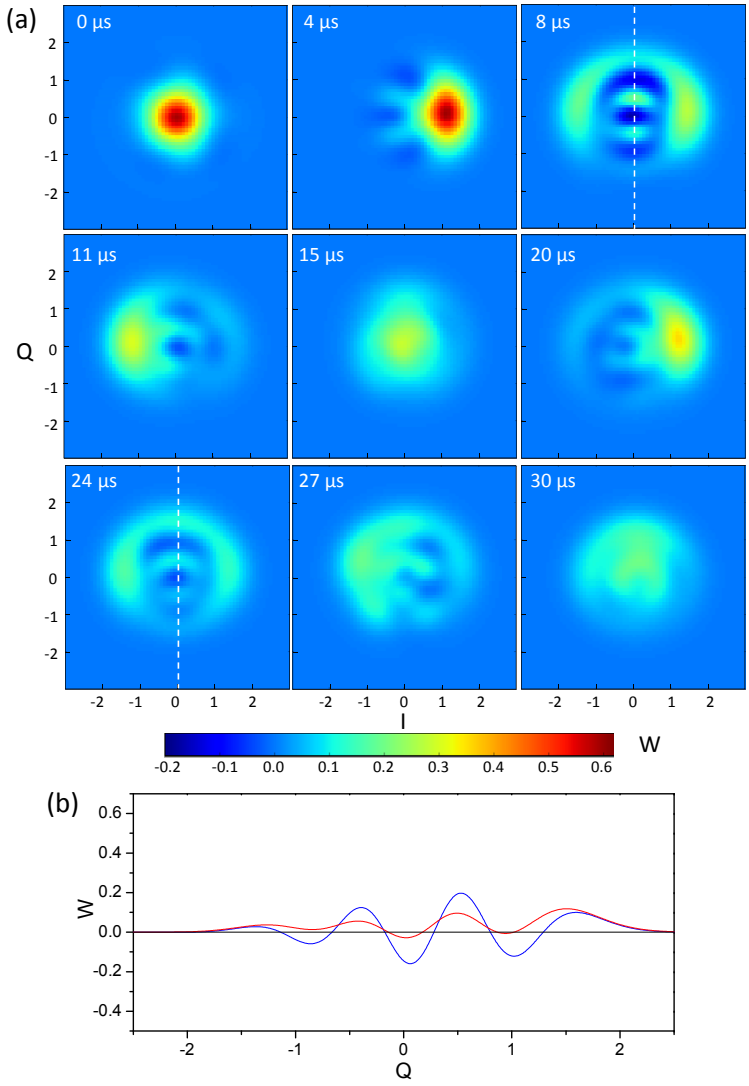

Figure 7.6. Measured QZD of the field initially in the vacuum state, confined in the exclusion circle of radius 2 (blockade on n=4), and reconstructed with the maxlike method. Here $p_{n,\beta}$ is measured for $n \in \{0, 1, 2, 3, 4, 5\}$ and $\beta \in \{0, 1, -1, i, -i\}$, and the reconstructed density matrix is 6×6. a) Snap shots of the Wigner function taken every quarter-period, at times indicated in each frame. b) Cross section of the Wigner function after 0.5 (blue) and 1.5 (red) periods.

at half a period.

The QZD with a blockade on n=4 is shown in fig. 7.6. The same drive amplitude is used as for the blockade on $n=3$ and gives approximately the same Rabi frequency $\Omega_{+,3} \simeq \Omega_{+,4}$. At half integer periods the state is in a superposition of amplitudes $\zeta = \pm 1.5$ and fringes with three minima lie between them. At half a Zeno period the minimas all reach negative values but are strongly reduced one period later.

In prevision of comparing the measured dynamics with simulation, we record the data at smaller time intervals for the same confined dynamics as in fig. 7.5 (blockade at n=3). Instead of measuring the full density matrix, which is time consuming, we only measure the photon number probabilities $p(n)$ for $n = \{0, 1, 2, 3, 4\}$. The results, plotted in fig. 7.7 (dots), show a Zeno period of about $13.5\,\mu s$ and a 5% transmission per period.

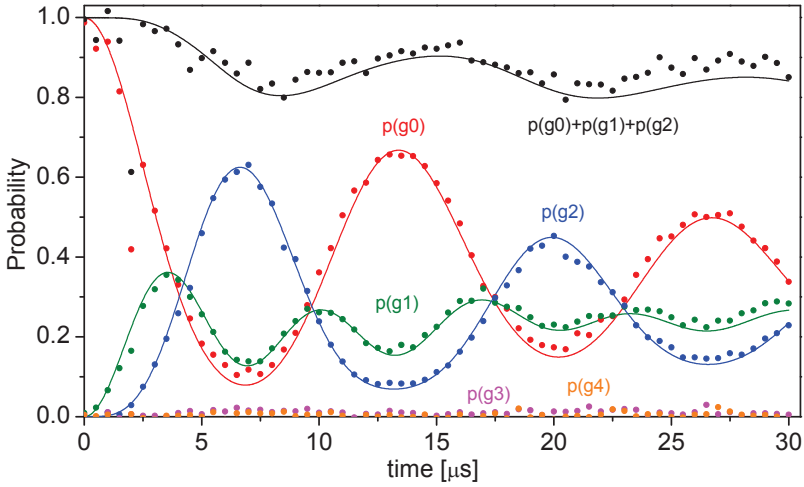

Figure 7.7. Evolution of the measured (dots) and simulated (lines) probabilities $p(n)$ during the QZD of the field initially in the vacuum state, and confined inside the exclusion circle with radius $\sqrt{3}$ (blockade on n=3).

7.2.2 Simulating the QZD of our transmon oscillator system

To understand the dynamics and identify the effect of the different decoherence channels we now simulate the QZD.

7.2.2.1 The model

We model our system as a harmonic oscillator truncated to 30 levels coupled to a three level transmon with the transition ω_{ef} resonant with the oscillator. The Hamiltonian of the system is

$$H = H_0 + H_c + H_{\mathrm{dr}}, \tag{7.1}$$

where the three terms are the free, coupling, and drive Hamiltonians respectively. In the lab frame these three Hamiltonians write

$$\begin{aligned} H_0 &= f_0 a^\dagger a + (f_0 - \alpha)|e\rangle\langle e| + (2f_0 - \alpha)|f\rangle\langle f| \\ H_c &= g_0[a_q a^\dagger + a_q^\dagger a], \\ H_{\mathrm{dr}} &= \varepsilon_{\mathrm{fill}} \cos(2\pi f_0 t)(a + a^\dagger) + \varepsilon_s \cos(2\pi f_{+,s} t)(a_q + a_q^\dagger) \end{aligned} \tag{7.2}$$

with $a_q = |g\rangle\langle e| + \sqrt{2}|e\rangle\langle f|$ and $f_{+,s} = f - \alpha + \sqrt{2}s\, g_0$. Going to the "rotating" frame applying the unitary transform $U = \exp(-i H_0' t/\hbar)$, with

$$H_0' = f_0 a^\dagger a + (f_{+,s})|e\rangle\langle e| + (f_0 - f_{+,s})|f\rangle\langle f|, \tag{7.3}$$

the terms of the Hamiltonian become

$$\begin{aligned} H_0^{\mathrm{rot}} &= -\sqrt{2}s\, g_0(|e\rangle\langle e| + |f\rangle\langle f|), \\ H_c^{\mathrm{rot}} &= -\sqrt{2}\, g_0(|e\rangle\langle f|a^\dagger + |f\rangle\langle e|a) \\ H_{\mathrm{dr}}^{\mathrm{rot}} &= \frac{\varepsilon_{\mathrm{fill}}}{2}(a + a^\dagger) + \frac{\varepsilon_{\mathrm{block}}}{2}(a_q + a_q^\dagger) \end{aligned} \tag{7.4}$$

where terms rotating at $2f_0$, $f_0 + f_s$ and $f_0 - f_s$ and averaging to zero have been neglected, as well as the far off-resonant coupling to the $|g\rangle \to |e\rangle$ transition.

The Hamiltonian is encoded in the tensorial basis $|q\rangle \otimes |n\rangle$ with the transmon levels $q \in \{g, e, f\}$ and oscillator Fock states $n < 30$. We model the dynamics of the density matrix ρ under H with the Lindblad master equation [23]

$$\dot{\rho}(t) = -\frac{i}{\hbar}[H, \rho] + \sum_n \frac{1}{2}[2C_n \rho C_n^\dagger - \rho C_n^\dagger C_n - C_n^\dagger C_n \rho], \tag{7.5}$$

where $C_n \in \left\{\sqrt{\Gamma_{\text{cav}}}a,\ \sqrt{\Gamma_1}a_q,\ \sqrt{\Gamma_\varphi}a_q^\dagger a_q\right\}$ are the collapse operators corresponding to the cavity decay, the transmon relaxation and the transmon dephasing.

7.2.2.2 Simulated evolution of $p(n)$ using QuTiP

The Lindblad equation is integrated using the *mesolver* (master equation solver) of the Python quantum toolbox QuTiP [25]. Prior to integration, the eigenstates of the Hamiltonian $H_0 + H_c$ are obtained and identified as the $|qn\rangle$ with $q \in \{g, +, -\}$ (eigenstates of our ef-resonance scheme). During integration QuTiP follows either the full density matrix or the occupation probabilities $p(qn) \equiv \text{Tr}(\rho|qn\rangle\langle qn|)$ of the $|qn\rangle$ states. These simulations best fit the data when using the parameters $g_0/2\pi = 7.5$ MHz, $\varepsilon_{\text{fill}} = 0.28\,\mu s^{-1}$ and $\varepsilon_{\text{block}} = \sqrt{2}\,\pi 0.54$ MHz, very close or equal to the measured values $g_0 = 7.45$ MHz, $\varepsilon_{\text{fill}} = 0.27\,\mu s^{-1}$ and $\varepsilon_{\text{block}} = \sqrt{2}\,\pi\,0.54$ MHz. For the decay parameters we take the run 3 values $T_1 = 1.6\,\mu s$ and $T_\varphi = 9\,\mu s$ mentioned above, and a cavity life time $T_{\text{cav}} = 35\,\mu s$ directly measured at the ef-resonance. The evolution is also simulated without any decay, as well as with each decay channel individually (i.e. finite T_{cav}, T_1 or T_φ).

All simulations of the $\{p(qn)\}$ for blockade at Fock state $|n = 3\rangle$ are shown in fig. 7.8. In absence of any of the three decay channels (top left panel), the $p(qn)$ oscillate as expected for ideal QZD except for a spurious population of $p(+3)$ of 7% at half integer periods. This is due to the imperfect blockade allowing a small population of $|g3\rangle$, which is then immediately transfered to $|+3\rangle$. By increasing the ratio $\varepsilon_{\text{fill}}/\varepsilon_{\text{blcok}}$ by 2 (top right panel) the population $p(+3)$ is reduced to 1.7%. Another discrepancy with the ideal QZD is that $p(g1)$ does not reach zero at half integer periods. This is due to off-resonant driving of the $|g2\rangle \to |+2\rangle$ transition. This is evidenced by $p(g1)$ being much larger when the

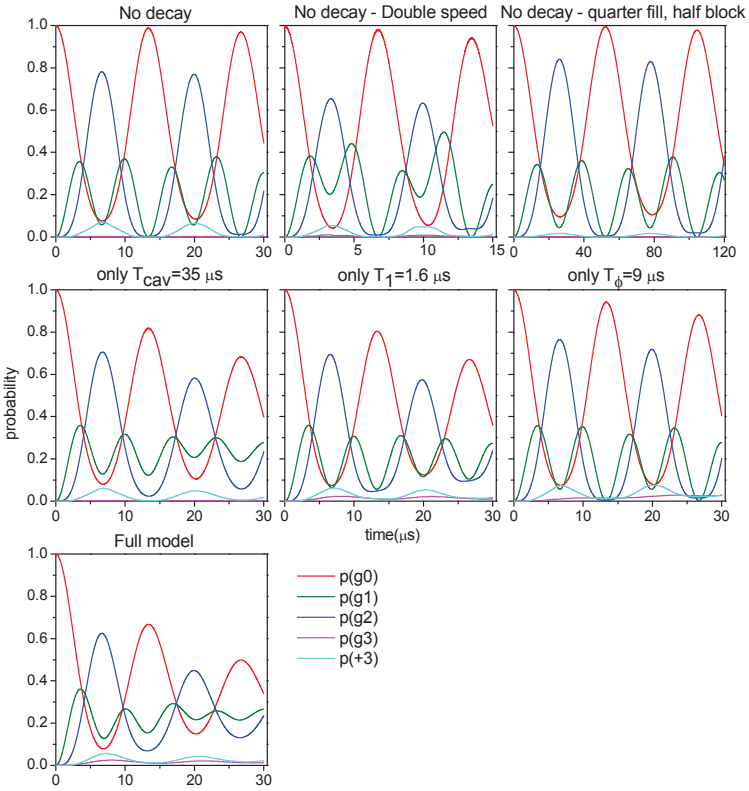

Figure 7.8. Simulation of the occupation probabilities $p(qn)$ as indicated, for the confined QZD with blockade at $n = 3$. Simulations based on the experimental parameters are performed without decay channels (top row), individual decay channels (middle row), and the full model (bottom panel). The first row compares the blocking and filling strengths used in the experiment (left) with stronger (center) ore weaker values.

blocking strength is doubled at a constant ratio $\varepsilon_{\rm fill}/\varepsilon_{\rm blcok}$ (top-center panel), and by the lower value when the blocking strength is divided by 2 (top-right panel). The dynamics shown in the top-right panel is closer to the ideal QZD but operating at these parameters would have required a much longer cavity lifetime.

Sticking to the drive strengths used in the experiment, we now

include the different decay channels individually (see middle row). A decay in the oscillations is observed, with a damping in $p(g0)$ of 32, 33 and, 12% after two periods due to the cavity decay, transmon relaxation and transmon dephasing, respectively. We deduce that the contributions of cavity losses and transmon relaxation to QZD decoherence are about the same in our experiment. The vulnerability to transmon relaxation is due to the spurious population $p(+3)$ mentioned above, and is thus reduced with a stronger blockade, as confirmed by simulation (not shown).

Lastly, the evolution is simulated with all decay channels (bottom panel) and fits well the measurements, as shown in fig. 7.7.

7.2.2.3 Wigner function of the simulated QZD

The Wigner function of the simulated evolution is also reconstructed at every quarter-period as for the data in section 7.2.1, as shown in fig. 7.9 (middle and bottom row). Qualitative agreement is found between the simulations and the experiments except for interference fringes extending along the positive I axis, indicating a coherent superposition with the small part of the wave function transmitted through the Zeno blockade. Note that the already mentioned asymmetry in Q is captured in the simulation, although with a smaller amplitude than in the experiment. Overall the model seems to underestimate the effect of dephasing.

We also compare the data and full model simulations to the case of ideal QZD in an oscillator Hilbert space truncated to 3 levels ($|0\rangle$, $|1\rangle$ and $|2\rangle$) and the result is shown in fig. 7.9 (top row). As expected, the state at every integer period is the same. No asymmetry in Q is observed, and the cross sections shown on the side in fig. 7.9 shows negative values reaching -0.4, two times greater than measured in the experiment (see fig. 7.9 experiment cross section: blue, Q>0).

Finally, as for the occupation probabilities $p(qn)$, the effect of blocking strength is investigated. The Wigner function after half a period is simulated without any decay for drive strengths $2 \times \varepsilon_{\text{block}}$, $\varepsilon_{\text{block}}$ and $0.5 \times \varepsilon_{\text{block}}$, keeping the ratio $\varepsilon_{\text{fill}} / \varepsilon_{\text{block}}$ constant. The results are shown in fig. 7.10. At the weakest blocking the Wigner function is almost symmetric in Q, quite similar to the ideal case,

and has great negative values at both negative and positive Q. As the blockade strength is increased the Q asymmetry re-appears and the negativity for $Q < 0$ becomes more shallow. This indicates that the asymmetry is induced by the blockade tone slightly shifting the adjacent $|g2\rangle \rightarrow |+2\rangle$ transitions (see section 2.3.4), and that the effect can be reduced by applying a weaker blockade.

Figure 7.9. Wigner function snapshots every quarter period of the QZD of the field initially inside the vacuum state, and confined in the exclusion circle of radius $\sqrt{3}$ (blockade on n=3). The measurement (middle row) is compared with the simulations of the full model (top row) and with the ideal case (bottom row). The evolution of the Wigner function is well captured by the simulation using the measured decoherence parameters. The asymmetry in Q at half integer periods, which does not occur in the ideal case, is captured by the full model simulations. The white dashed lines correspond to the cross sections shown on the left side after 0.5 (blue) and 1.5 (red) periods. In the ideal case the two cross sections are identical.

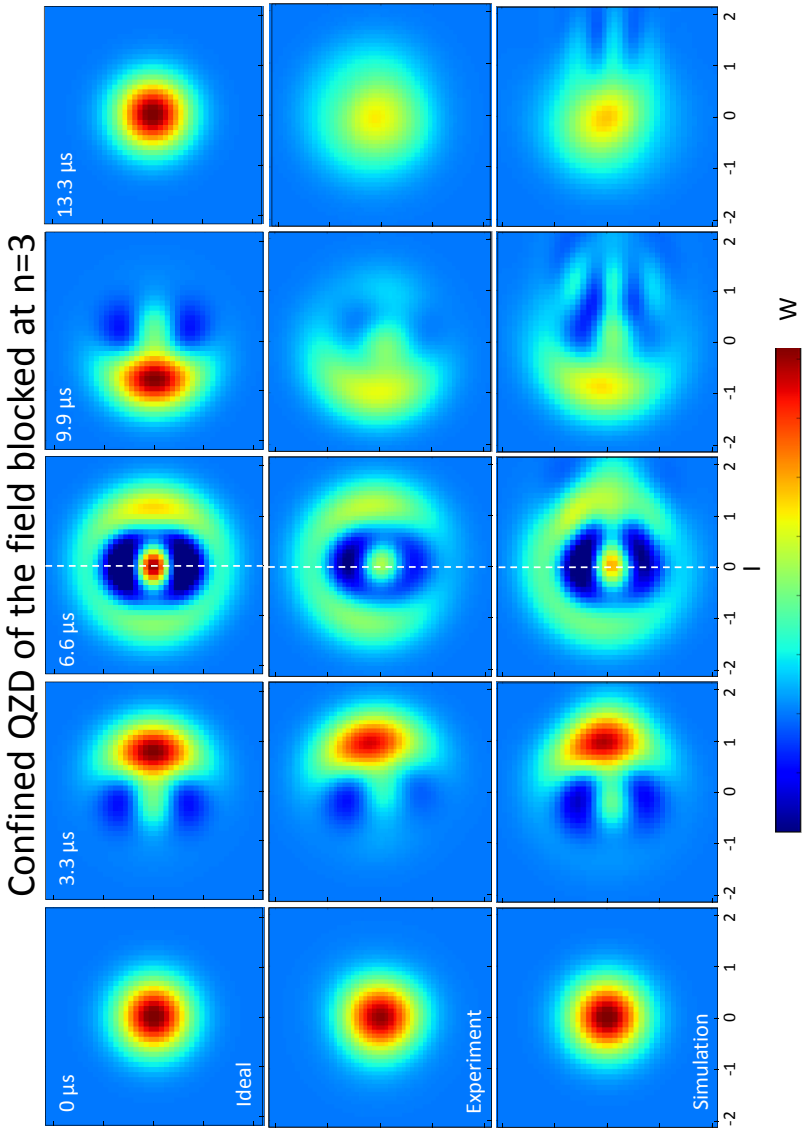
Confined QZD of the field blocked at n=3
0 µs
3.3 µs
6.6 µs
9.9 µs
13.3 µs
Ideal
Experiment
Simulation
Q
I
W
2
1
0
-1
-2
-0.2
-0.1
0.0
0.1
0.2
0.3
0.4
0.5
0.6

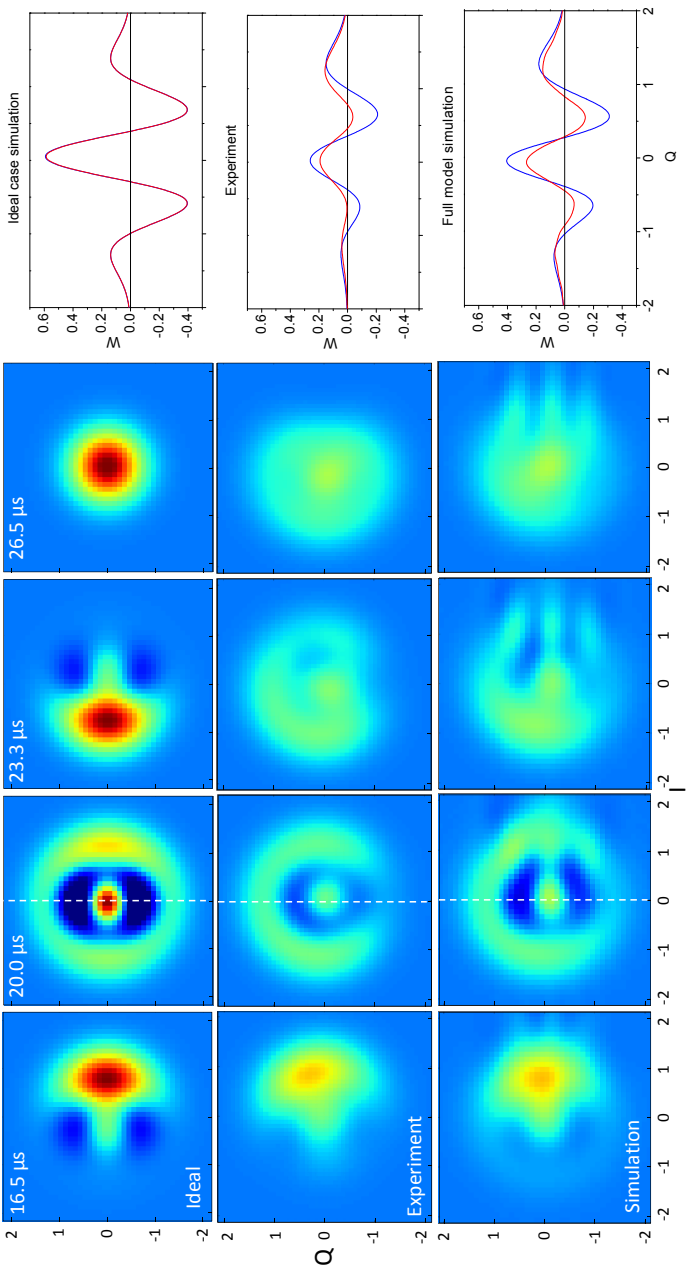
16.5 µs
20.0 µs
23.3 µs
26.5 µs
Ideal
Experiment
Simulation
Q
I
W
Ideal case simulation
Experiment
Full model simulation

Inducing the QZD with stroboscopic unitary kicks as discussed in section 2.3.1 could also reduce this effect as no blockade tone would be present while the cavity is being filled, and thus the levels remain unshifted.

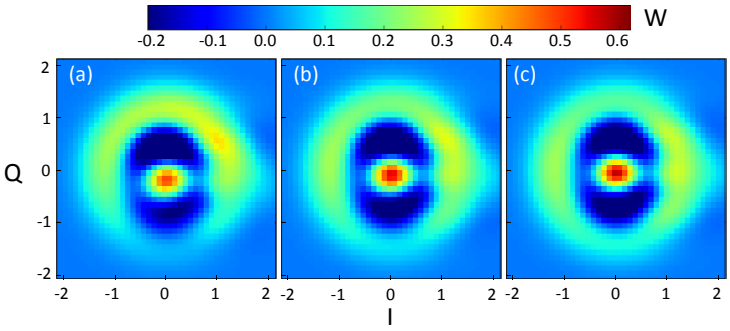

Figure 7.10. Wigner function of the cavity state after simulating the QZD up to half a Zeno period when the blocking strength is a) doubled, b) the same, or c) halved compared to the experiment, keeping the ratio $\varepsilon_{\text{fill}}/\varepsilon_{\text{block}}$ constant.

7.3 QZD of a coherent state collision with an EC

Here we consider the dynamics of the field prepared in a coherent state outside the EC and colliding with it, as discussed in section 2.3.1. The blockade at $n=2$ is obtained with the same drive amplitude as before, yielding roughly the same Rabi frequency on the $|g2\rangle \rightarrow |+2\rangle$ transition, and with the same field displacement rate $\dot{\zeta} = 0.27\,\mu s^{-1}$.

The evolution now takes place in a larger Hilbert space than in the confined case. For the maxlike reconstruction of an 18×18 density matrix, 1608 different observables are measured, consisting in 201 displacements indicated by dots in fig. 7.11, and eight photon number probabilities ($n=0,...,7$) measured at each displacement.

Head-on collision

For the first experiment the coherent state $|\beta = \sqrt{7}\rangle$ is prepared before the blockade and displacement is applied. The amplitude β of the state is chosen as the smallest possible such that it is still sufficiently unaffected by the EC, more precisely with only $p(2)$=2.2% and $p(1)+p(0)=0.7\%$. Figure 7.12a shows the measured evolution of the Wigner function at 3 μs intervals. As the state collides with the exclusion circle, the maximum of the Wigner function diminishes and the amplitude starts to spread along the EC and re-appears on the other side. After 15 μs the state is in a superposition of two components centered at $\zeta = \pm 1.6$. The fringes that appear between the two components form a

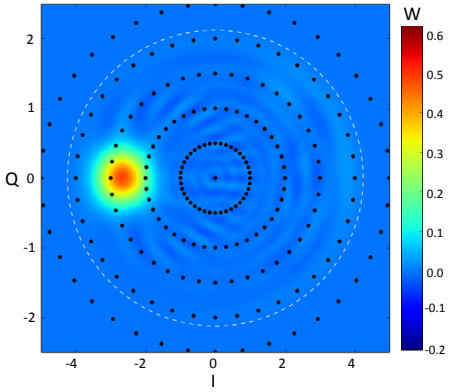

Figure 7.11. Wigner function of the state $|\beta = -\sqrt{7}\rangle$ reconstructed from the measurement of 1608 observables (201 displacements shown as black dots) using the maxlike algorithm. The white dashed circle shows the limit of the 18×18 density matrix used for the reconstuction.

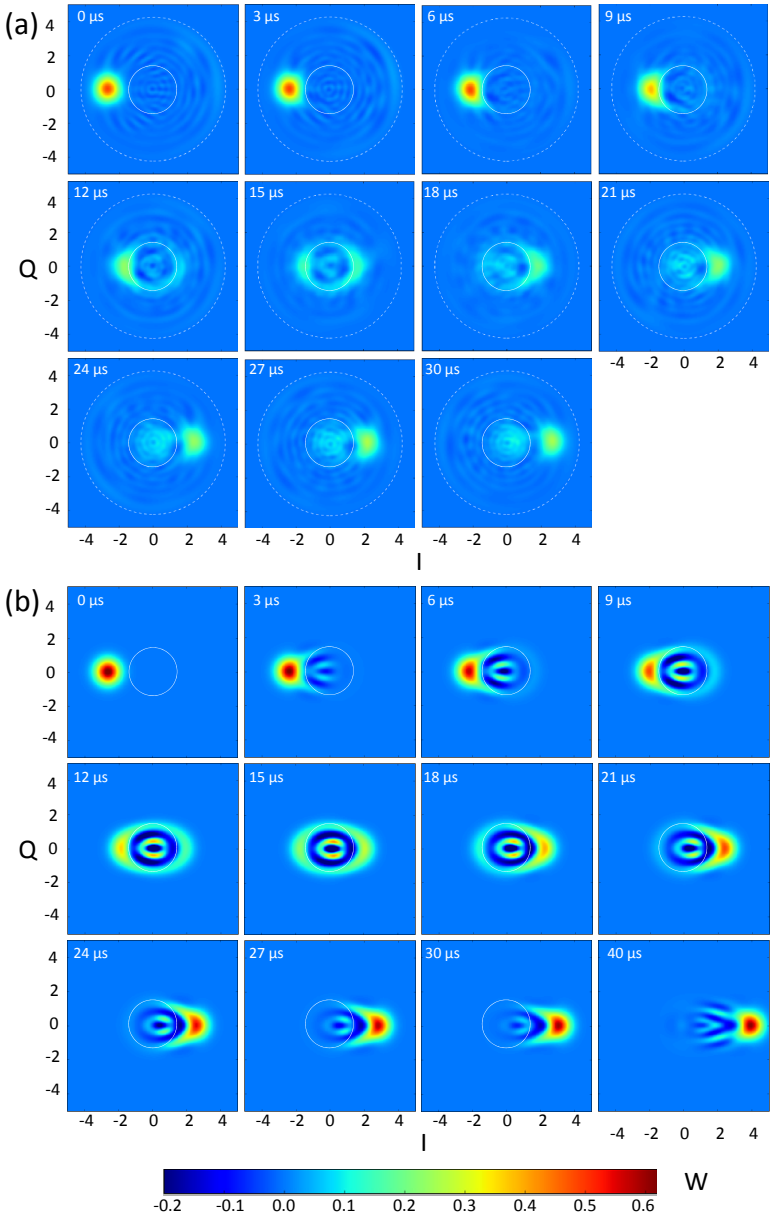

Figure 7.12. QZD of a head on collision with an EC of a radius $\sqrt{2}$. a) The coherent state $\left|\beta = -\sqrt{7}\right\rangle$ is prepared and is subsequently driven towards the EC. b) Calculated of the perfect QZD.

V-shape rotated by 90° located in the EC. The state that emerges after the collision is dominantly 'coherent-state like', but with about 1/3 of the weight trapped inside the EC due to imperfect blockade (partial transmission through the EC) and photon decay. Figure 7.12b shows the calculated evolution of the same experiment, but without decay, and induced by applying to $|\beta\rangle$ the operator $U_2 = \exp(-iH_2 t/\hbar)$ where the drive Hamiltonian

$$H_2 = \varepsilon'_{\text{fill}}(a_2^\dagger + a_2) \tag{7.6}$$

involves an annihilation operator

$$a_2 = a - \sqrt{2}|1\rangle\langle 2| - \sqrt{3}|2\rangle\langle 3| \tag{7.7}$$

that forbids $|n=1\rangle \leftrightarrow |n=2\rangle$ and $|n=2\rangle \leftrightarrow |n=3\rangle$ transitions, and a filling rate $\varepsilon'_{\text{fill}}$ adjusted to reproduce the experimental displacement rate. Under this drive the Hilbert space is compartmentalized into $\mathcal{H} = \mathcal{H}_{n<2} \oplus \mathcal{H}_{n=2} \oplus \mathcal{H}_{n>2}$ realizing the perfect QZD as discussed in section 2.2.1 and verified in fig. 7.14 below. Apart from the lack of decay, the spread of the state around the outside EC is captured in the calculation. The interference fringes that appear inside the EC are visible in the experiment but considerably sharper in the calculation. Since the last experimental frame is still quite close to the EC we calculate the state $10\,\mu s$ later (i.e. at 40 μs), which shows the interference fringes between the dominant part of the wavefunction transmitted around the EC and the small part trapped inside it.

Tangential collision

The second experiment follows an identical protocol with a different initial state $\left|\beta = -\sqrt{5} - i\sqrt{2}\right\rangle$. The coherent state amplitude $|\beta|$ is the same as before but its phase is tuned to get a tangential collision with the EC. This entails choosing $\sqrt{|\text{Im}[\beta]|} = 2$. The evolution of the Wigner function, measured at $3\,\mu s$ intervals, is shown in fig. 7.13a. When the state is driven along the positive I axis, the part of the state at higher Q collides with the EC first, causing it to phase shift earlier than the rest of the state. This happens gradually as the state is displaced further on to the EC, giving the appearance of the state rounding itself around the EC. The Wigner function of the state

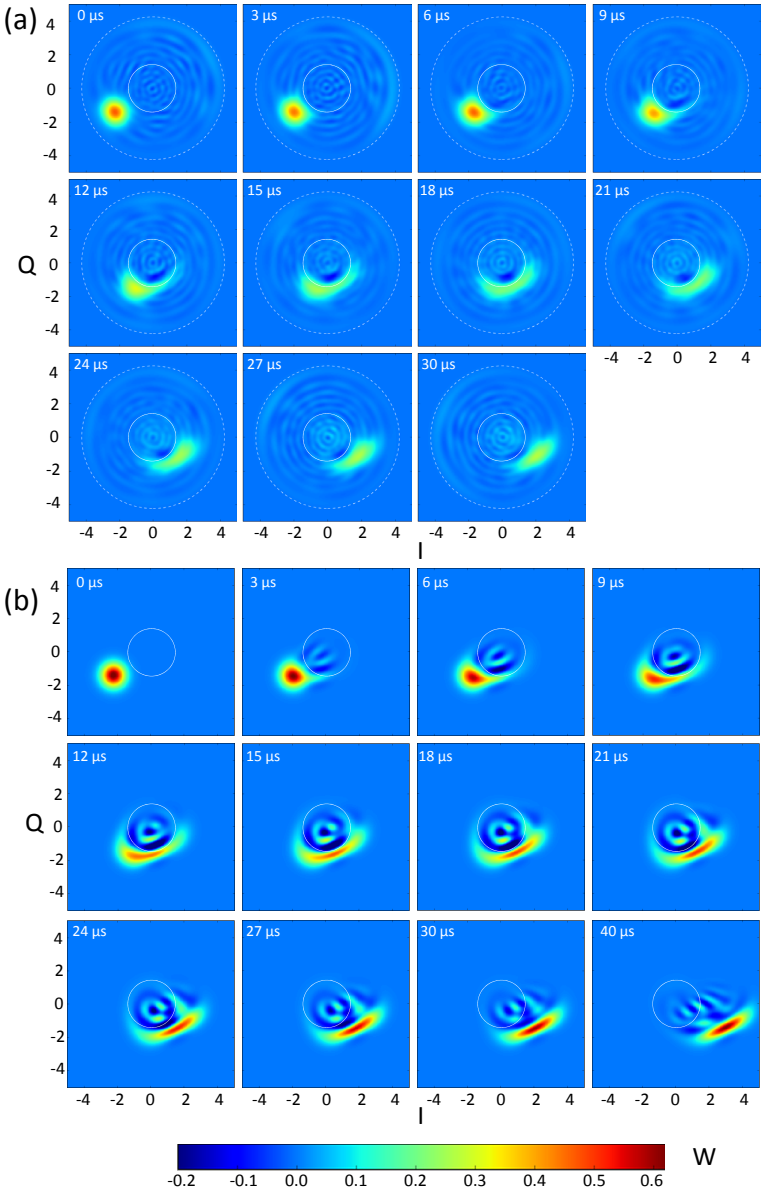

Figure 7.13. QZD of a tangential collision with an EC of a radius $\sqrt{2}$. a) The coherent state $|\beta = -\sqrt{5} - i\sqrt{2}\rangle$ is prepared and is subsequently driven towards the EC. b) Calculated of the perfect QZD.

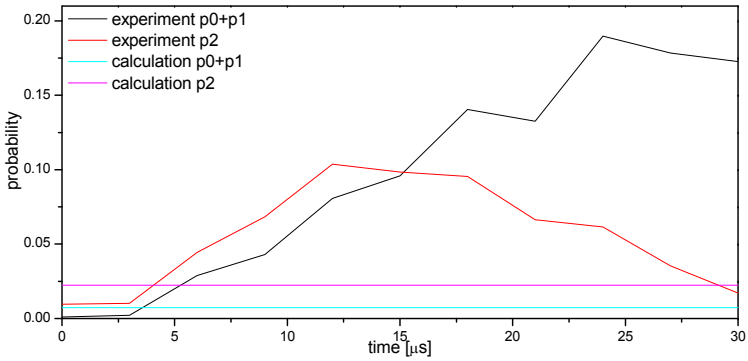

Figure 7.14. Population inside and on the EC during a tangential collision. For the calculation the populations stay constant which confirms the compartmentalization of Hilbert space $\mathcal{H} = \mathcal{H}_{n<2} \oplus \mathcal{H}_{n=2} \oplus \mathcal{H}_{n>2}$. In the experiment $p(2)$ increases due to the imperfect blockade as the collision approaches and falls after. The population $p(0)+p(1)$ inside the EC increases due to the imperfect blockade, and photon decay and dephasing.

emerging from the collision has an elongated shape. The simulated evolution, using the same method as in fig. 7.12b, is shown in fig. 7.13b. As for the head-on collision, the calculation highlights the interference fringes that appear inside the EC during the collision, and after it between the two components inside and outside the EC.

To investigate the elongated shape resulting form this tangential collision we plot in fig. 7.15 the cross sections of the Wigner function after 30 μs evolution, along the line indicated in the inset. For comparison we also plot the cross section of a coherent state (represented by a Gaussian of height $2/\pi$ and half width at half maximum $\sigma = 1/\sqrt{2}$). Due to the aforementioned experimental imperfections the height of the cross section extracted from measurements is $1/2.3$ of the height of the coherent state. When comparing to a scaled profile of a coherent state, the mesured state has a smaller width at half maximum (0.4 compared to 0.57). Note that the small asymmetry of the measured peak is due to small weights inside the EC as can be seen on the measurement curve at low values of $|\zeta|$. The calculated cross section of the perfect QZD has a slightly lower maxima than the coherent state due to the population

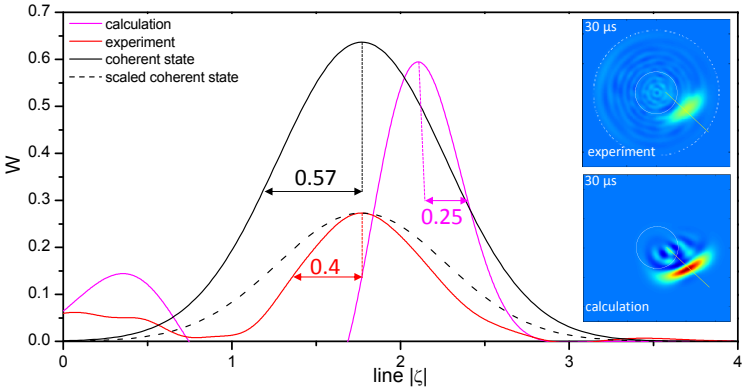

Figure 7.15. Cross sections of the Wigner function of states resulting from tangential collision with an EC, and a coherent state. The experimentally measured state (red) and the calculated state (magenta) are cross sections along the lines indicated in the insets, with 0 corresponding to the end almost at the phase space origin. The coherent state is represented by a Gaussian with a standard deviation $\sigma = 1/\sqrt{2}$ and a height $2/\pi$ (black solid). The height of the Gaussian is scaled down to 0.273 (black dashed) for comparison with the measurement. The half width at half maximum is indicated for comparisson of the respective widths.

blocked in $\mathcal{H}_{n<2} \oplus \mathcal{H}_{n=2}$. Compared to the width of 0.57 of the coherent state, the calculated QZD induces a squeezed state with a width of 0.25.

Even though the peak in the profile from the measurement has a smaller width than a coherent state one cannot say it is a squeezed state since the peak amplitude is significantly lower and large parts of the state are located away from the peak. The simulation however shows that a squeezing of more than half can be achievedusing this method.

7.4 QZD experiments by other groups

QZD in Rydberg atoms

Experimental realization of the quantum Zeno dynamics was first reported by Signoles *et al.* [45] in 2014.

The authors used Rydberg atoms prepared with principal quantum number $n_e = 51$ and with the highest angular momentum $J = 25$. The angular momentum projection on the quantization axis of the generalized Bloch sphere can take integer values $J - k$ with $k \in [0, 2J]$, and forms a Hilbert space of 51 nearly-equidistant levels $|n_e, k = 0\rangle$,...,$|n_e,$

$k=50\rangle$, corresponding to our harmonic oscillator. Starting in the state $|n_e, k=0\rangle$, a radio frequency field at frequency 230.15 MHz populates these k levels at a rate of 152 kHz. The Zeno blockade is induced by driving the transition $|n_e, k_z\rangle \rightarrow |n_g, k_z\rangle$ with a continuous microwave tone at a Rabi frequency $\sim$3 MHz and for $k_z=4$ and 5.

The monitored populations of the levels $|n_e, k\rangle$ bounce off a 'wall' at $k=k_z+1$ in presence of the Zeno blockade with $\sim$25% transmission through the wall. The Husimi Q-function[23] is also measured, showing the periodic behavior of confined QZD (see section 2.3.1), with a period of $1.46\,\mu s$. The Wigner function at roughly half a period shows fringes indicating a coherent superposition of the two amplitudes with opposite phase.

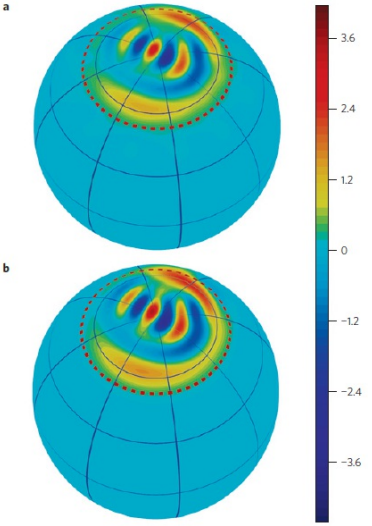

Figure 7.16. Figure reproduced from ref [45]© demonstrating the QZD in Rydberg atoms with spin $J=25$ blocked at $k_z=4$. a) Experimental Wigner function, $W(\theta,\phi)$, obtained from the reconstructed density matrix ρ of the spin state after QZD at the phase inversion time $t_1=0.76\,\mu s$. b) Results of the numerical simulation of the experiment. The fidelity of the calculated density matrix ρ_c with ρ is $\mathrm{Tr}^2\left[\sqrt{\sqrt{\rho}\rho_c\sqrt{\rho}}\right]=0.93$.

QZD in a Rb ensemble

In ref [4] Barontini *et al.* entangle $N=36$ Rb atoms at the antinode of a field in an optical microcavity using the QZD. The ensemble of atoms with two hyperfine levels $|0\rangle$ and $|1\rangle$ in their ground state form a collective spin with $N+1$ Dicke states $|n_N\rangle$ (corresponding to Fock states in our oscillator), with n the total number of atoms in $|1\rangle$. Driving the $|0\rangle \rightarrow |1\rangle$ transition induces Rabi oscillation of the collective spin, which plays the role of the coherent drive of our harmonic oscillator. The Zeno blockade is applied on $|0_N\rangle$ by driving an optical

transition. Starting in the state $|N_N\rangle$ and driving towards $|0_N\rangle$ yields a state close to the highly entangled W state, $|1_N\rangle = 1/\sqrt{N}(|10, ..., 0\rangle + |01, ..., 0\rangle + ... + |10, ..., 1\rangle)$.

QZD in dispersive circuit-QED

The confined QZD was also observed in circuit-QED by Bretheau *et al.* [8] in 2015.[7.1]

Similar to the platform used in this thesis, they used a transmon in a superconducting 3D cavity. The difference lies in the transmon not being frequency tunable, but fixed at 5.622 GHz, and dispersively coupled to the fundamental mode of the cavity at 7.804 GHz, used both for storing the quantum field and measuring the transmon. The photon number split frequencies $f(n) \equiv f_{ge} - n\chi$ are thus equidistant with a separation $\chi = 4.63\,\text{MHz}$. The transmon and cavity lifetimes are $T_1 = 11.5\,\mu s$, $T_2 = 8.9\,\mu s$, and $T_{\text{cav}} = 1.3\,\mu s$, respectively.

The QZD is induced by both a continuous filling at a rate $\dot{\zeta} = 3\,\mu s^{-1}$ and continuous blocking of $n_z = 2$, 3, 4 and 5 at a Rabi frequency $\Omega_R/2\pi = 6.24$ MHz. The photon number probability $p(n)$ up to n_z is monitored during $3\,\mu s$ of evolution showing 1.5 to 2 Zeno periods of the confined dynamics. Wigner functions are measured to produce snapshots of the evolution of the field over one period for each n_z, clearly showing negative values.

The main difference with the experiment in this thesis is the shorter cavity lifetime by a factor 30-40. This makes the authors choose a filling rate and a blockade strength 10 times higher (same ratio $\Omega_R/2\pi/\dot{\zeta} = 2$) in order to observe a few Zeno periods. This stronger blockade yields a ratio χ/Ω_R=1.3 about 8 times higher (here χ corresponds to $\delta_{+,4}$ in the ef-resonant scheme), and consequently a strong off-resonant drive of the unblocked Fock states. These states thus undergo a rather strong phase shift which is partially compensated by the negative Kerr effect. The dynamics observed is thus farther from the ideal QZD, although the essence of it is perfectly captured. The decay of the QZD oscillations is only 2-3 times faster than in the present thesis due to the fast drive compensating the short cavity time. Unlike in our experiment, the contribution of the transmon decay channels to this QZD decay is very likely negligible according to our analysis of decoherence, given the T_1 about 5 times longer than in this thesis and about 7-9 times longer than T_{cav}.

7.1. State confinement to the lowest levels (up to 7) of a superconducting anharmonic oscillator have also shown a superposition of two "coherent-like" states[10]

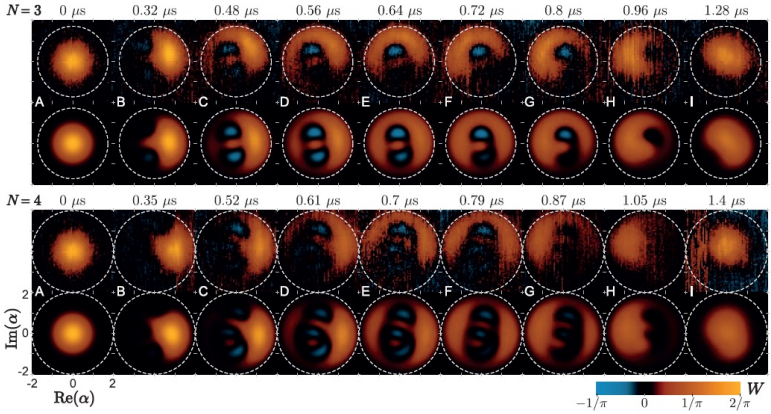

Figure 7.17. One period of the QZD both measured (top) and simulated (bottom) with a block on $n = 3$ and $n = 4$. Clear negativities are observed in both cases and a good agreement is between the experiment and simulations. Figure from [8]©.

Chapter 8
Perspectives

The quantum Zeno dynamics (QZD) has been an active domain of research during this PhD period. Some of the proposed experiments in refs. [39] and [40] have been implemented in this thesis work and by others ([45][8][4]). However, manipulation of states using the phase space 'tweezers' (see section 2.3.3) is yet to be demonstrated.

In terms of perspective for QZD experiments, we foresee the following possible improvements: A longer lifetime of the cavity is an important step towards reducing decoherence during the QZD and implementing the tweezers. A cavity with lifetimes T_{cav} 5-10 times longer ($\sim$0.25 ms) than used in our demonstration of QZD has been obtained at the end of this thesis. Even longer cavity lifetimes $T_{\text{cav}} \simeq$ 10 ms have been reported[41] for new cavity geometries in circuit-QED, which gives good prospects for the future. The other main decoherence source for the QZD found in our work is the transmon relaxation. It could be improved beyond $10\,\mu s$ by adapting the cavity dimensions to increase the transmon-readout mode detuning, thus reducing the Purcell effect, and by using better transmons as reported in chapter 5. A sufficient increase in T_{cav} alone would already allow for slower displacement of the cavity field, which in return would make the blocking more efficient, and the dynamics less sensitive to transmon relaxation. In our setup the coupling strength g_0 could also be increased by up to a factor $\sim$2 to increase the photon number splitting by the same amount, at the cost of a 16 times larger Kerr non-linearity K (from 300 Hz to $\sim$4.8 kHz), which would still be acceptable and is anyway an over estimate as shown in chapter 6.

With the sample reported in this thesis, the QZD using unitary kicks (see section 2.3.1) could be attempted. Using the unitary kicks would enable the implementation of exclusion circles with partial transmission without dephasing the transmitted component of the wave function, allowing for example the generation of a complex superpo-

sitions of coherent states. This would require optimal pulse shaping of the blocking pulse in order to minimize the off-resonant driving of the adjacent transitions but would leave the levels of the harmonic oscillator unperturbed during displacement of the cavity field.

In a more general perspective, as the QZD can be calculated from well established quantum theory, I think that QZD experiments do not answer any fundamental questions. However, its application in manipulating superposed coherent states, namely using the tweezers, could be used in attempts at quantum simulations and quantum information processing[31][36].

Appendix A

Energy spectrum of the ef-resonance scheme

We consider the case of a harmonic oscillator with frequency f_0 and annihilation operator a, coupled to a three-level system (3LS) with eigenstates $\{|g\rangle, |e\rangle, |f\rangle\}$ and lowering operator a_q. We also assume a weak anharmonicity $\alpha = f_{ef} - f_{ge} \ll f_{ge}$, such that a_q can be approximated by the annihilation operator of a harmonic oscillator restricted to three levels. The two subsystems obey the resonant condition $\nu_{ef} = \nu_0$ (detuning $\Delta = f_{ge} - f_0 = -\alpha$) and are subject to an exchange interaction with coupling frequency $g_0 \ll \alpha$, yielding the Hamiltonian

$$\begin{aligned} &H = H_0 + H_{3LS} + H_{coupling}, \\ &H_0 = h\, f_0\, a^\dagger\, a, \\ &H_{3LS} = h\,(f_0\, a_q^\dagger a_q - \alpha|e\rangle\langle e| - \alpha|f\rangle\langle f|), \\ &H_{coupling} = h\, f_0\,(a^\dagger\, a_q + a\, a_q^\dagger). \end{aligned} \tag{A.1}$$

This couplings make the Hamiltonian matrix diagonal by block in the tensorial basis $|x\, n\rangle = |x\rangle \otimes |n\rangle$ ($x = g, e, f$), with subsequent blocks of size 1, 2, 3, 3, 3... Using the reduced coupling $\epsilon = -g_0/\alpha$, these blocks write

$$\begin{gathered} [0]_{|g0\rangle}, \\ h\left(f_0\, I_2 - \alpha \begin{bmatrix} 0 & \epsilon \\ \epsilon & 1 \end{bmatrix} \right)_{|g1\rangle, |e0\rangle}, \\ h\left(n\, f_0\, I_3 - \alpha \begin{bmatrix} 0 & \sqrt{n}\,\varepsilon & 0 \\ \sqrt{n}\,\varepsilon & 1 & \sqrt{2\,(n-1)}\,\varepsilon \\ 0 & \sqrt{2\,(n-1)}\,\varepsilon & 1 \end{bmatrix} \right)_{Bn}, \end{gathered} \tag{A.2}$$

with I_k the identity matrix of dimension k and $B_n = \{|g\ n\rangle,\ |e\ (n-1)\rangle,\ |f\ (n-2)\rangle\}$ the basis for $n \geq 2$. The diagonalization of each block yields analytical eigenenergies and vectors, which for $n \geq 2$ are functions of the three real solutions of the cubic equation $x^3 - 2\,x^2 + [1 + 2\,\epsilon^2 - 3\,n\,\epsilon^2]\,x + n\,\varepsilon^2 = 0$. To shed light on the physics, we expand these analytical quantities in the small parameter ε. As shown in Fig., the levels form three distinct energy ladders$\{|\widetilde{g\,n}\rangle\}$, $\{|-n\rangle\}$ and $\{|+n\rangle\}$: The ladder$\{|\widetilde{g\,n}\rangle\}_{n\geq 0}$ corresponds to the almost unperturbed oscillator when the 3LS is left in its ground state. With eigenenergies and eigenvectors

$$\begin{array}{l} E(|\widetilde{g\,n}\rangle) = n\,h\left[\,\tilde{f}_0 + (n-1)\,K/2\right] + o(\epsilon^5) \\ |\widetilde{g\,n}\rangle = \left[1 - n\,\varepsilon^2/2, -\sqrt{n}\,\varepsilon, \sqrt{2\,n\,(n-1)}\,\varepsilon^2\right]_{Bn} + o(\epsilon^3) \end{array}, \tag{A.3}$$

this effective oscillator $\tilde{O}$ has a shifted frequency $\tilde{f}_0 = f_0 + \alpha\,(\epsilon^2 - \epsilon^4)$, and a small Kerr non-linearity $K = 2\,\alpha\,\epsilon^4$ inherited from the 3LS. The two other ladders $\{|\pm n\rangle\}$ (extended down to $n = 0$ by $|+0\rangle \equiv |-0\rangle \equiv |\widetilde{g\,0}\rangle$ and $|+1\rangle \equiv |-1\rangle \equiv |\widetilde{e\,0}\rangle$) have energies and eigenvectors

$$\begin{array}{rl} \{E(|\pm n\rangle)\} = & \{0, h\,[\nu_O - \alpha\,(1+\epsilon^2) + o(\epsilon^3)],\}..., \\ & h\left[n\,\nu_O - \alpha\left(1 \pm \sqrt{2\,(n-1)}\,\epsilon + n\,\epsilon^2/2 + o(\epsilon^3)\right)\right] \end{array}$$

$$\begin{array}{rl} \{|\pm n\rangle\} = & |g\,0\rangle, \begin{bmatrix} \epsilon \\ 1 - \dfrac{\varepsilon^2}{2} \end{bmatrix}, ..., \\ & \begin{bmatrix} \epsilon\sqrt{\dfrac{n}{2}} \pm \sqrt{\dfrac{n}{n-1}}\,\dfrac{7\,n-8}{8}\,\epsilon^2 \\ \dfrac{1}{\sqrt{2}} \pm \dfrac{n}{8\sqrt{n-1}}\,\epsilon + \dfrac{(33\,n-32)\,n}{64\sqrt{2}\,(n-1)}\,\epsilon^2 \\ \pm\dfrac{1}{\sqrt{2}} - \dfrac{n}{8\sqrt{n-1}}\,\epsilon + \dfrac{n^2}{64\sqrt{2}\,(n-1)}\,\epsilon^2 \end{bmatrix}_{Bn} + o(\epsilon^3). \end{array}$$

For $n \geq 2$ the zeroth-order approximation in ϵ of these eigenvectors are simply the symmetric and anti-symmetric superposition of $|e\,(n-1)\rangle$ and $|f\,(n-2)\rangle$. A particular "Fock state" $|\widetilde{g\,n}\rangle$ of selectively manipulable by addressing the $|\widetilde{g\,n}\rangle \to |\pm(n+1)\rangle$ transitions to the hybridized oscillator-transmon states, at frequencies $f_{\pm n} = f_{ge} \pm \sqrt{2\,n}\ g_0 + (3\,n+1)\ g_0\,\epsilon/2 + o(\epsilon^2)$ (with a Rabi frequency about $\sqrt{2}$ slower for all $n > 0$ than for the pure $|g\rangle \to |e\rangle$ transition).

Appendix B
Maximum likelihood algorithm adapted to Gaussian errors

This note is derived by Pierre Rouchon after discussions with Daniel Esteve, Kristinn Juliusson, Helene le Sueur and Denis Vion.

Take an integer a collection of $\bar{n} > 0$ and $\bar{K} = \{\alpha_1, ..., \alpha_{\bar{K}}\}$ a collection of $\bar{k}$ complex amplitudes.

We consider the following somehow idealized tomography of the density operator ρ of an harmonic oscillator from the following measurement data set:

$$\{p_{n,\alpha}\}_{n\in\{0,....,\bar{n}\},\alpha\in\bar{K}}.$$

For each n and α, the data $\{p_{n,\alpha}\}$ corresponds approximatively to $\mathrm{Tr}(\rho \boldsymbol{E}_{n,\alpha})$,

$$p_{n,\alpha} \approx \mathrm{Tr}(\rho \boldsymbol{E}_{n,\alpha})$$

where $\mathrm{Tr}(\rho \boldsymbol{E}_{n,\alpha}) = \boldsymbol{D}_{-\alpha}|n\rangle\langle n|\boldsymbol{D}_\alpha$, $\boldsymbol{D}_\alpha = \exp(\alpha \boldsymbol{a}^\dagger - \alpha^* \boldsymbol{a})$ is the coherent displacement operator of amplitude α, and $|n\rangle$ is the Fock state with n photon(s). The problem is to reconstruct ρ in a robust way knowing that the experimental data $p_{n,\alpha}$ are corrupted by Gaussian noises of standard deviations $\sigma^2_{n,\alpha} > 0$.

For each n and α, the probability to have $p_{n,\alpha} \in [s, s + ds]$knowing ρ reads :

$$\mathbb{P}\big(p_{n,\alpha} \in [s_{n,\alpha}, s_{n,\alpha} + ds_{n,\alpha}]|\rho\big) = \exp\Big(-\frac{(s_{n,\alpha} - \mathrm{Tr}[\rho \boldsymbol{E}_{n,\alpha}])^2}{2\sigma^2_{n,\alpha}}\Big)\frac{ds_{n,\alpha}}{\sigma_{n,\alpha}\sqrt{2\pi}}.$$

Denoting by Y the complete measurement data set, $Y \equiv p_{n,\alpha}$, and assuming that the $p_{n,\alpha}$ are statistically independent, we have

$$\begin{aligned}
&\mathbb{P}\left(Y \in \prod_{n,\alpha}[s_{n,\alpha}, s_{n,\alpha} + ds_{n,\alpha}]\,\middle|\,\rho\right) \\
= &\prod_{n,\alpha}\exp\left(-\frac{(s_{n,\alpha} - \mathrm{Tr}[\rho \boldsymbol{E}_{n,\alpha}])^2}{2\sigma^2_{n,\alpha}}\right)\frac{ds_{n,\alpha}}{\sigma_{n,\alpha}\sqrt{2\pi}} \\
= &\exp\left(-\sum_{n,\alpha}\frac{(s_{n,\alpha} - \mathrm{Tr}[\rho \boldsymbol{E}_{n,\alpha}])^2}{2\sigma^2_{n,\alpha}}\right)\prod_{n,\alpha}\frac{ds_{n,\alpha}}{\sigma_{n,\alpha}\sqrt{2\pi}}.
\end{aligned}$$

The Bayesian Mean estimate ρ_{BM} from the measurement data Y is defined by the very general relation (see, e.g.,[7]):

$$\rho_{\mathrm{BM}} = \frac{\int_{\mathcal{D}} \rho\, \mathbb{P}(Y|\rho)\mathbb{P}_0(\rho)d\rho}{\int_{\mathcal{D}} \mathbb{P}(Y|\rho)\mathbb{P}_0(\rho)d\rho},$$

where $\mathcal{D}$ is the convex set of density operators (here the underlying Hilbert space is of finite dimension) and $\mathbb{P}_0$ is some prior probability law of ρ (e.g., Gaussian unitary ensemble[33]).

Here ρ_{BM} is given by

$$\rho_{\mathrm{BM}} = \frac{\int_{\mathcal{D}} \rho \exp(f(\rho))\mathbb{P}_0(\rho)d\rho}{\int_{\mathcal{D}} \exp(f(\rho))\mathbb{P}_0(\rho)d\rho},$$

where $f(\rho)$, the log-likelihood function, reads

$$f(\rho) = -\sum_{n,\alpha} \frac{(s_{n,\alpha} - \mathrm{Tr}[\rho \boldsymbol{E}_{n,\alpha}])^2}{2\sigma_{n,\alpha}^2}$$

When the support of the likelihood function is mainly concentrated around its maximum at ρ_{ML}, it is known that ρ_{ML} is a good approximation of ρ_{BM}. Following [46], we can also compute an estimation of the Bayesian variance of $\mathrm{Tr}(\rho_{\mathrm{ML}}A)$, denoted by $\sigma^2_{\mathrm{ML}}(A)$ for any observable A and depending on the second-order derivatives of the log-likelihood function at its maximum ρ_{ML}. This transforms the variance $\sigma_{n,\alpha}$ on the data into variance on the MaxLike estimate ρ_{ML}. In particular when we take, for any complex number β,

$$A = \frac{2}{\pi} \exp(\beta \boldsymbol{a}^\dagger - \beta^* \boldsymbol{a}) \exp(i\pi \boldsymbol{a}^\dagger \boldsymbol{a}) \exp(-\beta \boldsymbol{a}^\dagger + \beta^* \boldsymbol{a})$$

we get via $\sigma^2_{\mathrm{ML}}(A)$ an estimation of the variance of the MaxLike estimate of the Wigner function at position β in the phase space.

Following [46], ρ_{ML} is characterized by the following necessary and sufficient conditions: there exists a nonnegative scalar λ_{ML} such that:

$$[\rho_{\mathrm{ML}}, \nabla f(\rho_{\mathrm{ML}})] = 0, \;\; \lambda_{\mathrm{ML}} P_{\mathrm{ML}} = P_{\mathrm{ML}} \nabla f_{\mathrm{ML}} \;\; \text{and} \; \nabla f_{\mathrm{ML}} \leqslant \lambda_{\mathrm{ML}} \mathbb{1}$$

where $P_{\rm ML}$ is the orthogonal projector on the range of $P_{\rm ML}$ and $\nabla f_{\rm ML}$ is the gradient at $\rho_{\rm ML}$ of the log-likelihood:

$$\nabla f(\rho) = -\sum_{n,\alpha} \frac{s_{n,\alpha} - {\rm Tr}[\rho \boldsymbol{E}_{n,\alpha}]}{\sigma^2_{n,\alpha}} \boldsymbol{E}_{n,\alpha}$$

We have also

$$\sigma^2_{\rm ML}(A) \equiv {\rm Tr}(A^{||} \boldsymbol{R}^{-1}(A^{||}))$$

where $B^{||} = B - \frac{{\rm Tr}(BP_{\rm ML})}{{\rm Tr}(P_{\rm ML})} P_{\rm ML} - (\mathbb{1} - P_{\rm ML}) B (\mathbb{1} - P_{\rm ML})$ is the orthogonal projector of any Hermitian operator B on the tangent space at $\rho_{\rm ML}$ to the submanifold of Hermitian operators with trace one and with ranks equal to the rank of $\rho_{\rm ML}$. Here above, the linear super-operator $\boldsymbol{R}$ reads for any Hermitian operator X,

$$\begin{aligned} \boldsymbol{R}(X) \;&=\; \sum_{n,\alpha} \frac{{\rm Tr}\big(x \boldsymbol{E}^{||}_{n,\alpha}\big)}{\sigma^2_{n,\alpha}} \boldsymbol{E}^{||}_{n,\alpha} + \frac{1}{2}(\lambda_{\rm ML}\mathbb{1} - \nabla f_{\rm Ml}) X \rho^{+}_{\rm ML} \\ &\quad + \frac{1}{2} \rho^{+}_{\rm ML} X (\lambda_{\rm ML}\mathbb{1} - \nabla f_{\rm Ml}) \end{aligned}$$

with $\rho^{+}_{\rm ML}$ the Moore-Penrose pseudo-inverse of $\rho_{\rm ML}$.

The maximization of f can be achieved by a gradient algorithm with orthogonal projection on $\mathcal{D}$. The computation of ρ_{k+1} from ρ_k, the value of ρ at step k, reads

$$\rho_{k+1} = \Pi(\rho_k + g \nabla f(\rho_k))$$

where

- $g > 0$ is a normalization parameter such that $g \, \|\nabla^2 f\|$ is not too large (order 1 to 10 in general). A rough estimation of size of the Hessian $\|\nabla^2 f\|$ is given by $\Sigma_{n,\alpha} \frac{{\rm Tr}^2(\boldsymbol{E}_{n,\alpha})}{\sigma^2_{n,\alpha}} = \Sigma_{n,\alpha} \frac{1}{\sigma^2_{n,\alpha}}$
- $A \mapsto \Pi(A) \in \mathcal{D}$ is the orthogonal projection of the Hermitian matrix A on the convex set $\mathcal{D}$, the set of Hermitian non negative matrices of unit trace. From first order stationary conditions attached to any unitary change of frames, $\Pi(A)$ and A commute and thus are diagonal in the same basis. Consequently denoting by $V \in \mathbb{R}^{\bar{n}+1}$, the vector of eigenvalues of A, the eigenvalues of $\Pi(A)$, denoted by $V \in \mathbb{R}^{\bar{n}+1}$ are simply derived from V by its orthogonal projection in the real Euclidean space $\mathbb{R}^{\bar{n}+1}$ on the simplex

$$S = \left\{ (x_0, ..., x_{\bar{n}}) \,\middle|\, \forall n, x_n \geqslant 0, \sum_n x_n = 1 \right\}.$$

According to KKT, the component w_n of W are characterized by the following system depending on the components v_n of V

$$\begin{aligned}
&\forall n \in \{0, ..., \bar{n}\}: \quad && w_n \geqslant 0, p_n \geqslant 0 \text{ and } w_n p_n = 0 \\
&\forall n \in \{0, ..., \bar{n}\}: \quad && w_n - p_n - v_n = q \\
&\qquad \sum_n w_n = 1
\end{aligned}$$

where $p_n \geqslant 0$ is the multiplier associated to the inequality constraint $x_n \geqslant 0$ and $q \in \mathbb{R}$ to the equality constraint $\Sigma_n w_n = 1$. These conditions are obtained from the Lagrangian

$$\mathcal{L}(w_0, ..., w_{\bar{n}}, p_0, ..., p_{\bar{n}}, q) = \sum_n \frac{(w_n - v_n)}{2} - p_n w_n - q\left(1 - \sum_n w_n\right)$$

and its minimization versus $(w_0, ..., w_{\bar{n}}, p_0, ..., p_{\bar{n}}, q)$ on the convex set where, for all $n, w_n \geqslant 0$ and $p_n \geqslant 0$.

Appendix C
Estimating thermal photon population in the resonator

This appendix calculates how to translate the relative amplitudes of the photon splitted ge spectroscopic peaks (see section 1.2.1.2) of the transmon into population of Fock state 1 (assuming it is small). We consider a Rabi pulses of duration T_p at the transmon excitation frequency $f_{ge,n=1}$ in presence of 1 photon in the cavity, which induces Rabi oscillation on the $|g\rangle \rightarrow |e\rangle$ transition at the Rabi frequency $f_R = \Omega_R / 2\ \pi$. The spectroscopic signal at $f_{ge,n=1}$ (see fig. 5.4 in chapter 5) is proportional to the probability $p_{e,1}$ of having the transmon excited at the end of the pulse, which we evaluate now. During the Rabi pulse, the number of thermal photons in the cavity fluctuates as shown in fig. C.1, with rising and lowering rates γ_+ and γ_- (here $\gamma_- = \kappa$ is the cavity decay rate). However, we anticipate from the experiment a very small average photon number $\bar{n}_{\text{th}}$ and thus a low $\gamma_+ = \gamma_- \bar{n}_{\text{th}}$. The general scenario of fig. C.1b (several photons entering and exiting the cavity during the pulse, several photons present at the same time, etc) is thus very unlikely, and we can focus on simpler scenari corresponding to a single appearance of one photon during T (scenario1 = 1 entrance + 1 possible exit), or two photons (scenario 2 = first entrance, first exit, second entrance, and possibly second exit).

In scenario 1, p_e is simply the product of the excited population $\sin^2(\pi\, f_R \tau)$ acquired during the overlap of the Rabi and 1 photon pulse, by the probability $\sim 1 - \bar{n}_{\text{th}}$ to have zero photon at $t = 0$, the probability $\gamma_+ e^{-\gamma_- t_1} dt_1$ to have one photon entering the cavity between t_1 and $t_1 + dt_1$, the probability $\gamma_- e^{-\gamma_- \tau} d\,\tau$ to have the photon leaving after τ, the probability $e^{-\gamma_+ (T_p - t_1 - \tau)}$ that a second photon does not enter, and the probability $e^{-\Gamma_1 (T_p - t_1 - \tau)}$that the transmon has not relaxed at the end of the Rabi pulse, integrated over $t_1 < T_p$ and $\tau < T_p - t_1$:

$$p_{e,1} = (1 - \bar{n}_{\text{th}}) \gamma_+ \gamma_- \times \int_{t1=0}^{T_p} \int_{\tau=0}^{T_p - t1} \sin^2\left(\frac{\Omega_R \tau}{2}\right) e^{-\gamma_- \tau - \gamma_+ (T_p - \tau) - \Gamma_1 (T_p - t_1 - \tau)} d\,t_1\, d\,\tau \tag{C.1}$$

$$
\begin{aligned}
&= \bar{n}_{\rm th}(1-\bar{n}_{\rm th})(\gamma_-)^2\, e^{-\Gamma_A T_p} \times \\
&\quad \int_{t1=0}^{T_p}\left[e^{\Gamma_B t_1} \int_{\tau=0}^{T_p - t1} \sin^2\!\left(\frac{\Omega_R\,\tau}{2}\right) e^{\Gamma_B \tau} d\,\tau \right] d\,t_1 \\
&= \frac{\bar{n}_{\rm th}(1-\bar{n}_{\rm th})}{2} \times \frac{(\gamma_-)^2}{\Gamma_B^2+\Omega_R^2} \times \left\{ \frac{\Omega_R^2(\Gamma_B^2+\Omega_R^2) e^{(\Gamma_B+\Gamma_1)T_p}}{\Gamma_1(\Gamma_B+\Gamma_1)\left[(\Gamma_B+\Gamma_1)^2+\Omega_R^2\right]} - \right. \\
&\quad \frac{e^{\Gamma_B T_p}\Gamma_B\Omega_R^2 - \Gamma_1\left[\Gamma_B^2 + (1-e^{\Gamma_B T_p})\Omega_R^2\right]}{\Gamma_B\Gamma_1(\Gamma_B+\Gamma_1)} - \\
&\quad \left. \frac{\left[\Gamma_B(\Gamma+\Gamma_B)^2 - \Omega_R^2\right]}{(\Gamma+\Gamma_B)^2+\Omega_R^2}\cos(\Omega_R T_p) - \frac{(\Gamma+2\Gamma_B)\Omega_R}{(\Gamma+\Gamma_B)^2+\Omega_R^2}\cos(\Omega_R T_p) \right\}
\end{aligned}
$$

with $\Gamma_A = \gamma_+ + \Gamma_1$ and $\Gamma_B = \gamma_- - \gamma_+ - \Gamma_1$. The term $e^{-\gamma_- T_p}$ reaches zero rapidly as soon as T_p reaches a few cavity lifetimes $1/\gamma_-$, which makes the oscillating terms in the curly bracket vanish. Introducing $k = \Omega_R/\gamma_-$ and $u = \Gamma_1/\gamma_-$, and assuming $\gamma_- \gg \gamma_+, \Gamma_1$, we find

$$
\begin{aligned}
p_{e,1} \;\simeq\; & \frac{k^2}{2(1+k^2)(u+u^2)} e^{-\gamma_- \bar{n}_{\rm th} T_p}\, \bar{n}_{\rm th} \times \\
& \left(\frac{1+k^2}{k^2+(1+u)^2} - e^{-\Gamma_1 T_p}(1+u) \right).
\end{aligned}
\tag{C.2}
$$

Given $\gamma_- T_p \gg 1$ and $\Gamma_1\ T_p \gg 1$, we have neglected in the above reasoning the smaller contribution of a single photon entering before the Rabi pulse starts.

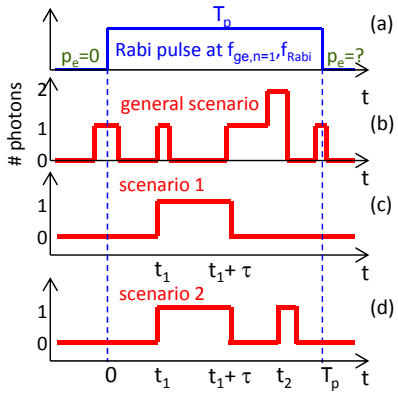

Figure C.1. Schematic illustration of the protocol and induced dynamics. a) Protocol of a spectroscopy pulse exciting the transmon in the presence of a photon. b) General scenario allowing arbitrary photon numbers. c) Scenario starting with no photons and considering a single excitation during T_p d) Same as c) except it allows for a repeated excitation after the previous one has decayed.

The contribution of scenario 2 with a second photon entering the cavity during the Rabi pulse after the first one has left is also negligible for the following reason: After the first excitation of the transmon and the first photon decay, the transmon frequency is shifted by χ and the transmon state $|e\rangle$ accumulates a deterministic phase $\varphi = \chi\,(t_2 - t_1 - \tau)$ at a rate faster than γ_+ so that at the entrance of the second photon at time t_2, the phase has been randomized and the new Rabi oscillation can increase or decrease $p_{e,1}$ with comparable probabilities. Consequently $p_{e,1}$ is well approximated by eq. C.2, provided it yields a very small $\bar{n}_{\mathrm{th}}$. It varies proportionally to $e^{-\gamma_- \bar{n}_{\mathrm{th}} T_p}\,\bar{n}_{\mathrm{th}}$, with a "geometrical" factor involving the ratios of the secondary rates to the main rate γ_-. This exponential scaling makes the method particularly sensitive, but only valid at small $\bar{n}_{\mathrm{th}}$.

Appendix D
Published article

Manipulating Fock states of a harmonic oscillator while preserving its linearity

K. Juliusson[1], S. Bernon[1], X. Zhou[1], V. Schmitt[1], H. Le Sueur[2],
P. Bertet[1], D. Vion[1], M. Mirahimi[3], P. Rouchon[4], and D. Esteve[1]
[1] *Quantronics group, SPEC, CEA, CNRS, Université Paris-Saclay, CEA Saclay, 91191 Gif-sur-Yvette, France.*
[2] *Centre de Sciences Nucléaires et de Sciences de la Matière, 91405 Orsay, France.*
[3] *INRIA Paris-Rocquencourt, Domaine de Voluceau, B.P. 105, 78153 Le Chesnay Cedex, France. and*
[4] *Centre Automatique et Systèmes, Mines-ParisTech, PSL Research University, 60, bd Saint-Michel, 75006 Paris, France.*
(Dated: July 18, 2016)

We present a new scheme for controlling the quantum state of a harmonic oscillator by coupling it to an anharmonic multilevel system (MLS) with first to second excited state transition frequency on-resonance with the oscillator. In this scheme that we call 'ef-resonant', the spurious oscillator Kerr non-linearity inherited from the MLS is very small, while its Fock states can still be selectively addressed via an MLS transition at a frequency that depends on the number of photons. We implement this concept in a circuit-QED setup with a microwave 3D cavity (the oscillator, with frequency 6.4 GHz and quality factor $Q_O = 2\times10^6$) embedding a frequency tunable transmon qubit (the MLS). We characterize the system spectroscopically and demonstrate selective addressing of Fock states and a Kerr non-linearity below 350 Hz. At times much longer than the transmon coherence times, a non-linear cavity response with driving power is also observed and explained.

The harmonic oscillator being an exactly solvable system with a single degree of freedom, is often taken as a model system in many areas of physics. In particular, for demonstrating coherent control of simple quantum systems, physicists have used cold electromagnetic resonators in the quantum regime, with their quantum states controlled by a single atom, be it a real one in cavity-QED [1] or an artificial one in circuit-QED [2, 3]. For instance, the preparation of a single photon Fock state by passing an atom through a cavity [4], or of an arbitrary quantum state using the Law and Eberly protocol [5–7] in circuit-QED, are landmark results. In circuit-QED relevant to this work, the resonator has a frequency ν_O in the microwave domain, and the artificial atom is a superconducting quantum bit that can be regarded as an ancillary multilevel system (MLS) with states $|g\rangle$,$|e\rangle$,$|f\rangle$,$|h\rangle\ldots$ possibly tunable in energy. The MLS can be used resonantly [6, 7], or off-resonantly [8] when its coupling to the resonator is sufficiently strong to split the transition frequency ν_{ge} into different lines at frequencies ν_n that depend on the photon number n [9]. In this so-called "photon number split" regime, any particular Fock state $|n\rangle$ is addressed at frequency ν_n, and symmetrically, the resonator can be driven coherently at a frequency $\nu_{O,|x\rangle}$ that depends on the MLS state $|x\rangle$. This allows for both manipulating and measuring the oscillator field in various ways, for instance by MLS-state conditional cavity phase shift [10], photon-number selective phase gates [11] that could lead to universal control of the oscillator field [12], or by Wigner and quantum state tomography of the field [13, 14].

This off-resonant method has been demonstrated with transmon qubits [15] coupled dispersively to the resonator, i.e. with detunings $|\Delta_{xy} = \nu_{xy} - \nu_O|$ between any ν_{xy} transition of the transmon and ν_O much larger than the coupling frequency g_{xy} between this transition and the cavity field. In this dispersive regime, the frequencies $\nu_n = \nu_{ge} + n\chi$ are equidistant and separated by the so-called dispersive shift $\chi \simeq 2\alpha\varepsilon^2$ [15], with $\alpha = \nu_{ef} - \nu_{ge}$ the transmon anharmonicity, $\varepsilon = g_O/\Delta$, $g_O \equiv g_{ge}$ the transmon-oscillator coupling, and $\Delta = \nu_{ge} - \nu_O$ their detuning. A drawback of this scheme is to transfer part of the transmon MLS anharmonicity to the oscillator [16, 17], which can drastically perturb its coherent dynamics [14, 18, 19] and necessitate careful design [16] and correction protocols [11]. This non-linearity [14, 15, 17] results in a shift of the oscillator frequency ν_O (or Kerr non-linearity) of about $K = \alpha\varepsilon^4$ per photon. K scaling as χ^2/α cannot be minimized (at fixed α) without losing the selectivity between Fock states. In this work, we propose a different transmon-oscillator coupling scheme (see Fig.1) that yields a much smaller Kerr non-linearity for the same Fock state selectivity. The idea consists in having the ef transition resonant with ν_O, i.e. $\Delta = -\alpha$, to displace significantly the qubit excited levels even at small coupling g_O, while at the same time staying in the dispersive regime for the first transition ν_{ge} to get a small non-linearity. We explain in details in the next section this 'ef-resonant' condition when the MLS is a slightly anharmonic three level system, for which analytic results can be obtained. Then, we describe in section II our implementation of the proposal, and characterize it experimentally in section III.

I. THE 'EF-RESONANT' COUPLING SCHEME FOR A HARMONIC OSCILLATOR

To explain the interest of our coupling scheme in the simplest way, we first consider the case of a harmonic oscillator (O) with frequency ν_O and annihilation operator a, coupled to a three-level system (3LS) with eigenstates

$\{|g\rangle, |e\rangle, |f\rangle\}$ and lowering operator a_q. We also assume a weak anharmonicity $\alpha = \nu_{ef} - \nu_{ge} \ll \nu_{ge}$, such that a_q can be approximated by the annihilation operator of a harmonic oscillator restricted to three levels. The two subsystems obey the resonant condition $\nu_{ef} = \nu_O$ (detuning $\Delta = \nu_{ge} - \nu_O = -\alpha$) and are subject to an exchange interaction with coupling frequency $g_O \ll \alpha$, yielding the Hamiltonian

$$\begin{array}{l} H = H_O + H_{3LS} + H_{coupling}, \\ H_O = h\nu_O a^\dagger a, \\ H_{3LS} = h\left(\nu_O a_q^\dagger a_q - \alpha\,|e\rangle\langle e| - \alpha\,|f\rangle\langle f|\right), \\ H_{coupling} = hg_O\left(a^\dagger a_q + a a_q^\dagger\right). \end{array} \tag{1}$$

This coupling makes the Hamiltonian matrix block-diagonal in the basis $|xn\rangle \equiv |x\rangle \otimes |n\rangle$ ($x = g, e, f$), with subsequent blocks of size 1, 2, 3, 3, 3... Using the reduced coupling $\varepsilon = -g_O/\alpha$, these blocks write

$$[0]_{|g0\rangle}, h\left(\nu_O I_2 - \alpha\begin{bmatrix} 0 & \varepsilon \\ \varepsilon & 1 \end{bmatrix}\right)_{|g1\rangle,|e0\rangle}, h\left(n\nu_O I_3 - \alpha\begin{bmatrix} 0 & \sqrt{n}\varepsilon & 0 \\ \sqrt{n}\varepsilon & 1 & \sqrt{2\,(n-1)}\varepsilon \\ 0 & \sqrt{2\,(n-1)}\varepsilon & 1 \end{bmatrix}\right)_{Bn}, \tag{2}$$

with I_k the identity matrix of dimension k and $B_n = \{|gn\rangle, |e\,(n-1)\rangle, |f\,(n-2)\rangle\}$ the basis for $n \geq 2$. The diagonalization of each block yields analytical eigenenergies and vectors, which for $n \geq 2$ are functions of the three real solutions of the cubic equation $x^3 - 2x^2 + \left[1 + 2\epsilon^2 - 3n\epsilon^2\right]x + n\varepsilon^2 = 0$. To shed light on the physics, we expand these analytical quantities in the small parameter ε. As shown in Fig. 1, the levels form three distinct energy ladders$\{|\widetilde{gn}\rangle\}$, $\{|-n\rangle\}$ and $\{|+n\rangle\}$: The ladder$\{|\widetilde{gn}\rangle\}_{n\geq 0}$ corresponds to the almost unperturbed oscillator when the 3LS is left in its ground state. With eigenenergies and eigenvectors

$$\begin{array}{l} E(|\widetilde{gn}\rangle) = nh\left[\widetilde{\nu}_O + (n-1)K/2\right] + o(\epsilon^5) \\ |\widetilde{gn}\rangle = \left[1 - n\varepsilon^2/2, -\sqrt{n}\varepsilon, \sqrt{2n\,(n-1)}\varepsilon^2\right]_{Bn} + o(\epsilon^3)\,, \end{array} \tag{3}$$

this effective oscillator $\tilde{O}$ has a shifted frequency $\widetilde{\nu}_O = \nu_O + \alpha\left(\varepsilon^2 - \varepsilon^4\right)$, and a small Kerr non-linearity $K = 2\alpha\varepsilon^4$ inherited from the 3LS. The two other ladders $\{|\pm n\rangle\}$ (extended down to $n = 0$ by $|+0\rangle \equiv |-0\rangle \equiv \left|\widetilde{g0}\right\rangle$ and $|+1\rangle \equiv |-1\rangle \equiv \left|\widetilde{e0}\right\rangle$) have energies and eigenvectors

$$\begin{array}{l} \{E(|\pm n\rangle)\} = \{0, h\left[\nu_O - \alpha\left(1 + \varepsilon^2\right) + o(\varepsilon^3)\right], ..., h\left[n\nu_O - \alpha\left(1 \pm \sqrt{2\,(n-1)}\varepsilon + n\varepsilon^2/2 + o(\varepsilon^3)\right)\right]\} \\ \{|\pm n\rangle\} = |g0\rangle, \begin{bmatrix} \varepsilon \\ 1 - \frac{\varepsilon^2}{2} \end{bmatrix}, ..., \begin{bmatrix} \epsilon\sqrt{\frac{n}{2}} \pm \sqrt{\frac{n}{n-1}}\frac{7n-8}{8}\varepsilon^2 \\ \frac{1}{\sqrt{2}} \pm \frac{n}{8\sqrt{n-1}}\varepsilon + \frac{(33n-32)n}{64\sqrt{2}(n-1)}\varepsilon^2 \\ \pm\frac{1}{\sqrt{2}} - \frac{n}{8\sqrt{n-1}}\varepsilon + \frac{n^2}{64\sqrt{2}(n-1)}\varepsilon^2 \end{bmatrix}_{Bn} + o(\varepsilon^3) \end{array}. \tag{4}$$

For $n \geq 2$ the zeroth-order approximation in ϵ of these eigenvectors are simply the symmetric and anti-symmetric superposition of $|e\,(n-1)\rangle$ and $|f\,(n-2)\rangle$. A particular "Fock state" $|\widetilde{gn}\rangle$ of $\tilde{O}$ is selectively manipulable by addressing the $|\widetilde{gn}\rangle \to |\pm\,(n+1)\rangle$ transitions to the hybridized oscillator-transmon states, at frequencies $\nu_{\pm n} = \nu_{ge} \pm \sqrt{2n}g_O + (3n+1)g_O\varepsilon/2 + o(\varepsilon^2)$ (with a Rabi frequency about $\sqrt{2}$ slower for all $n > 0$ than for the pure $|g\rangle \to |e\rangle$ transition). Note that these frequencies $\nu_{\pm n}$ do not vary linearly with n as in the usual dispersive case, but as $\sqrt{n}$. Selective addressing of $|\widetilde{gn}\rangle$ requires the separation $\Delta\nu_{\pm n} = \nu_{\pm(n+1)} - \nu_{\pm n}$ to be larger than the transition linewidth. A second condition is that the driving strength of the $\nu_{\pm n}$ transition is low enough to avoid driving off-resonantly the neighboring transitions at $\nu_{\pm(n+1)}$.

It is now interesting to compare the Kerr non-linearity $K = 2\alpha\,(g_O/\Delta)^4$ obtained here with the value $K' =$

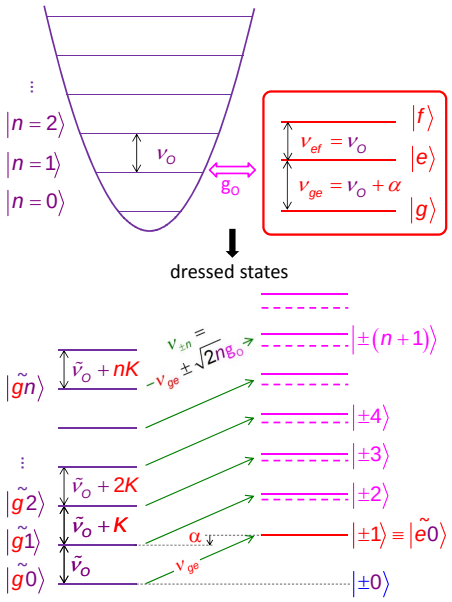

Figure 1. 'MLS ef-resonant' scheme for manipulating Fock states $|n\rangle$ of a quantum harmonic oscillator. Left: the oscillator with angular frequency ν_O is coupled with a coupling frequency g_O to a multilevel system (MLS) with eigenstates$\{|g\rangle, |e\rangle, |f\rangle, ...\}$, the $|e\rangle \leftrightarrow |f\rangle$ transition of which is resonant with ν_O, whereas the $|g\rangle \leftrightarrow |e\rangle$ transition is detuned by α. Right: The resulting energy diagram consists of a quasi-harmonic ladder $\{|\widetilde{gn}\rangle\}$ when the 3LS is left unexcited, and of two anharmonic ladders of levels $|\pm n\rangle$ that correspond approximately to symmetric and anti-symmetric superpositions of $|e\,(n-1)\rangle$ and $|f\,(n-2)\rangle$ states for $n \geq 2$. The $|\widetilde{gn}\rangle \leftrightarrow |\pm\,(n+1)\rangle$ transitions can be driven at different frequencies $\nu_{ge} \pm \sqrt{2\,(n-1)}g_O$ to manipulate selectively any $|\widetilde{gn}\rangle$.

$\Delta^{'}\left(g_O^{'}/\Delta^{'}\right)^4$ that would be obtained for a two-level system or the value $K" = \alpha"\left(g_O"/\Delta"\right)^4$ obtained in perturbation for a transmon in the far dispersive regime $g_O", \alpha" \ll \Delta"$ [17], keeping the same separation $S = \sqrt{2}g_O = 2\alpha"\left(g_O"/\Delta"\right)^2$ between the first two Fock state dependent excitation frequencies. With respect to the far dispersive case, the new non-linearity is thus reduced by a factor $K''/K = \left(\alpha/\alpha''\right)(\alpha/S)^2/2$ that can be made large easily. This reduction factor, which reaches several hundreds (at fixed transmon anharmonicity $\alpha = \alpha"$) in our implementation of section II, is what makes our 'ef-resonant' scheme interesting. What we show here with a simple ef-resonant 3-LS is that getting out of the perturbation regime $\alpha" \ll \Delta"$ reduces drastically the Kerr nonlinearity. However considering only three levels makes the argumentation only qualitative for a transmon at large number of photons in the oscillator, and a quantitative evaluation requires taking into account at least the fourth transmon level as we do in section III.

II. EXPERIMENTAL IMPLEMENTATION

We implement the proposed 'ef-resonant' scheme in a three-dimensional circuit-QED setup [20] combining a cavity with input (1) and output (2) ports and a tunable transmon qubit [15] (see Fig. 2a-b). To be superconducting at low temperature and have a high internal quality factor, the cavity is made of two blocks of pure aluminum, which are milled, pierced, polished, and chemically etched over about 20 µm. The transmon is fabricated on sapphire by double-angle evaporation of Al and oxidation, through a suspended shadow mask made by e-beam lithography. It has two pads connected by a 2.6 mm long wire including a magnetic flux tunable Josephson junction with a SQUID geometry located 50 µm above the bottom pad. This enables tuning the transmon energy spectrum and reaching the 'ef resonant' condition. The transmon is only partly inserted in the cavity so that the SQUID remains about 0.1 mm outside, in the applied external magnetic field. More precisely, the bottom part of the transmon with the SQUID is held and protected by a copper block, the other side being inserted in the cavity through a slit in the bottom wall. The two halves of the cavity are then pressed one against the other with an indium seal in-between.

In our design the TE120 cavity mode is used as the quantum oscillator O at frequency $\nu_O \sim 6.4$ GHz whereas mode TE210 at frequency $\nu_R \sim 7.3$ GHz is used for reading the quantum state of the transmon dispersively [2, 3]. The transmon and the ports are thus placed very close to a node of mode O so that the corresponding coupled quality factor Q_O is dominated by the internal losses, and the transmon-oscillator coupling g_O is about 10 MHz. They are also placed at an antinode of mode R to get a strong transmon-readout coupling $g_R \sim 150$ MHz and thus a large enough dispersive shift $\chi_R \sim 10$ MHz, and a low coupled quality factor $Q_R \sim 15 \times 10^3$ allowing fast readout of the transmon. The exact positions as well as the precise transmon geometry are determined using the CST 3D microwave simulator and methods adapted from [17]. Attention is paid to keep the transmon's charging energy (one electron) below 300 MHz × h in order to avoid variations of the level f energy due to charge parity fluctuations [21]. For better measurement efficiency, output port 2 is about 6 times more strongly coupled to each mode than input port 1.

The equivalent circuit of the system is shown in Fig. 2c. The transmon-cavity system is mounted inside a coil placed in a mu-metal shield, and is attached to the cold plate of a cryofree dilution refrigerator with base temperature 35 mK. It is connected to the electrical setup of Fig. 2d, which includes a home made quantum limited Josephson parametric amplifier (JPA) similar to [22]. Simple continuous microwave measurements at a single frequency are done with a vectorial network analyzer (VNA), whereas pulsed measurements involving ν_O, ν_R, and one or two transmon frequencies use heterodyne modulation and homodyne demodulation as described in

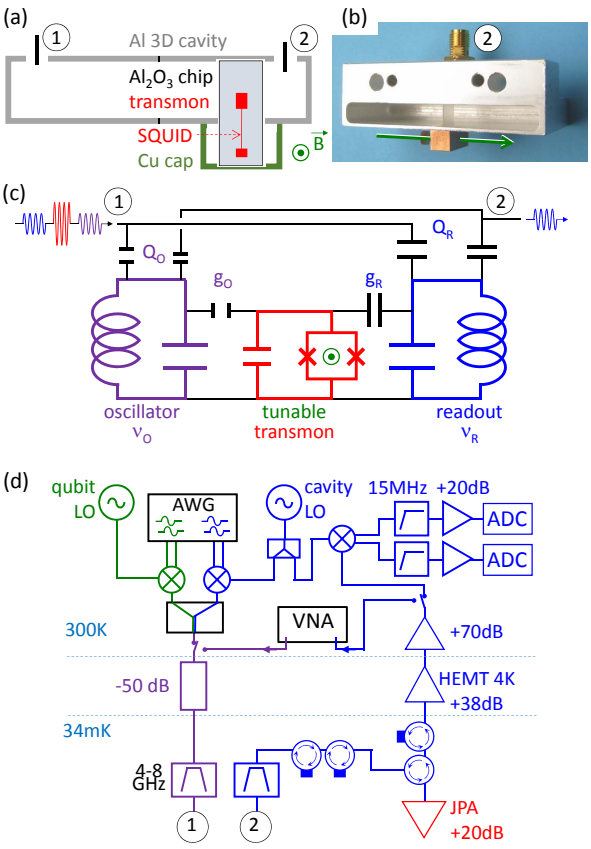

Figure 2. Circuit-QED implementation of the 'ef-resonant' scheme. (a) The harmonic oscillator O and the MLS are the mode 120 of a superconducting Al cavity and a tunable transmon qubit with a SQUID. The transmon chip is inserted only partly in the cavity, the SQUID being exposed to a dc magnetic field $\vec{B}$. The transmon is weakly coupled to O and strongly to the cavity mode 210 used for dispersive readout of the transmon state. The two modes have quality factors $Q_O = 2 \times 10^6$ and $Q_R = 15 \times 10^3$. (b): Picture of one half-cavity with chip and Cu cap. (c) Equivalent electric circuit of the system with relevant frequencies $f_{R,O}$, quality factors $Q_{R,O}$, and coupling frequencies $g_{R,O}$. O is driven coherently and resonantly through port 1 (purple pulse). Fock state $|gn\rangle$ are manipulated by driving the $|\widetilde{gn}\rangle \rightarrow |+n\rangle$ transition (red pulse). A projective measurement on Fock state $|\widetilde{gn}\rangle$ is obtained by a π pulse at ν_{+n} followed by a readout pulse (in blue). (d) Electrical setup at room temperature (300K) and inside the dilution refrigerator: Cavity resonances are measured with continuous waves using a vectorial network analyzer (VNA) whereas pulsed experiments use heterodyne modulation and demodulation. Microwave pulses at the cavity (qubit) frequencies $\nu_{O,R}$ (ν_{+n}) are obtained by single sideband mixing of a continuous microwave (LO) with an intermediate frequency modulated pulse generated by two channels of an arbitrary waveform generator (AWG). All pulses travel along an attenuated and filtered line to cavity port 1. The readout signal transmitted at port 2 is filtered, isolated from backward propagating noise, amplified with a parametric amplifier (JPA) in reflection, a high electron mobility transistor (HEMT), and room temperature amplifiers, then demodulated to produce two quadratures, which are finally filtered, amplified and digitized (ADC).

Fig. 2d.

III. EXPERIMENTAL RESULTS

A. Spectroscopic characterization

Once at 35 mK, the system is first characterized with the VNA as a function of the current in the coil (see Fig. 3a-b). The lowest transition frequencies of the hybridized readout mode-transmon system yields two peaks at frequencies (red points) that are periodic in flux Φ, one period corresponding to one flux quantum $\Phi_0 = h/2e$. Away from the avoided crossing, these peaks tend to ν_R and ν_{ge}. At $\Phi \simeq 0.5\Phi_0$, modes R and O are unperturbed and one gets their frequencies (central peaks of panels b-top and b-bottom) as well as the total quality factor $Q_O = 2.2 \times 10^6$ of the oscillator, which corresponds to an energy relaxation time $T_O = 54\,\mu s$. At $\Phi = 0.23\Phi_0$ and $0.31\Phi_0$ the transmon frequency ν_{ge} anti-crosses ν_R and ν_O, yielding the double peaks of panels b-top and b-bottom, separated by twice the coupling frequencies $g_R = 149\,\text{MHz}$ and $g_O = 7.45\,\text{MHz}$. The setup for pulsed spectroscopy is then used to excite the transmon-oscillator system with one or several pulses, and then detect this excitation from a change of the transmission $S_{21}(\nu_R)$ of the readout mode (see pulses in Fig. 2c). Figure 3c shows how the readout line is dispersively shifted when the transmon is left in $|g\rangle$, partly excited in $|e\rangle$ with a single pulse at ν_{ge}, or partly excited in $|f\rangle$ with the same first pulse and a second one at ν_{ef}. The different readout lines g,e and f do not overlap so that at the top of any peak, a change of the qubit state induces a complete suppression of the transmission. The $\nu_{ef}(\Phi)$ dependence (green line in panel a) is thus obtained by finding first $\nu_{ge}(\Phi)$ and then scanning for each Φ a second tone around ν_{ef} and measuring $S_{21}(\nu_{R,e})$ at the top of the e readout peak.

The 'ef-resonant' condition that we target occurs at $\Phi_{ef-r} = 0.291\Phi_0$ (vertical cyan line in panel a), when the ef transition crosses ν_O, leading to the hybridization discussed in section I and to the splitting of the ef peak into two symmetric peaks $\nu_{e0\rightarrow\pm1}$ (shown in magenta in panel b-middle). The dataset of panel b yields the effective anharmonicity $\alpha = -261\,\text{MHz}$ ('effective' means here in presence of the additional readout mode that shifts dispersively the transmon levels). From now on, the system is further characterized at Φ_{ef-r} with $S_{21}(\nu_{R,g})$ being measured at the top of the g readout peak (see panel c). At this point, we obtain the qubit relaxation time $T_1 = 1.9\,\mu s$ and coherence time $T_2^* = 2.4\,\mu s$. The photon resolved transition frequencies $\nu_{\pm n}$ are then found by filling mode $\widetilde{O}$ with a coherent state $|\beta\rangle = \sum \sqrt{p_\beta(n)}\,|n\rangle$ using a first resonant excitation pulse at $\nu_{\widetilde{O}}$ and scanning the frequency of a second pulse about ν_{ge}. Panel d shows the peaks at frequencies ν_n for $n = -1, 0, 1, ..., 16$, resulting from three different values of β; the peak amplitudes for each β approximately reproduce the Poisson distribu-

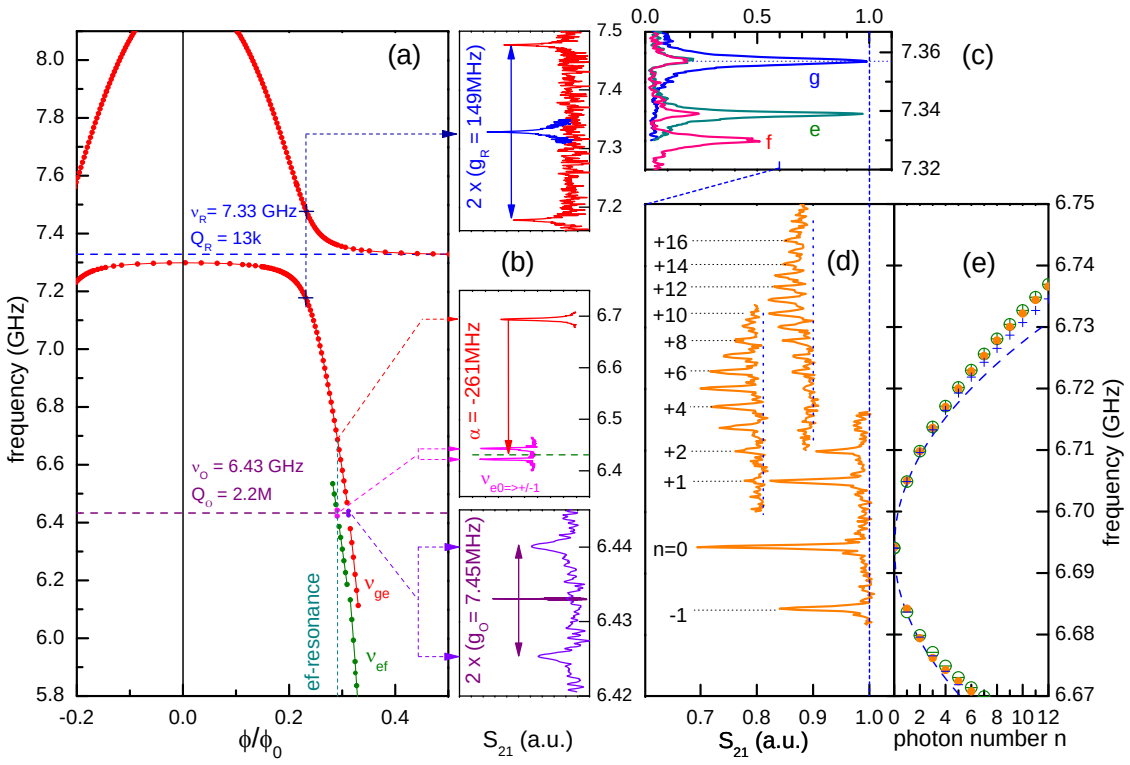

Figure 3. Spectroscopic characterization of the system. (a) Measured transition frequencies as a function of the magnetic flux ϕ applied through the transmon SQUID. Blue and purple horizontal dashed lines correspond to the readout and oscillator frequencies ν_R and ν_O, red dots to the hybridization of ν_{ge} and ν_R, and the green line to ν_{ef}. The 'ef-resonant' condition is obtained at $\nu_O = \nu_{ef}$. (b) Spectra determining the qubit-resonator coupling frequencies $g_{R,O}$, as well as the qubit anharmonicity α. Top: spectra around ν_R with ν_{ge} either far away (blue peak) or anti-crossing ν_R (two red peaks). Bottom: spectra around ν_O with ν_{ge} either far away (purple peak) or anti-crossing ν_O (two violet peaks). Middle: spectrum at the 'ef-resonant' working point showing the ge (red) and $\left|\widetilde{e0}\right\rangle \rightarrow |\pm 1\rangle$ (magenta) transitions. (c) Readout resonator resonance when the qubit is left in $|g\rangle$ or excited in $|e\rangle$ or $|f\rangle$. Note that the residual thermal population of level e is well below 1%. The dashed line indicates the frequency at which the readout mode transmission S_{21} is measured in panel (d). (d) Qubit spectra measured at the 'ef-resonant' point for three different fillings of $\tilde{O}$ ($\beta \simeq 0.54$, 4.5 and 10 - last two horizontally shifted for clarity), showing transitions $|\widetilde{gn}\rangle \leftrightarrow |\pm n\rangle$ (noted $\pm n$) from $-n = -1$ to $n = 17$. (e) Transition frequencies $\nu_{\pm n}$ deduced (orange dots) from spectroscopy (d), calculated in section I (+ and - symbols), and numerically computed by diagonalization of the system Hamiltonian (+ and - open circles). Lines correspond to the parabolic approximation $\nu_{\pm n} \simeq \nu_{ge} \pm \sqrt{2n} g_O$.

tions $p_\beta(n)$ expected for coherent states. As opposed to the dispersive case and as expected, the peaks get nearer to each other with increasing n: in panel e their frequencies (orange dots) are compared to the analytical expression of section I (calculated with three transmon levels) and to the $\nu_{\pm n}$ values resulting from the numerical diagonalization of an effective oscillator-transmon Hamiltonian also including the fourth transmon level h (the numerical diagonalization with only three levels coincide with analytical results). A good agreement is found between the experiment and the effective four-level transmon model using the measured values of ν_O, $\nu_{ge}(\Phi_{ef-r})$, α and g_O, as well as the shifted energy $h\,(3\nu_{ge} - 848\,\mathrm{MHz})$ of eigenstate $|h\rangle$ calculated from $\nu_R(\Phi_{ef-r})$ and g_R.

B. Oscillator field characterization by selective π pulses on $+n$ transitions

Having characterized the system energy diagram, we now address individually the photon number resolved transitions $+n$ to fully characterize the field and probe the harmonic character of oscillator $\widetilde{O}$: as an example, we fill $\widetilde{O}$ with coherent states $|\beta\rangle$ and retrieve them by standard quantum state tomography. This tomography involves the measurement of the occupation probabilities $p(n)$ of several Fock states $|n\rangle$. As done in [14] for the dispersive case, the Fock state population $p(n)$ is simply transferred to a qubit excited state, which is then read out. In our 'ef-resonant' scheme this transfer between $|\widetilde{gn}\rangle$ and $|+n\rangle$ consists in applying a π pulse on the $+n$ transition. These π pulses at frequencies ν_{+n} have a Gaussian shape with 140 ns-long standard deviation, and

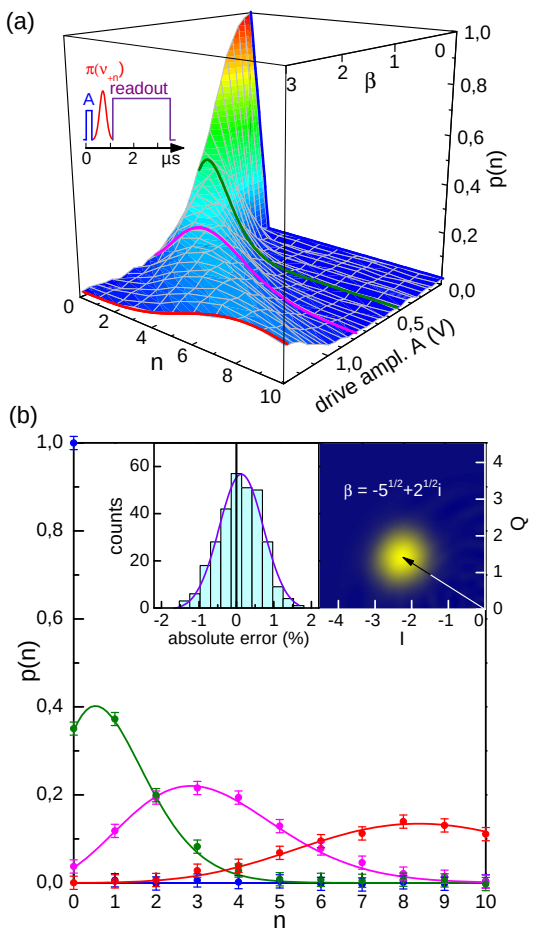

Figure 4. Generation and measurement of coherent states $|\beta\rangle$ in the oscillator mode: a state is obtained from a 0.3 µs long rectangular pulse with frequency $\nu_{\widetilde{O}}$ and amplitude A (expressed here in Volt on the AWG of fig. 2d); a π pulse on one of the $+n$ transition then excites conditionally the transmon and the variation $\Delta S_{21}(\nu_R, A, n)$ of the cavity transmission is measured. (a) Occupation probability $p(n)$ of Fock state $|n\rangle$ for $n \in [0, 10]$ and for increasing A. $p(n)$ is obtained by dividing $\Delta S_{21}(\nu_R, A, n)$ by a calibration factor c_n resulting from a fit of the coherent model $\beta(A) = kA$ to the whole dataset: the fitted coefficients$\{c_0, ..., c_{10}\} = \{0.764,\ 0.835,\ 0.847,\ 0.846,\ 0.833,\ 0.854,\ 0.846,\ 0.834,\ 0.847,\ 0.832,\ 0.841\}$ differ by less than 3%, except for c_0 that corresponds to a transition between transmon states not hybridized with mode O. (b) $p(n)$ cuts (also shown in a) at $A = 0$ (blue), 0.45 (green), 0.8 (magenta) and 1.3 V (red) showing both measured data (dots with $\pm 2\sigma$ error bars) and expected Poisson distributions (lines). Residual errors between data and fit are homogeneously distributed all over the dataset (not shown) and Gaussianly distributed with a standard deviation $\sigma = 0.6\%$ and a shift of 0.1% (left inset). Right inset is the reconstruction of the Wigner function of a targeted state $|\beta = -\sqrt{5} + i\sqrt{2}\rangle$ by tomography and maximum likelihood analysis (see text).

are calibrated in amplitude for $n \in [0, 10]$.

Because of many possible imperfections in the transfer or readout process of $p(n)$, such as different relaxation times of $|+n\rangle$ for different n during drive and/or readout, the $p(n)$ measurement method is carefully calibrated as described now: A series of rectangular pulses with fixed frequency $\widetilde{\nu}_O$, fixed 0.3 µs long duration, and increasing amplitudes A are used to generate a priory coherent states $|\beta\rangle$ in $\widetilde{O}$; immediately after, a π pulse is applied on one of the $+n$ transition, and the relative decrease $s(n, A) = \triangle S_{21}(\nu_{R,g})$ of the readout mode transmission is measured with a final pulse; this signal, averaged over 40000 sequences (separated by $\sim 6T_O$ to let the field relax to its ground state) is measured for $n \in [0, 10]$ and for 26 values of A. Then a model assuming that the coherent amplitude $\beta = kA$ is proportional to the input amplitude A and that the raw signal $s(n, A)$ reproduces the Poisson distribution $p_\beta(n)$ of coherent states $|\beta\rangle$ up to calibration coefficients c_n that depend only on n, is fitted to the whole data set. The fit $s(n, A) = c_n p_{kA}(n)$, shown in Fig. 4, yields the eleven parameters $\{c_0, ..., c_{10}\}$ as well as the filling rate $k = 2.29\,\mathrm{V}^{-1}$. The residual error of the fit is homogeneously and Gaussianly distributed with a standard deviation of only 0.6%, which confirms the validity of the model.

The calibration coefficients c_n being known, the occupation probabilities $p_\rho(n) = s(n, \rho)/c_n$ can now be measured to fully characterize any state ρ of the oscillator field using standard quantum field tomography [23] and maximum likelihood techniques [24]. As a demonstration, we target a coherent state $|\beta = -\sqrt{5} + i\sqrt{2}\rangle$, prepare it using a coherent rectangular pulse with proper amplitude and phase, and then measure it. This is done by recording the Fock state probabilities $p(n, \gamma)$ for $n \in [0, 7]$ and for 240 different complex displacements γ of $|\beta\rangle$, and then reconstructing the field density matrix ρ in a Hilbert space truncated to 18 photons, by maximizing the likelihood of the $\{p(n, \gamma)\}$ dataset. The corresponding Wigner function is shown in the bottom inset of Fig. 4b. The fidelity $\mathrm{Tr}\left(\sqrt{\sqrt{\rho}\,|\beta\rangle\langle\beta|\,\sqrt{\rho}}\right)$ of the reconstructed ρ to the targeted state is of order 98% immediately after the calibration (the calibration has to be redone every three days, typically).

C. Non-linearities of the oscillator

We now check experimentally our claim of a very small Kerr effect for the 'ef-resonant' scheme. With the $g_O = 7.45\,\mathrm{MHz}$ and $\alpha = -261\,\mathrm{MHz}$ values determined spectroscopically, the Kerr non-linearity calculated for the three level transmon model of section I is $K = -346\,\mathrm{Hz}$ per photon. However, when diagonalizing numerically the Hamiltonian of the system including the fourth transmon energy level, the Kerr effect is found to be even smaller, to depend on n, and to cancel and reverse its sign at about 20 photons. Such an ultra-small Kerr effect would yield no sizable phase accumulation of the different Fock states over the cavity relaxation time $T_O = 54\,\mu s$. This makes it difficult to measure it dynamically, by recording either the trajectory of a field state in phase space as in

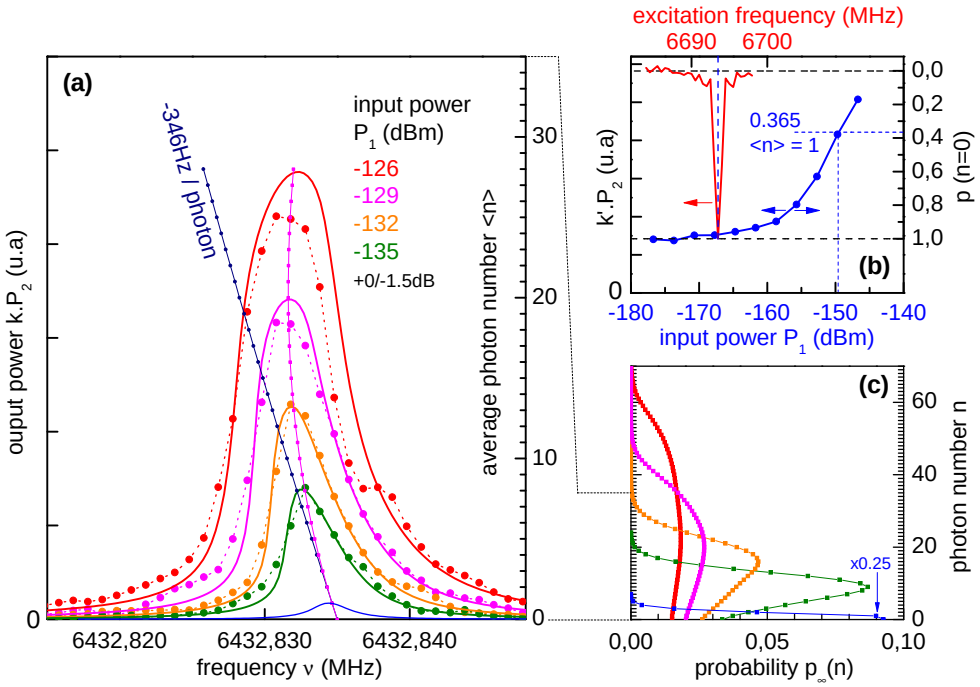

Figure 5. Steady state non-linearities of oscillator $\widetilde{O}$ in the 'ef-resonant' condition. (a) Transmitted power (in linear units) measured with the VNA (dots joined by dotted lines) for input powers P_1 varying from -135 dBm to -126 dBm by steps of 3dB. Solid lines are the steady state average photon number $< n >$ in mode $\widetilde{O}$ simulated numerically (see text) for the same P_1 values according to calibration, and for $P_1 = -149.6\,\mathrm{dBm}$ ($< n >= 1$) at resonance. The non-linearity in frequency calculated with four transmon levels (magenta line) is smaller than -346 Hz/photon Kerr constant (dark blue line). A large non-linearity in power is however observed (see text). b) Calibration of P_1 versus $< n >$. Red: variation of the transmitted readout amplitude $|P_2(\nu)|$ when keeping mode $\widetilde{O}$ in its ground state and detuning the qubit excitation frequency ν of a π pulse away from the +0 transition at ν_{ge} (dashed vertical line). Blue: Same readout amplitude after the resonant qubit π pulse when filling $\widetilde{O}$ by a continuous tone with frequency $\nu_{\widetilde{O}}$ and variable input power P_1. The average photon number $< n >$reaches 1 at $P_1 = -149.6\,\mathrm{dBm}$ (blue dashed lines - see text). (c) Simulated photon number distributions $p_\infty(n)$ at the top of each simulated resonance of panel (a). The blue curve for$< n >= 1$ has been multiplied by 0.25 for clarity.

[14, 18], or the power dependence of the resonance line shape at short time as in the supplementary information of [14]. Consequently, we simply measure the steady-state transmitted power $P_2(\nu)$ of mode $\widetilde{O}$ as a function of the excitation frequency ν at several input powers P_1, using the VNA with a narrow enough measuring bandwidth of 1 kHz. The corresponding curves are shown in Fig. 5a (dots) in arbitrary units of the output power P_2 (left scale).

Analyzing quantitatively the dataset requires a precise knowledge of the average photon number $< n >$ in the resonator as a function of ν and P_1. In this aim, we perform the following additional in-situ calibration and data analysis. We first use the transmon to determine experimentally the input power $P_{1,1} = -149.6\,\mathrm{dBm}$ that populates the cavity with $< n >= 1$, which corresponds to $p_{\beta=1}(n = 0) = 0.365$ (see Fig. 5b) assuming a coherent steady state $\rho_1 = |\beta = 1\rangle\langle\beta = 1|$. Then quantum simulations of the oscillator O coupled to the effective 4 level transmon are performed using the QuTiP Python toolbox [25], the already mentioned measured parameters, and the calibrated P_1. Solid lines in Fig. 5a show the resonance lines $< n > (\nu)$ obtained with the steady state solver of QuTiP. By scaling vertically the experimental curves so that simulation and experiment match for $P_1 = -135\,\mathrm{dBm}$, we obtain a fair agreement for all curves, leading to the following results: First the resonance lines display indeed a very small Kerr effect, with a shift towards lower frequency with increasing P_1 significantly smaller than K (oblique dark blue line), and changing sign between $< n >= 15$ and 25, in good agreement with the calculated shift (magenta line).

A second and unanticipated effect is that although the non-linearity in frequency is small, a large non-linearity in input power is observed, with P_2 and $< n >$ increasing by a factor of only 3 when P_1 is increased by a factor 8 (see extreme curves in Fig. 5a). Simulating the time evolution of the system initialized in its ground state and driven coherently at $\widetilde{\nu}_O$ reveals the cause of this non-linearity in P_1: the small hybridization of the oscillator with the transmon (see Eq. 3) that has finite coherence times (T_1, T_2^*), progressively induces Fock state dephasing. The increasing field perfectly coherent at the beginning of the dynamics slowly becomes incoherent when ap-

proaching the steady state,which reduces its amplitude. This is illustrated in Fig. 5c by the photon number distributions $p_{P1,t=\infty}(n)$ obtained from the steady state solver at the top of each resonance curve of panel a: although $p_{P1,t=\infty}(n)$ corresponds almost exactly to the Poisson distribution for ρ_1 (which validates the calibration of P_1 in the previous section), the other distributions for larger $< n >$ are less and less Poissonian. Large coherent states can nevertheless be obtained at times shorter than a few tens of T_2^*, as observed in the previous section for a duration of the coherent drive $t \simeq T_2^*/8$. Note that the transmon-induced cavity non-linearity in power observed and simulated here also exists in the dispersive regime, and is an effect that would deserve a theoretical evaluation.

IV. CONCLUSION

We have described a way to manipulate the quantum state of a harmonic oscillator by coupling it to a anharmonic multilevel system (MLS), without paying the price of a large Kerr non-linearity of the oscillator inherited from the MLS. We have demonstrated our 'ef-resonant' scheme using a 3D circuit-QED setup, in a new geometry involving a tunable transmon qubit partially inserted inside a single multimode superconducting cavity. Fock state manipulation was demonstrated by quantum state tomography of a coherent field in the cavity. The non-linearity was measured to be very small, provided the total field manipulation time is not much longer than the qubit coherence time. Our setup and coupling scheme provide a new platform for manipulating at will mesoscopic quantum fields inside a harmonic resonator, and producing non-classical states in various ways. In particular, the ef-resonant scheme would reduce the Kerr non-linearity of the promising platform proposed and developed [8, 26, 27] for encoding quantum information in Schrödinger cat states of the cavity field. We plan to use this scheme for demonstrating the quantum Zeno dynamics of the cavity field as proposed in [28].

ACKNOWLEDGMENT

We gratefully acknowledge discussions within the Quantronics group, technical support from P. Orfila, P. Senat, J.C. Tack, D. Duet, and V. Padilla, as well as financial support from the European research contracts CCQED and ScaleQIT.

[1] S. Haroche and J.M. Raimond, Eploring the Quantum (Oxford University Press, Oxford, 2006)
[2] A. Blais *et al.*, PRA **69**, 062320 (2004).
[3] A. Wallraff *et al.*, Nature (London) **431**, 162 (2004).
[4] M. Brune *et al.*, Phys. Rev. Lett. **76**, 1800 (1996).
[5] C. K. Law and J. H. Eberly, Phys. Rev. Lett. **76**, 1055 (1996).
[6] M. Hofheinz *et al.*, Nature, **454**, 310 (2008).
[7] M. Hofheinz *et al.*, Nature, **459**, 546 (2009).
[8] Z. Leghtas *et al.*, Phys. Rev A, **87**, 042315 (2013).
[9] D. I. Schuster *et al.*, Nature, **445**, 515 (2006).
[10] M. Brune *et al.*, Phys. Rev. Lett. **77** , 4887 (1996).
[11] R. W. Heeres *et al.*, Phys. Rev. Lett. **115**, 137002 (2015).
[12] S. Krastanov *et al.*, Phys. Rev. A **92** , 040303(R) (2015).
[13] S. Deléglise *et al.*, Nature, **455**, 510 (2008).
[14] G. Kirchmair *et al.*, Nature, **495**, 205 (2013).
[15] J. Koch *et al.*, Phys. Rev. A, **76**, 42319 (2007).
[16] J. Bourassa, F. Beaudoin, JM. Gambetta, and A. Blais, Phys. Rev. A **86**, 013814 (2012).
[17] S. E. Nigg *et al.*, Phys. Rev. Lett, **108**, 240502 (2012).
[18] Y. Yin *et al.*, Phys. Rev. A, **85**, 23826 (2012).
[19] B. Yurke and D. Stoler, Phys. Rev. Lett., **57**, 1 (1986).
[20] H. Paik *et al.*, Phys. Rev. Lett, **107**, 240501 (2011).
[21] D. Ristè *et al.*, Nature Comm., **4**, 1913 (2013).
[22] X. Zhou *et al.*, Phys. Rev. B, **89**, 214517 (2014).
[23] M.G.A Paris and J. Rehacek. Quantum State Estimation. Springer, 2004.
[24] Z. Hradil, J. Rehacek, J. Fiurasek, and M. Jezek, Maximum-likelihood methods in quantum mechanics, Lect. Notes Phys. **649**, 59 (2004).
[25] J. R. Johansson, P. D. Nation, and F. Nori, Computer Physics Communications **183**, 1760 (2012).
[26] B. Vlastakis *et al.*, Science, **342**, 6158 (2013).
[27] C. Wang *et al.*, Science, **352**, 6289 (2016).
[28] J.M. Raimond *et al.*, Phys. Rev. A, **86**, 32120 (2012).

Bibliography

[1] A. A. Abdumalikov Jr, J. M. Fink, K. Juliusson, M. Pechal, S. Berger, A. Wallraff, and S. Filipp. Experimental realization of non-Abelian non-adiabatic geometric gates. *Nature*, 496(7446):482–485, 2013.

[2] Vinay Ambegaokar and Alexis Baratoff. Tunneling Between Superconductors. *Physical Review Letters*, 10(11):486–489, jun 1963.

[3] Alain Aspect, Jean Dalibard, and Gérard Roger. Experimental Test of Bell's Inequalities Using Time- Varying Analyzers. *Physical Review Letters*, 49(25):1804–1807, dec 1982.

[4] Giovanni Barontini, Leander Hohmann, Florian Haas, Jérôme Estève, and Jakob Reichel. Deterministic generation of multiparticle entanglement by quantum Zeno dynamics. *Science*, 349(6254):1317–1321, sep 2015.

[5] Lev S. Bishop, J. M. Chow, Jens Koch, A. A. Houck, M. H. Devoret, E. Thuneberg, S. M. Girvin, and R. J. Schoelkopf. Nonlinear response of the vacuum Rabi resonance. *Nature Physics*, 5(2):105–109, feb 2009.

[6] Alexandre Blais, Ren-Shou Huang, Andreas Wallraff, S. M. Girvin, and R. J. Schoelkopf. Cavity quantum electrodynamics for superconducting electrical circuits: An architecture for quantum computation. *Physical Review A*, 69(6):62320, jun 2004.

[7] Robin Blume-Kohout. Optimal, reliable estimation of quantum states. *New Journal of Physics*, 12:43034, 2010.

[8] L. Bretheau, P. Campagne-Ibarcq, E. Flurin, F. Mallet, and B. Huard. Quantum dynamics of an electromagnetic mode that cannot contain N photons. *Science*, 348(6236):776–779, may 2015.

[9] John S. Bell. *On the einstein podolsky rosen paradox*. 1964.

[10] J. Claudon, A. Zazunov, F. W. J. Hekking, and O. Buisson. Rabi-like oscillations of an anharmonic oscillator: Classical versus quantum interpretation. *Physical Review B*, 78(18):184503, nov 2008.

[11] Claude N. Cohen-Tannoudji. The Autler-Townes Effect Revisited. In Raymond Y. Chiao, editor, *Amazing Light*, pages 109–123. Springer New York, 1996.

[12] Audrey Cottet. *Implémentation d'un bit quantique dans un circuit supraconducteur/Implementation of a quantum bit in a superconducting circuit*. PhD thesis, Université Pierre et Marie Curie-Paris VI, 2002.

[13] David K. Cheng. *Field and Wave Electromagnetics*. Addison-Wesley, Reading, Mass, 2nd edition edition, jan 1989.

[14] John Clarke and Alex I. Braginski, editors. *The SQUID Handbook, Volume 2: Applications of SQUIDs and SQUID Systems*. Wiley-VCH, Weinheim, 1 edition edition, sep 2006.

[15] M. H. Devoret and R. J. Schoelkopf. Superconducting Circuits for Quantum Information: An Outlook. *Science*, 339(6124):1169–1174, mar 2013.

[16] Oliver Dial, Douglas T. McClure, Stefano Poletto, G. A. Keefe, Mary Beth Rothwell, Jay M. Gambetta, David W. Abraham, Jerry M. Chow, and Matthias Steffen. Bulk and surface loss in superconducting transmon qubits. *Superconductor Science and Technology*, 29(4):44001, 2016.

[17] A. Einstein, B. Podolsky, and N. Rosen. Can Quantum-Mechanical Description of Physical Reality Be Considered Complete? *Physical Review*, 47(10):777–780, may 1935.

[18] P. Facchi, D. A. Lidar, and S. Pascazio. Unification of dynamical decoupling and the quantum Zeno effect. *Physical Review A*, 69(3):32314, mar 2004.

[19] P. Facchi and S. Pascazio. Quantum Zeno Subspaces. *Physical Review Letters*, 89(8):80401, aug 2002.

[20] P. Facchi and S. Pascazio. Quantum Zeno dynamics: mathematical and physical aspects. *Journal of Physics A: Mathematical and Theoretical*, 41(49):493001, 2008.

[21] Serge Haroche. College de France abroad Lectures-Quantum information with real or artificial atoms and photons in cavities. https://www.quantumlah.org/media/lectures/QT5201E-Haroche-Slides-3.pdf.

[22] Zdeněk Hradil, Jaroslav Řeháček, Jaromír Fiurášek, and Miroslav Ježek. 3 Maximum-Likelihood Methodsin Quantum Mechanics. In Matteo Paris and Jaroslav Řeháček, editors, *Quantum State Estimation*, number 649 in Lecture Notes in Physics, pages 59–112. Springer Berlin Heidelberg, 2004.

[23] Serge Haroche and Jean-Michel Raimond. *Exploring the Quantum*. Oxford University Press, aug 2006.

[24] G. Ithier, E. Collin, P. Joyez, P. J. Meeson, D. Vion, D. Esteve, F. Chiarello, A. Shnirman, Y. Makhlin, J. Schriefl, and G. Schön. Decoherence in a superconducting quantum bit circuit. *Physical Review B*, 72(13):134519, oct 2005.

[25] J. R. Johansson, P. D. Nation, and Franco Nori. QuTiP 2: A Python framework for the dynamics of open quantum systems. *Computer Physics Communications*, 184(4):1234–1240, apr 2013.

[26] B. D. Josephson. Possible new effects in superconductive tunnelling. *Physics Letters*, 1(7):251–253, jul 1962.

[27] Gerhard Kirchmair, Brian Vlastakis, Zaki Leghtas, Simon E. Nigg, Hanhee Paik, Eran Ginossar, Mazyar Mirrahimi, Luigi Frunzio, S. M. Girvin, and R. J. Schoelkopf. Observation of quantum state collapse and revival due to the single-photon Kerr effect. *Nature*, 495(7440):205–209, mar 2013.

[28] Jens Koch, Terri M. Yu, Jay Gambetta, A. A. Houck, D. I. Schuster, J. Majer, Alexandre Blais, M. H. Devoret, S. M. Girvin, and R. J. Schoelkopf. Charge-insensitive qubit design derived from the Cooper pair box. *Physical Review A*, 76(4):42319, oct 2007.

[29] P. J. Leek, M. Baur, J. M. Fink, R. Bianchetti, L. Steffen, S. Filipp, and A. Wallraff. Cavity Quantum Electrodynamics with Separate Photon Storage and Qubit Readout Modes. *Physical Review Letters*, 104(10):100504, mar 2010.

[30] D. T. McClure, Hanhee Paik, L. S. Bishop, M. Steffen, Jerry M. Chow, and Jay M. Gambetta. Rapid Driven Reset of a Qubit Readout Resonator. *Physical*

Review Applied, 5(1), jan 2016.

[31] Mazyar Mirrahimi, Zaki Leghtas, Victor V. Albert, Steven Touzard, Robert J. Schoelkopf, Liang Jiang, and Michel H. Devoret. Dynamically protected cat-qubits: a new paradigm for universal quantum computation. *New Journal of Physics*, 16(4):45014, 2014.

[32] B. Misra and E. C. G. Sudarshan. The Zeno's paradox in quantum theory. *Journal of Mathematical Physics*, 18(4):756–763, apr 1977.

[33] Madan Lal Mehta. *Random Matrices*. Academic Press, oct 2004.

[34] Y. Nakamura, Yu A. Pashkin, and J. S. Tsai. Coherent control of macroscopic quantum states in a single-Cooper-pair box. *Nature*, 398(6730):786–788, apr 1999.

[35] Simon E. Nigg, Hanhee Paik, Brian Vlastakis, Gerhard Kirchmair, S. Shankar, Luigi Frunzio, M. H. Devoret, R. J. Schoelkopf, and S. M. Girvin. Black-Box Superconducting Circuit Quantization. *Physical Review Letters*, 108(24):240502, jun 2012.

[36] Nissim Ofek, Andrei Petrenko, Reinier Heeres, Philip Reinhold, Zaki Leghtas, Brian Vlastakis, Yehan Liu, Luigi Frunzio, S. M. Girvin, Liang Jiang, Mazyar Mirrahimi, M. H. Devoret, and R. J. Schoelkopf. Demonstrating Quantum Error Correction that Extends the Lifetime of Quantum Information. *ArXiv:1602.04768 [quant-ph]*, feb 2016.

[37] Hanhee Paik, D. I. Schuster, Lev S. Bishop, G. Kirchmair, G. Catelani, A. P. Sears, B. R. Johnson, M. J. Reagor, L. Frunzio, L. I. Glazman, S. M. Girvin, M. H. Devoret, and R. J. Schoelkopf. Observation of High Coherence in Josephson Junction Qubits Measured in a Three-Dimensional Circuit QED Architecture. *Physical Review Letters*, 107(24):240501, dec 2011.

[38] David M. Pozar. *Microwave Engineering*. Wiley, feb 2004.

[39] J. M. Raimond, P. Facchi, B. Peaudecerf, S. Pascazio, C. Sayrin, I. Dotsenko, S. Gleyzes, M. Brune, and S. Haroche. Quantum Zeno dynamics of a field in a cavity. *Physical Review A*, 86(3):32120, sep 2012.

[40] J. M. Raimond, C. Sayrin, S. Gleyzes, I. Dotsenko, M. Brune, S. Haroche, P. Facchi, and S. Pascazio. Phase Space Tweezers for Tailoring Cavity Fields by Quantum Zeno Dynamics. *Physical Review Letters*, 105(21):213601, nov 2010.

[41] Matthew Reagor, Hanhee Paik, Gianluigi Catelani, Luyan Sun, Christopher Axline, Eric Holland, Ioan M. Pop, Nicholas A. Masluk, Teresa Brecht, Luigi Frunzio, Michel H. Devoret, Leonid Glazman, and Robert J. Schoelkopf. Reaching 10 ms single photon lifetimes for superconducting aluminum cavities. *Applied Physics Letters*, 102(19):192604, may 2013.

[42] M. D. Reed, L. DiCarlo, B. R. Johnson, L. Sun, D. I. Schuster, L. Frunzio, and R. J. Schoelkopf. High-Fidelity Readout in Circuit Quantum Electrodynamics Using the Jaynes-Cummings Nonlinearity. *Physical Review Letters*, 105(17):173601, oct 2010.

[43] Chad Rigetti, Jay M. Gambetta, Stefano Poletto, B. L. T. Plourde, Jerry M. Chow, A. D. Córcoles, John A. Smolin, Seth T. Merkel, J. R. Rozen, George A. Keefe, and others. Superconducting qubit in a waveguide cavity with a coherence time approaching 0.1 ms. *Physical Review B*, 86(10):100506, 2012.

[44] D. Ristè, C. C. Bultink, M. J. Tiggelman, R. N. Schouten, K. W. Lehnert, and L. DiCarlo. Millisecond charge-parity fluctuations and induced decoherence

in a superconducting transmon qubit. *Nature Communications*, 4:1913, may 2013.

[45] Adrien Signoles, Adrien Facon, Dorian Grosso, Igor Dotsenko, Serge Haroche, Jean-Michel Raimond, Michel Brune, and Sébastien Gleyzes. Confined quantum Zeno dynamics of a watched atomic arrow. *Nature Physics*, 10(10):715–719, oct 2014.

[46] Pierre Six, Philippe Campagne-Ibarcq, Igor Dotsenko, Alain Sarlette, Benjamin Huard, and Pierre Rouchon. Quantum state tomography with non-instantaneous measurements, imperfections and decoherence. *Physical Review A*, 93(1), jan 2016.

[47] D. Vion, A. Aassime, A. Cottet, P. Joyez, H. Pothier, C. Urbina, D. Esteve, and M. H. Devoret. Manipulating the Quantum State of an Electrical Circuit. *Science*, 296(5569):886–889, may 2002.

[48] Brian Vlastakis, Gerhard Kirchmair, Zaki Leghtas, Simon E. Nigg, Luigi Frunzio, S. M. Girvin, Mazyar Mirrahimi, M. H. Devoret, and R. J. Schoelkopf. Deterministically Encoding Quantum Information Using 100-Photon Schrödinger Cat States. *Science*, 342(6158):607–610, nov 2013.

[49] A. Wallraff, D. I. Schuster, A. Blais, L. Frunzio, R.-S. Huang, J. Majer, S. Kumar, S. M. Girvin, and R. J. Schoelkopf. Strong coupling of a single photon to a superconducting qubit using circuit quantum electrodynamics. *Nature*, 431(7005):162–167, sep 2004.

[50] Frederick C. Wellstood, Cristian Urbina, and John Clarke. Low-frequency noise in dc superconducting quantum interference devices below 1 K. *Applied Physics Letters*, 50(12):772–774, mar 1987.

[51] Yi Yin, H. Wang, M. Mariantoni, Radoslaw C. Bialczak, R. Barends, Y. Chen, M. Lenander, Erik Lucero, M. Neeley, A. D. O'Connell, D. Sank, M. Weides, J. Wenner, T. Yamamoto, J. Zhao, A. N. Cleland, and John M. Martinis. Dynamic quantum Kerr effect in circuit quantum electrodynamics. *Physical Review A*, 85(2):23826, feb 2012.

[52] X. Zhou, V. Schmitt, P. Bertet, D. Vion, W. Wustmann, V. Shumeiko, and D. Esteve. High-gain weakly nonlinear flux-modulated Josephson parametric amplifier using a SQUID array. *Physical Review B*, 89(21):214517, jun 2014.

[53] CST Microwave Studio.

[54] Louis N. ridenour (edito-in-chief and R. H. Dicke Montgomery, E. M. Purcell C. G., editors. *Radiation Laboratory Series*. McGraw-Hill Book Company, 1948.